REPUBLIQUE ALGERIENNE DEMOCRATIQUE ET POPULAIRE

MINISTERE DE L'ENSEIGNEMENT SUPERIEUR ET DE LA RECHERCHE SCIENTIFIQUE

UNIVERSITE DES SCIENCES ET DE LA TECHNOLOGIE SAAD DAHLEB DE BLIDA

FACULTE DES SCIENCES DE L'INGENIEUR

DEPARTEMENT D'ELECTRONIQUE

MEMOIRE DE MAGISTER

Thème

STUDY AND TEST OF A SOLAR ASTROLABE FOR TAMANRASSET OBSERVATORY

Présentée par DJAFER DJELLOUL Sous la Direction de Dr IRBAH ABDENOUR (C.R.A.A.G) et M. NAMANE ABDERAHMANE (U.S.T.S.D)

Composition du jury :

Président	**Ben SEBTI Messaoud**	**Maître de conférences**	**U.S.T.S.D**
Examinateur	**SADSAOUD Hamid**	**Maitre de Recherches**	**C.R.A.A.G**
Examinateur	**SMARA Youcef**	**Maître de conférences**	**U.S.T.H.B**
Invité	**NOUREDINE Mohamed**	**Maître de conférences**	**I.N.E.L.E.C**

Année universitaire : 2001/2002

People's Democratic Republic of Algeria

Ministry of Higher Education & Scientific Research

University of Blida

Faculty of Engineering
Department of Electronics

Thesis Report

Presented in Partial Fulfillment of the Magister Degree

Title

STUDY AND TEST OF A SOLAR ASTROLABE FOR TAMANRASSET OBSERVATORY

Presented by

DJAFER Djelloul

Jury members:

Chairman:
Mr.BENSEBTI Messaoud (Maître de Conférences, Université de Blida)

Examiners:
Mr.SADSAOUD Hamid (Maître de Recherches, C.R.A.A.G)
Mr. SMARA Youcef (Maître de Conférences, U.S.T.H.B)

Supervisor:
Mr. IRBAH Abdenour (Maître de Recherches, C.R.A.A.G)

Co-supervisor:
Mr. NAMANE Abderrahmane (Chargé de cours, Université de Blida)

Guest :
Mr.NOUREDINE Mohammed (Maître de Conférences, I.N.E.L.E.C)

Date:

To my beloved mother.
To my beloved father.
To my friends and sisters.

GENERAL INTRODUCTION

Among the important quantities in astronomy and astrophysics there is the Sun diameter. From this quantity, the ephemeredes are established, the dates of contacts for the solar eclipses are calculated, and the standard solar models are elaborated. In parallel with the astrophysical studies of the Sun, astrometric observations may lead to improved values for this particular reference. The measurement of the solar diameter is not as simple as may be thought. During the last centuries and years a big discussion and disputation about its constancy and variation took place.

Following the suggestions of Newcomb (1835-1909) during the "Conférence internationale des étoiles fondamentales" held in Paris in 1896, a set of astronomical constants was adopted [1]. Astronomers were asked to use it in order to ensure an easy comparison of measurements made in different observatories. The adopted solar parallax was equal to 8″.26. For the semi-diameter of the Sun, the value 959″.63 was given, based on a study made by Auwers (1838-1915) in Berlin [1]. In 1891, Auswers gave two values of Sun diameter in his conclusion. The first one is the above-adopted value, which is obtained from a large set of Heliometer observations. The second one, which is obtained from observations made with transit instruments, is 962″.73 . The difference of 3″.10 in diameter (1″.55 in the radius) between them was considered as due to a so-called irradiation. From that time, the ephemeredes (Nautical Almanac, Connaissance des Temps, American Ephemeris,) use the second value under the form of Sun semi-diameter 16′ 1″.18 (961″.18) for the eclipses and the value 15′59″.63 (959″.63), with the corresponding variations due to the changes in the distance between the Earth and the Sun, for the ephemeredes [1].

Many authors, mainly since the beginning of the 19th century, have studied the problem of Sun diameter variations using a long series of Sun diameter data. Among them, we can mention Sofia et al, who found a decrease of 0″.010 per year over the period 1925-1979 [2] and a decrease of 0″.019 per year between 1700 and 1990 [3]. In contrast, other authors have found irregularities, for example Leone (1973)[43] and Dunham (1980)[44] gave values of Sun diameter variations between 1″ and fractions of it. At Calern observatory in France, Laclare.F has been fortunate enough to be able to obtain a long series of solar diameter measurements. He has found relatively short-term variations by using Fourier analysis [1]. Such variations and discrepancies in the solar diameter are not a new phenomenon; they can be seen from modern analysis of observations in the past. An example is to be found in a preliminary work by Smith and Messina [4] from which the following values for the horizontal diameter of the Sun were given [1],

- At Capetown the Sun semi-diameter is 961″.21 ± 0″.10 for 10 annual means from 1837 to 1887
- At Paris the value is 961″.89 ± 0″.16 for 25 annual means from 1837 to 1906.

The annual means of these 19th century observations, given by the authors, are based on a total number of transits, which are 798 for the Capetown and 2461 for Paris. But, as noticed by Smith and Messina, the long series have not been performed with the same instrument and, of course, due to their length, by the same observer.

The usage of early measurements to investigate long-term trends in the solar diameter started with the pioneering work of Eddy and Boornazian [45]. These authors deduced from the Greenwich meridian circle observations between 1936 and 1953 that the solar diameter had shown a secular decrease at a mean rate of 0.8″ per century. However, this result was disputed by Pakinson *et al.* [46] who criticized Eddy and Boornazian's interpretation of the Greenwich data and demonstrated that different observers obtained discordant results with the same instrument [5]. They also shown that series analysis of timing of both Mercury transits and the total solar eclipses since 1715 revealed no evidence of a secular decrease in the solar diameter. Soon afterwards, Gilliland (1981)[47], by combining circle measurements since 1836 with mercury transit data since 1715, suggested that a secular decrease in the solar diameter by 0.1″/century was "likely". Débarbat (1982) deduced that measurements of the horizontal Sun diameter at noon between 1666 and 1673 revealed irregularities of periodical nature. Subsequently, Ribes *et al.* made an analysis of 50 year measurements using Picard and La Hire between 1666 and 1718 and their results indicated that around 1700 the solar diameter was some 4″ greater than it is now [1]. Selections of the ancient and recent values of Sun semi-diameter are summarized in Table 1.

Author	Date of publication	Radius of Sun(″)	Used Method	Number of measurements/period
Mouton	1660	959.4±3.3	PP	86
Auzout	1666	965.2±0.2	MI	2
Picard	1670	964.6±0.2	MI	304
Richer	1672	961.9±5.2	DP	26
Picard	1674	962.9±3.5	DP	154
La Hire	1683	963.2±2.8	MI	14
La Hire	1684	965.4±3.8	DP	304
La Hire	1701	963.6±3.8	DP	6980
Louville	1724	962.4±2.0	DP	10
Bouguer	1753	957.3±2.0	DP	105
Lalaude	1764	961.4±1.5	HE	12
Lalaude	1764	961.4±1.5	HE	12
Bessel	1824	960.9±1.4	ME	92
(Airy)	1837	960.9±1.4	ME	92
Goujon	1842	962.2±0.7	ME	1575
(Smith –M)	1877	961.5±0.7	ME	1363
Auwers	1880	959.6±0.5	HE	2840
(Gething)	1895	961.04±0.44	ME	10302
Schur	1896	960.07±0.55	ME	760
Ambronn	1897	959.9±0.6	HE	920
(Cimino)	1907	961.34±0.54	ME	27249
(Smith-M)	1946	961.34±0.20	ME	3468
Wittman	1973	960.24±0.16	DTIL	Year 1972
Wittman	1973	960.013±0.16	DP	20
Wittman	1974	960.0±0.8	DP	246
Wittman	1978	960.29±1.8	PP	2159
Duvall&al	1980	959.50±0.10		Year 1979-1980
Sofia,Dunham, Fiala	1980	959.77±0.06	SE	Year 1978
Wittman	1981	960.26±0.04	DTIL	May-June 1981
(Ribes)	1981	961.2±0.5	ME	349

Leister	1984	959.4±0.8	AS	804
Journet	1984	959.03±0.4	AS	1170
Laclare	1978	959.4±0.3	AS	8000
Leister	1988	958.84±0.07	AS	1982.5-1986
Laclare	1988	959.45±0.02	AS	2679(1975-1987)
Journet	1988	959.03±0.02	AS	1176
Wan Lai&Zhao Jun-Liang	1989	959.65±0.02	AS	Year 1989
Sato &Soma	1989	959.64±0.02	SE	Year 1987
Leister&Benevides Soares	1990	959.03±0.02	SE	Year 1989
Noel	1991	960.8±0.6	AS	189
Ribes	1991	959.32±0.02	PHM	1981-1991
Wittman	1991	960.66±0.02	LDO	1986-1990
Maiev,Twigg& Sofia	1992	959.60±010	SDSBF	
Kubo	1993	959.82±0.02	SE	1980
Akimov	1993	959.82±0.04	SE	1991
Wittman	1993	960.66±0.02	DTIL	1993
Sofia,Heaps&Twigg	1994	959.53±0.06	SDSBF	1994
Bode,Buchner &Musharot	1995	959.66±0.04	SE	1985
Noel	1995	960.64±0.10	AS	1990-1994
Neckel	1995	960.64±0.03	LDS	72
Wittman	1997	959.73±0.05 960.53±0.02	DS CCD	126/1996 427/1996
Brown&Christensen Dalsgaard	1998	959.68±0.02	SDM	1998
Kliliç	1998	959.33±0.05	SA(2prismes)	170/1998
Sanchez	1998	959.33±0.04	SCCDA	100/1998
Noel	1998	959.85±0.03 960.50±0.03 960.39±0.13	SA (2 prismes)	123/1996 120/1997 822/1990-1997
Sato &Soma	1998	959.64±0.02	SE	1987
Jilinki	1998	959.20±0.02	SCCDA	3500/1996-1997
Sinceac	1998	959.45±0.01	SA	349/1996-1997
Jilinski et al.	1999	959.14±0.03	SCCDA	2600/1996-1997
Laclare et al.	1999	959.60±0.01	SA	418/1996-1998
Delmas	2000	959.52±0.01	DORaySol	266/1999

Table 1. Solar Diameter Observations. PP: Projected transit time, MI: micrometer, HE: heliometer, ME: transit time at meridian circle, AS: solar astrolabe, SDM: solar diameter monitor, SCCD: solar astrolabe with CCD, DTIL: drift timing in Izana & lacarno, SE: solar eclipse, SDSBF: solar disk sextant on balloon flight, PHM: Photoelectric measurement, LDO: limb darking observation. DS CCD: drift scan CCD. LDS: Limb darking Scans.

The observed variations of solar diameter in the past based on classical techniques have given inconclusive results [6]. The principle of these classical methods is based on timing the meridian transits of Sun borders. However, since the interval of data is more or less 9 years, they are not useful to disclose eventual variations of Sun diameter that is connected with 11 years, the period of solar activity [6,7]. In addition the observation of meridian transits gives individual results of relatively low precision. Nevertheless, its accuracy can be improved by accumulating many observations in a short time period making them comparable with more precise techniques such as solar eclipses. However, all these methods are strongly affected by several types of systematic errors [6]. Many instruments may be adopted to measure the Sun radius. The one that has shown its performance and permitted collections of a huge set of data is the solar astrolabe [8,9].

The solar astrolabe, which is a modified version of Danjon astrolabe, has some advantages over the meridian circle [10]. For instance, the later can give only two measurements during a day (horizontal and vertical radius), where the astrolabe gives a number of measurements that is twice the number of observing zenithal distances. Furthermore, the astrolabe provides a compact and a more stable local reference defined by the mercury mirror and the angle of the prism (see chapter II). The meridian circle is a more complicated instrument. Its precision depends on three instrumental parameters that are not easily controlled, especially in the quite critical environmental conditions that are prevalent during Sun observations [11]. In the other hand and according to Cullen, the effect of irradiance on meridian observations of the Sun is variable, since it depends on the Sun zenithal distance. For the astrolabe and for a given zenithal distance this effect should be constant [6].

The experiment of visual measurement of Sun diameter using an adapted Danjon astrolabe has been initiated in 1975 by F.Laclare at Calern observatory (France). Since this date and during more than two solar cycles, diameter measurements were regularly recorded. These visual observations revealed evidence of oscillations in the solar data; see Figure 1(a) [9,11]. The same experiment has begun at Sao Paulo (Brazil) in 1974 and more lately at Santiago (Chile), in 1990. Oscillations of Sun semi-diameter were always noticed.

The mean error source in visual measurement of Sun diameter is the observer's estimation of the Sun transit instant. This is due of course of the fact that each observer has his way of observation and his own eye spectrum. In 1989, in order to eliminate this error and improve the diameter measurement accuracy, some modifications were brought to the solar astrolabe. The main ones are the introduction of a CCD camera and a system of acquisition [11]. A comparison of the two measurement sets of Sun diameter (visual and CCD) made during the same time period have shown good agreement between them [12]. From that time, the two methods of measurement are operating together. A CCD astrolabe of the same type as that of the Calern instrument but equipped with a variable prism started operating at the National Observatory of Rio de Janeiro in January 1997, and the recent values still show variation; see Figure 1(b).

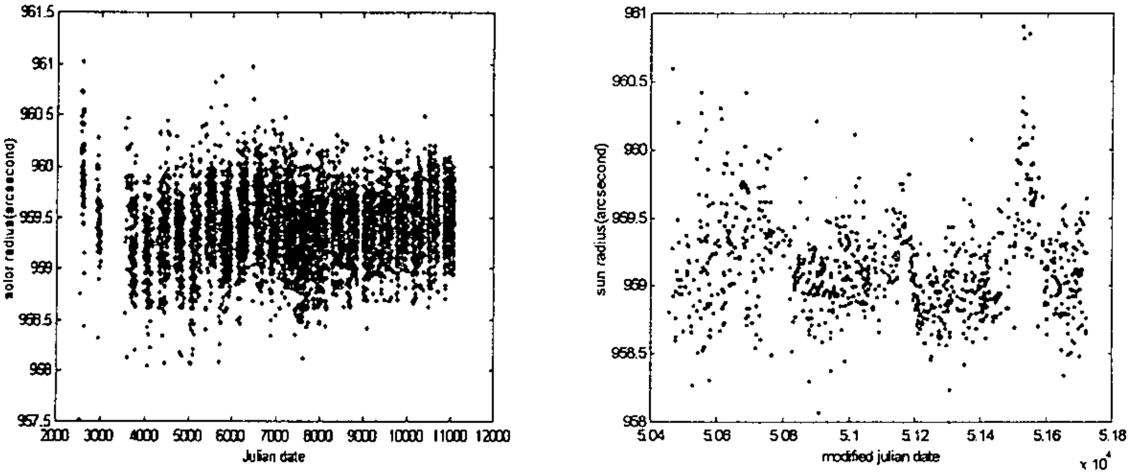

(a) *(b)*

Figure 1. (a) Solar radius measurement obtained with Calern observatory astrolabe. (b) Solar radius measurement obtained with Rio de Janeiro astrolabe during 1997 to 2000 (West observation).

The principal cause of the variability of the Sun is its magnetic field. The theoretical studies have shown that its predominant effect is a surface effect [14]. The theory of the stellar structure foresees that the variations of the radius associated with magnetic activity are of the order of 10^{-7}, a non-measurable quantity [14]. According to the theory, the solar radius is a quantity that, at the actual level of observation precision, depends only on the basic physics, while the apparent variations of the observed radius are very high, about $0''.4$ over a magnetic cycle [12]. It is very difficult to interpret these results, since we do not know if these observed variations reflect real variations of the Sun radius, or are the effects of other phenomena less known. The variations may also come from the fact that the real observed radius belongs to the solar atmosphere, a fluid medium, that is subjected to a big density variations, temperature changes and tide effect. But, if real variations of the radius, or one portion, are original variations, serious constraints will be subjected to the theory of the stellar structure. So, it is absolutely necessary to ameliorate the observation techniques in order to understand more precisely the origin of Sun diameter variations. Conjointly, the other phenomena that can have an effect on the measurement of the Sun radius must be well studied. These complex phenomena whose effects remain poorly known are the terrestrial atmosphere variability, solar atmosphere and the instruments used.

In 1966, results were announced of a measurement series of the solar flattening done at Princeton, that implicated the theory of the general relativity of Einstein. These measurements showed a difference $\Delta r=0''.0866\pm0''.0066$ between the polar radius and the equatorial radius, with a quadrupolar moment $J_2=2.47\pm0.23.10^{-5}$ [15]. The advance of the perihelia of Mercury's orbit, which is also related to Sun flattening, is one of the most interesting tests of the general relativity. Now then, the quadrupolar moment found by the observations found out an acceleration of the perihelia different of that general relativity might explain. [16]. The big discussion launched by these results has opened the way to other experiments, intended to measure the Sun flattening. These experiences have found values more and well moderated for the flattening, confirming the first results. So, the observations done with the Solar Disk Sextant have given a value $J_2=1.8.10^{-7}$, with all uncertainties taken into account, which remain compatible with the estimations of the general relativity [14]. A recent analysis of the heliosismological data obtained by the satellite **SOHO** (Solar Heliospheric Satellite) confirms the last values obtained by direct measurement of Sun flattening [14].

The analysis of all flattening data showed also a variation with the solar cycle and the method of measurement. The variations of Sun flattening seemed to be conforming to those of the observed solar radius with the astrolabe [16]. Measurements with the solar astrolabe have also put in evidence a radius dependent on the heliographic latitude, be the Sun flattening. Still, to have a good measurement of the variation of the Sun flattening, it is necessary to do a dense series of observations during a long period of time and with many methods and instruments.

The various studies oriented to the ancient and recent measurement have shown that the solar variability has an influence on the terrestrial climate [18]. A good correlation was found between the variation of the period of the solar cycle and the anomalies of the temperature of the north hemisphere. In addition, between the variations of the measured values of Carbon 14 and the number of sunspots [14]. A relation has been found between the variability of the solar diameter and the stratospheric wind to a period of 1000 days. This shows that the solar variability induces in one part the variations of the observed radius, and in the other part it forces the circulation of the stratospheric winds [17]. The data of Sun semi-diameter obtained at Calern observatory extends during 24 years was compared to some solar activities and measurements. Figure 2 shows Sun semi-diameter variations and sunspot numbers. We notice that there exists an anticorrelation between them . This result confirms the work of Gilliland [12,13], which was established using observations from Washington and Greenwich. The same anticorrelation is naturally found with the irradiance data [13], since the solar activity and the irradiance are correlated [13]. Figure 3(a) represents a best anticorrelation between Calern semi-diameter data and the shifts of low-degree heliosismological pressure p-modes observed during the cycle [12,13]. In 1984, Delache linked the variations of the observed diameter with the neutrino flux measurements [8], and in 1988 Gough mentioned an eventual connection between sunspot number, solar neutrino, and the Sun diameter. This connection between the observed diameter and the neutrino flux is seen to be correlated; see Figure 3(b)

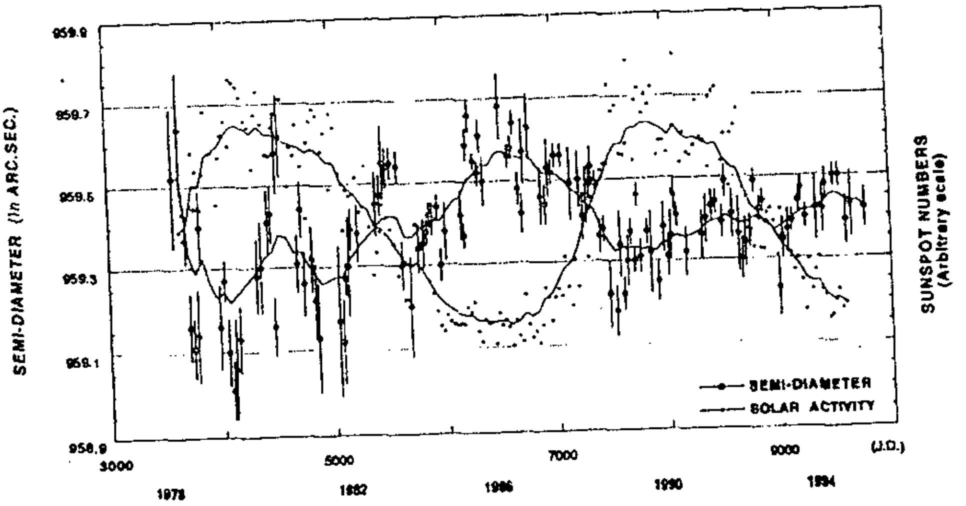

Figure 2. Semi-diameter variations and Sunspot numbers.

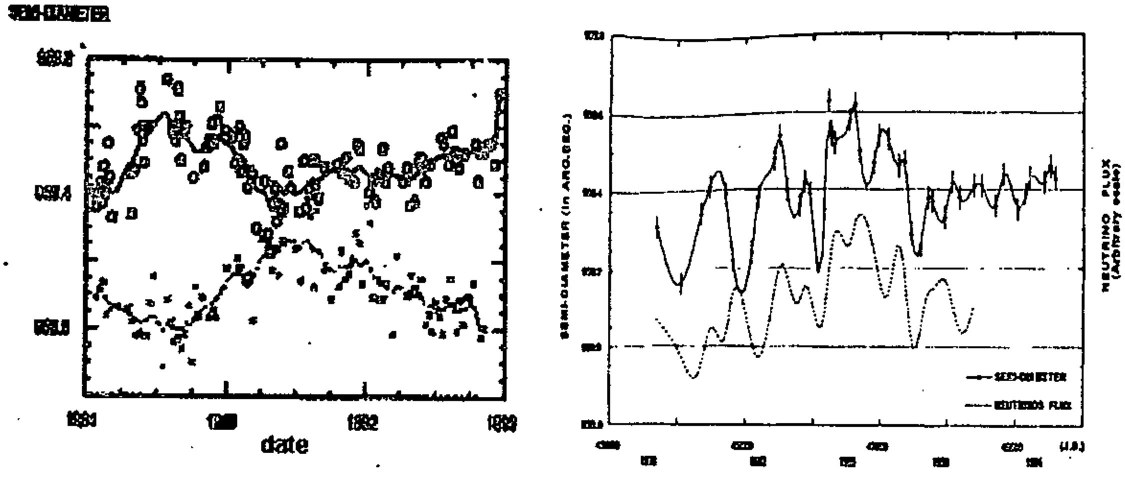

(a) *(b)*

Figure 3. (a) Semi-diameter and p-modes frequency shifts [13]. (b) Semi-diameter variation and neutrino flux [13].

It is for the objective to respond to the problematic imposed by the solar diameter measurement along the time and the observed variations, that a solar experiments are realized and others in progress to perform the measurement in a high angular resolution of this parameter. Between these experimentations we have,

- The astrolabe network distributed in latitude.

- **DORaySols** (Definition et Observation du Rayon Solaire): They are a new generation of automatic solar astrolabes. They are equipped with an acquisition system, a CCD càmera and a prism of variable angle. These prisms allow performing several measurements during a day (3000 measurements a year) [13].

- **Picard** (The name given to this mission to rend homage to the French astronomer who has effectuated measurements of Sun diameter): This spatial micro-satellite will be launched in 2005-2007 for 3 to 4 years. Its main objectives are the measurement of Sun diameter and the solar irradiance. These measurements will permit the comparison of the results deduced from space and the ground as well as the evaluation of the atmospheric turbulence.

- **Sodism II:** it is a replica of the Picard's telescope on the ground. It will be installed at Calern observatory (France).

- **M.I.Sol.F.A.** (Monitor d'Images Solaires Franco-Algérien). It is a monitor of image quality, which will give the information of the Earth atmosphere state at the moment of observation. This instrument will be installed just near DORaySol an Sodism II at Calern observatory.

Picard, Sodism II, and Misolfa will all observe at the same time. They will be used to define the effects induced by the Earth's atmosphere on ground measurements done by the astrolabes that will continue to observe for a long period of time.

To validate the semi-diameter variations observed with astrolabes, we must have a huge data sets record under good conditions, during a long period of time and with a minimum period of discontinuities. So, it is necessary to have,

- A site where the meteorological conditions and the atmospheric turbulence are favorable for this type of experiment.

- A location where the Sun is always so high on the sky during all the year to limit the effects of atmospheric refraction.

- Automatic instruments that permit the collection of huge data sets of Sun diameter measurement.

For that reason, a ground network of solar astrolabes (DORaySol) installed at different latitudes is necessary. The actual ground astrolabe network contains two DORaySols currently in operation, the one of Calern (France) and Rio de Janeiro(Brazil) observatories. The third one will be that of Tamanrasset observatory, which will be installed soon. Figure 4 presents the ground DORaySol network.

Figure 4. The ground network solar astrolabes.

A preliminary meteorological study of Tamanrasset observatory, where the astrolabe will be installed, has been done over the last 3 years. This study has shown a mean humidity of 20.5%, a mean atmospheric pressure of 866.4 hp, a mean nebulosity of 2 octas, a mean temperature of 22.8 °C, and a mean wind speed of 3.7 m/s (see Annex 1). This preliminary study supports that Tamanrasset observatory would be a favorable place for this type of observation. In addition, its location allows the collection of a huge data sets of Sun diameter measurements. With DORaySol installed it will permit collections more than 4000 diameters per year. This can be deduced from Figure 5 that represents the Sun trajectory for Tamanrasset observatory.

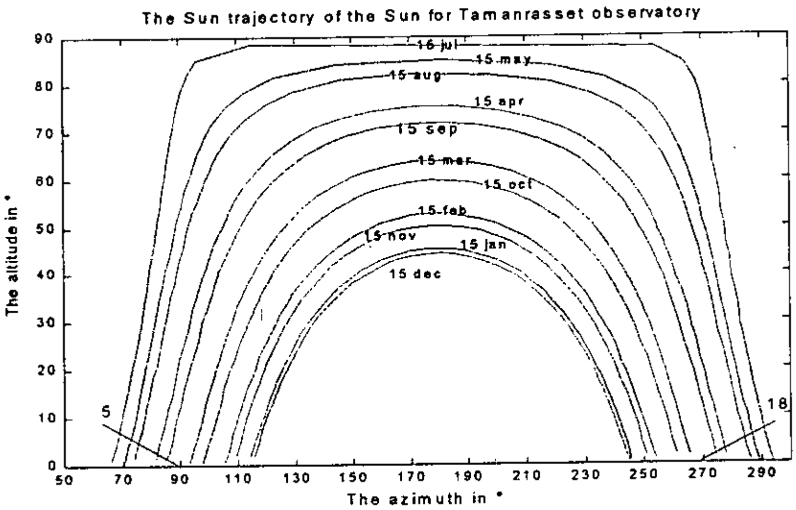

Figure 5. Sun trajectory for Tamanrasset observatory.

The present work is oriented, after the study of the astrolabe, its principle of operation and the theory behind the Sun diameter measurement, to:

1- Look for the suitable method to process the Sun images, develop the necessary techniques to extract the Sun edge and build the procedures to calculate the Sun diameter.

2- Study of the measurement quality with the CCD astrolabe and the effect of the atmospheric turbulence on Sun diameter measurement.

3- Chose and build the acquisition system that will be installed around the solar astrolabe of Tamanrasset and provide the necessary programs for its operation.

In chapter I we present the theory behind the principle of Sun semi-diameter measurement. All the parameters that enter in Sun diameter calculation and all the necessary corrections that must be taken into consideration are introduced. In addition, the reduction procedure will be given.

Chapter II describes the astrolabe and the different transformations to which it is subjected. It presents the experimental principles of Sun diameter measurement and the related problems.

The object of chapter III consists in presenting the wavelet transform and its characteristics that are suitable for Sun images, which present non-stationary defects. In addition, it describes the two algorithms (the Mallat's algorithm and the *à trous* algorithm) used to implement this processing method. Finally, it presents the different steps to extract the Sun image edge and the way to determine the transit instants of the Sun through the defined height circles.

Chapter IV is an application of the wavelet transform to two sets of Sun images acquired by the solar astrolabe of Calern. A comparison between the two algorithms to implement the wavelet transform of is presented. Also the methods to calculate the error on the Sun semi-diameter measurement and the error on the transit instants determination are given. Finally the relation between these two types of errors with the atmospheric turbulence characterized by the Fried parameter are discussed.

In chapter V, the main work is oriented to select the acquisition system and to implement the software that pilots the astrolabe of Tamanrasset. The different elements of the proposed acquisition system are tested in the laboratory for future installation around the astrolabe.

CHAPTER I SUN RADIUS MEASUREMENT THEORY

After a brief describing of some aspects of celestial mechanics that introduce the different coordinate systems on the sky and on the Earth, this chapter gives the principle of Sun diameter measurement. The necessary corrections that must be applied to this measurement are presented. Finally, the steps details to calculate the Sun diameter will be given.

I.1 Celestial sphere

The Celestial sphere is an imaginary spherical surface. It is centred on the observer on which the stars and planets have apparently been placed. Its radius is infinite. The boundary between the visible and invisible portions of the celestial sphere is called the Horizon. The poles of the horizon, those points directly overhead and beneath, are called the Zenith and the Nadir.

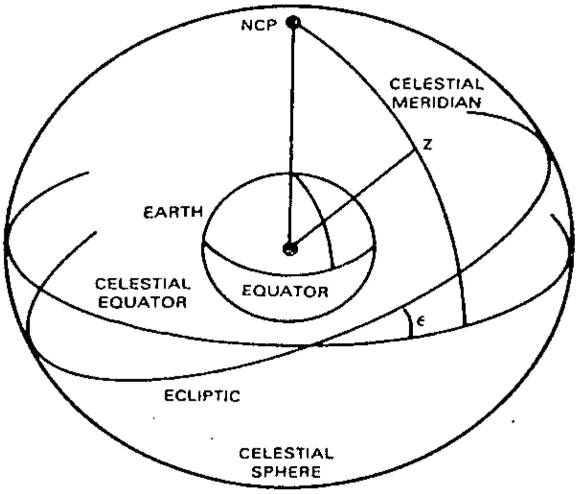

Figure I-1. Celestial sphere with principal great circles (ecliptic, celestial equator, celestial meridian) indicated, NCP marks the North Celestial Pole, Z the astronomical zenith and ε is the obliquity of the ecliptic.

The celestial sphere appears to rotate around a fixed axis. This point is known as the North Celestial Pole (NCP) in the northern terrestrial hemisphere and South Celestial Pole (SCP) in the southern terrestrial hemisphere. The axis of the Earth's rotation pierces the celestial sphere in these two points. The great circle passing through the celestial poles and the Zenith is called the celestial meridian. Clearly, it also passes through the Nadir. The celestial meridian intersects the horizon at the north and south points. The great circle passing through the astronomical Zenith and Nadir and orthogonal to the celestial meridian at the Zenith, is called the prime vertical; see Figure I-1.

The Sun and planets move in a nearly coplanar fashion on the celestial sphere. This plane is approximately that of the ecliptic (the intersection of the instantaneous mean orbital plane of the Earth with the celestial sphere). The angle between the ecliptic and the celestial equator is known as the obliquity of the ecliptic. It is about 23°.5. The two intersections of the ecliptic with the celestial equator are known as the equinoctial points.

I.2 Celestial coordinate systems

Celestial coordinates fix the location of an object on the sky. There are various systems suitable for different purposes. Each needs a fundamental circle and a fixed point; see Figure I-2.

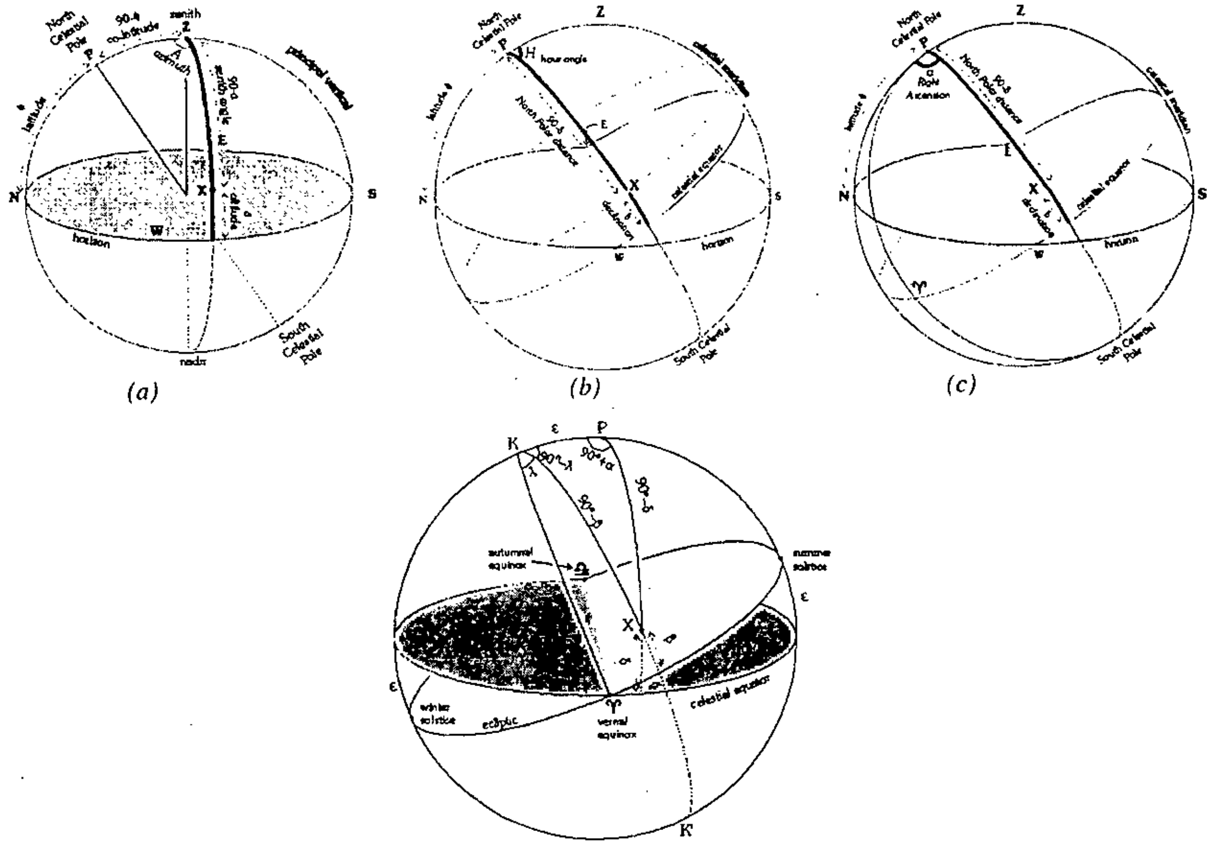

(a) (b) (c)

(d)

Figure I-2. (a) Definition of the horizontal coordinate system.(b) Definition of The HA-dec coordinate system.(c) Definition of the RA-dec coordinate system. (d) Definition of the ecliptic coordinate system.

(1) Horizontal or "alt-az" system: The horizontal or alt-az system depends on a place (because the sky appears different from different points on Earth) and on time (because the Earth rotates, and each star appears to trace out a circle centred on the North Celestial Pole). The altitude *(a)* of an object X is the angular distance along the vertical circle from the horizon to X. It is measured from -90° at Nadir to +90° at Zenith. Alternatively, the zenithal distance (z) of X is (90° - altitude). Any two objects with the same altitude lie on a small circle called a parallel of altitude (Almucantar, or the small circle). The azimuth (A) of an object X is the angular distance around the horizon from the north cardinal point to the vertical circle through X. It is measured from 0° to 360° westwards (clockwise), see Figure I-2(a).

(2) Equatorial or "HA-dec." system: It is a system of celestial coordinates which is fixed on the sky and independent of the observer's time and place. The fundamental circle for this system is changed to the celestial equator. To fix the coordinates of an object X on the celestial sphere, we draw the meridian through X. The declination *(δ)* of X is the angular distance from the celestial equator to X. It is measured from -90° at the SCP to +90° at the NCP. Any point on the celestial equator has declination 0°. Alternatively, the North Polar Distance of X is "90° - declination". Any two objects with the same declination lie on a parallel of declination. The Hour Angle (H) or HA of object X is the angular distance between the meridian of X and the celestial meridian. It is measured clockwise in hours; see Figure I-2(b).

(3) Equatorial or "RA-dec." system: The first equatorial system (HA and declination) is still tied to the observer's here-and-now. For this system, a fixed point is chosen on the celestial equator called the vernal equinox or the First Point of Aries. The declination *(δ)* of object X is measured in the same way as before. The Right Ascension *(α)* or RA of object X is the angle along the celestial equator measured counter clockwise from the vernal equinox to the meridian of X. Like HA, RA is measured in hours 0-24h but it goes in the opposite direction. The relationship between the hour angle and right ascension is given by :

$$H = ST - \alpha \tag{I.1}$$

Where TS is Sidereal Time and at the same time the hour angle of the vernal equinox.

(4) Ecliptic coordinate system: The apparent path followed by Sun is called the ecliptic. In the ecliptic system , the fundamental great circle is the ecliptic. The zero-point is still the vernal equinox. K is the northern pole of the ecliptic and K' is the southern one. To fix the ecliptic coordinates of an object X on the celestial sphere, we draw the great circle from K to K' through X. The ecliptic (or celestial*)* latitude of X (β) is the angular distance from the ecliptic to X, measured from -90° at K' to +90° at K. Any point on the ecliptic has ecliptic latitude 0°. The ecliptic (or celestial) longitude of X (λ) is the angular distance along the ecliptic from the vernal equinox to the great circle through X. It is measured eastwards (like R.A.) but in degrees, 0°-360°.

I.3 Conversion between system coordinates

To convert between the horizontal and equatorial coordinates for an object X, we use the Astronomical Triangle XPZ, see Figure I-3 (a), with help of cosine and sine rules (see Annex 2). To convert between ecliptic and equatorial coordinates we use the Astronomical Triangle KPX (Figure I-3(b)) and the equations of the sine and the cosine rules.

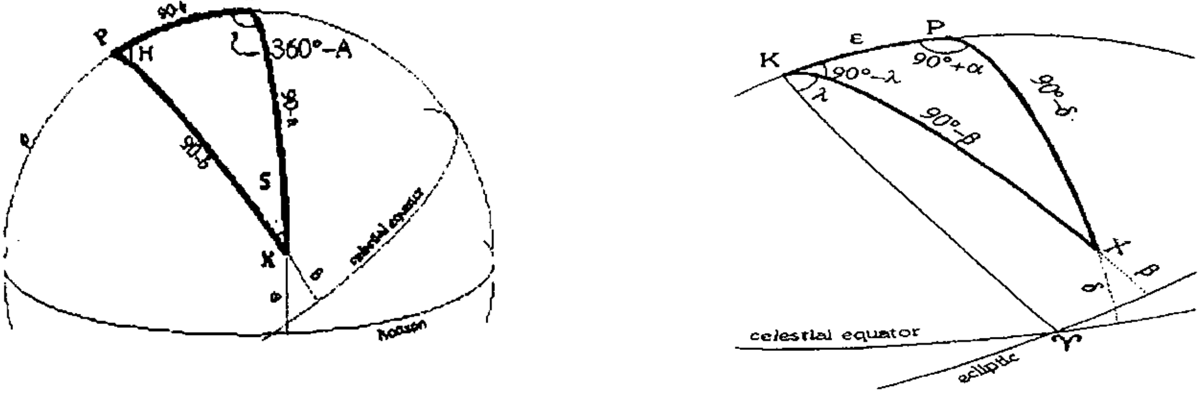

(a) *(b)*

Figure I-3. (a) The Astronomical triangle to convert between horizontal and equatorial coordinates. Z is the zenith, P is the North Celestial Pole, X is the object, H the hour angle, a the right ascension, δ the declination and S the parallactic angle(b). *The astronomical triangle to convert between ecliptic and equatorial coordinates, K is the ecliptic pole, P the NPC, δ the declination, β the ecliptic latitude, λ the ecliptic longitude and ε the obliquity.*

For the transformation from horizontal and equatorial coordinates, the following equations are deduced,

$$\cos z = + \sin \varphi \sin \delta + \cos \varphi \cos \delta \cos H$$

$$\sin z \cos A = -\cos\varphi \sin\delta + \sin\varphi \cos\delta \cos H \qquad (I.2)$$

$$\sin z \sin A = \cos\delta \sin H$$

$$\sin z \cos S = +\sin\varphi \cos\delta - \cos\varphi \sin\delta \cos H$$

$$\sin z \sin S = \cos\varphi \sin H \qquad (I.3)$$

$$\sin\delta = +\sin\varphi \cos z - \cos\varphi \sin z \cos A$$

$$\cos\delta \cos H = +\cos\varphi \cos z + \sin\varphi \sin z \cos A \qquad (I.4)$$

$$\cos\delta \sin H = \sin z \sin A$$

$$\cos\delta \cos S = +\sin\varphi \sin z + \cos\varphi \cos z \cos A \qquad (I.5)$$

$$\cos\delta \sin S = \cos\varphi \sin A$$

where A is the azimuth, z the zenithal distance, φ is the observer latitude, δ is the declination, S the parallactic angle and H the hour angle.

I.4 Geographic coordinate systems

There is quite a variety of local and global coordinate systems that may be used to describe locations on the surface of the Earth. The most important geographic coordinate systems are: Geodetic coordinates system, Astronomical coordinates system and the Geocentric coordinates system.

I-4.1 Geodetic coordinates

It is based on a model for the size and the shape of the Earth. The Earth's surface is nearly that of an oblate spheroid. Two independent parameters uniquely specify such an ellipsoid. It is important to realise that the definitions of the geodetic coordinates are independent of the numerical values of the parameters of the ellipsoid. The difference between the long and short axes of this ellipse is about 0.3%. The value of flattening *f*, adopted by the IERS in 1989 is :

$$f = (a - b) / a = 1.0 / 298.275 \qquad (I.6)$$

Where a is the equatorial axis, and b is the polar axis of the ellipsoid [40].

I.4.2 Astronomical coordinates

The observatory coordinates that can be measured with only local information are astronomical or geographic longitude and latitude. The local gravity vector and the direction of the celestial pole define them.

I.4.3 Geocentric coordinates

The position of a point relative to a terrestrial reference frame may be expressed in three ways:

(i) Geocentric equatorial rectangular coordinates, x, y, z

(ii) Geocentric longitude, latitude and radius, λ, ϕ', ρ

(iii) Geodetic longitude, latitude and height, λ, ϕ, ρ

The relationship between the geodetic and the geocentric latitudes of a point is illustrated in Figure I-4(a) which represents a meridional section through the reference spheroid. The geocentric radius ρ is usually expressed in units of the equatorial radius of the reference spheroid. The following relationships hold between the geocentric and the geodetic coordinates:

$$x = a\rho\cos(\phi')\cos(\lambda) = (aC + h)\cos\phi\cos\lambda \tag{I.7}$$

$$y = a\rho\cos\phi'\sin\lambda = (aC + h)\cos\phi\sin\lambda \tag{I.8}$$

$$z = a\rho\sin\phi = (aS + h)\sin\phi \tag{I.9}$$

Where a is the equatorial radius of the spheroid , C and S are auxiliary functions that depend on the geodetic latitude and on the flattening f of the reference spheroid. The polar radius b and the eccentricity e of the ellipse are given by:

$$b = a\,(1 - f) \tag{I.10}$$

$$e^2 = 2f - f^2 \quad \text{or} \quad 1 - e^2 = (1 - f^2) \tag{I.11}$$

It follows from the geometrical properties of the ellipse that:

$$C = \{\cos^2\phi + (1 - f)^2\sin^2\phi\}^{-1/2} \tag{I.12}$$

$$S = (1 - f)^2 C \tag{I.13}$$

Geocentric coordinates may be calculated directly from geodetic coordinates. The reverse calculation of geodetic coordinates from geocentric coordinates can be done in closed form [19] but it is always done by iterative procedure. An iterative procedure for calculating λ,ϕ, h from x, y, z is as follows:

Step 1: we calculate $\lambda = \tan^{-1}(y/x)$ $r = (x^2 + y^2)^{1/2}$ $e^2 = 2f - f^2$

Step 2 : we calculate the first approximation to ϕ from: $\phi = \tan^{-1}(z/r)$

Step 3 : we perform the following iterations until ϕ is unchanged to the required precision.

$$\phi_1 = \phi \qquad C = (1 - e^2\sin^2\phi_1)^{1/2} \qquad \phi = \tan^{-1}(z + aCe^2\sin\phi_1)/r)$$

Step 4: we calculate $h = r/\cos\phi - aC$

The quantity $\phi - \phi'$ is some time known as the "reduction of the latitude" or "the angle of the vertical". Its value is of the order of 10' in mid-latitudes. The maximum departure of ϕ from $\phi'$is $\tan^{-1}\{e^2/[2(1-e^2)^{1/2}]\}$ when $\sin\phi = 1/(2 - e^2)^{1/2}$.

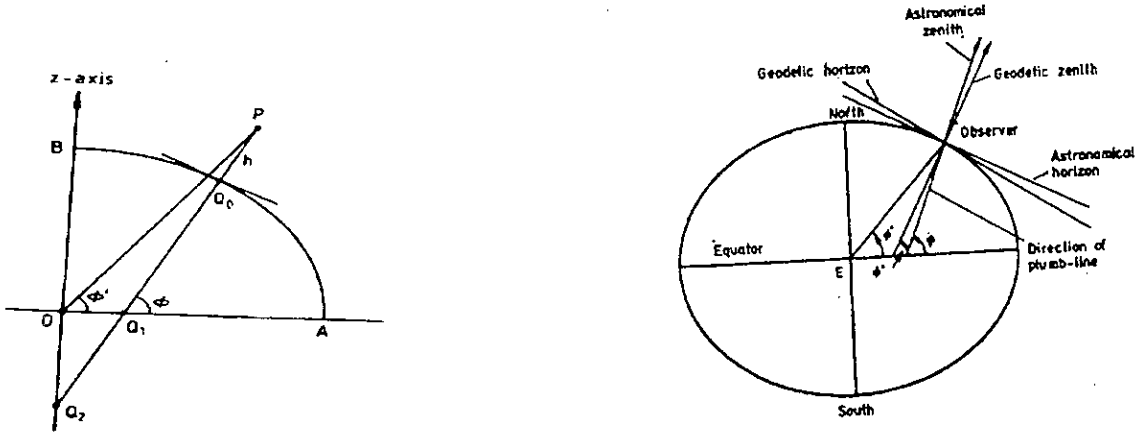

(a) *(b)*

Figure I-4. (a) Relation between geodetic and geocentric coordinates. O is the centre of Earth. OA is the equatorial radius, OB is the polar radius, OP is the geocentric radius, PQo is the normal to the reference spheroid. Q_oQ_1 *= aS.* Q_0Q_1 *= aC.* ϕ *= Geodetic latitude.* ϕ' *= Geocentric latitude. (b) The station error.*

There is again a third definition of latitude. Geodetic measurements on the Earth's surface show local irregularities in the direction of gravity, due to variations in density and shape in the Earth's crust. The direction in which a plumb line hangs is affected by such anomalies and these are referred to as station error. The geodetic or geographic latitude ϕ'' of the observer is the astronomical latitude corrected for *station error;* see Figure I-4 (b).

I.5 Heliographic coordinates

Figure I-5 (a) represents the heliocentric celestial sphere, K is the pole of the ecliptic and P_0 is the Sun's rotational pole. The great circle UNV is the solar equator, N denoting its ascending node on the ecliptic. The rotation axis (the solar equator), is specified by two parameters I and Ω. These are respectively the inclination of the equator to the ecliptic and the longitude of the node N. The adopted values are,

$$I = 7^\circ.25 \tag{I.14}$$

$$\Omega = 73^\circ\ 40' + 50''.25\ (t - 1850) \tag{I.15}$$

where t is the time expressed in years.

The variation in Ω is due to precession (see Annex 2), and secular changes in the ecliptic is ignored. The prime meridian is shown as P_0O. It cuts the equator at the point O, which is assumed to rotate with sidereal period of 25.38 days. This reference point was originally chosen to coincide with the node of 1854 January 1 at 12^h UT. The position of the point O is given by the arc NO. It is denoted by W and given by,

$$W = (360^\circ/25.38)\ (JD - 2398220.0) \tag{I.16}$$

Where JD is the Julian Date.

Now suppose that X is any point on the solar surface. Its heliographic latitude and longitude are defined as $B = 90° - P_0X$, and $L = OP_0X$. Let E be the center of the apparent solar disc called the subearth point. This point lies on the ecliptic at longitude $I_0 - 180°$, where I_0 is the geocentric longitude of the Sun. So, $EN = \Omega - I_0 + 180°$. If (L_0, B_0) are the heliographic coordinates of the center of the disc, then $P_0E = 90° - B_0$, $EP_0N = 360° - W - L_0$, $P_0NE = 90° - I$, and $P_0N = 90°$. Applying the sine and cosine formula (see Annex 2) to the triangle P_0NE we get,

$$\text{Sin } B_0 = \sin (I_0 - \Omega) \sin I \tag{I.17}$$

$$\cos B_0 \cos (L_0 + W) = \cos I \sin (\Omega - I_0) \tag{I.18}$$

$$\cos B_0 \cos (L_0 + W) = - \cos (\Omega - I_0) \tag{I.19}$$

These equations are sufficient to determine (L_0, B_0) for any time once $\dot{W}$ is calculated. If P_1 in Figure I-5(a) represents the celestial pole, then the position angle may be computed as the sum of the angles P_1EK and KEP_0.

Consider first, the spherical triangle KP_1E, in which $KE = 90°$ and $KP_1 = \varepsilon$ (the obliquity of the ecliptic). The spherical angle EKP_1 is the ecliptic longitude of P_1 minus the ecliptic longitude of E. So $EKP_1 = 270° - I_0$. From this spherical triangle, we get:

$$\tan P_1EK = - \cos I_0 \tan \varepsilon \tag{I.20a}$$

where $P_1KE \in [- \varepsilon, +\varepsilon]$ for $I_0 \in [0°, 360°]$

Consider the triangle KEP_0, we have again, $KE = 90°$, $P_0K = I$, and $P_0KE = I_0 - \Omega - 90°$. Applying the cosine and sine formulae we get,

$$\tan KEP_0 = - \tan I \cos (\Omega - I_0) \tag{I.20b}$$

where $KEP_0 \in [-I, +I]$ for $I_0 \in [0°, 360°]$

Hence, the position angle of the axis is given by

$$P = -\tan^{-1}[\tan I \cos (\Omega - I_0)] - \tan^{-1}[\cos I_0 \tan \varepsilon] \tag{I.21}$$

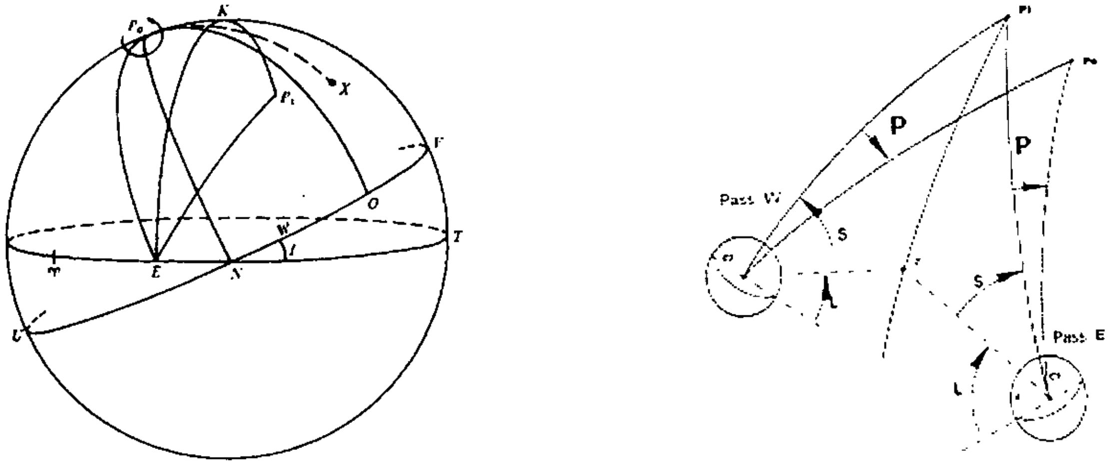

(a) (b)

Figure I-5.(a) Heliographic coordinates, (b) Heliographic latitude.

In our case, the vertical diameter that is measured by the astrolabe is aligned with the great circles c_1z and c_2z. Its heliographic latitude is given by,

$$L = 90° - (P+S) \tag{I.22}$$

Where S is the parallactic angle computed positively toward the east; see Figure I-5(b) .

I.6 Solar radius determination

I.6.1 Classical method

The average distance of the Earth from the Sun is called the astronomical unit. Modern methods, using radar, have greatly simplified the task of finding this distance [40]. However, if a radar signal were directed toward the Sun, its echo would be very difficult to detect against the background of other radio signals that the Sun itself emits. Therefore, an indirect approch is used. A radar signal is directed toward a given planet or asteroid, and the time required for the echo of that signal to be heard is noted. Since we know the speed with which the radar signal travels, we may then compute the distance to the object. Knowing both the distance and period of an object that orbits the Sun, we can calculate the astronomical unit using Kepler's third law,

$$\frac{p_1^2}{p_2^2} = \frac{r_1^2}{r_2^2} \tag{I.23}$$

For the case of Mars we have,

$$\frac{(1.88)^2}{(1)^2} = \frac{(x+78{,}389{,}294)^3}{x^3}$$

$$x = 149{,}597{,}890 \text{ Km (The astronomical unit)}$$

Where p_1 is the period of Mars and p_2 is that of the Earth. r_1 is the average distance of Mars from the Sun and r_2 is the average distance of the Earth from the Sun.

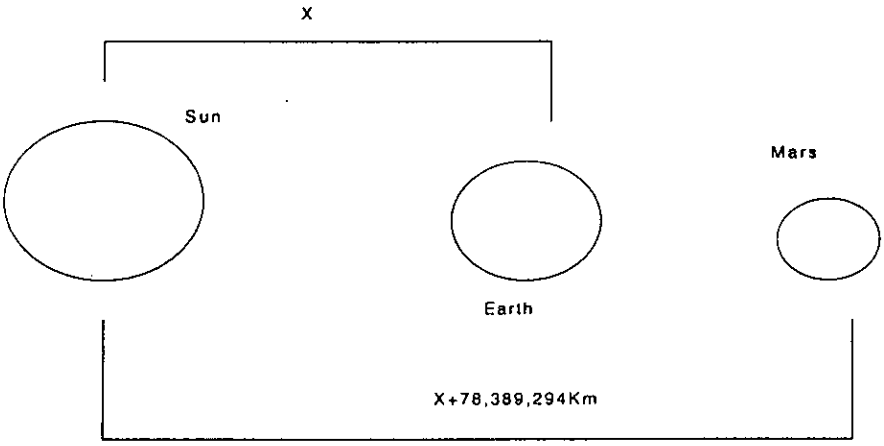

The approximate determination of the diameter of the Sun follows directly from the knowledge of its distance from the Earth as well as the apparent angle that its diameter makes with our eye.

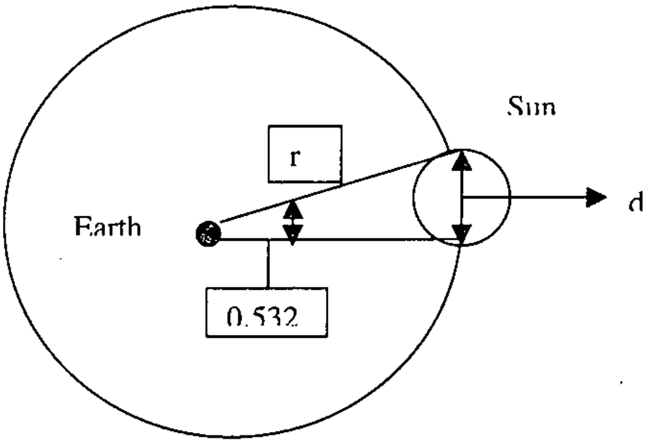

Figure I-6. Classical Sun diameter measurement.

$$\frac{0.532^\circ}{360^\circ}=\frac{d}{2\pi(149{,}598{,}000Km)}$$
$$d = 1{,}390{,}000 \text{ Km}$$

To seek an accurate Sun diameter that can be used for scientific purposes, we must look for more methods using precise instruments. The ground instrument that recently shows efficiency is the modified Danjon astrolabe for Sun diameter measurement.

I.6.2 Astrolabe measurement principle

Figure I-7 shows the principle of the measurement. P stands for the celestial pole and Z for the zenith. φ is the latitude and $H = ST - \alpha$ is the hour angle of the Sun. The Almucantar is the parallel of altitude. z_1 and z_2 are the zenithal distances computed at the time of crossing of the same Almucantar by the upper edge (Sun in c_1) and lower edge (Sun in c_2). For the two instants, the center of the Sun in c_1 and c_2 is located on two close parallels of declination, δ_1 and δ_2.

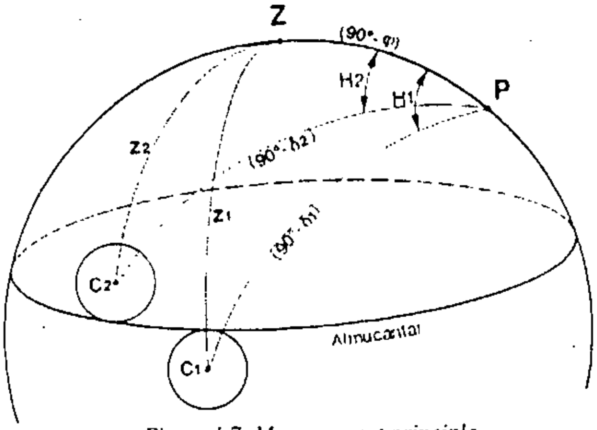

Figure I-7. Measurement principle.

Figure I.7 is simplified as shown in Figure I.8 by neglecting the curvature of the parallels of the altitude and of the diurnal trajectory of the Sun located between the two parallels of declination designated by δ_1 and δ_2.

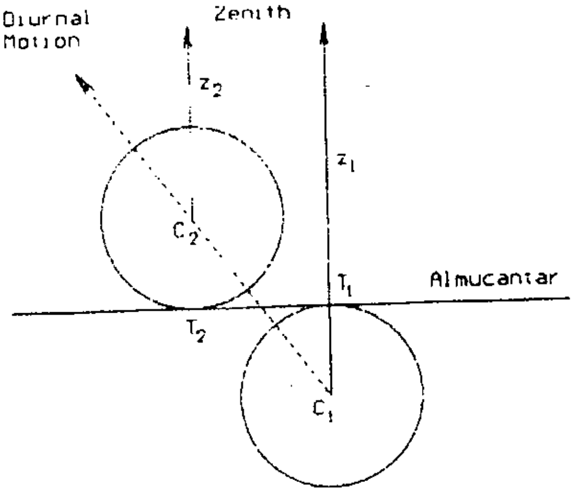

Figure I-8. Measurement principle of the Sun semi-diameter with the astrolabe neglecting the curvatures of the parallels of declination and Almucantar.

If t_1 and t_2 are the recorded times of the transits T_1 and T_2 respectively of the solar borders through Almucantar, and if z_1 and z_2 are the zenithal distances of the center of the Sun computed with t_1 and t_2 respectively, the Sun semi-diameter R is given by[12]:

$$R = 1/2|z_1 - z_2| \tag{I.24}$$

So, all that we need is a precise instrument that can measure the two transit instants at T_1 and T_2. From Figure I-8 it is apparent that the measured diameter will have always a vertical direction with respect to the local frame and the transits of the borders of the Sun are observed always at the same zenithal distance. This is a great advantage, since the results should be free from the effects of errors on the refraction and an eventual effect of irradiance should be constant [20].

Since the solar diameter is a function of zenithal distance, so, this must later be corrected for the effects of the parallax, the atmospheric refraction and the instrumental effects.

I.7 Parallax

The difference between the geometric directions to a celestial body from two points in space is denoted in general by the term parallax. Because of parallax, the directly observed positions of celestial bodies relative to the reference circles depend upon the point of observations.

I.7.1 Geocentric parallax

The geometrical direction for a celestial body from an observer on the surface of the Earth, and from the center of the Earth, lie in a plane that passes through the geometric zenith. The angle P between these directions, which is the geometric parallax, is therefore the difference between the observed angular distance from the geocentric zenith z'_g and the geocentric distance z_g from the geocentric Zenith,

$$P = z'_g - z_g \qquad (I.25)$$

where $z'_g \geq z_g$; see Figure I-9.

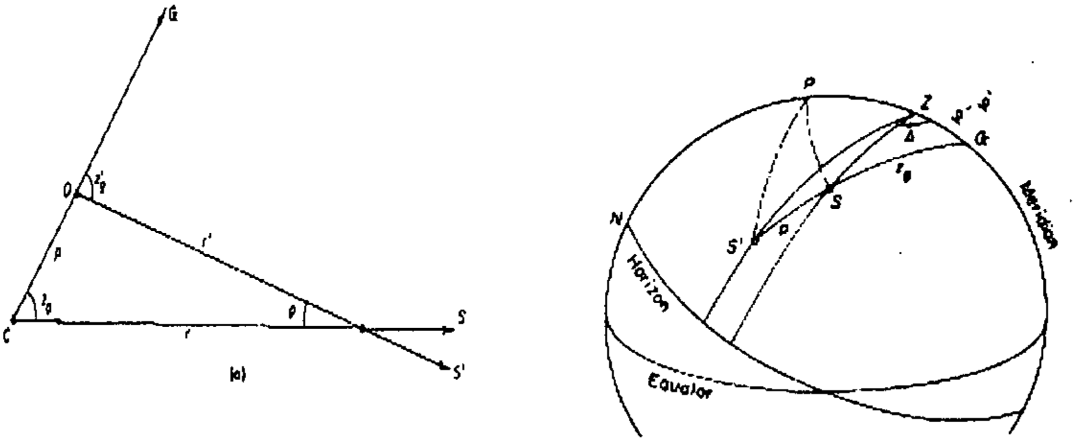

(a) (b)

Figure I-9. Geocentric parallax, (a) C is the center of the Earth, O is the observer, G is the geocentric zenith, S is the geocentric direction and S' is the topocentric direction. (b) Z is the geodetic zenith, P is the celestial pole, and G is the geocentric zenith.

The angle P is the angle subtended at the body by the radius ρ from the center of the Earth to the observer. The geocentric parallax vanishes at the geocentric zenith, and it is a maximum at the horizon where z'_g is 90°.

The displacement P on the celestial sphere by geocentric parallax is entirely a displacement in geocentric zenithal distance and therefore very nearly in a vertical circle In accordance with equation I.25, the geocentric parallax depresses a celestial body toward the horizon. However, since the geocentric zenith does not coincide with geodetic zenith, the topocentric position will in general be displaced both in azimuth and altitude from the geocentric position.

To determine the exact values of the effects of geocentric parallax, the geographic location of the observer must be expressed in geodetic terms. Therefore, when high accuracy is required and the parallax is large, astronomical coordinates should be corrected for local deflection of the vertical, and the elevation above the spherical should be included in the geodetic coordinates. From the law of sines for plane triangles, we have,

$$\sin \mathrm{P} = \frac{\rho}{r}\sin z'_g \tag{I.26}$$

where r is the geocentric distance of the body. The value of P at $z'_g = 90°$ is called the horizontal parallax; denoting it by ϖ, we have,

$$\sin \mathrm{P} = \sin \varpi \sin z'_g \tag{I.27}$$

From this equation and equation I.25,

$$\sin \mathrm{P} = \sin \varpi \sin (\mathrm{P} + z_g) \tag{I.28}$$

Expanding and dividing by cos P gives,

$$\tan P = \frac{\sin\varpi \sin z_0}{1 - \sin\varpi \cos z} \tag{I.29}$$

The solution of I.29 is,

$$P = (\varpi - \frac{1}{6}\varpi^3)\sin z_g + \frac{1}{2}\varpi^2 \sin 2z_g + \frac{1}{3}\varpi^3 \sin 3z_g + \ldots \tag{I.30}$$

The value of ϖ when ρ is the equatorial radius a of the standard spheroid, is the equatorial horizontal parallax ϖ_0. Its value is given by $\sin(\varpi_0) = a/\mathrm{r}$ or $1/\mathrm{r}$ when a is the unit distance. The equatorial horizontal parallax ϖ_0 of the Sun is defined as $\sin(\varpi_0) = a/1\mathrm{AU}$ or $\varpi_0 = 8.794''$. The equatorial horizontal parallax of a body at its mean geocentric distance r_0 is called the mean equatorial horizontal parallax, π [40]:

$$\sin \pi = a/\mathrm{r}_0,$$

$$\pi = \sin \pi + \frac{1}{6}\sin^3(\pi) + \ldots\ldots$$

$$\sin \mathrm{P} = \frac{\rho}{a}\frac{r_0}{r}\sin\pi \sin z'_g \tag{I.31}$$

If the Earth were spherical, the horizontal parallax would be the angular semi-diameter that the Earth would appear to have if viewed from the body. Since the direction to the body from any point on the Earth where P=ϖ would then be tangent to the surface of the Earth. But because of the nonspherical form of the Earth, a tangent to the surface does not in general coincide with the direction $z'_g = 90°$ at the point of tangency. The difference depends both on the latitude of the point and on the azimuth of the tangent. Hence the angle subtended by ρ at an external point when $z'_g = 90°$ is not strictly the same as the angle subtended by the radius of the Earth at this external point.

Ordinarily it is sufficiently accurate to put p = sin p, and neglect the parallax in azimuth. Then $z_g = z' - (\varphi - \varphi')\cos A$, where z' is the topocentric zenithal distance from the geodetic zenith, and A is the angle in azimuth measured westward from the meridian.

Disregarding deflections of the vertical, z' is the observed zenithal distance from the astronomical zenith. To this approximation, the parallax in altitude, in terms of the equatorial horizontal parallax ϖ_0, expressed in seconds of arc, is

$$p''=\frac{\rho}{a}\varpi''_0\sin[z'-(\varphi-\varphi')\cos A] \tag{I.32}$$

which is to be added to the observed altitude in order to obtain the geocentric altitude above the astronomical horizon. Since $\varpi/\varpi_0 = \rho/a$, and

$$\rho/a= 1-f\sin^2(\varphi)+\frac{5}{8}f^2\sin^2(2\varphi)+...$$

the horizontal parallax at any latitude is [40],

$$\varpi=\varpi_0(1-f\sin^2\varphi+\frac{5}{8}f^2\sin^2 2\varphi+...) \tag{I.33}$$

where f is the flattening of the Earth. Neglecting flattening in addition to the other approximation gives $p''=\varpi''\sin z'$.

The horizontal parallax ϖ at latitude φ is sometimes called the reduced parallax for this latitude. The difference $\varpi_0-\varpi=[1-(\rho/a)]\varpi_0$ is known as the reduction of the equatorial parallax, sometimes as the augmentation of the horizontal parallax, for the latitude. It is the correction required to ϖ for the flatting of the Earth in order to obtain the equatorial horizontal parallax ϖ_0. From equation I.33 we have:

$$\varpi_0-\varpi=\varpi_0\left[\frac{1}{2}f(1-\cos 2\phi)-\frac{5}{16}f^2(1-\cos 4\phi\right]+... \tag{I.34}$$

From the plane triangle of figure I-9, we have

$$\frac{\sin\rho}{\rho}=\frac{\sin z_g}{r'}=\frac{\sin z_g'}{r}$$

$$\sin p=\rho/r\sin z_g'=\varpi_0\ \rho\sin z'_g \tag{I.35}$$

where $\varpi_0 = 1/r$ if a is the unit distance. From the equation I.25, we obtain the relation between the topocentric zenithal distance (z'_g) and the geocentric zenithal distance (z_g) as follows,

$$z'_g=z_g+\varpi_0\rho\sin z_g \tag{I.36}$$

I.8 Astronomical refraction

Refraction is the bending of the path of the light when it passes through a medium of changing index of refraction

I.8.1 Dispersion by refraction

Since the angle of refraction depends upon the wavelength of light, a phenomenon that occurs simultaneously with refraction is that of dispersion. The general effect of atmospheric refraction is normally to increase the altitude of a celestial body without altering the azimuth. Its amount depends upon the state of the atmosphere at every point on the path of ray at the time. So, its determination is a difficult proposition. Because of continual variation and irregularities throughout the atmosphere, the refraction is subject to irregular fluctuations and anomalies, especially near the horizon, that cannot be determined by theory [40].

On the hypothesis that the atmosphere is horizontally stratified, that is the index of refraction μ is radially symmetric, $\mu = \mu(r)$ where r is the distance from the centre of the Earth; and from the law of refraction we have,

$$\mu r \sin \zeta = \text{const} \qquad \text{(I.37)}$$

hence, ζ is the angle that the direction of the ray makes with r, and is therefore equivalent to the angle of incidence on each stratum Figure I-10(a).

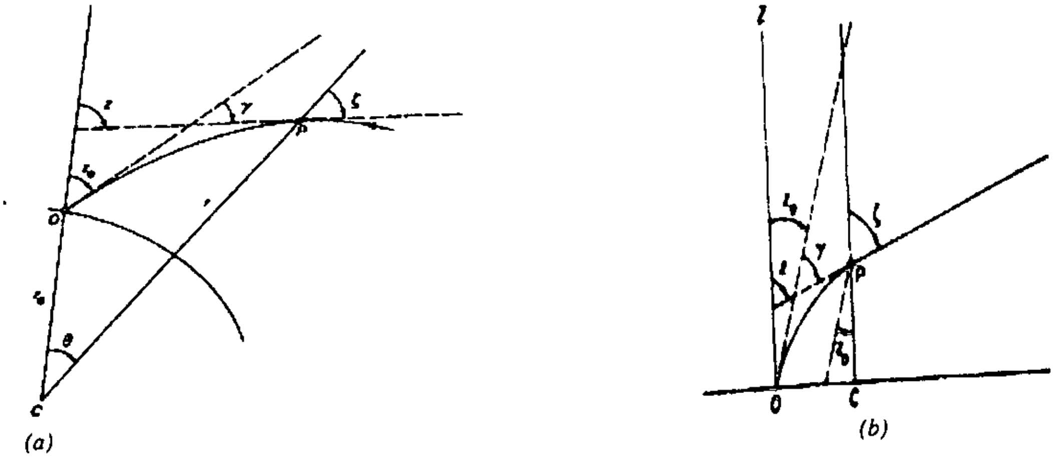

Figure I-10. (a) The astronomical refraction, (b) The approximate refraction.

The angle, which the direction of the ray at any point P makes with the radius vector r_0 to the observer is

$$(z) = \theta + \xi \qquad \text{(I.38)}$$

hence, θ is the geocentric zenithal distance of P from the zenith of the observer.

At the observer, where $r = r_0$, $\mu = \mu_0$ and $\theta = 0$, the apparent zenithal distance is $z_0 = \xi_0$. The constant in equation I.37 is equal to

$$\mu\, r_0 \sin \xi = k,$$

and hence

$$\tan \xi = k/(\mu^3 r^3 - k^2)^{1/2} \qquad \text{(I.39)}$$

The change in the direction of the ray, i.e., the total amount of refraction from any point P on the path, to the observer is

$$\gamma = z - z_0$$

and therefore

$$\begin{aligned} d\gamma &= dz \\ &= d\theta + d\xi \end{aligned} \qquad \text{(I.40)}$$

Differentiating Equation I.40 and dividing by $r\mu \sin \xi$, we have

$$d\xi = -\tan \xi \, \frac{d(r\mu)}{r\mu};$$

and from differential geometry

$$d\theta = \tan \xi \, \frac{dr}{r} \qquad \text{(I.41)}$$

Therefore by Equation I.39 and I.40, we get

$$d\gamma = +\tan \xi \, d\left(\log \frac{\mu_0}{\mu}\right) \qquad \text{(I.42)}$$

$$d\theta = k\,(r^2\mu^2 - k^2)^{-1/2} \frac{dr}{r} \qquad \text{(I.43)}$$

The integration of equation I.43 gives the path of the ray and the integration of equation I.42 gives the astronomical refraction

$$\delta z = \int_1^{\mu_0} \left\{ \left(\left(\frac{r\mu}{r_0\mu_0} \operatorname{cosec} z_0 \right)^2 - 1 \right\}^{-1/2} \frac{d\mu}{\mu} \qquad \text{(I.44)}$$

The integration requires $\mu(r)$ to be known. The index of refraction for a given wavelength depends almost entirely on density, since the composition of the atmosphere up to great heights is virtually uniform and constant except for variation of the relativity small water vapour content. From the distribution of the density with height, and laboratory determination of the relation of μ to density, the function $\mu(r)$ may be derived. However, it is not to be expected that this function is of a form that will enable a rigorous analytical theory of refraction to be constructed. Several different empirical laws have been formulated that represent more or less closely the relation of μ to the density ρ; among them are the Dale-Gladstone law [40],

$$\mu - 1 = c\rho \qquad \text{(I.45a)}$$

and the Clausius-Mosotti equation

$$\frac{\mu^2-1}{\mu^2+2}=c\rho \tag{I.45b}$$

where c is a constant

I.8.2 Approximate refraction

Different approximations are given for refraction. A first approximation may be derived by putting [40]:

$$\frac{r}{r_0}=1+s \tag{I.46}$$

and expanding equation I.44 into a series. The quantity s is only about 0.01 at a height of 40 miles, beyond which the atmosphere is ineffective in producing appreciable approach refraction. Neglecting s^2, we have,

$$(r^2\mu^2-k^2)^{-1/2}=\frac{1}{r_0}\left\{\left(\mu^2-\mu_0^2\sin^2 z_0\right)+2s\mu^2\right\}^{-1/2} \tag{I.47}$$

We next Expand by the binomial theorem for values of z_0 that are small enough to keep $\left(\mu^2-\mu_0^2\sin^2 z_0\right)$ large compared with $2\mu^2 s$. Under this condition, by equation I.42, we get

$$\delta z=\mu_0\sin z_0\int_1^{\mu_0}\frac{d\mu}{\mu(\mu^2-\mu_0^2\sin^2 z_0)^{1/2}}-\mu_0\sin z_0\int_1^{\mu_0}\frac{s\mu\,d\mu}{(\mu^2-\mu_0^2\sin^2 z_0)^{3/2}}+\ldots \tag{I.48}$$

Retaining only the first term of the development, we have

$$\delta z=\sin^{-1}(\mu_0\sin z_0)-z_0 \tag{I.49}$$

Putting $\mu_0 = 1+ x$ and developing in powers of x by Maclauran's theorem by neglecting powers higher than the first, we get

$$\delta z = (\mu_0 - 1)\tan z_0 \tag{I.50}$$

To this approximation, the refraction is independent of the structure of the atmosphere, and is entirely determined by the local conditions at the observer. Physically, this approximation is equivalent to neglecting the curvature of the Earth Figure I.10(b).

We notice from Figure I.10(a) that,

$$\xi = z = z_0 + \gamma \tag{I.51}$$

From the law of refraction, when a ray passes through a parallel-stratified medium, the final direction is the same as if the entire medium had the density of the last medium. Hence, the result can be obtained directly,

$$\sin\xi = \mu_0\sin z_0 \tag{I.52}$$

or, by equation I.51, taking $\cos\gamma = 1$ and $\sin\gamma = \gamma$:

$$\gamma = (\mu_0 - 1) \tan z_0 \qquad (I.53)$$

Adopting 1.0002927 for the index of refraction at the standard conditions (0°C and 760 mm) and the Dale-Gladstone law, we have from the formula and the ideal gas law, in terms of the temperature t in degrees Centigrade and the mercury level of the barometer B in millimetres at the observer,

$$\delta z = \frac{1}{760} * 273.0.0002927 * 206264''.8 * B \frac{\tan z_0}{273+t}$$

$$= 21''.7 * \frac{B}{27+t} \tan z_0 \qquad (I.54)$$

At standard conditions we have

$$\delta z = 60''.4 * \tan z_0 \qquad (I.55)$$

This approximation is very close at small zenithal distances, because near the Zenith the curvature of the atmosphere has less effect on the path of the ray, as there is less total change in the direction of *r*; but it becomes useless at altitude below 30°.

The approximation obtained by retaining the two terms of equation I.48 is of the form

$$\delta z = A \tan z_0 + B \tan^3 z_0 \qquad (I.56)$$

The constants A and B may be expressed in terms of physical constants, or separately determined from the observation. We can write equation I.55 as,

$$\delta z = (\mu_0 - 1)(1 - H_0) \tan z_0 - (\mu_0 - 1)\left[H_0 - 1/2(\mu_0 - 1)\right] \tan^3 z_0 \qquad (I.57)$$

In which H_0 is the ratio of the height of the homogeneous atmosphere to the radius of the Earth. This expression is a common element of all expressions for refraction, and is the fundamental refraction formula for many practical purposes, but it is not sufficiently precise for astronomical purposes at very low altitudes. H_0 and $\mu_0 - 1$ are given by dreadful empirical formulae that include, the air index, the atmospheric pressure, the air absolute temperature, the wavelength of the light involved, the barometer's mercury height and temperature, the hygrometry percentage, the partial pressure of the water vapor at the given temperature, the latitude of the station, the altitude of the station and the curvature of the radius of the Earth at the place of the observation [40].

With $H_0 = (7.990.10^5 \text{cm})/(6.3709.10^8 \text{ cm})$ and $\mu_0 - 1 = 0.0002927$, we have

$$\delta z = 60''.29 \tan z_0 - 0''.06688 \tan z_0 \qquad (I.58)$$

The model of atmospheric refraction chosen is the model of Laplace. It is deduced from the equation I.48 by retaining its first three terms:

$$\delta z = (\mu_0 - 1)(1 - H_0) \tan z_0 - (\mu_0 - 1)\left[H_0 - 1/2(\mu_0 - 1)\right] \tan^3 z_0 + 3(\mu_0 - 1)\left(\frac{(1-\mu_0)}{2} - H_0\right)^2 \tan^5 z_0 \qquad (I.59)$$

With $$\mu_0 - 1 = (\bar{n} - 1)\frac{273.16}{760}\frac{P}{T} - 5.5.10^{-8}\frac{273.16}{T}p \qquad (I.60)$$

And $$10^{7}(\bar{n} - 1) = 2876.04 + \frac{16.288}{\lambda^{2}} + \frac{0.136}{\lambda^{4}} \qquad (I.61)$$

$$P=H(1-26.4*10^{-5}\cos 2\varphi-19.6*10^{-8}h-16.3*10^{-5}\theta \qquad (I.62)$$

P the reduced atmospheric pressure (mm col.Hg).
T the absolute temperature of the air.
P the partial pressure of the water vapor.
λ the wavelength in µm.
H the read barometric height
φ the latitude of the station
h the altitude of the station (m)
θ the barometer temperature (°C)

With the error on H_0, which induces a very small error in R, we can take:

$$H_0=4.5054*10^{-6}T \qquad (I.63)$$

For a recorded value f from the hygrometer, in humidity percentage, the relation calculates the partial pressure of the water vapor for the temperature t of the air is given by,

$$p=\frac{f}{100}F(t) \qquad (I.64)$$

With

$$F(t)=4.581Exp(0.07292t-0.000284t^{2}) \qquad (I.65)$$

Equation I.65 is an interpolation formula of the saturated vapor pressure of the water. It is given according to the data published by "Bureau des longitudes" [14]. Replacing H_0 and μ_0-1 by their expressions in Laplace formula, we obtain the atmospheric refraction that affects the zenithal distance.

I.9 Topocentric and Geocentric solar radius

There is a differnce between the radius of the Sun seen from the observer's location(topocentric) and the center of the Earth (geocentric). Let O be the point of observation, C the center of the Earth and R_s the Sun radius seen by the angles s and s', see Figure I-11, in this case we can write,

$$R_s = r\sin s = r'\sin s' \qquad (I.66)$$

Hence

$$s' \cong rs/r' \text{ or}$$

$$s' - s = (r - r')\, s/r' \qquad (I.67)$$

As

$$r \cong r' + \rho \cos z_g \qquad (I.68)$$

then

$$s' - s \cong \varpi_0\, \rho s \cos z_g \qquad (I.69)$$

$$s \cong s' + \varpi_0\, \rho s \cos z_g \qquad (I.70)$$

r being measured in Astronomical Units, the geocentric radius is given by

$$R_s = r \sin s \cong r(\, s' - \varpi_0\, \rho s \cos z_g) \qquad (I.71)$$

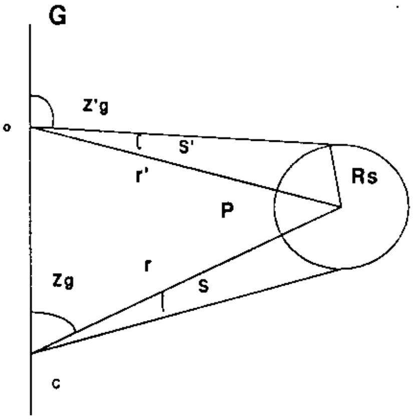

Figure I-11. Geocentric Sun radius vs Topocentric one.

I.10 Data reduction procedure of solar radius

It was shown from section I.6.2 that the vertical solar semi-diameter is given by equation I.24., where z_1 and z_2 are the zenithal distances computed at the successive crossing times t_1 and t_2. The resolution of the spherical triangle at the time of observation yields the geocentric zenithal distance of the Sun center z^*. We have from equation I.2, replacing z by z^* ,that:

$$\cos z^* = \sin \varphi \sin \delta + \cos \varphi \cos \delta \cos (H) \qquad (I.72)$$

The topocentric zenithal distance after the necessary corrections is written as:

$$Z = Z(ST) = \arccos\{\sin \varphi \sin \delta + \cos \delta \cos \varphi \cos (ST - \alpha)\} + \rho \varpi_0 \sin z^* + R + \Delta C \pm P_j \qquad (I.73)$$

where ST is the sidereal time at the moment of observation, φ is the latitude of the instrument, α and δ are the equatorial coordinates of the Sun computed at the time of observation, $\rho\varpi_0 \sin z^*$ is the altitude parallax correction where ρ is the geocentric radius of the instrument, ϖ_0 is the equatorial horizontal parallax, z^* is the geocentric zenithal distance at the time of observation, and R the correction due to the atmospheric refraction. ΔF is the correction to the focal plane position, ΔC is a correcting term dealing with the curvature of the declination and altitude parallels. The P_j stands for the personal error in the visual case, since each observer has a personal way of appreciating the contact of both images and will consequently choose a time of crossing either earlier or later than the accurate one. This error has an opposite sign for both edges and of course it disappears in the case of CCD acquisitions.

From Figure I-11 the angle s' that gives the topocentric angular semi-diameter is equal to $1/2(|z_1 - z_2|)$. It must be decreased by the amount ($\rho\varpi_0 s \cos z^*$) to give the angular geocentric semi-diameter. It remains to multiply that last one by the heliocentric radius vector r of the Earth measured in AU to get the value of the solar radius at one AU,

$$R_s = \{\frac{1}{2}|z_1 - z_2| - \rho\, \varpi_0\, s \cos z^*\} r + P_j \tag{I.74}$$

The following relation gives the local sidereal time ST at the moment of observation,

$$ST = \frac{TU}{K} + T_g - L + N\cos\frac{\varepsilon}{15} \tag{I.75}$$

Where TU is the observed universal instant deduced from the Coordinated Universal Time (UTC) instant related to the International Atomic Time (TAI) (see Annex 3), K is the ratio between the universal time and the sidereal time (K=0.997269566, see Annex 3). L is the longitude of the station, N is the nutation of longitude, ε is the ecliptic obliquity, and T_g is the Greenwich Mean Sidereal Time (GMST). In conformity with IAU conventions for the motion of the Earth's equator and equinox, GMST is linked directly to UT1 through the following equation

GMST (in seconds at UT1=0) = 24110.54841 + 8640184.812866 * T+ 0.093104 * T^2 - 0.0000062 * T^3 (I-76)

Where T is in Julian centuries from 2000 Jan 1 at 12h UT1

$$T = d / 36525 \tag{I.77}$$

Where d = JD - 2451545.0.

The observations using the solar astrolabe are dated in UTC. They are transferred to UT0 as follow (see Annex 3),

$$UT1 = UT0 - \left[\frac{x}{15}\sin\lambda_0 + \frac{y}{15}\cos\lambda_0\right]\tan\varphi_0 \tag{I.78}$$

Rearranging we find that

$$UT0 - UTC = UT1 - UTC + \left[\frac{x}{15}\sin\lambda_0 + \frac{y}{15}\cos\lambda_0\right]\tan\varphi_0 \tag{I.79}$$

The difference UT1 – UTC, x and y are given by the International Earth Rotation Service (IERS) at the time of observation. φ_0 and λ_0 are the geographic coordinates of the station, which can be corrected and known exactly using the following equations(see Annex 3),

$$\varphi = \varphi_0 + x \cos\lambda_0 - y \sin\lambda_0 \tag{I.80}$$

$$\lambda = \lambda_0 + (x \sin\lambda_0 + y \cos \lambda_0) \tan \varphi_0 \tag{I.81}$$

Knowing UT1, we can calculate Terrestrial Time (TT) used to calculate the Sun ephemeredes (see Annex 3). It is defined as,

$$TT = UTC + (\text{number of leap seconds}) + 32.184 \tag{I.82}$$

The number of leap seconds is given by the Bulletin A of the IERS. The calculation of TT gives access to the Sun ephemeredes which provide α, δ, r, s and ϖ . Having the ephemeredes, we can calculate the topocentric zenithal distance, and finally using equation I.74 to calculate the semi-diameter after applying the necessary corrections. The following steps summarise the method of reduction,

Step 1: - Reading of UTC1 and UTC2, the true instants of Sun transit.
- Reading of the station geographic coordinates and the date of observation.
- Reading of the parameters of atmospheric conditions at the moment of observation. These parameters are: the atmospheric pressure, the air temperature, the barometer temperature and the humidity.
- Reading of the instantaneous coordinates of the celestial pole, UT1-UTC, and TAI-UTC from the IERS bulletins that correspond to the moment of observation.

Step 2: - Computation of the vector radius to the station according to the chosen ellipsoidal model for the Earth.
- Correction of the station latitude for station error and altitude effect.
- Correction of the station longitude and latitude for polar motion.

Step 3: - Computation of the Julian date and the Greenwich Mean Sidereal Time (GMST).

Step 4: - Computation of UT0 and the ephemeredes time TDT or TT (Terrestrial DynamicTime).

Step 5: - Computation of the Sidereal Time (ST).

Step 6: - Computation of the Sun ephemeredes at the true time of observation.

Step 7: - Computation of the geocentric zenithal distance.
- Computation of the topocentric zenithal distance (correction for the geocentric Parallax).

Step 8: - Correction of the topocentric zenithal distance for the atmospheric refraction.
- Computation of the topocentric diameter.
- Computation of the geocentric diameter.

The precision of the above procedure depends mainly on the acuracy of the two measured instants. UTC1 and UTC2. A small error on them will affect the complete procedure. So, it is imprtant to have a precise and stable reference system.

CHAPTER II THE SOLAR ASTROLABE AT CALERN OBSRVATORY

This chapter presents a detailed description of the solar astrolabe and the different modifications undergone during the last years. The new generation of solar astrolabes are presented along with the methodology of Sun observation and the principle of measurement. Finally, the accuracy of Sun diameter measurement with the astrolabe will be discussed.

II.1 History of the astrolabe

The astrolabe is believed to have been a Greek instrument invented by Hipparchus of Biythynia (150 B.C.). The astrolabe has played an important part in the history of civilization. Its earliest known description due to John Philoponus from Alexandria dating from the VI century. Alexandrian knowledge seems to migrate through the Christian abbeys of Syria after the Arab conquest of Egypt. With the Abbasids, Islamic science became acquainted with Greek sources as well as Indian and Persian, and through them those of the ancient Babylonians and Egyptians. Following the Muslim conquest of Spain the Astrolabe entered Europe. One of the medieval sources was the XIth century manuscript "Mensura Astrolabi" by Hermanus Contractus. It describes the use and design of the astrolabe. This manuscript was brought to the knowledge of his fellow abbots of Reims, Chartes, Liége and Reichman and Gerbert d'Aurillac who studied the mathematics in the school of Cordoba, before becoming Pope Silvester II. Since the XIIIth century, the astrolabe started spreading throughout Europe from the Iberian Peninsula and Sicily into the great university cities of Europe. The astrolabe has remained one of the most important tools of astronomers until the end of the XVIIIth century. The Astrolabe is a multiple–purpose astronomical instrument. It can be used to solve numerous problems involving the position of celestial objects, simple surveying, and time determination. There are three distinct types of astrolabes: planispheric, universal and mariners [21].

In its most usual form, the astrolabe consists of an evenly balanced circle or disk of metal. It is hung by a ring and provided with a rotating alidade or diametrical rule with sights. It turns within a circle of degrees for measuring the altitudes of the Sun or stars. On its face it displays a circular map of the stars, the retie. It is cut from a sheet of metal with pointers to show the position of the brighter stars relative to one another, and to the zodiacal circle showing the Sun's position for every day of the year. Lying below the retie are one or more interchangeable plates engraved with circles of altitude and azimuth. To obtain the time, the user first measured the altitude of the Sun, then having noted the Sun's position for the day in the zodiacal circle, he rotates the retie until the Sun's position matches with the circle on the plate that corresponds to the observed altitude. A line drawn through this point of coincidence and the centre of the instrument, given by the edge of the alidade, to a marginal circle of hours showed the time. All the stars positions can then be referenced to the local celestial coordinates engraved on the tyrant that stays below the retie. Among the accessories often found in the back plates of astrolabes were shadow scales for simple surveying and finding heights or distances, a calendar scale showing the Sun's position in the zodiac for every day of the year and a diagram to convert equal to unequal hours and vice-versa. The measurement of altitude could be measured with an accuracy of about 1 degree. The first serious use of this instrument was in October of 1092. It was used to determine the time of a lunar eclipse [21].

The astrolabe was the most widely used astronomical instrument of the Middle Ages. It was also perhaps the astronomical instrument used over the longest period of time. The astrolabe served at least three purposes: (i) as observing device, it could be employed to find altitudes of celestial objects above the horizon, to determine the heights of towers or mountains, or for surveying in general; (ii) as computing devices, it could be used to find the directions to a specific region;(iii) as time keeping device, it could be used to tell time by day or by night.. Figure (I-1) shows some ancient astrolabes:

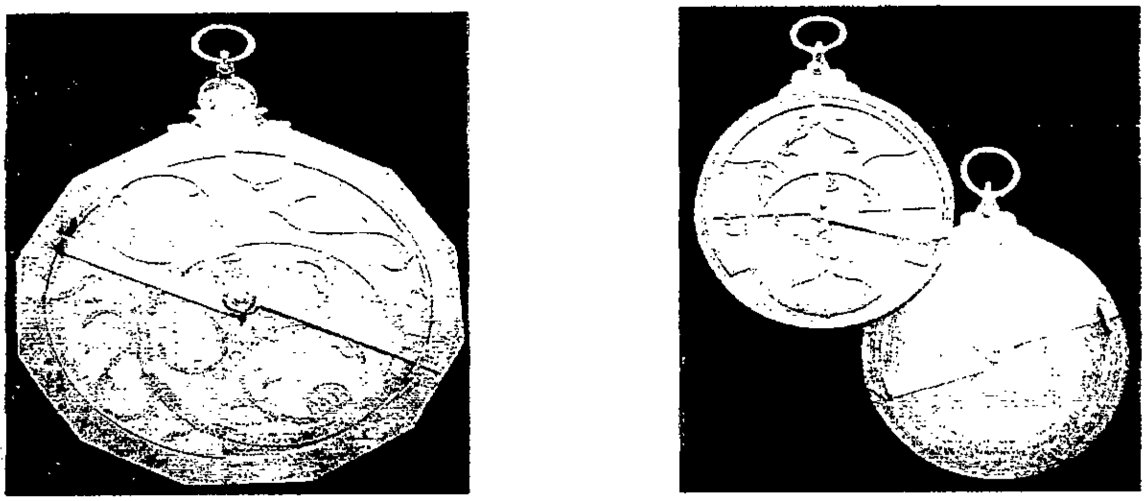

Habermal Astrolabe (ca.1500). Small *Astrolabe (ca.1500).*

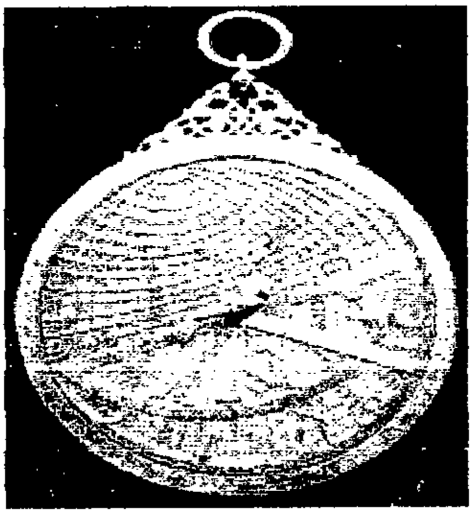

Al-Sarraj Astrolabe(1328).

Figure I-1. Some ancient astrolabes.

From the XIX^{th} - Century when Gauss and Delambre conceived the equal heights method, the astronomical instruments evolution become spectacular. Toward 1880 Chandler had the idea of an instrument that he called Almucantar that used the method of Gauss-Delambre. At nearly the same time, Beck designed the Nadir instrument and imagined the principle of the prism astrolabe. Between 1900 and 1905, Claude and Driencourt designed the prototype of the prism astrolabe, which was studied then and modified by several astronomers such as: Nusl and Money in 1901, Reevs in 1921, Backer in 1930 and Svoboda in 1935. In 1921, Baillard imagined also an astrolabe of a prism used to register the solar passages on a photographic beach [14].

II.2 Prism astrolabe and its principle

The prism astrolabe in use since 1900 under its simple shape. Figure (I-2), which is supposed to be drawn on the vertical of a star, recalls its principle.

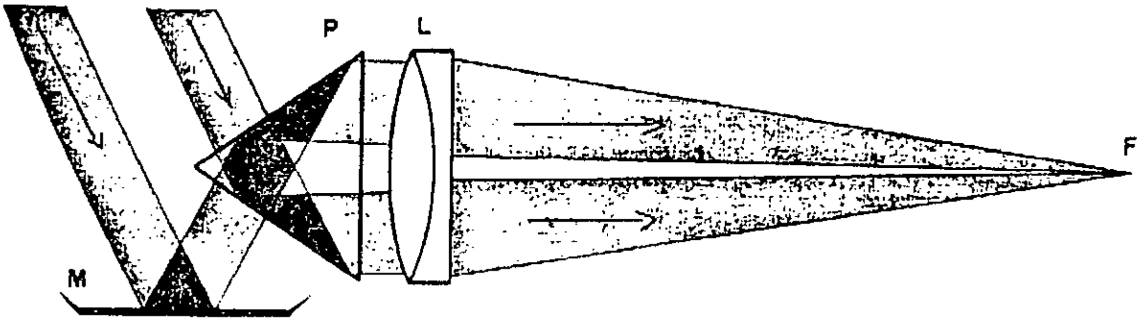

Figure I-2.Principle of the prism astrolabe.

An equilateral glass prism P is placed in front of a horizontal telescope of objective L. Its rear face is perpendicular to the optical axis. A mercury bath M is placed in front of the incident rays. If a star is at a zenithal distance of 30° (defined by the prism), two images are formed. One is a direct image, and the other is a reflected one by the mercury bath. The two star images move toward each other until they become tangent in the focal plane of the astrolabe telescope. Then they move away from each other beyond this position. If the zenithal distance is different from 30° the two images are distinct [14]. The observer estimates the instant where the two images are tangent. The necessary condition that an object crosses the height circle defined by the instrument is,

$$\phi - z \leq \delta \leq \phi + z \qquad (II.1)$$

Where ϕ represents the latitude of the observation place, z the zenithal distance and δ the declination of the observed star [22].

II.3 Danjon astrolabe

The old astrolabes suffer of the same defect due to their optics. Several studies are dedicated to solve this problem. Some of them are those of Conderc, Dungeon, Chandon and Gougenhein. Finally, the astronomer Danjon and from the prism astrolabe of Claude and Driencourt has imagined since 1938 an instrument endowed of a "biréfringent" Wollaston. Prism. This prism constitutes an impersonal micrometer. It has eliminated the optical defects and minimised the personal errors [14,22]. This astrolabe became one of the best instruments for the positional astronomy since 1953 [23,24]. It permits in a very precise way to measure the instant of passage of a star under the effect of the diurnal rotation of the Earth through a height circle defined by the characteristics of the prism. Since its operation, the Danjon astrolabe has been subjected to several transformations in order to be adapted to the observations of objects other than stars. The possibility to observe objects of the solar system and stars makes the astrolabe a good instrument for dynamic reference adjustment.

A.Danjon made of the astrolabe a first-class instrument. It has eliminated many systematic errors that affect the time measurement. Figure II-3 shows the prototype of the new impersonal astrolabe of A.Danjon and its principle components [14]. It is achieved by

J.Texereau in 1951 at the observatory of Paris and entered in regular service in 1953. The obtained results (a standard deviation of 0.009 sec on time measurement and 0 " .10 on latitude measurement) proved the quality of the instrument. Following the numerous demands of astrolabes, the Optical society and Precision of Levallois (OPL) was in charge of manufacturing a perfect set of several instruments. Observations with the first OPL astrolabe began at the observatory of Paris in 1956, and B.Guinot announced excellent results after one year and a half of observations. He has reached a standard deviation of 0.0043 sec in time and 0 " .050 in latitude [24].

The instrument consists of mobile horizontal glasses in azimuth. They are preceded by an equilateral glass prism, whose back face is perpendicular to the optical axis. Ahead and below the prism is the mercury bath. The prism and the mercury bath are protected from the surrounding turbulence by a cover that has an open-type screen on its higher part to let the passage of the incident rays. For a star passing through a zenithal distance of 30°, one part of the incident rays penetrates through the glasses by internal reflection on the upper face of the glass prism. The other one penetrates after a first reflection on the mercury bath and a second internal reflection on the other face of the prism. The two resulting images are formed in the field of the glasses, one going down while the other going up.

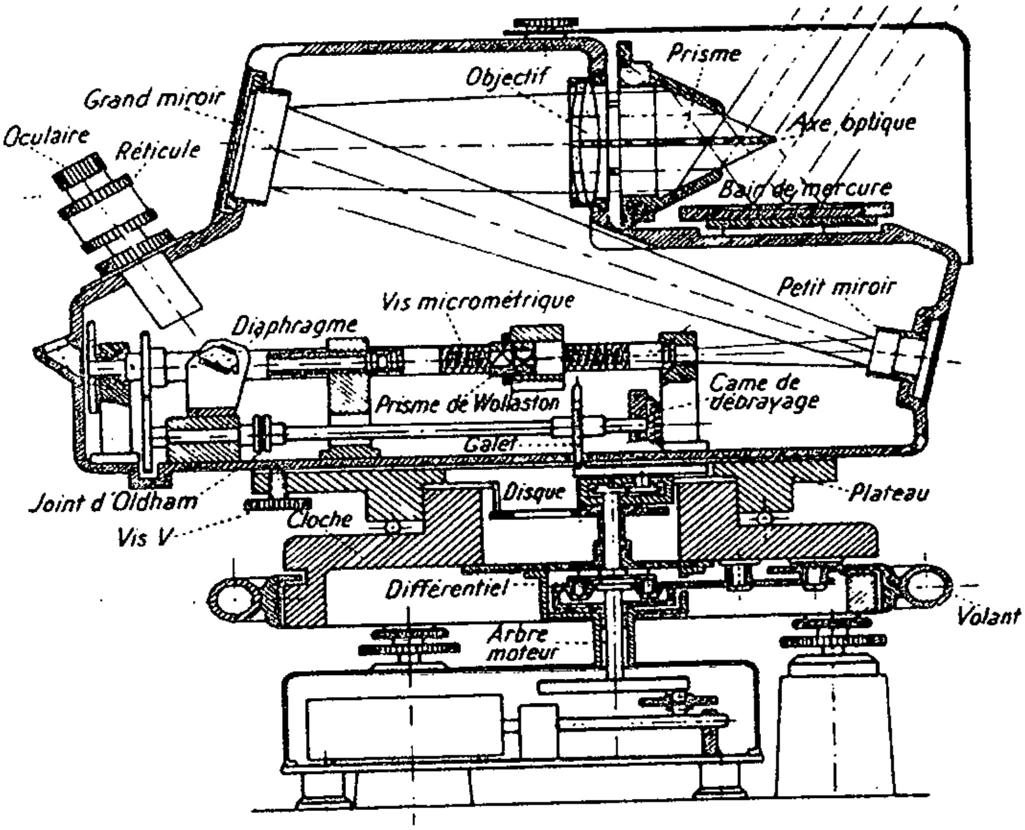

Figure II-3. OPL type of Danjon Astrolabe.

II.4 Solar astrolabe

F.Laclare achieved in 1974 at the observatory of Calern (Nice, France), the first observations of the Sun with a Danjon astrolabe. In order to protect the original glass prism, the brightness of the Sun is reduced to a value similar to that of the moon with the help of a solar filter. This filter is constituted with a shield in silica covered by a dielectric of multiple layered coating that has an optical density around 5.5.

At first, F.Laclare has used the above original equilateral prism that allowed the observation for a zenithal distance of 30°. Installed at an altitude of 44°N, the instrument endowed by this prism at the beginning, had a major handicap. It permitted the observation of the Sun only for declinations superior to 14°. That is less than three months per year. In addition, only one complete passage of the Sun can be observed during a day.

The advancement of the technology has permitted the use of other materials to design prisms. Several ceramic prisms working in reflection enriched the astrolabe of Calern observatory, and the choice of using different zenithal distances became possible. Currently, the solar astrolabe of Calern uses 11 prisms made of zerodur material that maintains a very high angular stability during a long time. These prisms permit the observation of 22 passages of the Sun by height circles defined by the following zenithal distances 30°, 34°, 37.5°, 41.5°, 45°, 49°, 52.5°, 56.5°, 60°, 65°, 70°. Figure II-4 gives the synoptical schema of the solar astrolabe as it was operating in CERGA since 1978.

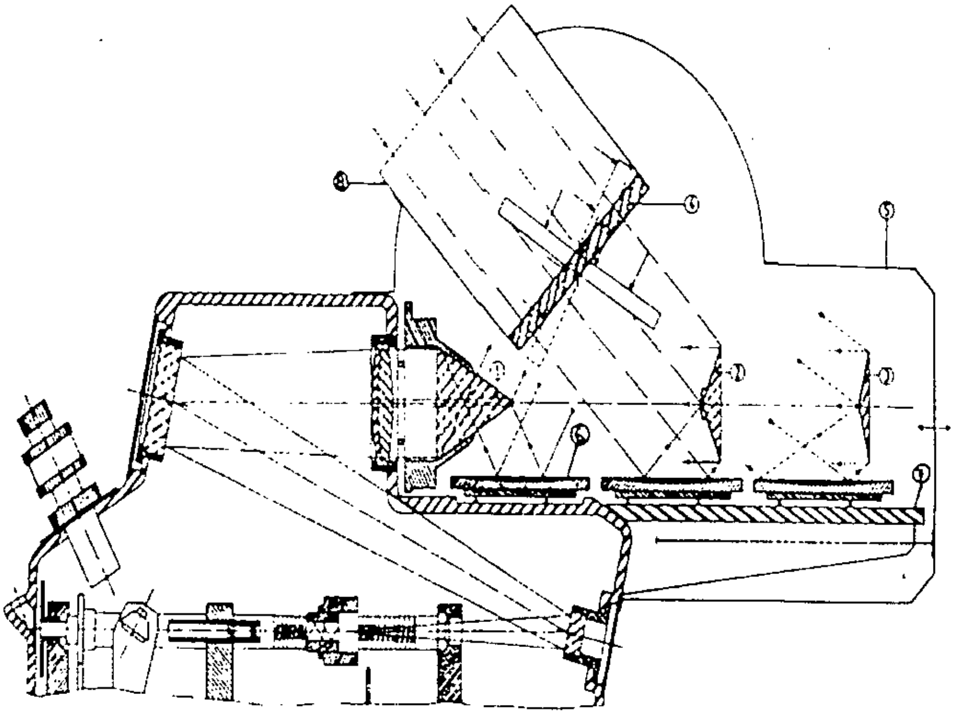

Figure II-4. The solar astrolabe used for solar observatory at Calern observatory
1-equilateral prism 2- 135° reflector prism 3- 150° reflector prism 4- solar filte.
5- removable protector 6- mercury bath 7- platinum 8-tube of incident rays.

II.4.1 Prisms

II.4.1.1 Equilateral classical prism

This kind of prism worked in transmission and was used for a zenithal distance of 30°. It has been studied for a long time by various authors [22,25]. In the case of the Sun observation, the entry face of this prism has been treated by a coating of multiple dielectric layers in order to permit the observation of stars and the Sun. The fact that the dilatation coefficient of the borosilicate with which the prism was made is not negligible, it induced a variation of zenithal distance. This disadvantage of its thermal instability was the object of several studies [14].

II.4.1.2 Zerodur prisms

These prisms has been proposed since 1967 by D.V.Thomas. They operate in reflection and assure higher stability of the instrumental zenithal distance due to their dilatation coefficients which are practically zero[14]. The shape of these prisms and their optical installation showed the best linkage between the angle of the prism and the zenithal distance of observation. Presently, the astrolabe of Calern is provided with 11 prisms of this type.

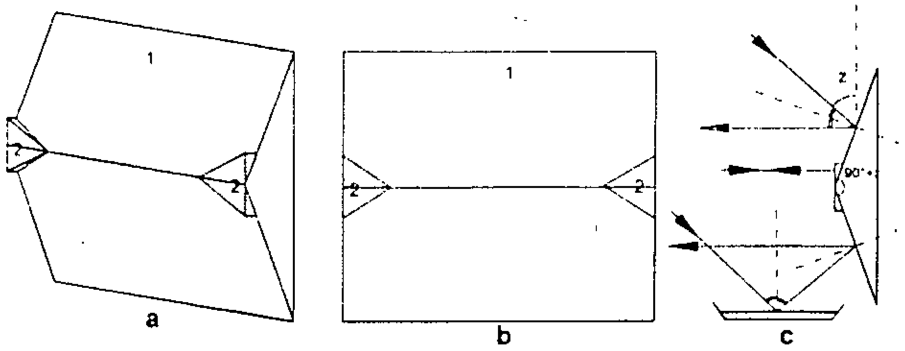

Figure II-5 . Zerodur reflector prism.

II.4.1.3 Variable angle reflector prism

In 1986 F.Laclare imagined this type of prism, which is initially destined to a new CCD astrolabe. This prism works by a system of coil compensation and can be adapted easily to automation. While using this prism, measurement showed a good stability of its angle between the passage of the two Sun edges [14]. This characteristic made it recommended in the case of solar diameter measurement where the zenithal distance of observation need not to be known, but must be stable [27].

Made with zerodur, the two reflecting faces of this prism can revolve around an axis as shown in Figure II-6. The support of this prism is of the same type as the one of the fixed angle prisms. It assures a good stability and a simple regulating procedure. Several models have been tested and the problem of coils remains the most critical one. The mercury bath must advance back and forth according to the angle of the prism. In addition, it must have a big enough surface to cover the observation bench of zenithal distances. The visual observations since 1986 and the CCD observations since 1989 have shown the performance of this prism.

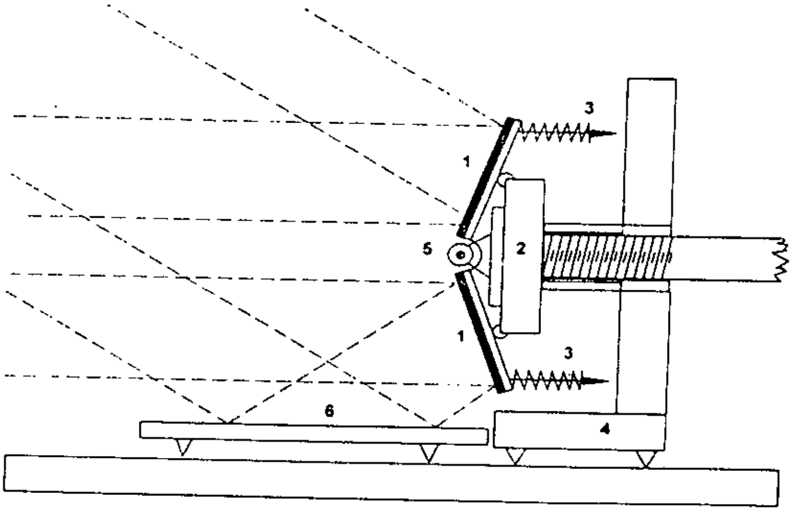

Figure II-6 .Prism of variable angle.
1-reflecting blade 2- pushing jack 3- spring of tension 4- support 5- rotation axis 6-mercury bath.

II.4.2 Solar filters

The use of an optical instrument to observe the Sun, requires the attenuation of the incident rays without changing their spectrum, this is the role of the solar filter (neutral density filter). In the case of the Danjon astrolabe, the prism that defines the zenithal distance of the observation and the micrometer of Wollaston are the main optical pieces that must be protected from Sun's rays. There are two possible locations for the solar filter: either in front of the objective of the telescope or in front of the prism.

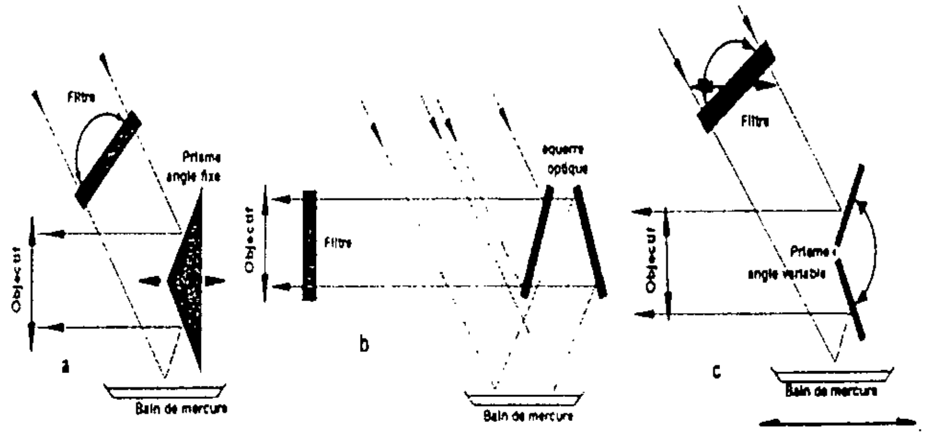

Figure II-7. Solar filters.
a- Setting in front of the prism b- setting in front of the objective c- setting in front of the prism of variable angle.

The solar filters designed with adopted silica are made of parallel planes whose outside faces carry Chrome - Nickel coatings of 5.5 optical density. Such planes must be perfectly parallel . Otherwise, they would change the zenithal distance of observation if the filter is positioned in front of the prism. Without influence on the measurement of solar diameter, this defect makes more uncertain the measurement of Sun position . The forward installation of the prism is so difficult to achieve technically because of the large dimension of the filter. Moreover, it must be perpendicular to the two images, which are in certain cases relatively distant from each other. On the other hand, if one places the filter rightly forward the objective, the defect of non parallelism of its faces does not affect the measurement anymore. At Calern Observatory, F.Laclare opted for a thick rectangular solar filter in silica placed in front of the prism [14,22,27].

II.4.3 Mercury bath

The mirror of mercury constitutes with the prism the instrumental reference of the astrolabe. If the prism defines the zenithal distance of observation, the mercury bath materializes the horizontal plane.

II.5 DORaySol instrument

Figure II-8 represents the diagram of the new generation of solar astrolabes named DORaySol (Definition et Observation du Rayon Solaire). The principle of Sun diameter measurement is the same as that of the solar astrolabe. In this instrument, the optical system of the solar astrolabe (refracting telescope) is replaced by a reflecting telescope. The acquisition is done via a CCD camera and a system of acquisition. The prism used is a prism of variable angle that permits the observation through a wide range of zenithal distances.

The rotating shutter permits the acquisition of an image each 250 ms, either direct or reflected on the mercury bath (only one image of the two Sun images appears at a given instant in the field of the objective, the rotating shutter masks the other). F.Laclare and G.Merlin designed the rotating shutter in 1991. It is composed of a half disc in rotation around the optical axis and a photoelectric cell that detects the position of the rotating sector and launches the acquisition process each 250 ms. Figure II-9 presents the possible reflecting telescope configurations. The DORaySol instrument is equipped with a reflecting telescope of a Cassegrain focus configuration.

II.6 Observational methodology of the solar radius

The basic principle of the astrolabe is shown in Figure II-10. An equilateral glass prism with one of its faces vertical is in front of a horizontal telescope. Two star images are formed from light passing through the prism. Direct rays internally reflected by its lower face produce one, and rays reflected by the horizontal mercury surface and then internally by the upper face produce the other. These two images will coincide when the zenithal distance of the star is equal to that defined by the prism; a zenithal distance of 30° in Figure II-10 is given as an example. A star can be observed with the astrolabe if it crosses the defined parallel (Almucantar) some time during its diurnal motion. Each star will make two transits through the parallel of latitude, one east and one west the observer's meridian. The time transition of the observed star through the defined height circle is automatically recorded.

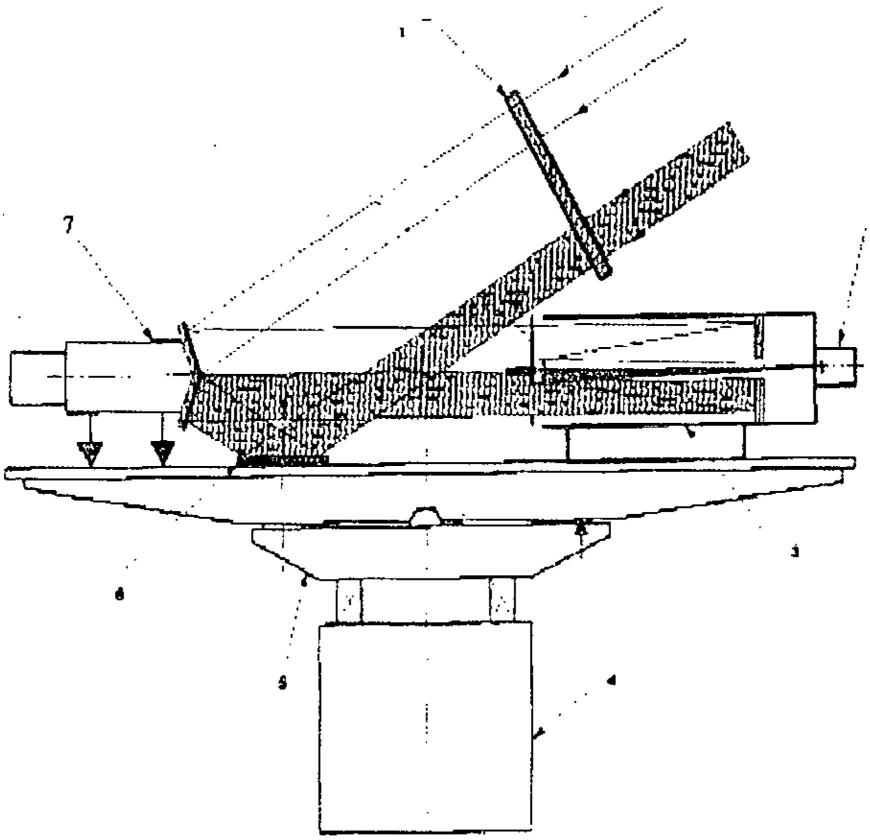

Figure II-8. DORaySol Instrument.
1-Solar filter 2- CCD camera 3- Reflecting telescope 4-fixed plate 5-Rotating plate 6- Mercury bath 7- prism of variable angle .

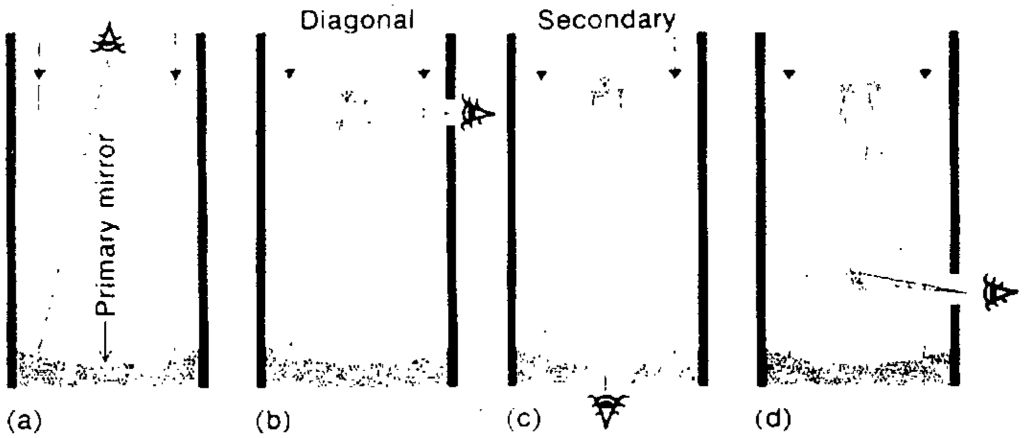

Figure II-9. Four reflecting telescopes using different focal points.
(a) Prime focus, (b) Newtonian focus, (c) Cassegrain focus, (d) Coudé focus.

In the Danjon astrolabe, through the ocular we see a reticule, four horizontal threads and four verticals. These threads represent a practical reference system during observation. Figure II-11 shows the typical aspect of observation in the case of stars. The sense of movement is given by the arrows direction. When the images are on one parallel of the horizontal threads, the observer launches the micrometer and maintains the two images on this parallel with the help of a differential corrector. A chronograph records the instants of electrical contacts. The mean instant calculated after twenty contacts represents the transition instant [14].

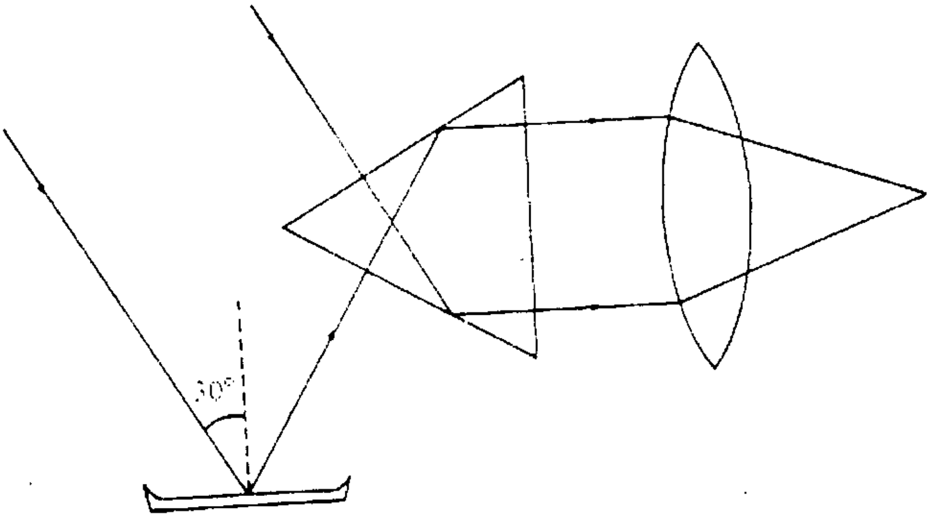

Figure II-10. Basic principle of an astrolabe.

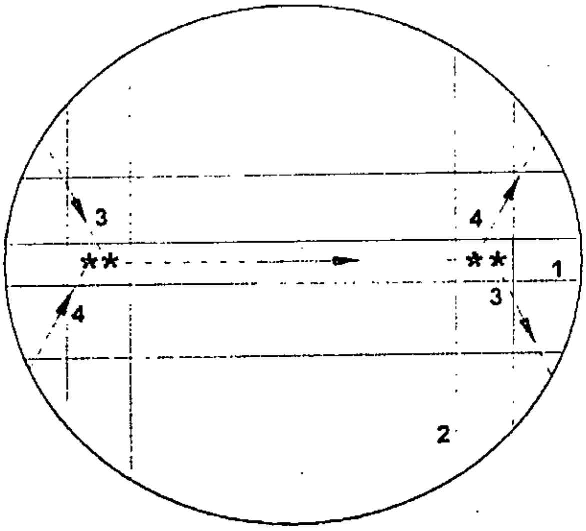

Figure II-11. Observation of a star transit.
1 Horizontal reticule wire 2 vertical reticule wire 3 Direct image 4 reflected image.

In the case of solar observation, the observed image is not point-like as in the case of stars. Therefore, the entire image cannot be observed and the centre of the Sun disc in any case is not accessible. The observation consists then to record the transition instant by Almucantar of particular points of the edge of the solar disc, which are chosen to be diametrically symmetric. The transit instant of the Sun centre is the same as its edge. When the solar edge passes through a zenithal distance z_0 defined by the instrument, that of the centre passes through a zenithal distance of $z_0 \pm d$ (d is the apparent semi-diameter of the Sun) at the same instant.

The solar diameter is obtained from the transit instants of the solar borders through Almucantar, which is fixed automatically by means of the mercury mirror and the reflecting prism. The astrolabe gives two images of the same part of the solar limb, one direct and the other reflected by the mercury surface. Each of them moves in the astrolabe focal plane due to the diurnal motion of the Earth (Figure II.12). The instant when these two images become adjacent corresponds to the instant when the Sun's edge crosses the parallel of atitude. The precision of the results depends mainly on the stability of the Almucantar and the time reference.

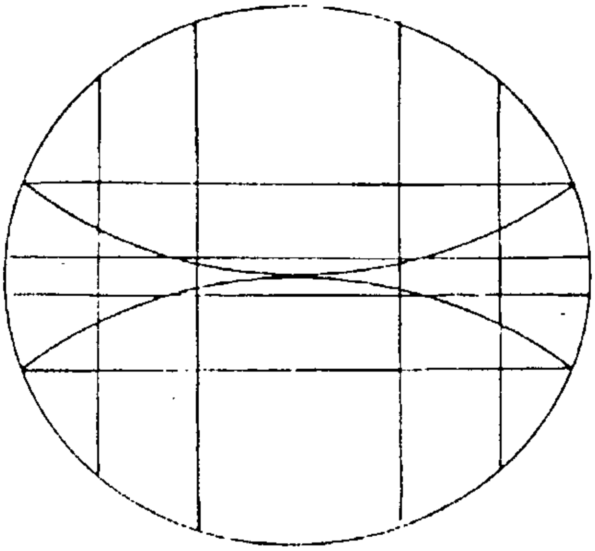

Figure II-12. Aspects of direct and reflected Sun edge images in the plane of the astrolabe.

II.7 Visual observations

In the case of visual observation, the tangency principle of Sun borders is the same as that of stars, if we assimilate the tangency points of the two Sun images to that of the two star images. Figure II.13 shows the solar astrolabe as used for the visual observation at Calern observatory [13].

The solar astrolabe uses as reference a parallel of altitude, which is defined by the angle above the horizon. A mercury surface provides a horizontal mirror. The constant angle is defined by a zerodur reflector prism (a set of 11 in the OCA" Observatoire de la Cote d'Azur " in France, two in OAM " Observatorio Abrahao de Moraes" in Brazil, and two for the astrolabe of Santiago in Chile), instead of the equilateral prism. After the protecting filter, the image is split by the reflector prism and mercury mirror to two images. After that they are focused by a refracting telescope (whose focal length is 3.50 m). A Wollaston prism gives the possibility to maintain the focusing in the case of a zenithal distance variation. A micrometer screw in translation compensates for the vertical shift of both images in order to extend the apparent duration of tangency. As for stars, the tangency of the two images of the observed Sun edges must be maintained parallel to the horizontal threads of the reticule.

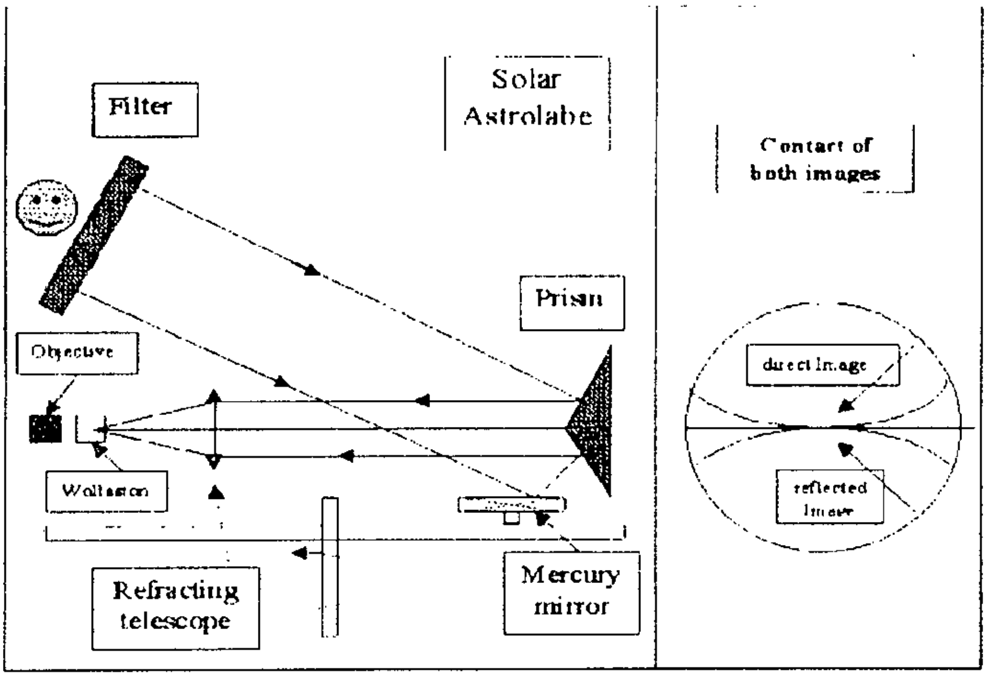

Figure II-13. Solar astrolabe for visual observations.

Atmospheric blurring of images is constantly fluctuating, but the human eye and the brain system are able to select and memorize the sharper images, provided enough time is available. Therefore, during the Sun transit, the observer keeps both images in tangential contact. In this instant the Sun's edge crosses the defined parallel of altitude (Almucantar). In practice, as the two images enter in the field of the instrument, and before the instant of their tangency, the observer has a few seconds to align the two images in relation to the system defined by the reticule of the ocular. The three necessary fine adjustments for a correct symmetry of the two images are presented in Figure II-14 [14].

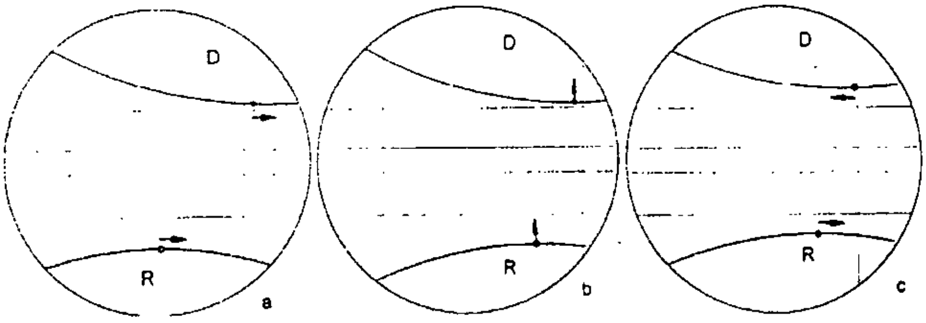

Figure II.14. The three fine adjustments for the solar observation.

a- A small rotation in azimuth, to displace the whole picture in relation to the vertical axis.
b- A tilt of the telescope in the vertical plane to displace the whole picture in relation to the horizontal axis.
c- Inclining the edge of the prism to move the two images symmetrically in relation to the horizontal axis.

In solar observations, a thermal variations in the interior of the astrolabe are created, inducing a displacement of the focal plane, and thus a variation of the instrumental zenithal distance. So, a stable focal point length is necessary for the quality of the measurements. The control of the variation of the focal distance is carried out by a dated autocollimation before and after each measurement. By setting a mirror in front of the objective and doing two autocollimations on the system of cross-wires, this gives a change in micrometer's units. Then an interpolation gives the value of the focal length at the time of contact. The average variation of the focal length during the few minutes between the crossings of both solar edges induces an error on the zenithal distance never bigger than 0.05 arcsecond [13].

The solar astrolabe has shown its quality in a series of visual observations done in France, Brazil, Turkey, Chili and Spain. The long series of visual observation done by F.Laclare during more than twenty years is the reference basis for the other series. The visual observations done by many observers can not be analyzed in the same way, since each observer has its manner to observe the Sun and his way to estimate the instant of tangency. In addition, each observer's eye has his own spectral response. So, it happens that two observers observe two different diameters.

The principal problem with visual observations is related to the definition of the observed edge. It is very difficult to respond to many questions such as: does the way of observation of the observer remain constant with time? Which solar edge do is the human eye sensitive to? and in addition, do we always observe the same point of the solar edge. Each bad interpretation of the solar edge or the tangency of the two images results in a false transition instant and consequently a bad result [28].

In spite of the impersonal micrometer devised by Danjon, the personal biases to the observations remain one of the main unknowns. The legitimacy of visual observations for measuring the solar diameter has been disputed. The personal equation is extremely difficult to estimate. Therefore, the absolute value of the solar diameter obtained from visual observations can be strongly affected by personal biases. Nevertheless, for solar physics the eventual variations of the Sun semi-diameter are far more interesting than its actual value [28,29].

II.8 CCD observations

Since 1989, the use of a CCD camera has removed all personal bias and provided an improved definition of the observed solar limb. The measurement principle remains the same as that of visual observation, with some particularities. The ocular is replaced by a CCD camera, which transmits the acquired images to a video monitor and to a system of acquisition. In order to record the tangency instant of the two images (incident and reflected), a set of direct and reflected solar images is recorded and saved alternatively. A rotating shutter in front of the objective eliminates one of the two images at a given a time. The shutter takes 500 ms to make one turn, so, each image has 250 ms to be acquired and analyzed.

Each solar image gives the distribution of the apparent solar intensity I(x,y) in the CCD frame. The CCD camera lines and columns define this frame. For each image the solar edge is detected by determining the image line inflection point. The position of these points is adjusted by an parabolic arc (Figure II-15). The subsequent analysis is done in order to obtain the successive positions of the extremity of the vertical solar diameter in the same CCD frame. The sets of these positions, one for each successive direct and reflected image obtained during the limb transit, show the trajectories of the extremity of the vertical solar radius (Figure II-16). These coordinates are functions of times $x_d(t)$ and $y_d(t)$ (direct images), and $x_r(t)$ and $y_{r(t)}$ (reflected images) relative to the CCD frame. The instant of crossing of Almucantar is obtained when the two coordinates $y_d(t)$ of the direct image and $y_r(t)$ of the reflected image are equal.

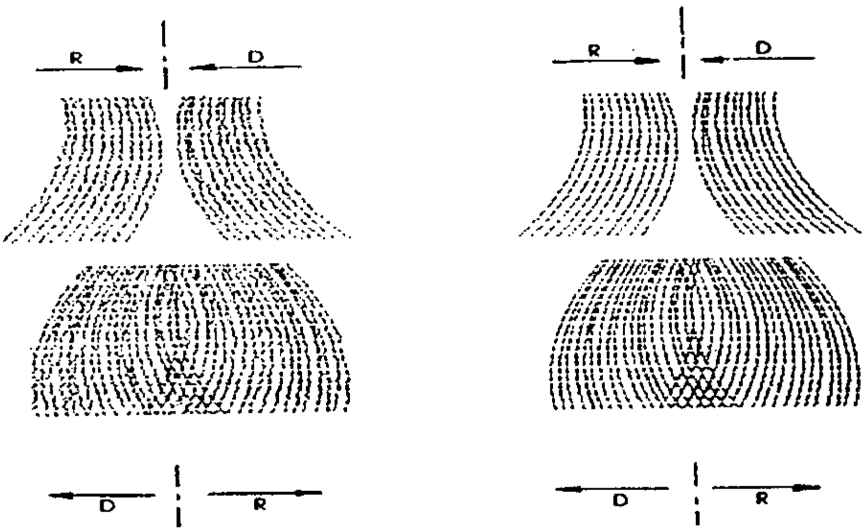

Figure II-15. Trajectories of the direct and reflected images on the CCD frame.

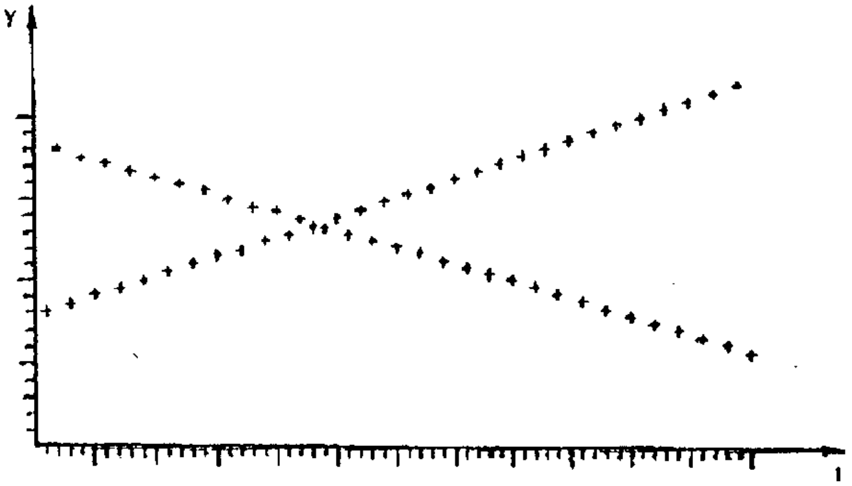

Figure II-16. The trajectories of the extremity of the vertical solar radius.

In the case of DORaySol, the necessary adjustments before each measurement to get symmetrical images are done by the bias of step-by-step motors; see Figure II-17 [14].

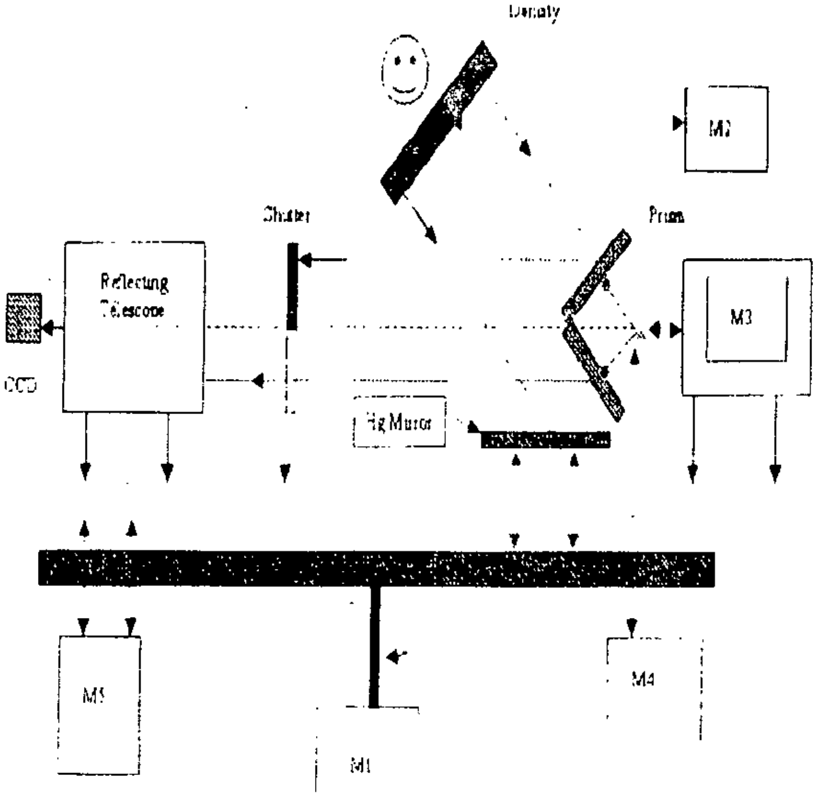

Figure II-17. The DORaySol instrument used for CCD observations in OCA.
M_1: Azimuth Motor
M_2: Filter Motor
M_3: Prism Motor
M_4: Prism Edge Inclination Motor
M_5: Optical Axis Tilt Motor.

When the best acquisition method and the best reduction procedure are used, the homogeneity of CCD measurements permits the expectation of a better precision than that of visual measurements. With the information quantity, the CCD observations gives us the opportunity to test several processing methods: cleaning of the images, deconvolution and specially the definition of the solar edge. Once the best processing method is chosen, it will be applied to the archived images. In addition, the CCD observations give access to certain parameters that help evaluate the atmospheric turbulence.

II.9 Accuracy of observations

The precision of the results depends on the stability of the instrumental zenithal distance and on the stability of the time reference clock, in addition to the precise knowledge of the atmospheric refraction variation during the short time interval of observation(~3 minutes). Another source of accidental or systematic effects are the variations of the instrumental zenithal distance induced by minute variations of the solar filter residual angle. These variations may be produced by temperature gradients inside the filter material. However, since the solar filter is made of a transparent type of CERVIT, such effects must be considered as negligible [6].

The atmospheric turbulence, refraction, Earth's motions and the impossibility of viewing the entire sky with a single instrument, are the limitation of ground-based astrometry.

The atmospheric refraction is generally computed for a given wavelength using the values of temperature, pressure, water vapor pressure at the instant of observation, using a standard model. These models are not perfect and there existence of systematic and random anomalies [20]. The random errors, which are time dependent, may amount to few hundredths of an arcsecond [20]. Even if unknown refraction parameters are determined at the same time as other observation reduction parameters, errors still exist. It is not possible to compute the modeled refraction more better than ± 0".02 tan z [20]. So, whatever the detector, and before the space techniques could possibly take over, the Earth's atmosphere is a major source of error in the measurement.

CHAPTER III SUN IMAGES PROCESSING

The introduction of the new generation of solar astrolabes based on CCD observations, the processing method of extracting the Sun edge from the acquired images, is the fundamental step in Sun semi-diameter measurement. Sun images present sunspots that must be localized and eliminated before edge detection. These non-stationary defects must be eliminated from the images without reducing the image resolution, since the principle of Sun semi-diameter measurement is based on the point of tangency of the Sun to the height circle defined by the astrolabe. This chapter presents the wavelet transform, a processing method that is suitable for this type of non-stationary signals. The algorithms to implement the processing method and the developed techniques to extract the Sun edge are given. Finally, the different steps to extract the two transit instants necessary to calculate the Sun diameter and the corrections to be taken into consideration are presented.

III.1 Fourier Transform

The most popular transformation is the Fourier Transform that can also be used for non-stationary signals if we are only interested in what spectral components exists but not where they occur in the signal. However, if we want to know what spectral component occur and at what time (interval), then the Fourier transform is not the right transform to use.

Fourier Transform decomposes a signal to complex exponential functions of frequencies. The way it is done is defined by the following two equations [29]:

$$X(f)=\int_{-\infty}^{+\infty} x(t).e^{-2j\pi ft}\,dt \tag{III.1}$$

$$x(t)=\int_{-\infty}^{+\infty} X(f).e^{2j\pi ft}\,df \tag{III.2}$$

t stands for time or space, f for frequency, x denotes the signal at hand and X denotes the signal in frequency domain. The signal x(t), is multiplied by an exponential term, at some certain frequency "f", and then integrated over all times.

The information provided by the integral corresponds to all time instances, since the integration is from minus infinity to plus infinity over time. It follows that no matter where in time the component frequency of "f" appears, it will affect the result of the integration equally as well. This is why the Fourier Transform is not suitable if the signal has time varying frequency. The Fourier Transform tells whether a certain frequency component exists or not. This information is independent of where in time this component appears. So, there is no information of frequency localization. To overcome this disadvantage of the FT and introducing the time business into the frequency plot, the Short Term Fourier Transform (STFT) was introduced .

III.2 Short Term Fourier Transform

The Short Term Fourier Transform comes from the approach of assuming that some portion of a non-stationary signal is stationary. In STFT, the signal is divided into small enough segments, where these latter can be assumed stationary. For this purpose, a window function "w" is chosen. The width of this window must be equal to the segment of the signal where its stationarity is valid. This window function is first located at the beginning of the signal, and then shifted to different locations along the processed signal until its end. At each location, the FT is taken as taking the FT of any signal.

The STFT is defined by the following equation:

$$STFT_X^{(w)}(t,f)=\int_t [x(t).w^*(t-t')].e^{-j2\pi ft}dt \qquad \text{(III.3)}$$

Where x(t) is the signal itself, w(t) is the window function, and * is the complex conjugate. As it can be seen, the STFT of the signal is nothing but the FT of the signal multiplied by a window function. The STFT principle is shown in Figure III-1.

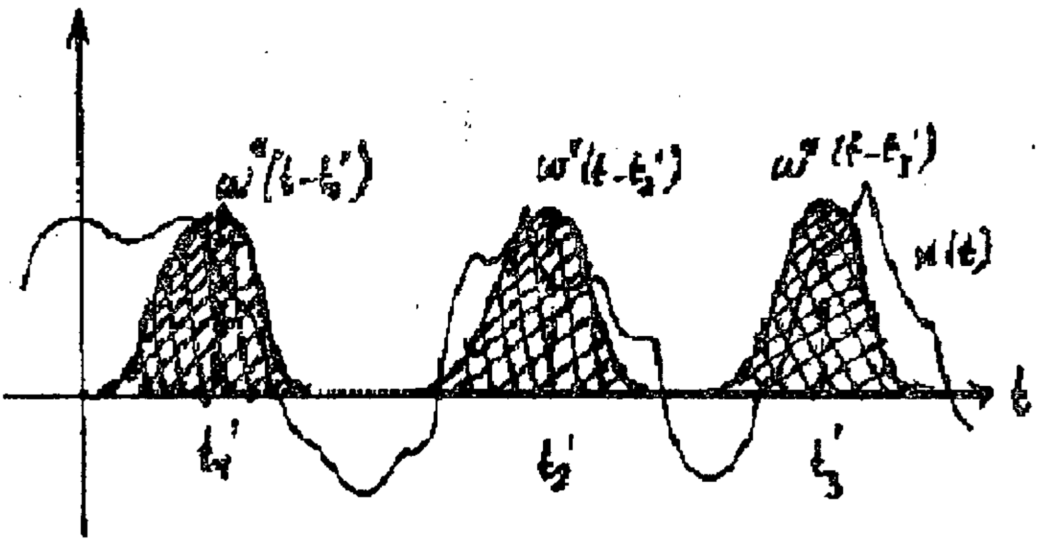

Figure III-1.Principle of STFT.

The problem with the STFT has something to do with the width of the window function used. In the case of FT there is no resolution problem in the frequency domain, since the existing frequencies are exactly known. Similarly there is no time resolution problem in the time domain, since we know the value of the signal at every instant of time. Conversely, the time resolution in the FT, and the frequency resolution in the time domain are zero. What gives the perfect frequency resolution in the FT is the fact that the window used in the FT lasts at all times from minus infinity to plus infinity. Now, in STFT, the window is of finite length. Thus, it covers only a portion of the signal that causes the frequency resolution to get poorer. If a window of infinite length is used, we get the FT that gives perfect frequency resolution but no time information. Furthermore, to obtain the stationarity, we must have a short enough window in which the signal is stationary. The narrower we make the window, the better the time resolution is and the best the assumption of stationarity would be, but weaker the frequency resolution would become.

The effect of the window length on the STFT is illustrated in Figure III-2(a). The window used is a Gaussian function of the form:

$$w(t)=e^{(-at^2/2)} \tag{III.4}$$

Where a is the window's length and t is the time. The signal used is a non-stationary signal; see Figure III-2(b). It contains four frequency components at different times. The interval 0 to 250 ms is a simple sinusoid of 300 Hz, and the other 250 ms intervals are sinusoids of 200 Hz, 100 Hz, and 50 Hz, respectively.

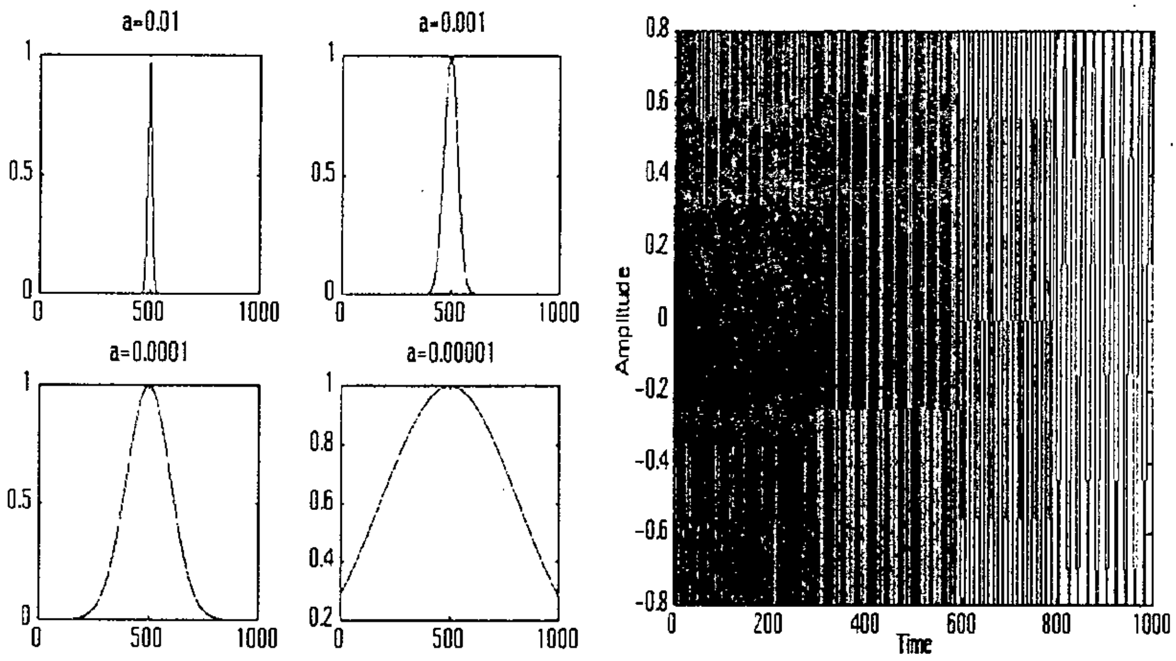

(a) *(b)*

Figure III-2. (a) The window function for different values of a. (b) The analyzed non-stationary signal.

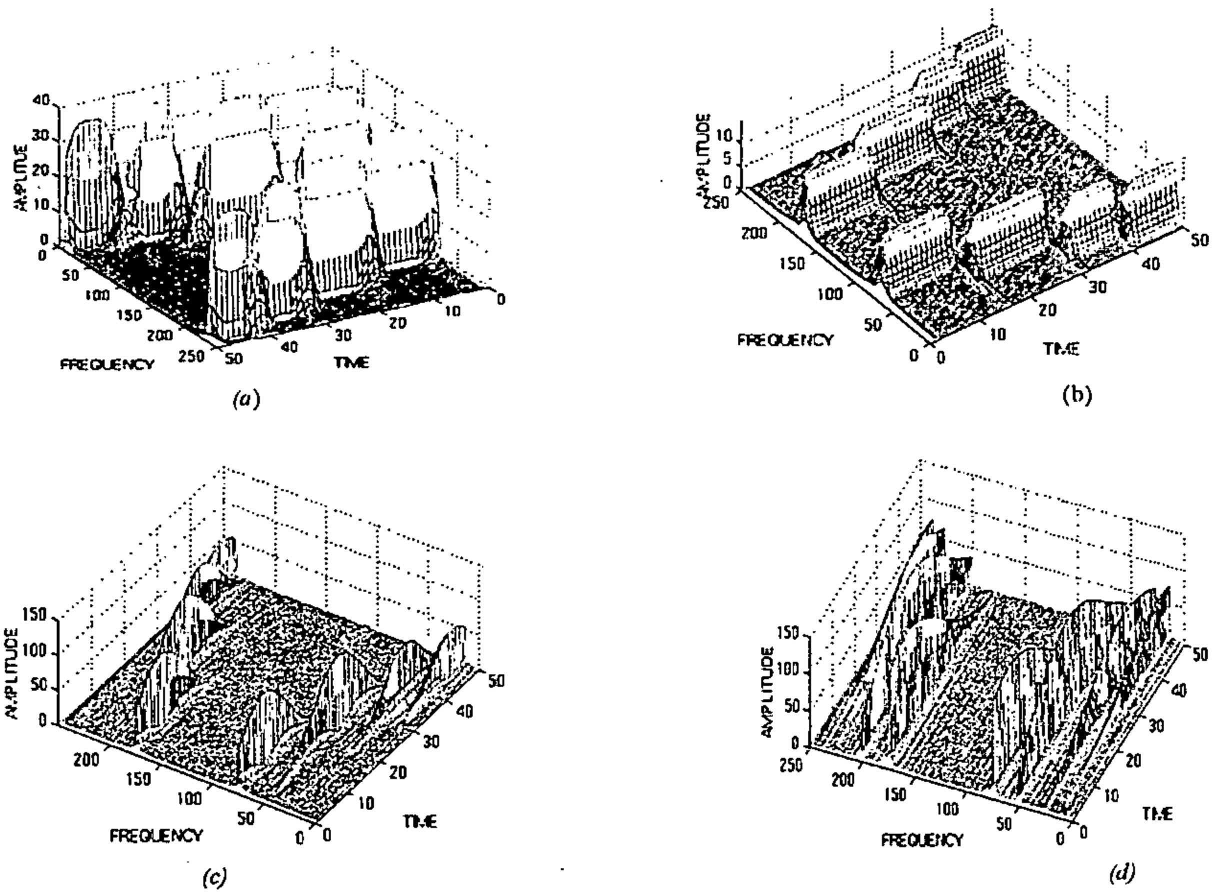

Figure III-3. The STFT of the signal. Four peaks are located at different time interval along the time axis corresponding to four different frequency components.

Figure III-3(a) represents the STFT of the signal using the above-defined gaussian with an a equal to 0.01. We notice that we have a very good time resolution, but relatively poor frequency resolution.

Figure III-3(b) shows the STFT of the signal with a equal to 0.001. The resolution in frequency increases where the resolution in time decreases.

Figure III-3 (c) represents the STFT of the signal with a equal to 0.0001. The peaks are not well separated from each other in time, unlike the previous case. However, in frequency domain the resolution is much better.

Figure III-3 (d) represents the STFT of the signal with a equal to 0.00001. The resolution in time is very poor or the frequency resolution is now better.

The above example illustrates the implicit problem of the STFT. The problem is not resolved by choosing a window function and using it in the entire analysis, since this later is application dependent. The Wavelet transform (WT) solves this dilemma of resolution.

III.3 Wavelet Transform (WT)

The WT was developed as an alternative to the STFT in order to overcome some resolution related problems of this later. The WT works as follow: we pass the time-domain signal from various highpass and low pass filters that filter out either high or low frequency portions of the signal. This procedure is repeated and each time some portions of the signal correspond to some frequencies is removed from the signal. The STFT gives a fixed resolution at all times, whereas WT gives variable resolution as shown in Figure III-4.

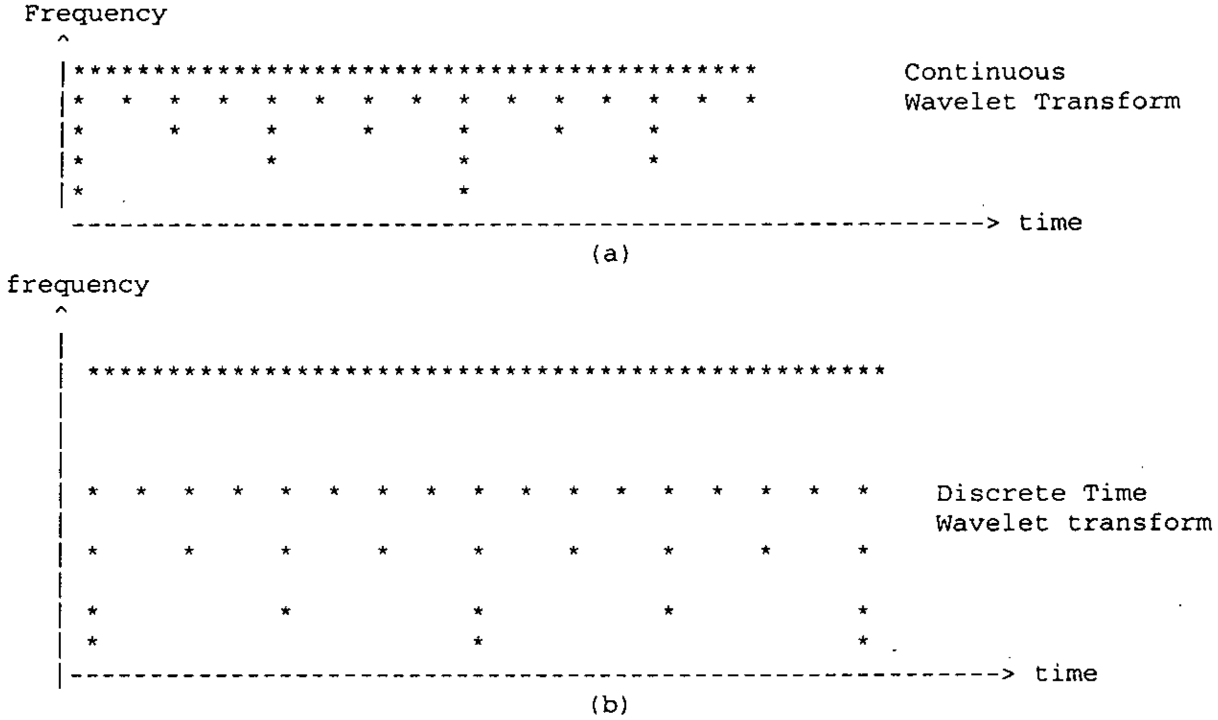

Figure III-4. Variable resolution of the WT. (a) Continuous wavelet transform (b) discrete time wavelet transform.

In Figure III-4(a), the top row shows that at higher frequencies we have more samples corresponding to smaller intervals of time. So higher frequencies can be resolved well in time. The bottom row shows less number of points that characterize the signal. Therefore, low frequencies are not resolved well in time.

Where in Figure III-4(b), the time resolution of the signal works the same as above, but now, the frequency information has different resolutions at every stage too. Lower frequencies are better resolved in frequency whereas higher frequencies are not.

III.3.1 Continuous Wavelet Transform (CWT)

The fundamental idea of the wavelet analysis is to break the signal down into its components and to follow their evolution in the time domain. The wavelet analysis is based on the integral [21]:

$$C_{a,b} = \int_{-\infty}^{+\infty} f(t)\psi_{a,b}(t)dt \tag{III-5}$$

The convolution between the function to be analyzed *f(x)*, and the wavelet functions $\psi_{a,b}(t)$. The set of wavelets $\psi_{a,b}(t)$ forms a wavelet family where each family member is generated through translation and dilatation of a mother wavelet $\psi(t)$:

$$\psi_{a,b}(t)=\frac{1}{\sqrt{|a|}}\psi(\frac{t-b}{a}) \qquad \text{(III-6)}$$

The dilatation parameter (the scale), a, changes the size of the wavelet and the translation parameter, b , shifts the wavelet on the time axis. Consequently all wavelets of a family have the same shape but their scale and localization in the time domain are different. Both parameters, a and b are reel numbers.

The parameter scale in the wavelet analysis is similar to the scale used in maps. High scales correspond to a non-detailed global view (of the signal), and low scales correspond to a detailed view. Similarly, in terms of frequency, low frequencies (high scales) correspond to global information of a signal, whereas high frequencies (low scales) correspond to detailed information of a hidden pattern in the signal (that usually lasts a relatively short time).

The normalization factor $\frac{1}{\sqrt{|a|}}$ ensures that the wavelet of a family has the same norm as their mother wavelet, that is,

$$\int_{-\infty}^{+\infty}|\psi_{a,b}|^2\,dt=\int_{-\infty}^{+\infty}|\psi|^2\,dt \qquad \text{(III-7)}$$

Putting equation (III-6) into equation (III-5) the wavelet transform finally reads which maps the function onto a 2 dimensional field .

$$C_{a,b}=\frac{1}{\sqrt{|a|}}\int_{-\infty}^{+\infty}f(t)\psi(\frac{t-a}{a})dt \qquad \text{(III-8)}$$

Which maps the function *f(t)* onto a 2 dimensional field $C_{a,b}$.

The wavelet functions must obey the admissibility condition,

$$\int_{-\infty}^{+\infty}\psi_{a,b}(t)dt=0 \qquad \text{(III-9)}$$

which assures the reversibility of the wavelet analysis. That means, the function *f(t)* can be retrieved from $C_{a,b}$ without loosing information . The Inverse Wavelet Transform (IDWT) in this case is,

$$f(t)=\frac{1}{C}\int_{-\infty}^{+\infty}\int_{-\infty}^{+\infty}\frac{C_{a,b}\psi_{a,b}(t)}{a^2}dadb \tag{III-10}$$

where

$$\frac{1}{C}=\int_{-\infty}^{+\infty}\frac{|\hat{\psi}(w)|^2}{w}dw \tag{III-11}$$

and $\hat{\psi}(w)$ is the Fourier transform of $\psi(t)$.

III.3.2 Discrete Wavelet Transform (DWT)

To be practically computed by using computing devices the CWT must be discretized As in the FT and STFT, the most intuitive way of doing this is simply sampling the time-frequency (scale) plane. Again intuitively, sampling the plane with a uniform sampling rate sounds like the most natural choice. However, in the case of WT, the scale change can be used to reduce the sampling rate.

At higher scales (lower frequencies), the sampling rate can be decreased according to Nyquist's rule. In other words, if the time-scale plane needs to be sampled with a sampling rate of N1 at scale a_1, the same plane can be sampled with a sampling rate of N2, at scale a_2. The actual relationship between N1 and N2 is,

$$N_2=\frac{a_1}{a_2}N_1 \tag{III.12}$$

At lower frequencies the sampling rate can be decreased which will save a considerable amount of computation time [29].

The scale parameter a is discretized first on a logarithmic grid. The time parameter is then discretized with respect to the scale parameter. The most common value of the base of the logarithm is 2 because of its convenience. If 2 is chosen, only the scales 2, 4, 8, 16, 32, 64,etc. are computed. The time axis is then discretized according to the discretization of the scale axis. Since the discrete scale changes by factors of 2, the sampling rate is reduced for the time axis by a factor of 2 at every scale.

Expressing the above discretization procedure in mathematical terms. The scale discretization is $a=a_0^{\ j}$ where translation is $b=ka_0^{\ j}b_0$. In this case the continuous wavelet function defined by equation (III-6) becomes:

$$\psi_{j,k}(t)=a_0^{\ -j/2}\psi(a_0^{\ -j}t-kb_0) \tag{III.13}$$

which represents the Discrete Wavelet Transform (DWT).

III.4 Multiresolution signal decomposition

Although the time and frequency resolution problems are results of a physical phenomenon (the Heisenberg uncertainty principle) and exist regardless of the transform used, it is possible to analyse any signal by using an alternative approach called the Multiresolution Analysis (MRA). The MRA analyses the signal at different frequencies with different resolutions [30].

Multiresolution analysis [49] results from the embedded subsets generated by the interpolations at different scales. A function $f(x)$ is projected at each step j onto the subset V_j. This projection is defined by the scalar product $c_j(k)$ of $f(x)$ with the scaling function which is dilated and translated:

$$c_j(k) = < f(x), 2^{-j}\phi(2^{-j}x - k) > \qquad \text{(III-14)}$$

where <> denotes the scalar product.

As $\phi(x)$ is a scaling function which has the property :

$$\frac{1}{2}\phi(\frac{x}{2}) = \sum_n h(n)\phi(x-n) \qquad \text{(III-15)}$$

or

$$\hat{\phi}(2v) = \hat{h}(v)\hat{\phi}(v) \qquad \text{(III-16)}$$

where $\hat{h}(v)$ is the Fourier transform of the function $\sum_n h(n)\delta(x-n)$, we get

$$\hat{h}(v) = \sum_n h(n)e^{-2\pi nv} \qquad \text{(III-17)}$$

Equation (III-14) permits to compute directly the set $c_{j+1}(k)$ from $c_j(k)$. If we start from the set $c_0(k)$ we compute all the sets $c_j(k)$, with $j>0$, without directly computing any other scalar product:

$$c_{j+1}(k) = \sum_n h(n-2k)c_j(n) \qquad \text{(III-18)}$$

At each step, the number of scalar products is divided by 2. Step by step the signal is smoothed and information is lost. The remaining information can be restored using the complementary subspace ψ_{j+1} of V_{j+1} in V_j. This space can be generated by a suitable wavelet function $\psi(x)$ with translation and dilation.

$$\frac{1}{2}\psi(\frac{x}{2}) = \sum_n g(n)\phi(x-n) \qquad \text{(III-19)}$$

or

$$\hat{\psi}(2v) = \hat{g}(v)\hat{\phi}(v) \qquad \text{(III-20)}$$

We compute the scalar products $< f(x), 2^{-(j+1)}\psi(2^{-(j+1)}x - k) >$ with:

$$\psi_{j+1}(k)=\sum_{n} g(n-2k)c_j(n) \quad \text{(III-21)}$$

With this analysis, we have built the first part of a filter bank [51]. In order to restore the original data, Mallat uses the properties of orthogonal wavelets, but the theory has been generalized to a large class of filters by introducing two other filters $\tilde{h}$ and $\tilde{g}$ named conjugated to **h** and **g**. The restoration is performed with:

$$c_j(k)=2\sum_{l}[c_{j+1}(l)\tilde{h}(k+2l)+\psi_{j+1}(l)\tilde{g}(k+2l)] \quad \text{(III-22)}$$

In order to get an exact restoration, two conditions are required for the conjugate filters:

. Dealiasing condition:

$$\hat{h}(v+\frac{1}{2})\hat{\tilde{h}}(k+2l)+\hat{g}(v+\frac{1}{2})\hat{\tilde{g}}(v)=0 \quad \text{(III-23)}$$

. Exact restoration

$$\hat{h}(v)\hat{\tilde{h}}(v)+\hat{g}(v)\hat{\tilde{g}}(v)=1 \quad \text{(III-24)}$$

The principle of multiresolution is sketched in Figure III-5.

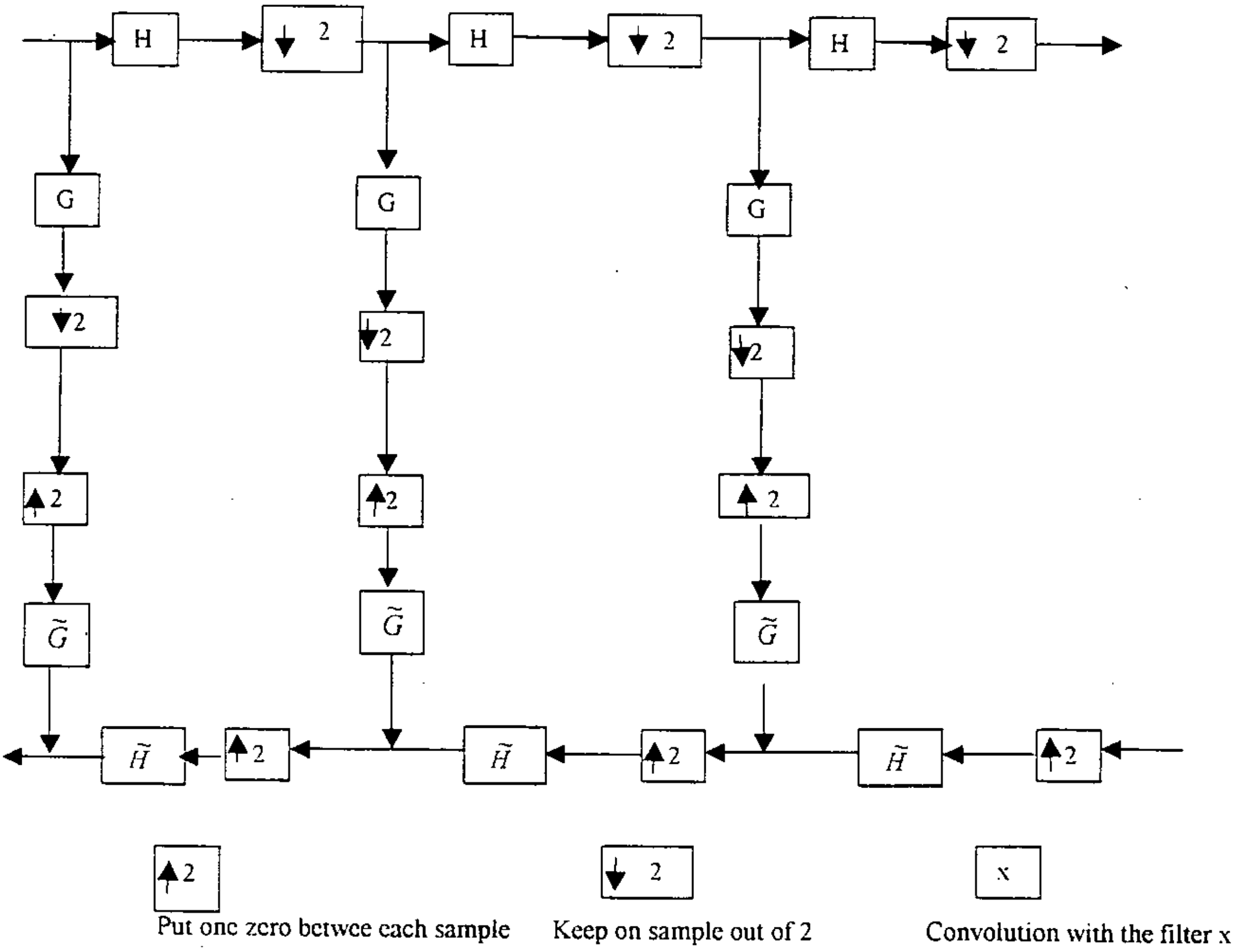

Figure III-5. The filter bank associated with the multiresolution analysis.

In the decomposition, the function is successively convolved with the two filters H (low frequencies) and G (high frequencies). Each resulting function is decimated by suppression of one sample out of two. The high frequency signal is left, and we iterate with the low frequency signal (upper part of Figure III-5) . In the reconstruction, we restore the sampling by inserting a **0** between each sample, then we convolve with the conjugate filters $\tilde{H}$ and $\tilde{G}$, we add the resulting functions and we multiply the result by **2**. We iterate up to the smallest scale (lower part of Figure III-5).

Orthogonal wavelets correspond to the restricted case where:

$$\hat{g}(\nu) = e^{-2\pi\nu}\hat{h}^{*}(\nu + \frac{1}{2}) \qquad \text{(III-25)}$$

$$\hat{\tilde{h}}(\nu) = \hat{h}^{*}(\nu) \qquad \text{(III-26)}$$

$$\hat{\tilde{g}}(\nu) = \hat{g}^{*}(\nu) \qquad \text{(III-27)}$$

and

$$\left|\hat{h}(\nu)\right|^{2} + \left|\hat{h}(\nu + \frac{1}{2})\right|^{2} = 1 \qquad \text{(III-28)}$$

We can easily see that this set satisfies the two basic relations (III-23) and (III-24) . Daubechies wavelets are the only compact solutions. For biorthogonal wavelets [51] we have the relations:

$$\hat{g}(\nu) = e^{-2\pi\nu}\hat{\tilde{h}}(\nu + \frac{1}{2}) \qquad \text{(III-29)}$$

$$\hat{\tilde{g}}(\nu) = e^{2\pi\nu}(\nu + \frac{1}{2}) \qquad \text{(III-30)}$$

and

$$\hat{h}(\nu)\hat{\tilde{h}}(\nu) + \hat{h}^{*}(\nu + \frac{1}{2})\hat{\tilde{h}}^{*}(\nu + \frac{1}{2}) = 1 \qquad \text{(III-31)}$$

Many sets of filters were proposed, especially for coding. It was shown [52] that the choice of these filters must be guided by the regularity of the scaling and the wavelet functions.

The 2D algorithm is based on separate variables leading to a prioritizing of x and y directions. The scaling function is defined by:

$$\phi(x,y)=\phi(x)\phi(y) \tag{III-32}$$

The passage from a resolution to the next one is done by:

$$f_{j+1}(k_x,k_y)=\sum_{l_x=-\infty}^{+\infty}\sum_{l_y=-\infty}^{+\infty}h(l_x-2k_x)h(l_y-2k_y)f_j(l_x,l_y) \tag{III-33}$$

The detail signal is obtained from three wavelets:

. a vertical wavelet :

$$\psi^1(x,y)=\phi(x)\psi(y) \tag{III-34}$$

. a horizontal wavelet:

$$\psi^2(x,y)=\psi(x)\phi(y) \tag{III-35}$$

. a diagonal wavelet

$$\psi^3(x,y)=\psi(x)\psi(y) \tag{III-36}$$

which leads to three sub-images:

$$C_{j+1}^1(k_x,k_y)=\sum_{l_x=-\infty}^{+\infty}\sum_{l_y=-\infty}^{+\infty}g(l_x-2k_x)h(l_y-2k_y)f_j(l_x,l_y) \tag{III-37}$$

$$C_{j+1}^2(k_x,k_y)=\sum_{l_x=-\infty}^{+\infty}\sum_{l_y=-\infty}^{+\infty}h(l_x-2k_x)g(l_y-2k_y)f_j(l_x,l_y) \tag{III-38}$$

$$C_{j+1}^3(k_x,k_y)=\sum_{l_x=-\infty}^{+\infty}\sum_{l_y=-\infty}^{+\infty}g(l_x-2k_x)g(l_y-2k_y)f_j(l_x,l_y) \tag{III-39}$$

The process of decomposition in the case of two dimension is represented by the Figure III-6.

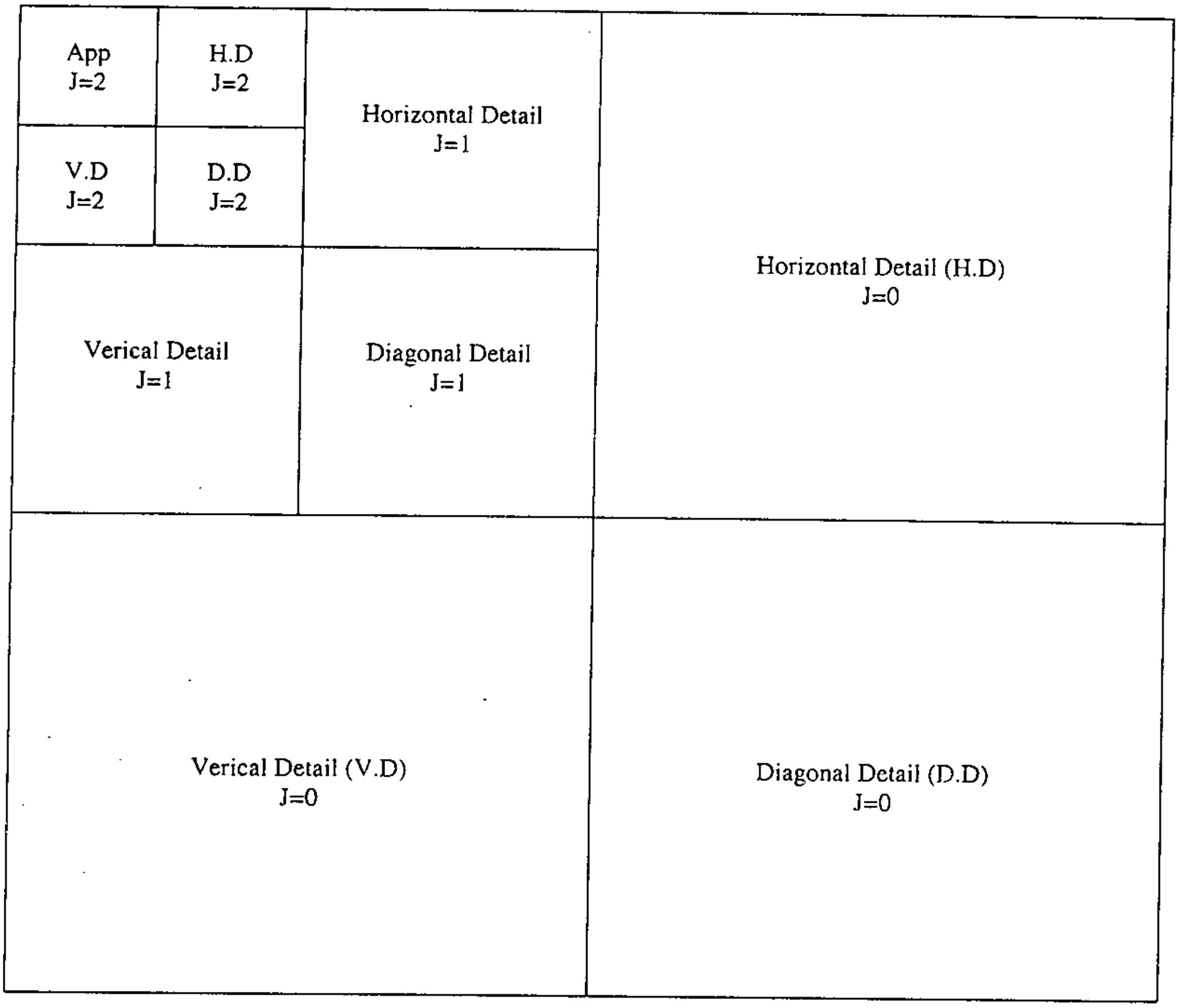

Figure III-6. Wavelet transform representation of an image.

The wavelet transform can be interpreted as the decomposition on frequency sets with a spatial orientation.

III.5 Wavelet examples

The research and theory applied to wavelets, permitted the definition of several base wavelets, each one is adapted to a specified applications. Between these wavelets we can state, Morlet wavelet, Haar wavelet, Daubechies wavelet, Meyer wavelet, Mexican Hat wavelet, Coiflets wavelet. Symlets wavelet, Biorthogonal wavelet,,. In our case, we will present the wavelet of Daubechies and the Mexican Hat that are used in the present work to process the Sun images.

III.5.1 Daubechies's wavelet

Ingrid Daubechies, one of the brightest stars in the world of wavelet research, invented what are called compactly supported orthonormal wavelets, thus making discrete wavelet analysis practicable. Different members of Daubechies of wavelets exist, the first wavelet is the Haar wavelet. It is a discontinuous function and resembles to a step function, see Figure III-7. It is defined by:

$$\begin{cases} \psi(x) = 1 & x \in [0, 0.5] \\ \psi(x) = -1 & x \in [0.5, 1] \\ \psi(x) = 0 & x \notin [0, 1] \end{cases} \tag{III-40}$$

The associated scaling function is defined as:

$$\begin{cases} \phi(x) = 1 - |x| & x \in [-1, +1] \\ \phi(x) = 0 & x \notin [-1, +1] \end{cases} \tag{III-41}$$

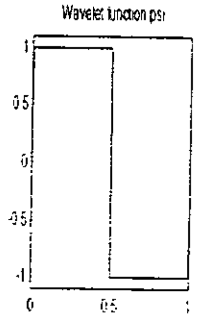

Figure III-7. The Haar wavelet.

Figure III-8 shows the next nine members of Daubechies's wavelet family.

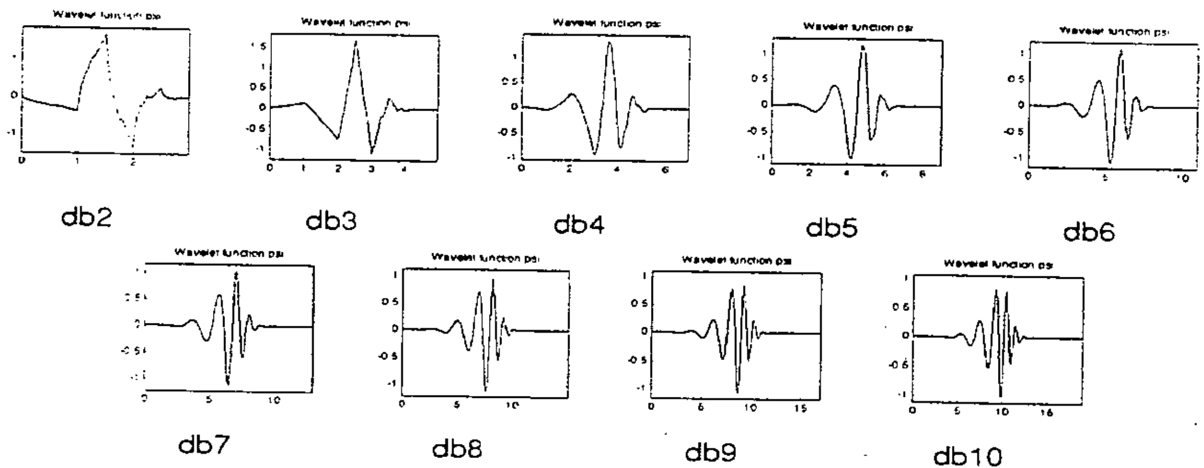

db2 db3 db4 db5 db6

db7 db8 db9 db10

Figure III-8. Some members of Daubechies's wavelet.

III.5.2 Mexican Hat wavelet

It is defined by:

$$\psi(x)=\frac{2}{3}\pi^{-1/4}(1-x^2)e^{-\frac{1}{2}x^2} \qquad \text{(III-42)}$$

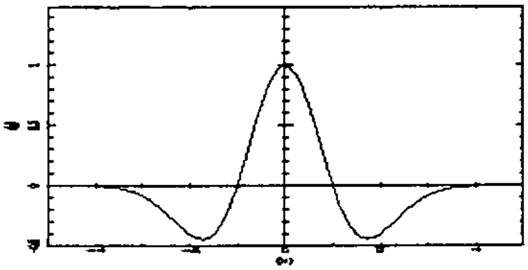

Figure III-9. Mexican Hat wavelet.

This function is proportional to the second derivative function of the Gaussian probability density function. This wavelet has no scaling function and it is derived from $\psi(x)$.

III.6 Algorithms to build wavelets

Two algorithms used in this work will be presented, the Mallat algorithm and the *à trous* algorithm.

III-6.1 Mallat's Algorithm

Given a signal s of length N, the DWT consists of $\log_2 N$ stages at most. Starting from s, the first step produces two sets of coefficients: approximation coefficients cA_1, and detail coefficients cD_1. These vectors are obtained by convolving s with the low-pass filter H for approximation, and with the high-pass filter G for detail, followed by dyadic decimation, as shown in Figure III-10.

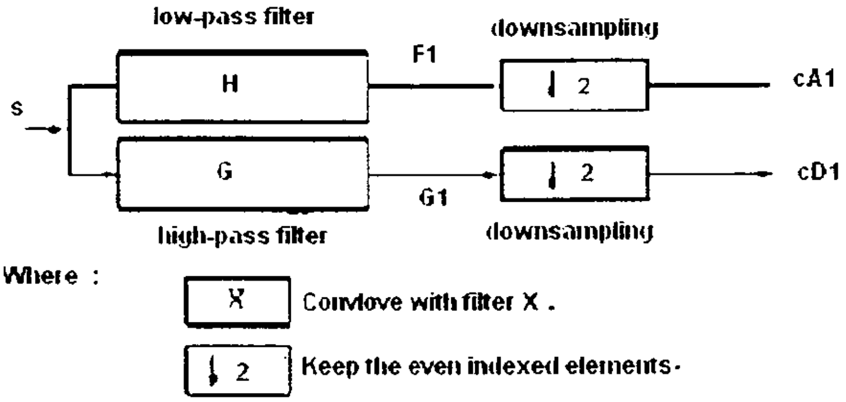

Figure III-10. Decomposition of a signal to approximations and details.

Precisely the process of decomposition works as follow:

The first step which is illustrated by Figure III-10, where,

The length of each filter is equal to $2N$. If n = length(s), the signals F1 and G1, are of length $n + 2N - 1$, and then the coefficients cA_1 and cD_1 are of length

$$\left(\frac{n-1}{2}\right)+N \tag{III-43}$$

The second is:

The approximation coefficients cA_1 is splitted in two parts using the same scheme, replacing s by cA_1 and producing cA_2 and cD_2, and so on.

III.6.1.1 Decomposition algorithm in one dimension

The algorithm is illustrated by the Figure III-11.

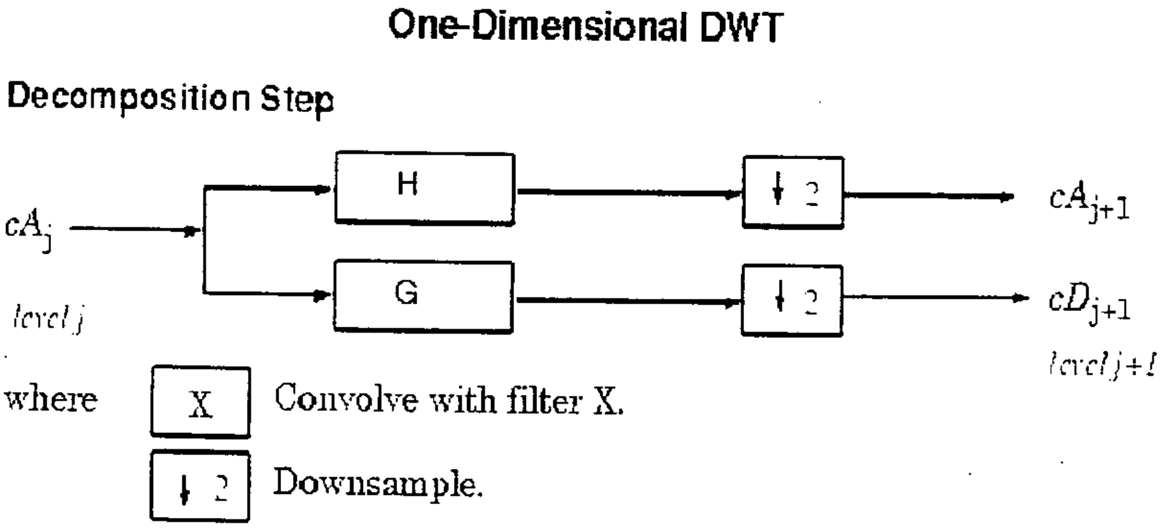

Figure III-11.Decomposition procedure.

Initialization cA_0=s

So the wavelet decomposition of the signal s analyzed at level j has the following structure: [cA_j, cD_j, ..., cD_1].
This structure contains for J = 3, the terminal nodes of the following tree represented by the Figure III-12.

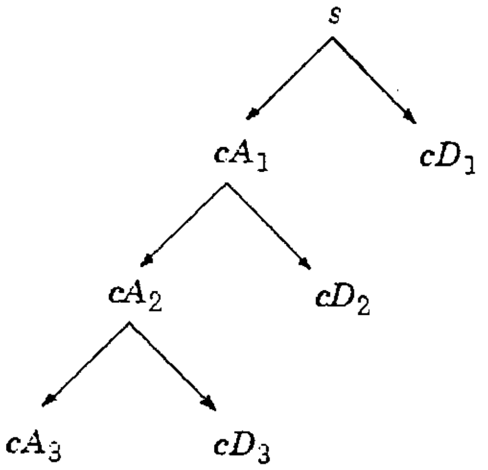

Figure III-12. The structure of decomposition for j=3.

III.6.1.2 Reconstruction algorithm in one dimension

Conversely, starting from cA_j and cD_j, the IDWT reconstructs cA_{j-1}, inverting the decomposition step by inserting zeros and convolving the results with the reconstruction filters. The reconstruction procedure is represented by Figure III-13.

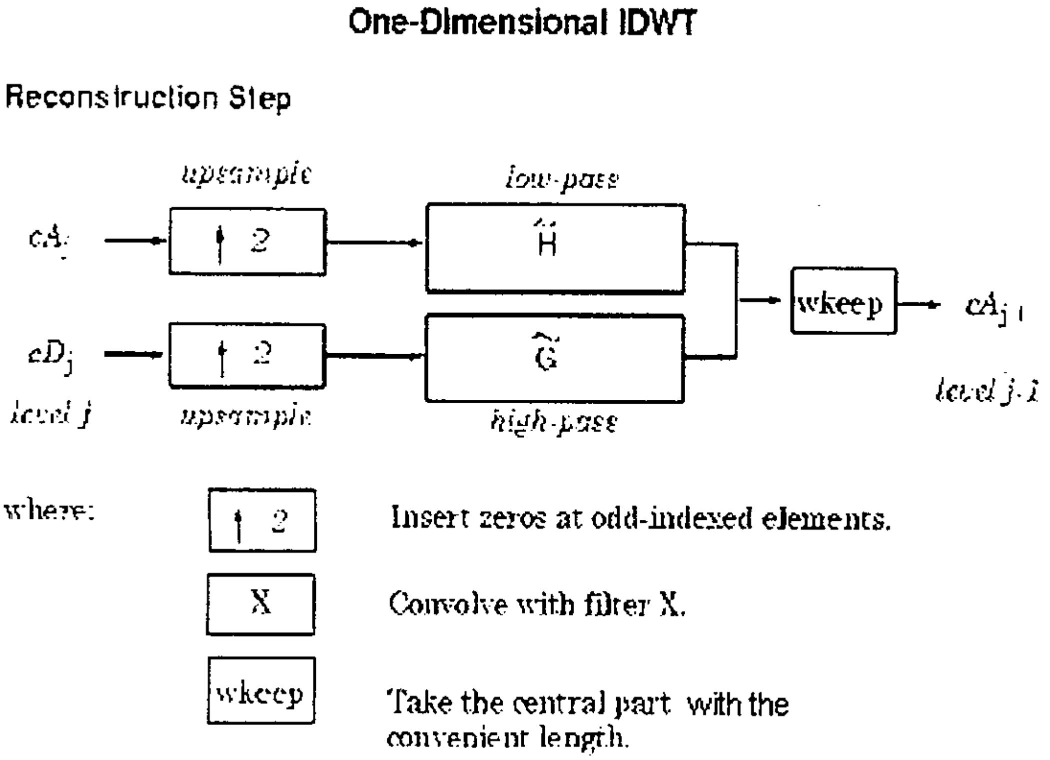

Figure III-13. Reconstruction procedure.

III.6.1.3 Decomposition and reconstruction algorithms in two dimensions

For images, a similar algorithm is possible for two-dimensional wavelets and scaling functions obtained from one-dimensional wavelets by tensorial product.

This kind of two-dimensional DWT leads to a decomposition of approximation coefficients at level *j* in four components: the approximation at level *j* + 1 and the details in three orientations (horizontal, vertical, and diagonal).

Figure III-14 and Figure III-15 describe receptively the basic decomposition and reconstruction steps for images:

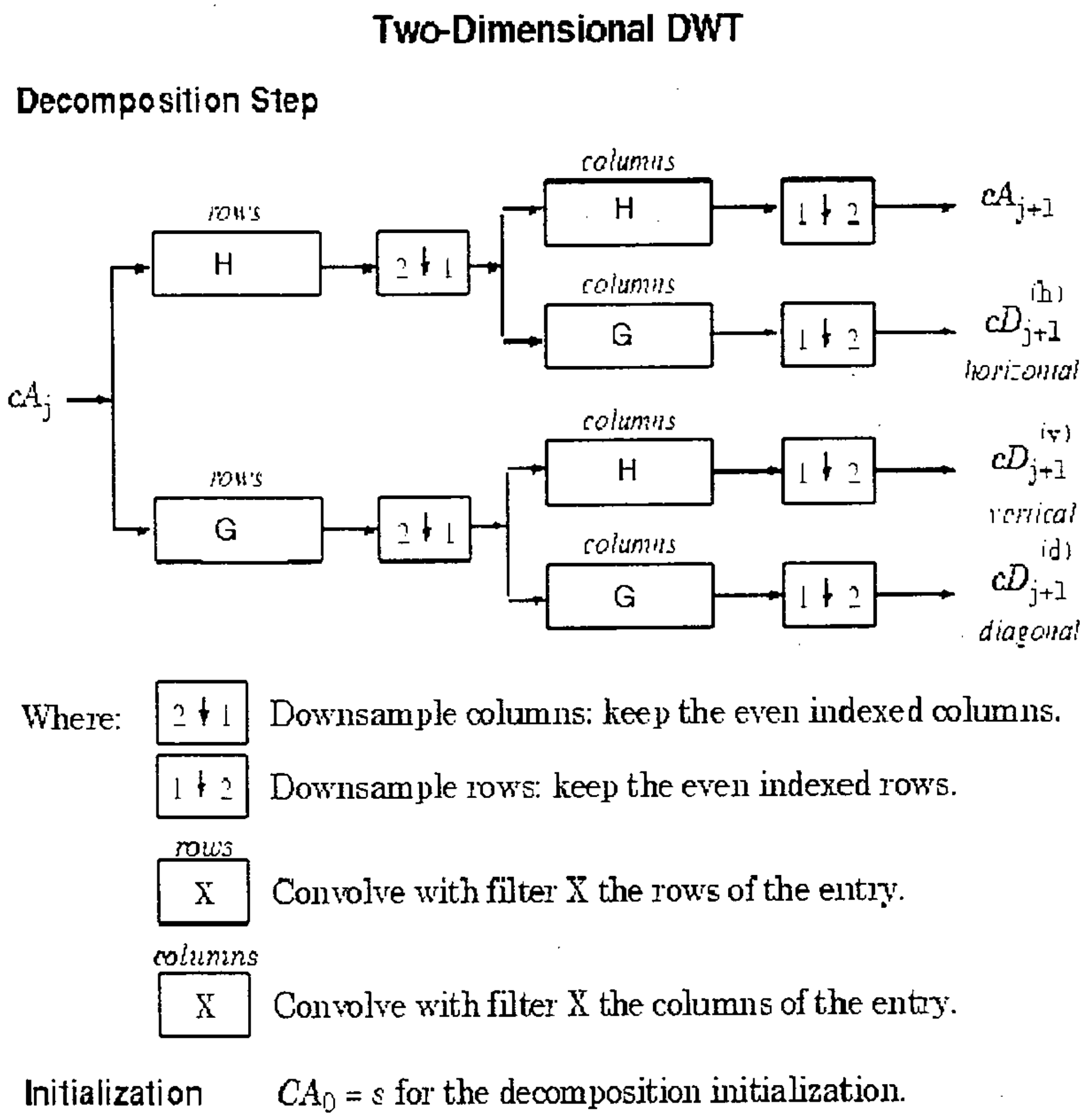

Where: 2↓1 Downsample columns: keep the even indexed columns.

1↓2 Downsample rows: keep the even indexed rows.

Convolve with filter X the rows of the entry.

Convolve with filter X the columns of the entry.

Initialization $CA_0 = s$ for the decomposition initialization.

Figure III-14. Decomposition steps in two dimensions.

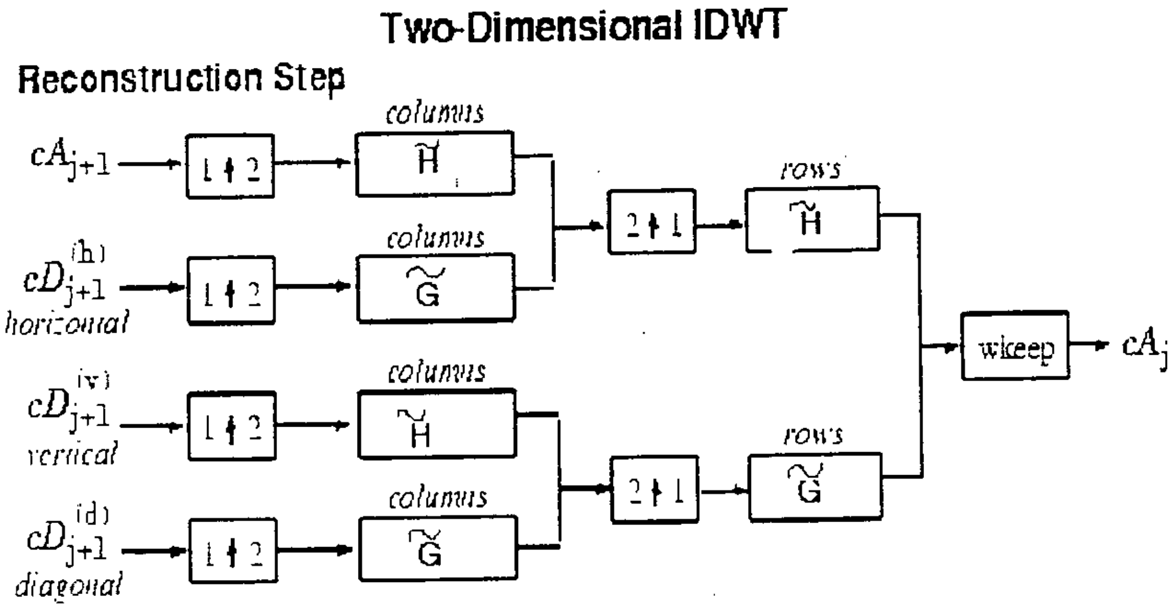

Where: $\boxed{2\uparrow 1}$ Upsample columns: insert zeros at odd-indexed columns.

$\boxed{1\uparrow 2}$ Upsample rows: insert zeros at odd-indexed rows.

rows $\boxed{X}$ Convolve with filter X the rows of the entry.

columns $\boxed{X}$ Convolve with filter X the columns of the entry.

Figure III-15. Reconstruction steps in two dimensions.

III.6.2 The *à trous* algorithm

The discrete approach of the wavelet transform can be done by a simple version of the so-called *à trous* algorithm (with holes). It is assumed that the wavelet coefficients { $c_0(k)$} are the scalar products at pixels k of the analyzed function *f(x)* with a scaling function $\phi(x)$ which corresponds to a low pass filter [31,32].

The first filtering is then performed by a twice-magnified scale leading to the { $\{c_1(k)\}$ set. The signal difference $\{c_0(k\}-\{c_1(k)\}$ contains the information between these two scales and is the discrete set associated with the wavelet transform corresponding to $\phi(x)$. The associated wavelet is therefore $\psi(x)$. It is given by,

$$\frac{1}{2}\psi(\frac{x}{2}) = \phi(x) - \frac{1}{2}\phi(\frac{x}{2}) \qquad \text{(III-44)}$$

The distance between samples increasing by a factor of 2 from the scale (i-1) (i>0) to the next one. The coefficients $c_i(k)$ are given by,

$$c_i(k)=\sum_l h(l)c_{i-1}(k+2^{i-1}l) \tag{III.45}$$

and the discrete wavelet transform $\psi_i(k)$ by:

$$\psi_i(k)=c_{i-1}(k)-c_i(k) \tag{III.46}$$

The coefficients $\{h(k)\}$ derive from the scaling function $\phi(x)$ are related by,

$$\frac{1}{2}\phi\left(\frac{x}{2}\right)=\sum_l h(l)\phi(x-l) \tag{III.47}$$

The reconstruction process is done by simple summation of the last approximation with the signal details of each resolution step. I mean, the last smoothed array c_{n_p} is added to the differences ψ_i.

$$c_0(k)=c_{n_p}(k)+\sum_{j=1}^{n_p}\psi_j(k) \tag{III-48}$$

The decomposition algorithm with wavelet is summarized as follow:

1- we initialize i to zero, and we start wit the data $c_i(k)$.

2- we increase i and we evaluate the discrete convolution of the data $c_{i-1}(k)$ with filter *h(n)* which gives the approximation signal.

3- The wavelet coefficients at the point k and at the scale i are given by:

$$\psi_i(k)=c_{i-1}(k)-c_i(k)$$

Two scaling functions $\phi(x)$ are tested with the *à trous* algorithm, the linear interpolation and the B_3-spline interpolation.

III.6.2.1 The linear interpolation:

The scaling function in this case is shown in Figure III-16. Its mathematical expression is given by,

$$\begin{cases} \phi(x) = 1 - |x| & x \in [-1,+1] \\ \phi(x) = 0 & x \notin [-1,+1] \end{cases} \qquad \text{(III-49)}$$

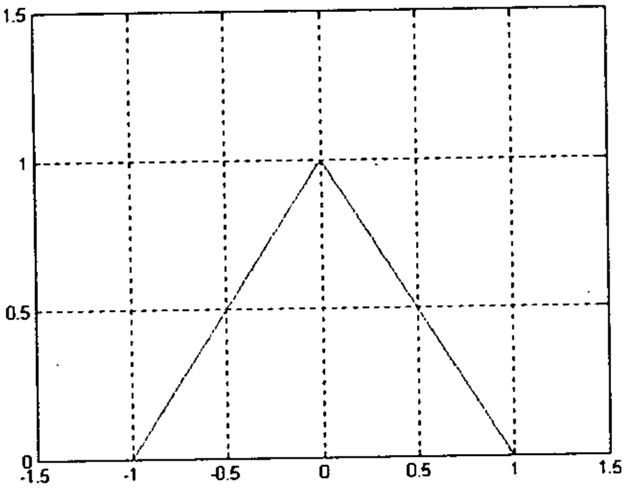

Figure III-16. Linear interpolation ϕ.

We have from equation III-47,

$$\frac{1}{2}\phi\left(\frac{x}{2}\right) = \frac{1}{4}\phi(x+1) + \frac{1}{2}\phi(x) + \frac{1}{4}\phi(x-1) \qquad \text{(III-50)}$$

c_1 is obtained by:

$$c_1(k) = \frac{1}{4}c_0(k-1) + \frac{1}{2}c_0(k) + \frac{1}{4}c_0(k+1) \qquad \text{(III-51)}$$

and c_{j+1} is obtained from c_j using,

$$c_{j+1}(k) = \frac{1}{4}c_j(k-2^j) + \frac{1}{2}c_j(k) + \frac{1}{4}c_j(k+2^j) \qquad \text{(III-52)}$$

The associated wavelet ψ with this scaling function calculated using equation III-44 is shown in Figure III-17. This wavelet is the Mexican Hat wavelet.

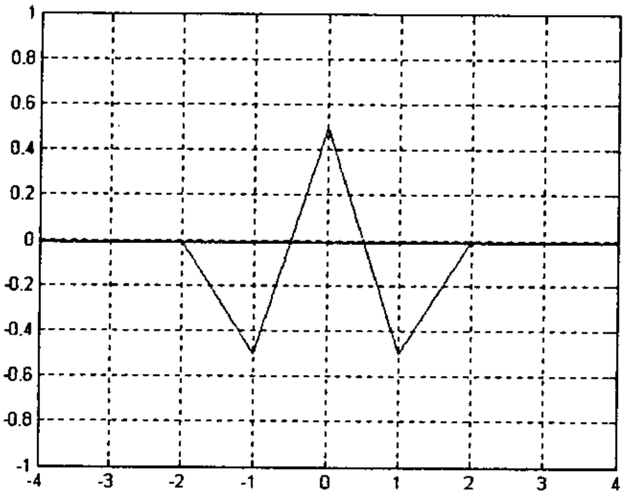

Figure III-17. The wavelet ψ.

The wavelet coefficients at the scale j using equation III-46 are:

$$W_{j+1}(k) = -\frac{1}{4}c_j(k-2^j) + \frac{1}{2}c_j(k) - \frac{1}{4}c_j(k+2^j) \qquad \text{(III-53)}$$

The above *à trous* algorithm is easily extensible to the two dimensional space. At each scale j, we obtain a set $\{\psi_j(k,l)\}$ which has the same number of pixels as the image, it is the advantage of the *à trous* algorithm, except that the wavelet used must be isotrope.

III.6.2.2 The B-spline interpolation

The B-spline interpolation of order *l* (*l* is odd) is written in general case as [33]:

$$B_s(x)=\frac{1}{2(2l-1)!}\sum_{k=0}^{2l}(-1)^k C_{2l}^k \left|x-l+k\right|^{2l-1} \qquad \text{(III-54)}$$

with $s=2l-1$. The filter coefficients *h(n)* associated are given by:

$$h(n) = \frac{C_{l+1}^{m-n}}{2^{l+1}} \text{ with } \quad m=\frac{l+1}{2} \qquad \text{(III-55)}$$

We choose the B-spline function of order 2 for the scaling function, it is given:

$$\phi(x)=B_3(x)=\frac{1}{12}\sum_{k=0}^{4}(-1)^k C_4^k \left|x-2+k\right|^3 \qquad \text{(III-56)}$$

Figure III-18 shows this $\phi(x)$ function.

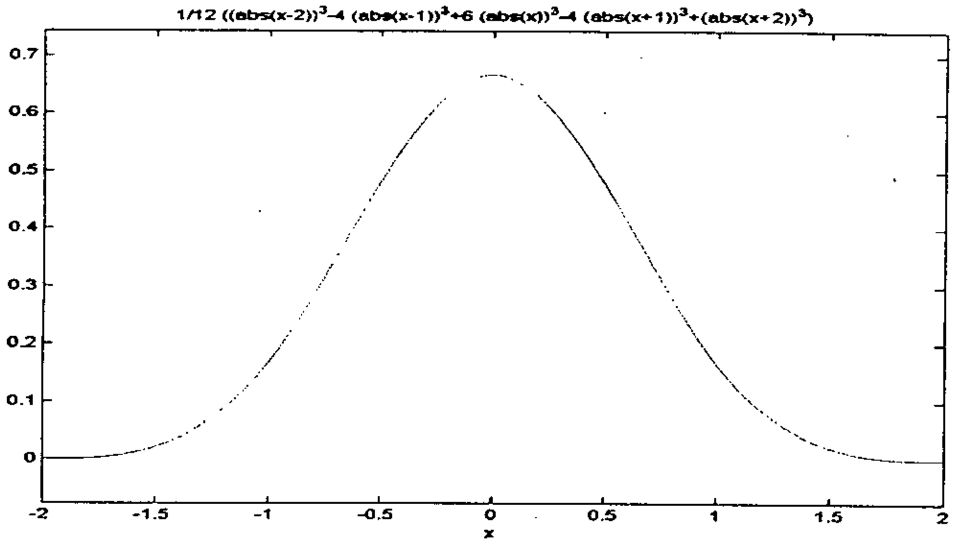

Figure III-18.The scaling function $\phi(x)$.

The associated wavelet $\psi(x)$ with this scaling function calculated using equation III-44, is shown in Figure III-19. It is the wavelet of Mexican Hat.

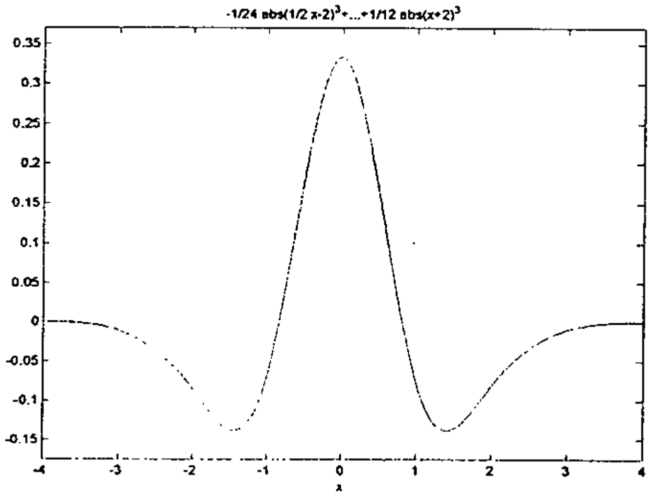

Figure III-19. The wavelet ψ.

Even though the two interpolations for the scaling function are tested, the one that will be presented and used in the present work is the B_3-spline interpolation.

III.7 Filters used to calculate the DWT and IDWT

The process of Sun images with wavelet transform is performed by using two algorithms, the *à trous* algorithm and Mallat's algorithm. Each one is implemented with a chosen set of filters(wavelets).

III.7.1 Filters with the *à trous* algorithm

In the case of B_3-spline interpolations for the scaling function, the associated wavelet is the Mexican Hat wavelet. The coefficients of the one dimensional filter *h* calculated from $\phi(x)$ are (1/16,1/4, 3/8,1/4,1/16) and in two dimensions are:

$$h(n) = \begin{pmatrix} 1/256 & 1/64 & 3/128 & 1/64 & 1/256 \\ 1/64 & 1/16 & 3/32 & 1/16 & 1/64 \\ 3/128 & 3/32 & 9/64 & 3/32 & 3/128 \\ 1/64 & 1/16 & 3/32 & 1/16 & 1/64 \\ 1/256 & 1/64 & 3/128 & 1/64 & 1/256 \end{pmatrix}$$

The filter *h* is a triangular low pass filter as shown in Figure III-20. Its transfer modulus is represented in Figure III-21.

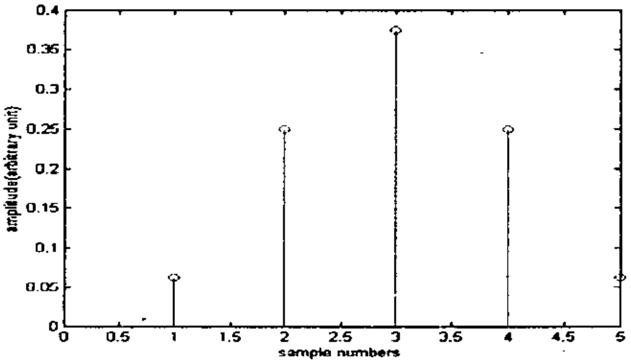

Figure III-20. The filter h(n).

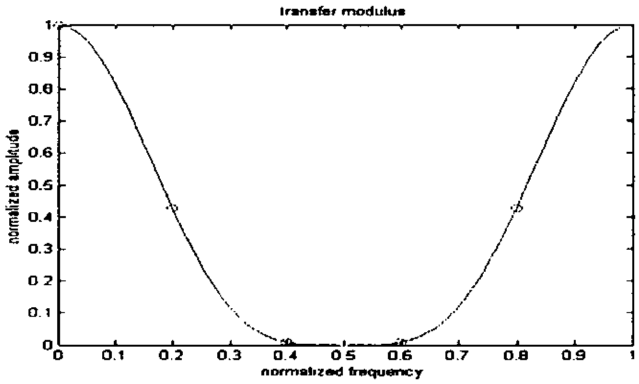

Figure III-21. The transfer modulus.

For the coefficients of the filter in the case of linear interpolation for the scaling function, see annex 7.

III.7.2 Filters with Mallat's algorithm

The wavelet used with the Mallat's algorithm is the Daubechies of order 3. For an orthogonal wavelet, in the multiresolution framework, we start with the scaling function ϕ and the wavelet function ψ. One of the fundamental relations between ϕ and ψ is the twin-scale relation (dilation equation or refinement equation):

$$\frac{1}{2}\phi(\frac{x}{2}) = \sum_{n \in Z} w_n \phi(x-n) \qquad \text{(III-57)}$$

if ϕ is compactly supported, the sequence (w_n) is finite and can be viewed as a filter. The filter W, which is called the scaling filter (nonnormalized), is:

- Finite Impulse Response (FIR)
- of length $2N$
- of sum 1
- of norm
  $\frac{1}{\sqrt{2}}$
- a low-pass filter

For our case the scaling filter is :

W=(0.2352 0.5706 0.3252 -0.0955 -0.0604 0.0249)

From filter W, four filters are defined of length 2N and of norm 1. They are organized as follow:

Filters	**Low-pass**	**High-pass**
Decomposition	**H**	**G**
Reconstruction	$\widetilde{\mathrm{H}}$	$\widetilde{\mathrm{G}}$

The relation between these filters is given by,

$$\begin{cases} \mathrm{G(k)} = (-1)^{k}\,\mathrm{H(2N+1-K)}, \ \text{for } \mathrm{k} = 1, 2, \ldots, 2\mathrm{N} \\ \widetilde{\mathrm{G}}\mathrm{(k)} = (-1)^{k}\,\widetilde{\mathrm{H}}\mathrm{(2N+1-K)}, \ \text{for } \mathrm{k} = 1, 2, \ldots, 2\mathrm{N} \end{cases} \qquad \text{(III-58)}$$

The four filters are computed using the scheme shown in Figure III-22 with the help of equation III-58.

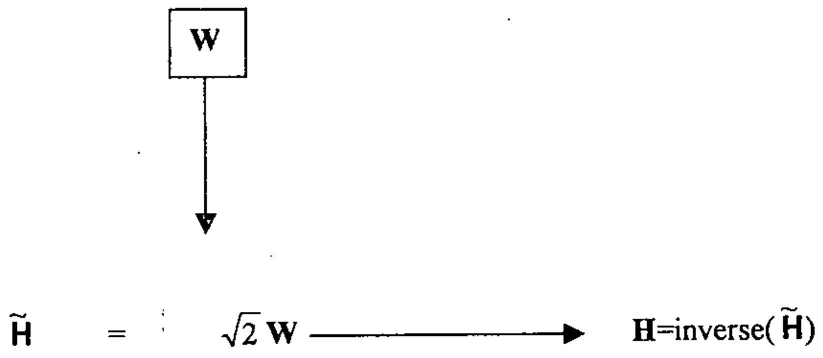

Figure III-22. Decomposition and reconstruction low pass filters.

Figure III-23 shows the four filters and their transfer modulus.

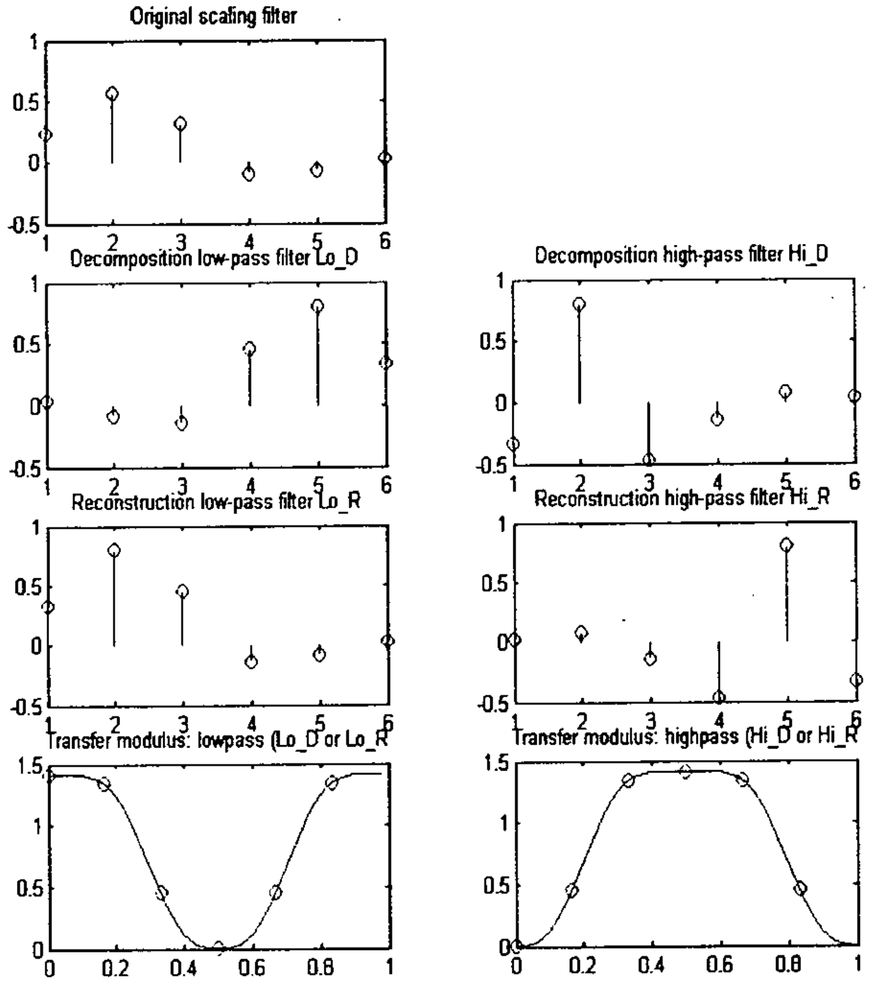
Original scaling filter

Decomposition low-pass filter Lo_D

Decomposition high-pass filter Hi_D

Reconstruction low-pass filter Lo_R

Reconstruction high-pass filter Hi_R

Transfer modulus: lowpass (Lo_D or Lo_R)

Transfer modulus: highpass (Hi_D or Hi_R)

Figure III-23. The four wavelet filters for Daubechies of order 3.

III.8 Sun image processing

The Sun images are processed by the wavelet transform to remove the sunspots, artificial defaults and noise. The implantation of wavelet is done by using two algorithms, the *à trous* algorithm and Mallat's algorithm. The decomposition by the two algorithms shows that the signature of the sunspots appears clearly in the detail images. To clarify this we use a real image acquired by the solar astrolabe of Calern that presents sunspots, see Figure III-24.

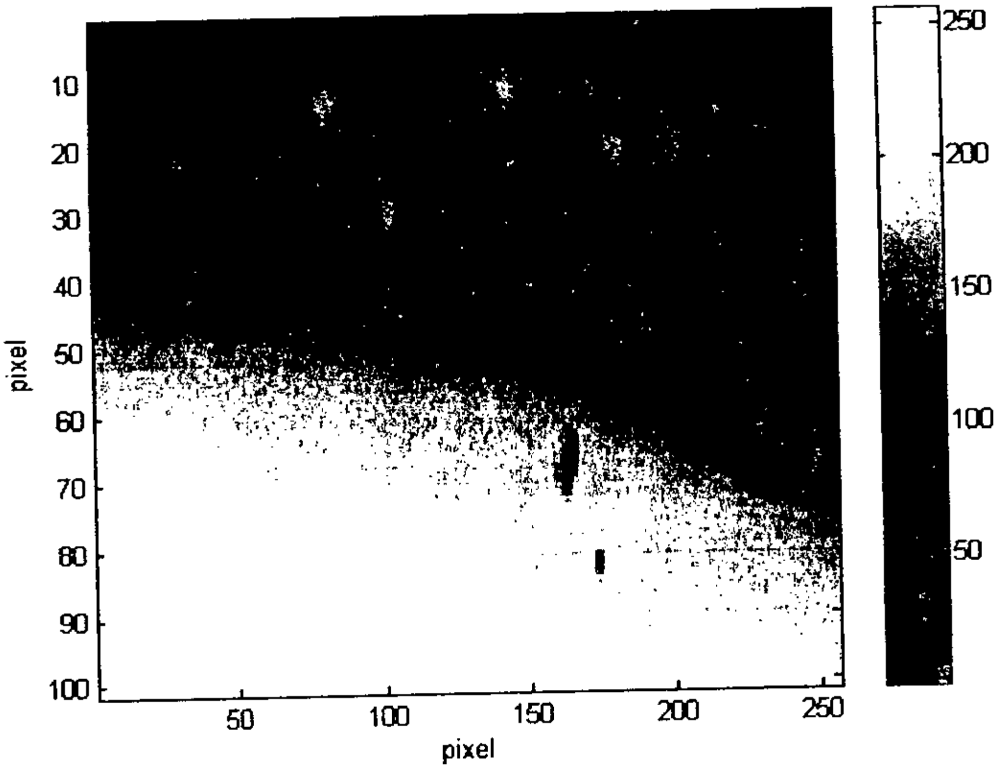

Figure III-24. A real Sun image acquired by the solar astrolabe of Calern observatory.

In the case of *à trous* algorithm the used wavelet is the Mexican Hat Wavelet and the interpolation of the scaling function is done by the B_3-spline function. Figure III-25 represents the decomposition process of the Sun image shown in Figure III-24. As it can be seen from Figure III-25 that, at each resolution step we have one approximation and one detail. In addition, the resolution of the original image is maintained along the process of the decomposition.

For the Mallat's algorithm the used wavelet is Daubechies's wavelet of order 3. Figure III-26 illustrates the decomposition at level 2. We notice that each step of resolution we have one approximation and three details; the horizontal detail, the vertical detail and the diagonal detail. In addition, the resolution of the original detail is reduced along the process of decomposition.

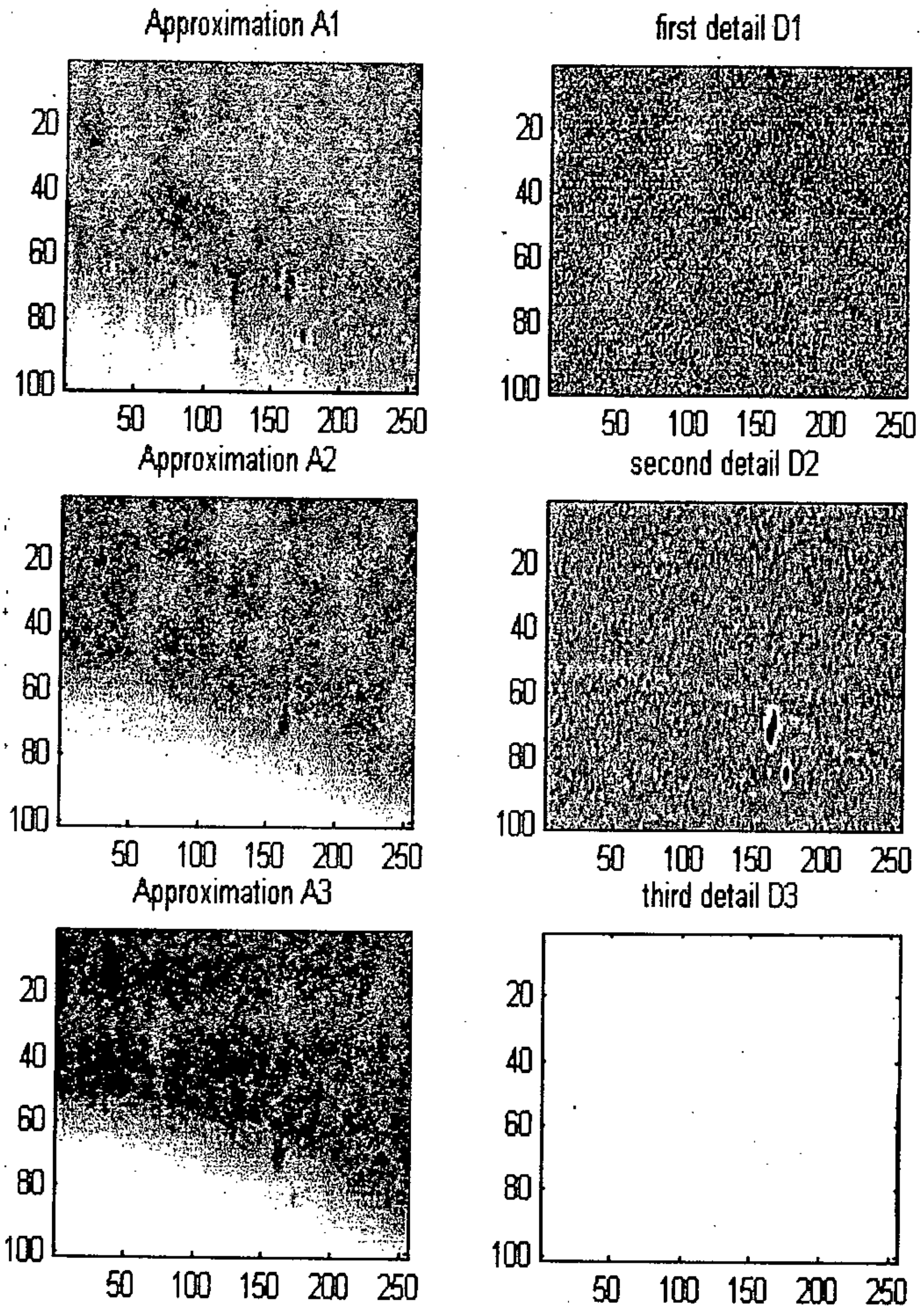

Figure III-25. Decomposition of the sun image with the à trous algorithm up to level 3 using a B3-spline interpolation for the scaling function. Both the x and y axis are in pixels.

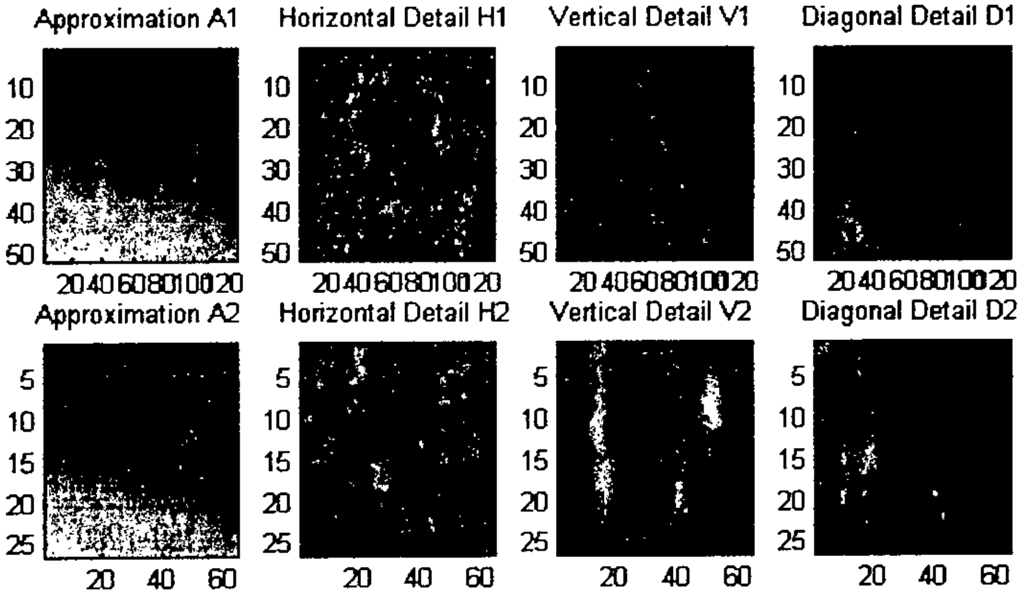

Figure III-26. Decomposition of the sun image with the Mallats algorithm using the wavelet of Daubechies of order 3. Both the x axis and the y axis are in pixels.

The processing steps of the Sun images are:

Step 1 : Elimination of the sunspots.
Step 2: Reducing the noise of the resulting image by increasing the signal to noise ratio.
Step 3: Edge extraction.
Step 4: Determination of the tangency point.

The four steps are the same for the two algorithms, with one exception that, instead of processing one detail using the *à trous* algorithm, we process the three details with Mallat's one. The above steps will be presented using the *à trous* algorithm with the B$_3$-spline interpolation for the scaling function.

III. 8.1 Sunspot elimination

The mean aberration of the Sun images is the existing of the sunspots . These non stationary effects are localized and eliminated by an iterative procedure. The localization is performed by decomposing the Sun images to details and approximations. As shown in Figure III-25 and III-26, the signature of the sunspots is present in the details images. The procedure then consists of eliminating them by applying a thresholding on the wavelet coefficients of the first detail. The threshold value is adjusted so that the coefficients are reduced to the noise level. Its value is equal to ± 3 sigma, where sigma is the standard deviation of the coefficients calculated on the whole detail image. Figure III-27 illustrates the thresholidng process on a profile of the first detail image. We can see from Figure III-28 the effect of the thresholding on the sunspot elimination. The steps of the algorithm are:

step1- We decompose the image to detail and approximation to level 1.

Step2. We threshold the detail image.

Step 3. We reconstruct the image

Step 4. We test if all the detail coefficients image are between + 3 sigma and -3 sigma.

Step 5. If is not the case, the steps 1 to 4 are repeated, if yes the algorithm is stopped.

Figure III-29 represents the image obtained from the original image after sunspots elimination..

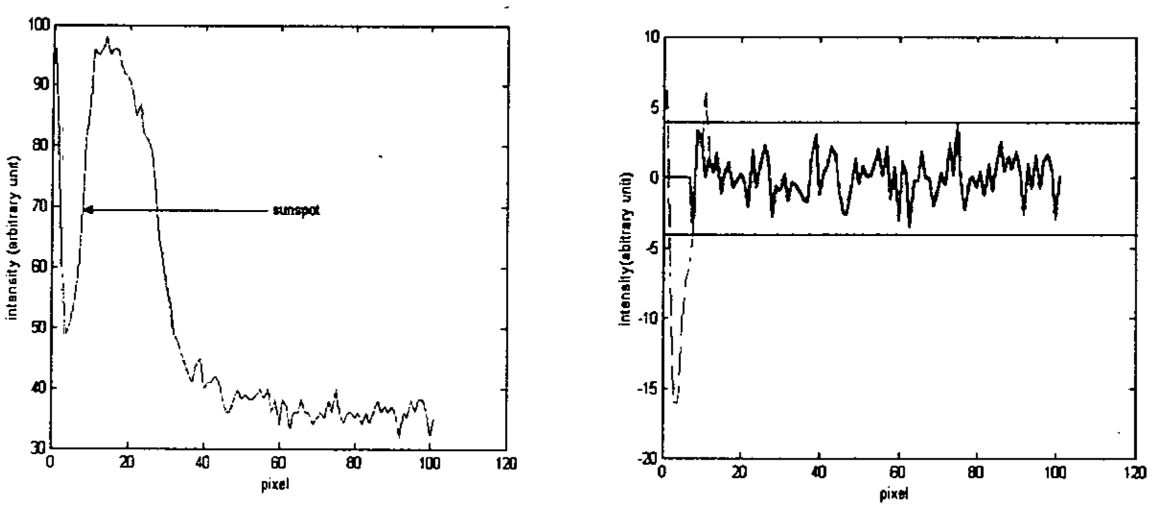

(a) *(b)*

Figure III-27. Sunspot elimination. (a) profile from an original image that passes through a sunspot. (b) Thresholding profile detail (-) superposed to the original detail (–).

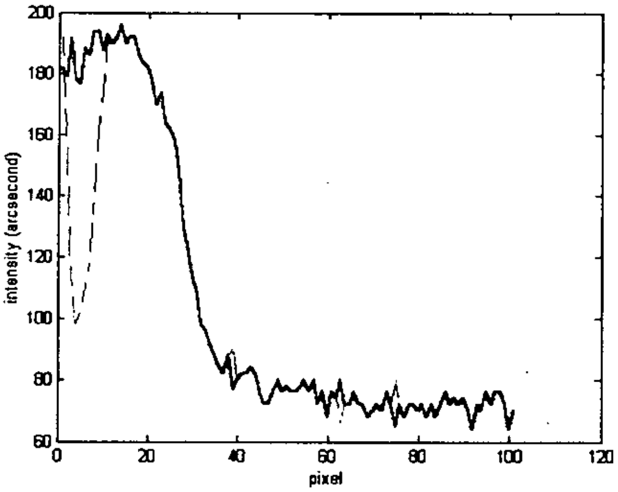

Figure III-28. Profile obtained after thresholding (-) superposed to the original profile (–).

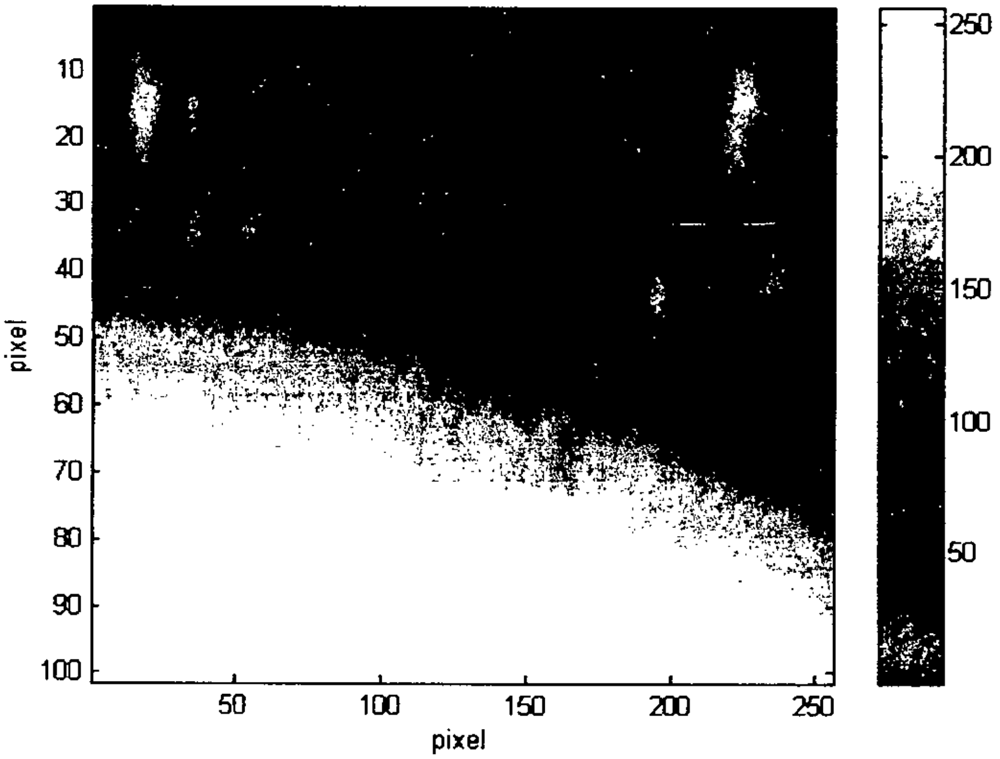

Figure III-29. The image obtained from the original image after sunspots elimination.

III.8.2 Reducing the noise in Sun images

The CCD images of the Sun are affected by noising spots (optical origin) and parasitic noises (photons noise, thermal noise). In order to increase the signal to noise ratio after sunspots elimination and noising spots, the residual noise in the images must be reduced. The wavelet analysis shows that the noise is localized in the first two detail images. So, these details are processed before reconstruction of the image from approximations and details. The noise reduction may be done by thresholding or filtering the details.

The first method is based on choosing a threshold value to be applied to detail images. Figure III-30(a) and Figure III-30(b) show the effect of thresholding on a profile of a Sun image after the elimination of the sunspots. The thresholding value in Figure III-30(a) is 1.5 sigma and in Figure III-30(b) is 0.5 sigma. The choice of the threshold value is delicate , since the thresholding process modify simultaneously the coefficients that intervene in the edge definition if the threshold value is not adequately chosen.

The second method, based on the filtering process to attenuate the noise in the detail images, is the appropriate method to use in order to prevent the effect induced by a non appropriate threshold value.

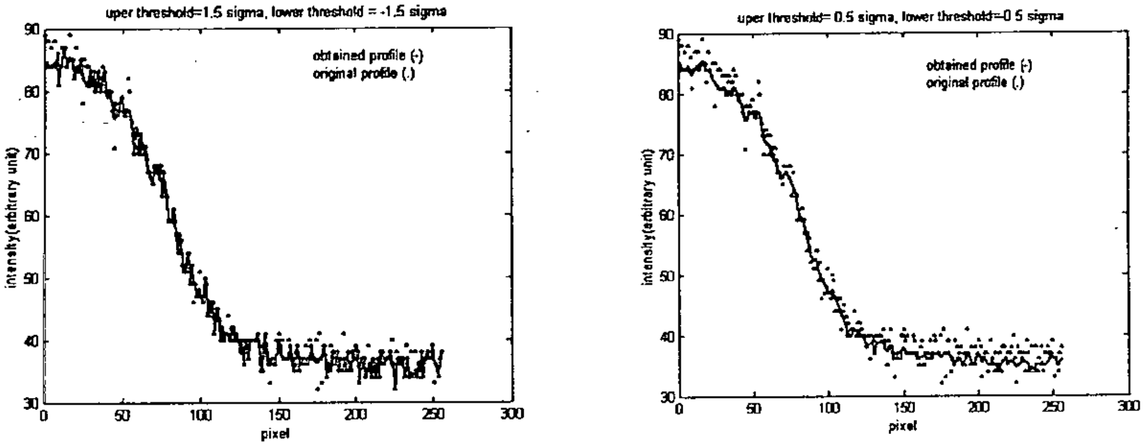

(a) (b)

Figure III-30. Noise reduction(thresholding method), sigma is the standard deviation of the whole detail image.

Several types of filters are tested on the detail images. Between them we have tested the following :

a- the filter with the coefficients (1/4 1/2 1/4).

b- the filter with coefficients (1/16 1/4 3/8 1/4 1/16).

c- the filter with coefficients (1/64 3/32 15/64 5/16 15/64 3/32 1/64).

All these filters are low pass filters, there characteristics are given in annex 7.

The comparison between these three filters using a profile of a Sun image after sunspots elimination is shown in Figure III-31; sigma represents the fluctuations between the obtained profile after the filtering process and the original one. The filter with best performance according to the others in case of time execution and best noise reduction is the filter (a). So, this filter will be used along this work to reduce noise in Sun images. Figure III-32 shows the final cleaned and filtered image.

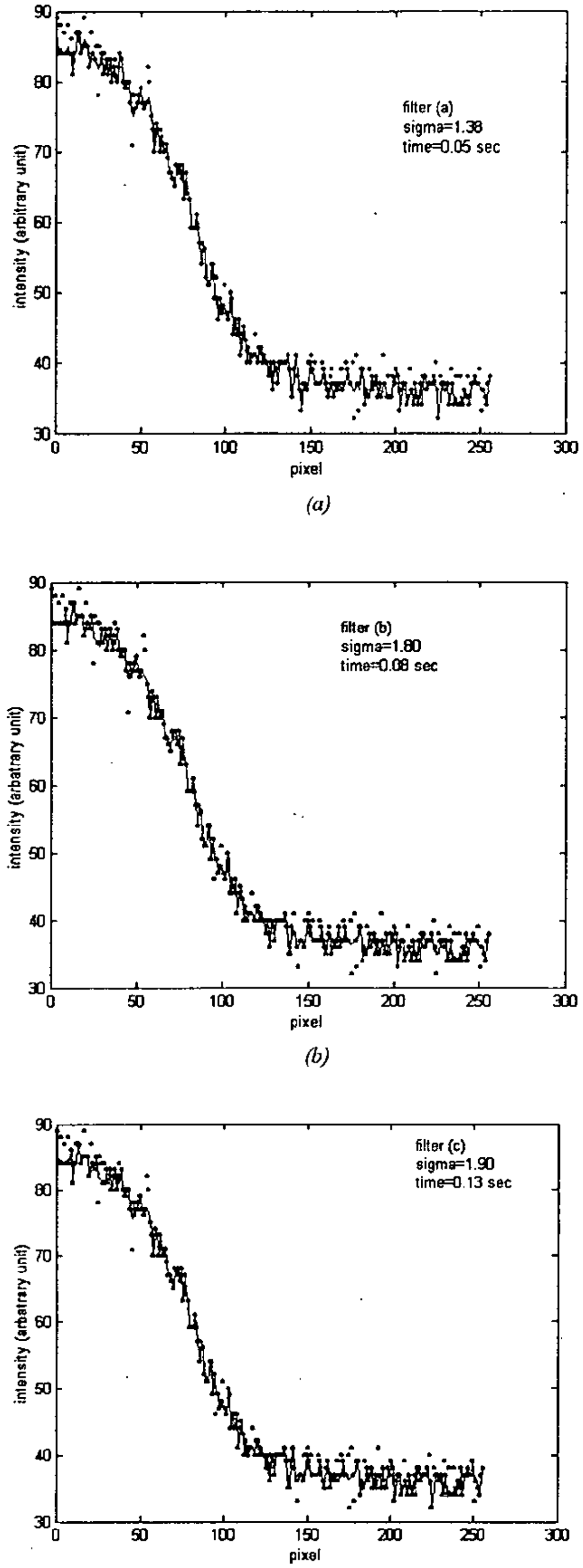

(a)

(b)

(c)

Figure III-31. Obtained profile after filtering process(-) superposed to the original profile(.). (a) the results with filter a, (b) the results with filter b,(c) the results with filter c.

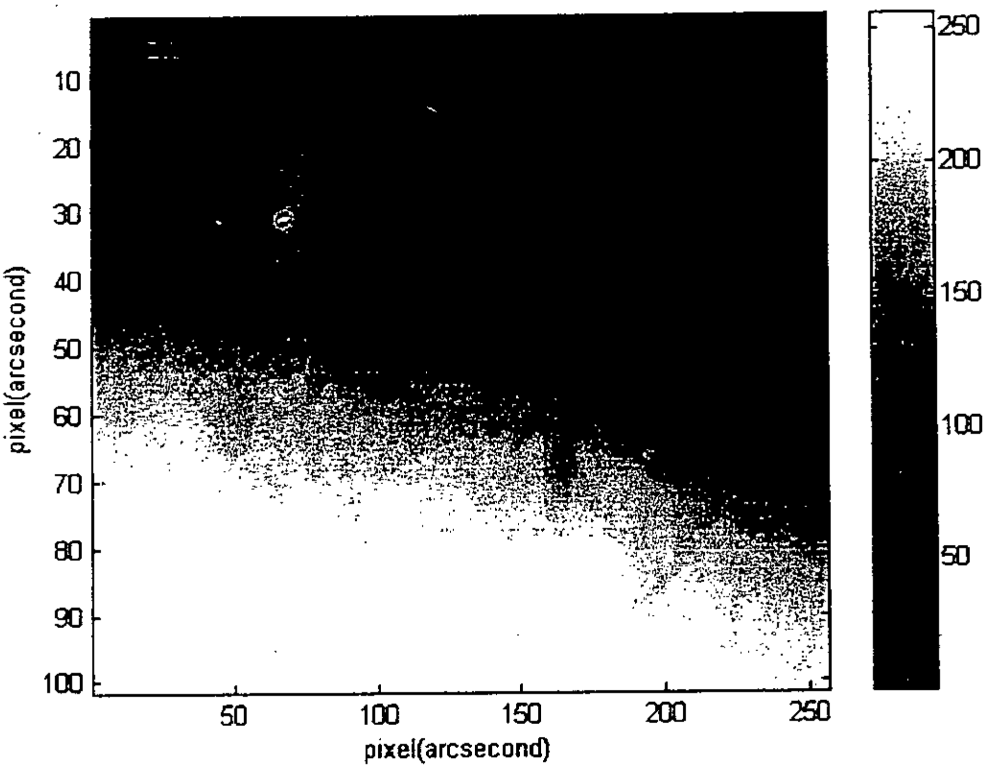

Figure III-32. The final cleaned and filtered image .

III.8.3 The Sun edge

III.8.3.1 Parabolic approximation

Even though if the solar flatness exists, the observed portion of the Sun image can not put it in evidence (it is about some thousandths of arcsecond). The Sun edge can be approximated for a first time by an arc of circle on the CCD images, but the apparent figure seamed to be close to a conical form, and this is for many reasons [14],

a- The form of the diffraction spot of the astrolabe, which, for a point source is elliptic, gives a parabolisation of the image of the disc solar, see Figure III-33 .

b- The optical defects of the objective toward the periphery of the focal plane, combined with the atmospheric turbulence, give the same effect.

c- The sections taken to determine the inflection points are not radial, but parallel to the CCD lines.

d- The integration time is 20 ms and the effect of the smearing is not zero along the azimuthal component (about 0.222 arcsecond).

all these reasons conduct us to approximate the Sun edge by a parabola [14]. The CCD matrix covers less than 5% of the Sun disc circumference and the Sun edge presents a curvature far from marked. Figure III-34 shows the real portions that exist between the Sun image given by the optic of the astrolabe, the Field of the ocular and the CCD matrix; the camera is the COHU 4710.

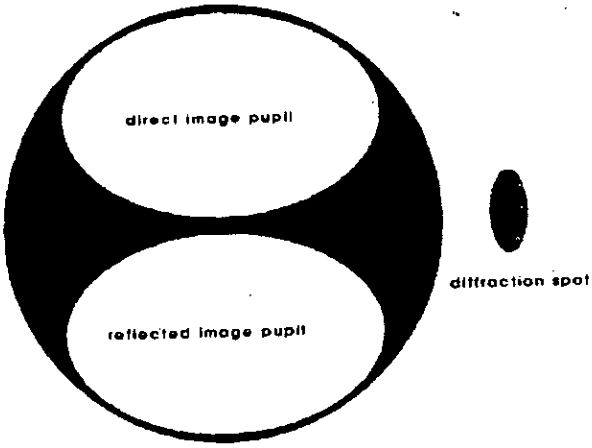

Figure III-33. Input pupils and the diffraction spot.

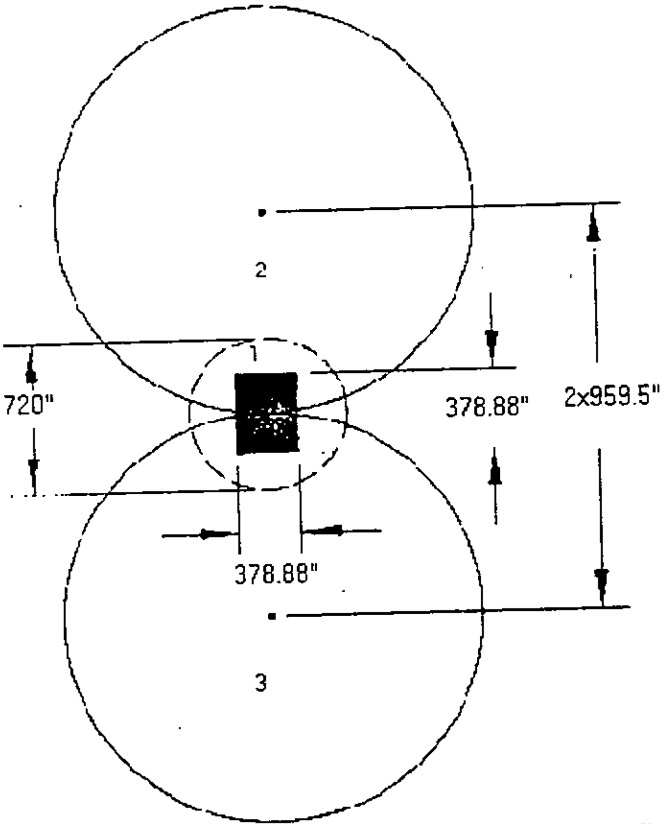

Figure III-34. The solar disc and the field of the CCD camera ,(1) is the ocular, (2) is the direct image,(3) is the reflected image.

III.8.3.2 Edge detection

The edge detection of the Sun image is the important step in Sun diameter measurement, since it includes the information of Sun transition point by the defined Almucantar. For this reason several methods are tested to determine the edge with high accuracy. The comparison between these methods is based on the cleaned real image acquired by the solar astrolabe shown in Figure III-32. After the detection of the edge, it is filtered by a median filter. The characterizations of the non-linear signal enhancement technique (Image Enhancement) performed by the median filter are: the smoothing of signals, the suppression of impulse noise and preservation of edges. In the one-dimensional case, the median filter consists of sliding a window of an odd number of elements along the signal and replacing the center sample by the median of the samples in the window.

Three methods are used to detect the edge of Sun image. These methods are presented in the following sections.

III.8.3.2.1 The first method

For this method, the steps to detect the Sun edge are as follow :

1- We compute the first derivative of the Sun image, be img1.
2- We look for the index of the maximum points in img1 , be Pmax.
3- We compute the second derivative of the image, be img2.
4- We take an interval of points in img2, be Pmax-n Pmax+n, n number of points.
5- We fit this interval of points by a straight line, $y=ax+b$.
6- The points where $y=0$, are the edge points.
7- We filter the extracted edge by a median filter of order 3.
8- The resulting edge is fitted by a parabola.

Figure III-35(a) represents the extracted edge before and after filtering, where Figure III-35(b) shows the edge fitted by a parabola. The standard deviation of edge points fluctuations around the parabola is 0.43 arcsecond, less than the pixel dimension (0.74 arcsecond). Figure III-36 represents the image and its extracted edge.

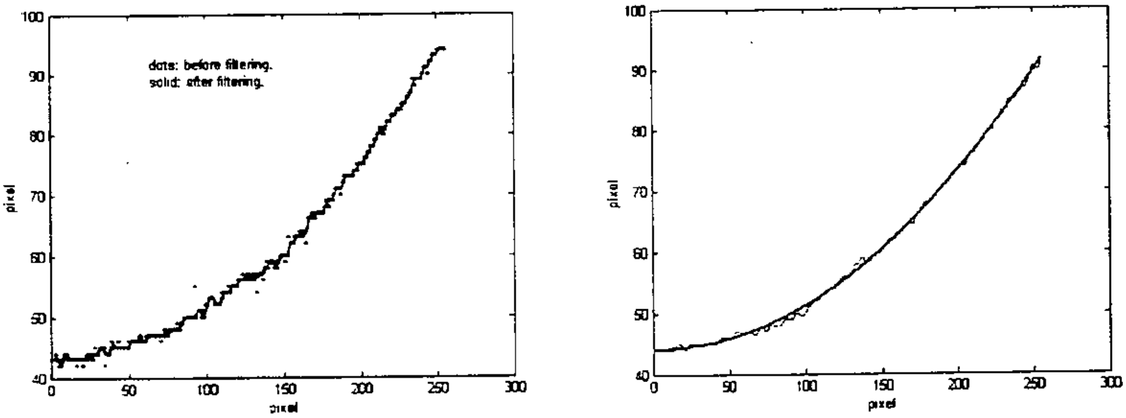

(a) (b)

Figure III-35. (a) The extracted edge before (dots) and after filtering(solid), (b) The extracted edge fitted by a parabola.

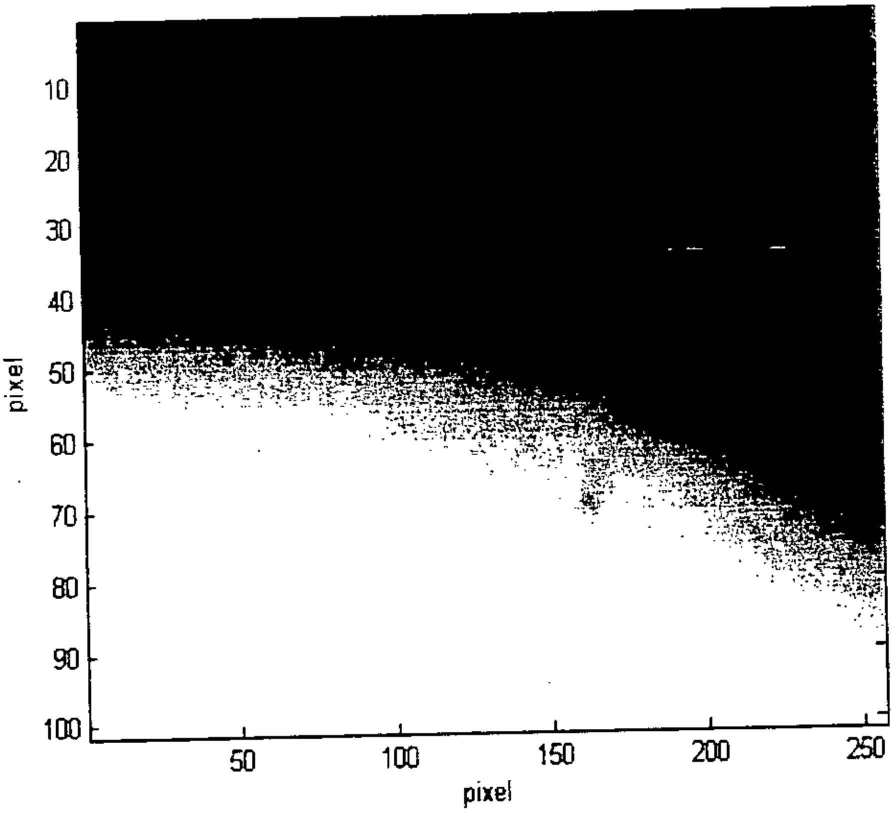

Figure III-36. The Sun image and its extracted edge.

III.8.3.2.1 The second method

It is summarized by the following steps,

1- We compute the first derivative of the Sun image, be img1.
2- We look for the index of the maximum points in img1 , be Pmax.
3- We take an interval of points in img1, be Pmax-n Pmax+n, n number of points.
4- We fit this interval of points by a parabola.
5- The inflection points of these parabolas are the edge points.
6- We filter the extracted edge by a median filter of order 3.
7- The resulting edge is fitted by a parabola

Figure III-37(a) represents the extracted edge before and after filtering, where Figure III-37(b) shows the edge fitted by a parabola. The standard deviation of edge points fluctuations around the parabola is 0.59 arcsecond, less than the pixel dimension (0.74 arcsecond). Figure III-38 represents the image and its extracted edge.

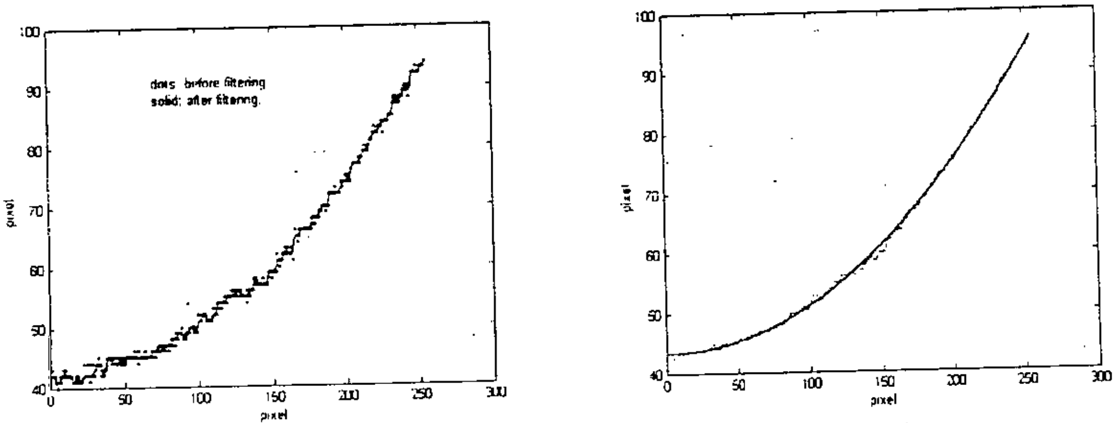

(a) (b)

Figure III-37. (a) The extracted edge before(dots) and after filtering (solid). (b) The extracted edge fitted by a parabola.

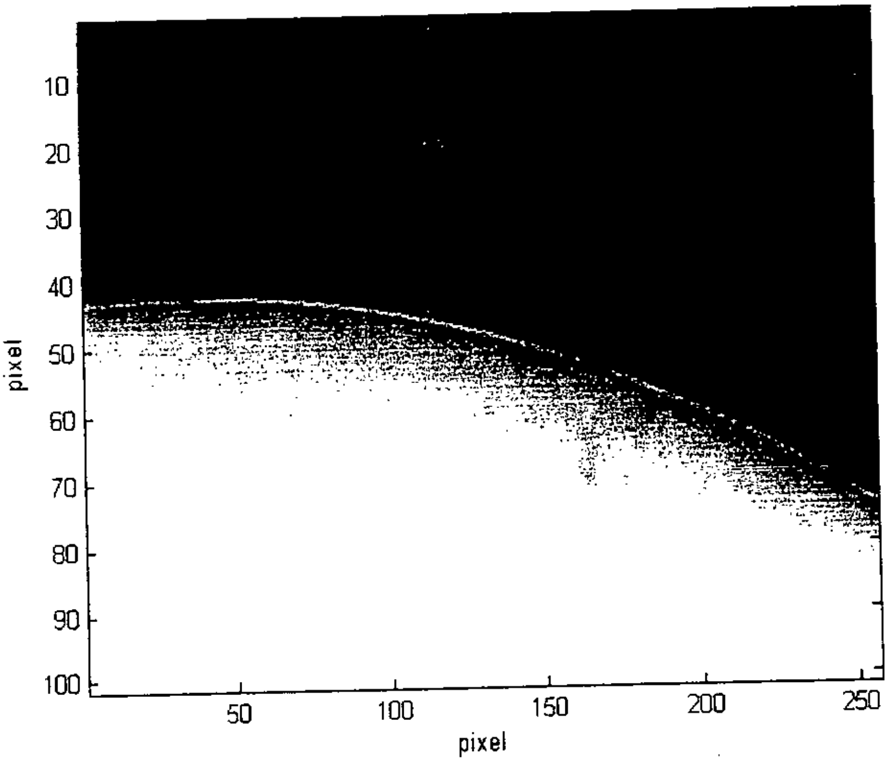

Figure III-38. The Sun image and its extracted edge.

III.8.3.2.3 The third method

The following steps summarize the method.

1- We compute the first derivative of the Sun image, be img1.
2- We look for the index of the maximum points in img1 , be Pmax.
3- We take an interval of points in the original image, be Pmax-n Pmax+n.
4- We fit this interval of points by a polynomial of degree three.
5- The point where the second derivative of this polynomial is zero, are the edge points.
6- We filter the extracted edge by a median filter of order 3.

7- The resulting edge is fitted by a parabola.

Figure III-39(a) represents the extracted edge before and after filtering, where Figure III-39(b) shows the edge fitted by a parabola. The standard deviation of edge points fluctuations around the parabola is 0.79 arcsecond, more than the pixel dimension (0.74 arcsecond). Figure III-40 represents the image and its extracted edge

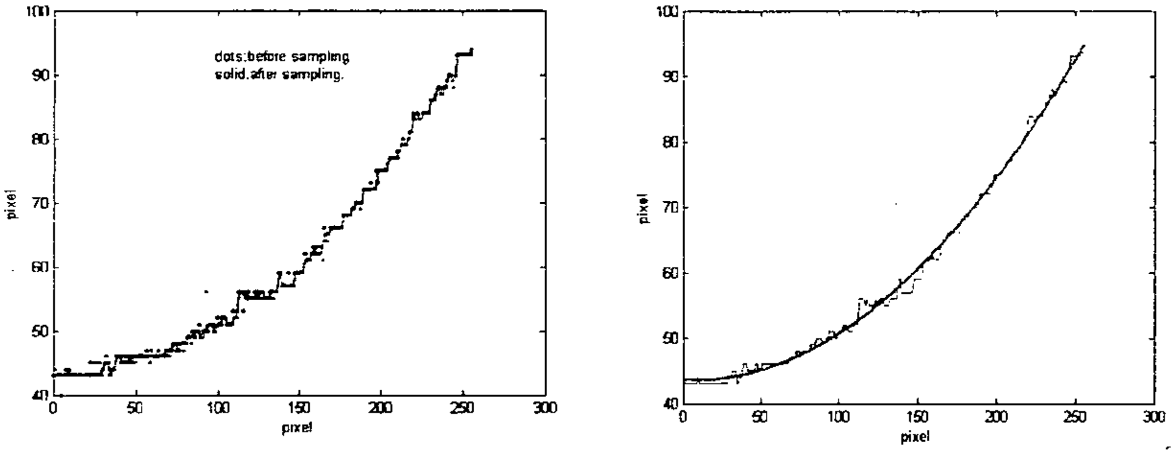

(a) (b)

Figure III-39. (a) The extracted edge before(dots) and after filtering (solid), (b) The extracted edge fitted by a parabola.

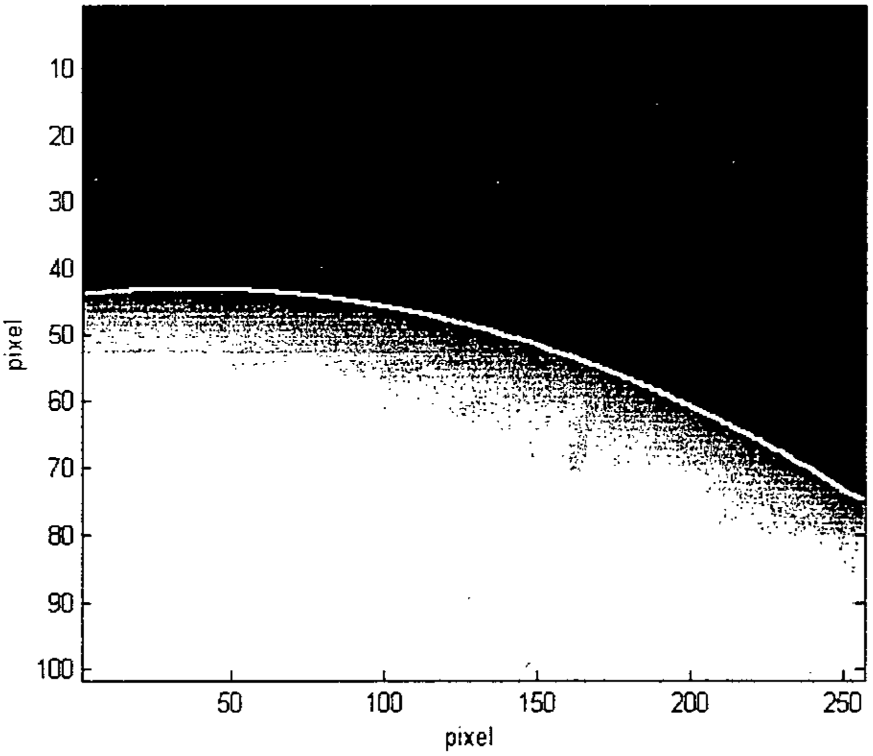

Figure III-40. The Sun image and its extracted edge

Due to the atmospheric turbulence and no correction of the diurnal motion using the solar astrolabe, in addition to the long integration time of the CCD camera (20 ms), the edge of the acquired images is not sharp and extends over more than 10 arcsecond. The classical methods of edge detection are applied to Sun images and the results showed that the standard deviation of the fluctuations, with some corrections, around parabola approximation are more than those found by the three methods. For example, the Sobel method gives a standard deviation of 3.28 arcsecond, that of Laplacian a sigma of 7.69 arcsecond and those of Derich and Canny give a close sigma value of 1.26 arcsecond. So according to the present study, the first method is the best one and it is it that will be used to detect the edge of Sun images.

The application of the first method of edge detection to a sequence of Sun images acquired by the solar astrolabe shows the results illustrated in Figure III-41. Figure III-41(a) shows the way that the direct and reflected Sun images move toward each other on the CCD frame for the first Sun transit (east), where Figure III-41(b) represents the way that the direct and reflected Sun images move toward each other on the CCD frame for the second Sun transit (west).

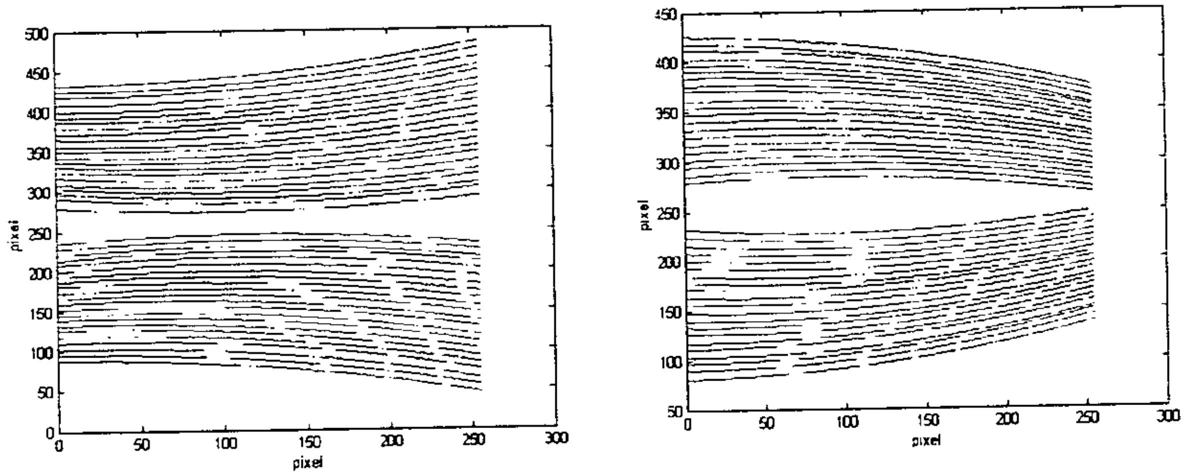

(a) (b)

Figure III-41. (a) a sequence acquired by the solar astrolabe of Calern that defines the upper transition point of the Sun (east transition). (b) The associated sequence that defines the lower transition instant of the Sun (east transition).

After the edge detection step, it comes the most important one which is the determination of the two tangency points where the upper and the lower Sun edges cross the defined height circle, see chapter1 section I.6.2.

III.8.4 Tangency point determination

After the step of approximating the inflection points, defining the Sun edge, by a parabola, it comes step of determining the instant where the Sun crosses the defined height circle. The tangency to the summit of the parabola is parallel to the CCD columns which in their turns are parallel to the Almucantar defined by the set of the prism and the mercury bath. This parallelism is handled by the instrumental settings (see chapter II, section II.7). The chosen points to represent one of the two extremities of the diameter on the Sun edge are the summits of the parabolas. The equation of the parabola gives access, with high precision to the position of each summit in the coordinate system of the CCD matrix, in x(the lines) and in y(collumns).

The variations of y reflects the variations of the zenithal distance of the Sun, the measured quantity, and it is the only coordinate taken into account in tangency point determination. That of x, denotes the displacement in azimuth of the Sun, it is only used to calculate the corrections due to the non-parallelism of the CCD lines and columns with the instrumental plane defined by the instrument as it will be seen later. A third coordinate , the UTC time of the Sun acquisition, is associated to each image, so to each summit. The set of the summits, located in x, y and time of each observation, are used to reconstruct the trajectories of the Sun on the CCD field.

Two independent equations $x=x(t)$ and $y=y(t)$ are obtained , and thus obviously the relation $y=y(x)$. By instrumental definition, the variation of y according to the time represents the position variation of the solar edge in zenithal distance. So the trajectories y(t) will permit the definition of the transit instant. The equation of the trajectories can be always written under the form of series development,

$$y = \sum_{k=0}^{n} a_k . t^k \tag{III.59}$$

where a_k are the unknowns and n is an integer number selected in advance.

The coefficients of equation III.59 can be obtained with high precision, since we dispose of 50 points (summits of the parabolas) to define the trajectories of each image (direct and reflected). In practice, the computation of the effect of the curvature of the two trajectories shows that the terms of the second order are negligible: the test are done by modeling the trajectories with parabolas. The field of the CCD is approximately two times less than that of the ocular and the curvature of the trajectories can not be determined practically. Therefore, the Sun trajectories are approximated by a strait lines.

For each passage we obtain two trajectories, a direct trajectory related to the direct image and a reflect trajectory related to the reflected image. These trajectories are given by the following system of equations,

$$\begin{cases} y = y_d + a_1.(t - t_0) \\ y = y_r + a_2.(t - t_0) \end{cases} \tag{III.60}$$

where the y_d refers to direct trajectory and y_r to the reflected trajectory.

The equality in absolute value of the t coefficients in the equation III.60 are valid only in the ideal case; where the CCD matrix is perfectly positioned (columns parallel to the horizon). With this permission, at the instant t_0 the summits of the direct and reflected images are situated respectively at the ordinates y_d et y_r. The instant t_m where the two summits have the same ordinate, is calculated simply by:

$$t_m = t_0 + \frac{y_r - y_d}{2.a_1} \tag{III.61}$$

Figure III-42 and Figure III-43 illustrate the image trajectories y(t) and x(t) materialized by the summits of the Sun images for a sequence acquired by the solar astrolabe of Calern after image processing and edge detection . We remark the high dispersion of the points on the *x(t)* trajectories due to the weak precision of the x coordinates of the parabolas summits. The spacing between the images is also highlighted (for a null spacing, the two trajectories would be superposed).

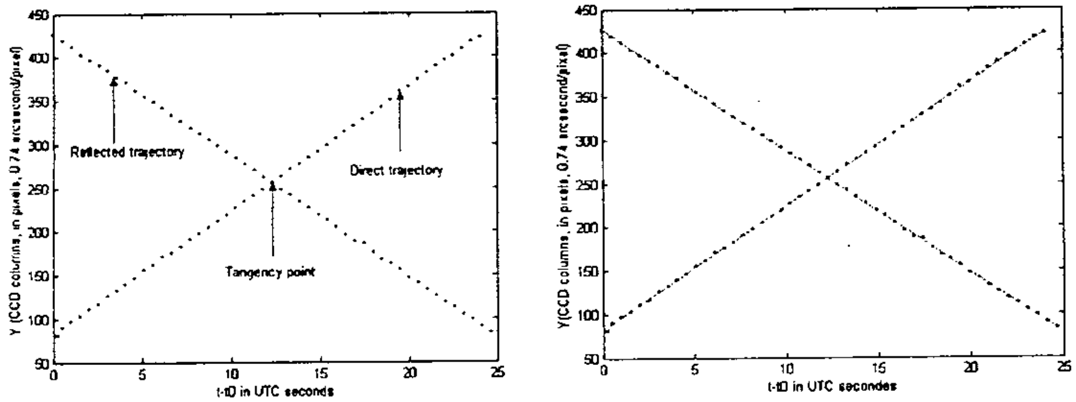

(a) (b)

Figure III-42. (a) trajectories of the Sun image along the zenithal ordinate,(b) the trajectories fitted by a straight lines.

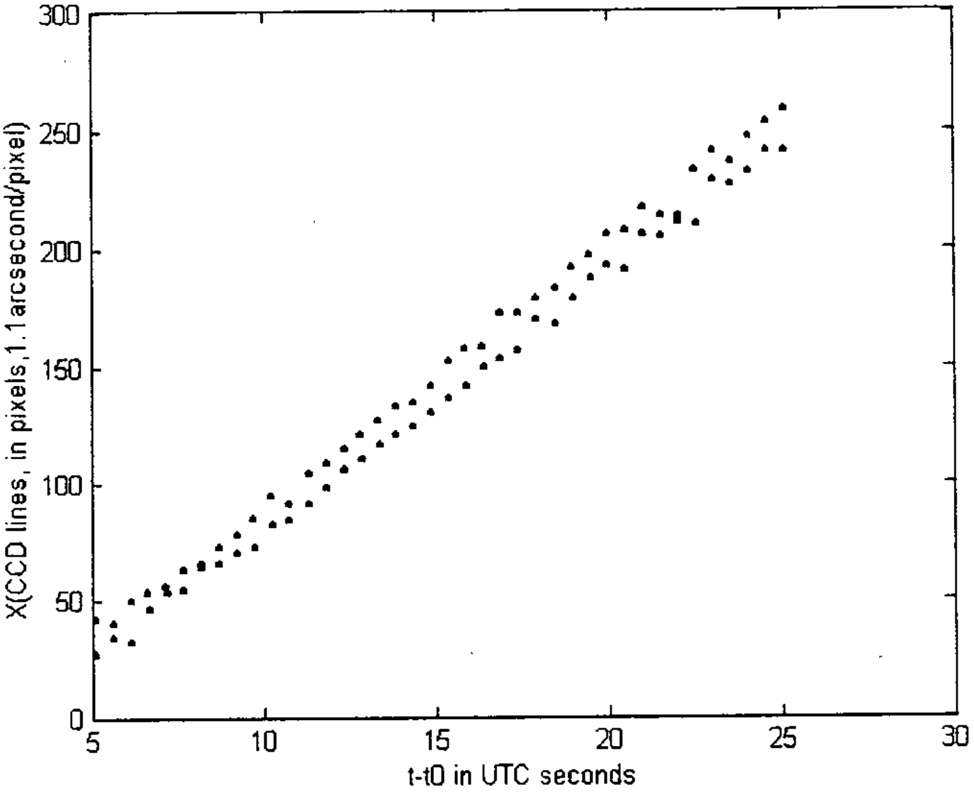

Figure III-43.Trajectories of the Sun images along the azimuth direction.

III.9 Inclination correction of the CCD

Since in practice the columns of the CCD are never perfectly horizontals, so, we must determine the slope of its inclination and consequently make the necessary correction. For this, the trajectories x(t), that represent the displacement in azimuth of the Sun image, are also computed. This computation furnishes the correction to be applied to the transition time t_m, calculated above, and at the same time correct the effect produced by the vertical non alignment of the direct and the reflected images, see Figure III-44.

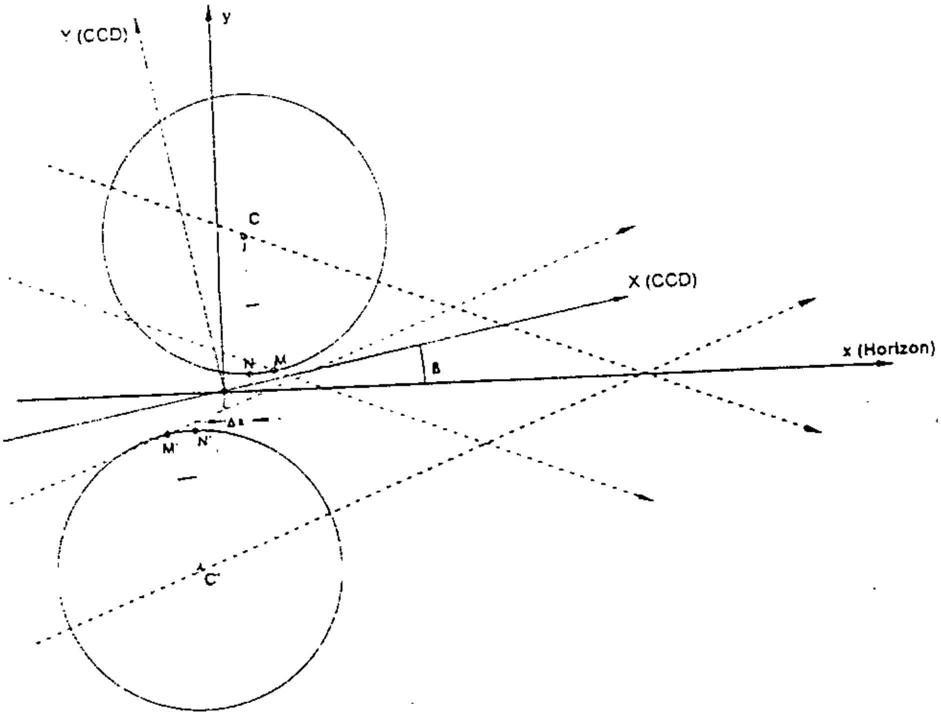

Figure III-44. The geometrical acquisition on the CCD reference.
Dots refers to the image trajectories, C and C' the center of the direct and reflected images, (x,y) the instrumental reference, (X,Y) the CCD reference, β the CCD rotation angle, Δx the spacing between the two images, M and M' the tangency points of the images on the CCD reference and N and N' the tangency points in the instrumental reference.

The theoretical expression that gives the variation of the zenithal distance of a celestial object in function of time can be written as (the terms of order 1 are taken into consideration),

$$z - z_0 = 15.\sin a.\cos\phi.(t - t_0) = 15.\cos\delta.\sin S.(t - t_0) \qquad \text{(III.62)}$$

where a is the azimuth of the object computed from east to weast , ϕ is the latitude of the observation place, δ the declination of the object and S the parallactic angle. The parameters are computed in seconds of the degree for z and in seconds for the time t. Reduced to the first term, this relation implies that $(t - t_0)$ remains small. It is the case of the solar astrolabe, since the period of Sun transition doesn't exceed 40 s and the quantity $(t - t_0)$ doesn't exceed 20 second, be $5'5$ or $1.5.10^{-5}$ radians. The corresponding equation in azimuth is written as,

$$a - a_0 = \frac{15.\cos\delta.\cos S.(t - t_0)}{\sin z} \tag{III.63}$$

Returning back to a coordinate system x,y on the CCD frame, supposed perfectly stetted, the above relations become,

$$\begin{cases} e_x.(x - x_0) = 15.\cos\delta.\cos S.(t - t_0) \\ e_y.(y - y_0) = 15.\cos\delta.\sin S.(t - t_0) \end{cases} \tag{III.64}$$

where e_x and e_y are the space sampling frequencies of the horizontal and vertical pixels of the CCD in arcsecond/pixel.

The same relations can be written for the reflected image by changing S by -S. Introducing the vertical non-alignment of the images, we can write that the summit of the direct image is situated at the point $(x_0 + \Delta x, y_0)$, where the summit of the reflected image will be at the point $(x_0 - \Delta x, y_0)$. This parameter setting implies that t_0 is the looked for transition point, since when $t = t_0$, the ordinates of the two summits are equal.

If in contrary, the CCD columns are inclined by an angle β on the horizon, a rotation of the same angle applied to the above coordinates gives the coordinates of the summits relative to the real CCD (X,Y) reference. In this case, the summit coordinates of the direct image are written as:

$$\begin{cases} X = 15(t - t_0).\cos\delta.\cos(S - \beta) + e_x(x_0 + \Delta x) + y_0.e_y.\sin\beta + bp\sin\beta \\ Y = 15.(t - t_0).\cos\delta\sin(S - \beta) - e_x(x_0 + \Delta x)\sin\beta + y_0.e_y.\cos\beta + bp.R(\cos\beta - 1) \end{cases} \tag{III.65}$$

The parameters b and p refer by their values (-1 or +1) to the observed edge and at the east or west passage. The equations for the summit coordinates of the reflected image are,

$$\begin{cases} X = 15(t - t_0).\cos\delta.\cos(S + \beta) + e_x(x_0 - \Delta x) + y_0.e_y.\sin\beta - bp\sin\beta \\ Y = -15.(t - t_0).\cos\delta\sin(S + \beta) - e_x(x_0 - \Delta x)\sin\beta + y_0.e_y.\cos\beta - bp.R(\cos\beta - 1) \end{cases} \tag{III.66}$$

The slope $\frac{dY}{dt}$, according that we consider the direct or the reflect image, is equal to $+15.\cos\delta\ .\ \sin(S - \beta)$ or $-15.\cos\delta.\sin(S + \beta)$. So, knowing the value of the angle S, it is possible to find the value of β.

Equalizing the ordinates of the direct and reflect images we get,

$$t_0 = t_m - \Delta x.e_x.\frac{\tan\beta}{15.\cos\delta.\sin S} - bp.R.\frac{1-\cos\beta}{15.\cos\delta.\sin S} \tag{III.67}$$

the expression (III.67) gives the true instant t_0 in function of the measured instant t_m and the error terms. The first error term is due to the spacing Δx between the images and the second one is a term that dependents on the Solar Semi-diameter.

Knowing the value of the angle β, we can apply a rotation of $-\beta$ to equation III.65 and equation III.66 which permits to replace the points of the two trajectories in an horizontal system. In this case, the coordinates (x,y) of the direct and reflected images become respectively as,

$$\begin{cases} x.e_x = (x_0 + \Delta x).e_x + bp.R.\sin\beta + 15.(t - t_0).\cos\delta.\cos S \\ y.e_y = y_0.e_y + bp.R.(1-\cos\beta) + 15.(t-t_0).\cos\delta\sin S \end{cases} \tag{III.68}$$

$$\begin{cases} x.e_x = (x_0 - \Delta x).e_x - bp.R.\sin\beta + 15.(t - t_0).\cos\delta.\cos S \\ y.e_y = y_0.e_y - bp.R.(1-\cos\beta) - 15.(t-t_0).\cos\delta\sin S \end{cases} \tag{III.69}$$

The transit instant is always defined as the point when the ordinates of the direct and reflected images are equal, but in this time, in an horizontal plane. Therefore the instant t_0 that we computed from the corrected time t_m is given by,

$$t_0 = t_m + b.R.\frac{1-\cos\beta}{15.\cos\delta.|\sin S|} \tag{III.70}$$

After the determination of the angle β, the correction above is systematically applied to transition instant given by t_m in order to obtain a correct evaluation of the true transition time. This correction is generally small, it is of the order of 4 to 5 ms for an mean inclination of the CCD lines of 20 arcminute and a mean separation in x of 20 pixels.

CHAPTER IV SOLAR DIAMETER MEASUREMENT WITH THE SOLAR ASTROLABE

This chapter presents an application of the developed methods to process the Sun images and the developed procedures to calculate the Sun diameter. The application is done using two selected sets of Sun images acquired by the Solar CCD Astrolabe of Calern during the year 1997. One set is dated to 10/09/97 and the other one to 09/09/97. These sets contain an even number of sequences. Each one is a series of one hundred images of 101x256 pixels in dimension(50 reflected images, and 50 direct images). Finally, the effects of the atmospheric turbulence on Sun diameter measurement will be presented.

IV.1 Diameter measurement procedure

Typical direct and reflected images are shown in Figure IV.1.

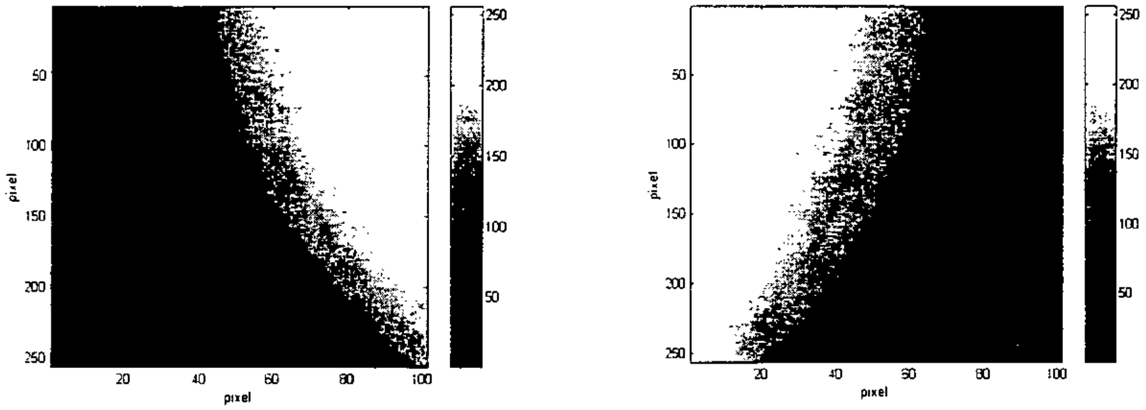

Figure IV-1. A direct and a reflected Sun images acquired by Calern CCD astrolabe.

The Sun diameter measurement is a function of the difference between the two transit instants of the Sun through the defined height circle, see chapter1, section I.6.2. The following steps illustrate the complete procedure to calculate it:

Step 1: - Reading of an acquired Sun image with the astrolabe (either direct or reflected).

Step2: - Initialisation parameters of the processing method.
- Decomposition of the image signal by the wavelet transform to details and approximation signals (images).
- Threshold the details to eliminate the sunspots and noisy spots.
- Reconstruction of the Sun image.
- Test if the residual noise in the current processed image and the preceding one is the same. If not, the second step is repeated from the beginning.

Step 3: - Filtering the image for eliminating the residual noise.
- Extraction of the Sun edge.
- Fit the extracted edge points by a parabola.
- Determination of the summit point of this parabola (its coordinates).
- Saving the result in a vector (the coordinate of the summit point, for the direct and reflected images, the direct summit points represent the direct trajectory, the reflected summit points the reflected trajectory).
- Test if the 100 images that correspond to one sequence are read. If not, the upper Steps are repeated.

Step 4: - Line adjustment of the direct and the reflected trajectories defined by the above vector of summit points.
- Determination of the intersection point of the adjusted direct and reflected trajectories. This point is the transit instant (UTC1 stands for the first Sun transition instant and UTC2 for the second one through the defined height circle).
- Steps 1 to 3 are repeated to determine the second transition point.

Step 5: - Correction of UTC1 and UTC2 to find the true instants of Sun transition.
- Reading of the station geographic coordinates and the date of observation.
- Reading of the parameters of atmospheric conditions at the moment of observation. These parameters are: the atmospheric pressure, the air temperature, the barometer temperature and the humidity.
- Reading of the instantaneous coordinates of the celestial pole, UT1-UTC, and TAI-UTC from the IRES bulletins that correspond to the moment of observation.

Step 6: - Computation of the vector radius to the station according to the chosen ellipsoidal model for the Earth.
- Correction of the station latitude for station error and altitude effect.
- Correction of the station longitude and latitude for polar motion.

Step 7: - Computation of the Julian date and the Greenwich Mean Sidereal Time (GMST) at the moment of observation.

Step 8: - Computation of UT0 and the ephemeredes time TT (Terrestrial Dynamic Time).

Step 9: - Computation of the Local Sidereal Time (LST).

Step 10: - Computation of the Sun ephemeredes at the true time of observation.

Step 11: - Computation of the geocentric zenithal distance.
- Computation of the topocentric zenithal distance (correction for the geocentric Parallax).

Step 12: - Correction of the topocentric zenithal distance for the atmospheric refraction.
- Computation of the topocentric diameter.
- Computation of the geocentric diameter.

IV.2 Error on tangency instant determination

Sun Diameter measurement with the solar astrolabe depends critically on a good determination of the transition instants of the solar edge by the small circle (Almucantar) defined by the instrument. Each instant is the intersection of the direct and the reflect trajectories of one Sun passage. Because of the temporal fluctuations observed on the two trajectories, the point of their intersection is not well defined. It is the error on this time determination, which induces the error on the diameter measurement . In our case, straight lines are used to approximate the two trajectories using a least-square fit, the error on their point of intersection is given by [28],

$$\Delta(t0) = \sigma_\tau T_{N-2:\varepsilon/2}\left[\frac{1}{N} + \frac{(t_0 - \bar{t})^2}{\sum_{i=1}^{N}(t_i - \bar{t})^2}\right]^{1/2} = K(t0)\sigma_\tau \qquad \text{(IV.1)}$$

Where $\sigma\tau$ is the standard deviation of the temporal fluctuations observed on the solar trajectory, $T_{N-2:\varepsilon/2}$ the student's distribution, $1-\varepsilon$ the confidence interval, t_0 the intersection time and N the number of images taken at the t_i instant relatively to the mean time $\bar{t}$.

IV.3 Choice of the implementation algorithm

The two algorithms described in chapter III (section III.6) are tested on the two sequences of Sun images acquired by the solar astrolabe of Calern stated at section IV.1. The first set, dated to 10/09/1997, contains 22 Sun image sequences (11 diameters), where the one dated to 09/10/1997, contains 28 Sun image sequences. Each image is a window of 101x256 pixels associated to its time of acquisition and the coordinates of the upper left corner of its window. The *à trous* algorithm is implemented using the B_3-spline interpolation for the scaling functions and the wavelet of Mexican Hat. For the Mallat algorithm the wavelet used is the wavelet of Daubechies of order 3. For each algorithm we determine the instants of Sun transition and the error handled to its determination using equation IV-1. Since each extracted edge is approximated by a parabola, the histogram of the fluctuations of the edge points around the parabolas are calculated. Finally the fluctuations of the summit points defining the two trajectories around the lines used for their adjustments are also given.

IV.3.1 The *à trous* algorithm

Figure IV-2(a) represents the histogram of the error made on tangency point determination for the two sets of Sun image. We notice that the error is not constant and varies from a minimum value of 0.71 msecond to a maximum value of 4.83 msecond. The mean error for the two sets is 1.81 msecond.

Figure IV-2(b) shows the histogram of the fluctuations of the edge points around the parabola used for approximation. These fluctuations varies from a minimum value of 0.35 arcsecond (less than 1 pixel) to maximum value of 2.52 arcsecond (more than three pixels). The mean value of these fluctuations for the two sets is 1.36 arcsecond (less than two pixels).

Figure IV-2(c) illustrates the histogram of the fluctuations of the summit points , that define the two Sun trajectories, around the two lines of adjustment. For the two sets, the minimum value of these fluctuations is 0.58 arcsecond (less that 1 pixel), where the maximum value is 2.44 arcsecond (more than three pixels). The mean value for these two sets is 1.27 arcsecond(less than 2 pixels).

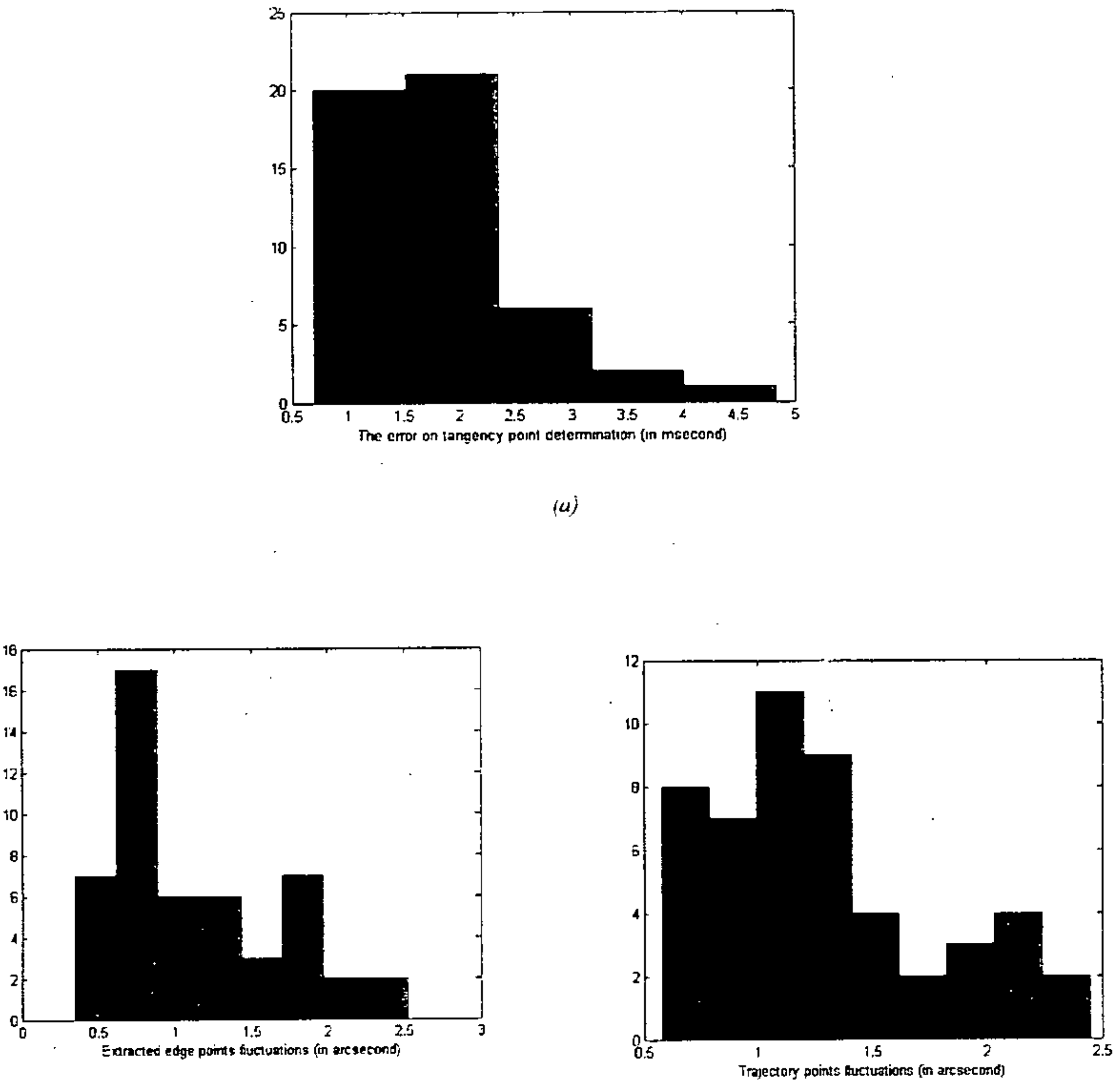

(a)

(b)

(c)

Figure IV-2. (a) *The histogram of the error made on tangency point determination.* (b) histogram of the extracted edge points fluctuations around the parabola of approximation. *(c) histogram of the fluctuation of the summit points defining the two trajectories around the two lines used for their approximation.*

IV.3.2 Mallat's algorithm

Figure IV-3(a) represents the histogram of the error made on tangency point determination for the two sets of Sun images. We notice that the error is not constant and varies from a minimum value of 0.72 msecond to a maximum value of 4.66 msecond. The mean error for the two sets is 1.80 msecond.

Figure IV-3(b) shows the histogram of the fluctuations of the edge points around the parabola used for approximation. These fluctuations varies from a minimum value of 0.38 arcsecond (less than 1 pixel) to maximum value of 2.33 arcsecond (more than three pixels). The mean value of these fluctuations for the two sets is 1.07 arcsecond (less than two pixels).

Figure IV-3(c) illustrates the histogram of the fluctuations of the summit points , defining the two trajectories, around the two lines used for adjustment . For the two sets, the minimum value of these fluctuations is 0.61 arcsecond (less that 1 pixel), where the maximum value is 2.38 arcsecond (more than three pixels). The mean value for these two sets is 1.28 arcsecond(less than 2 pixels).

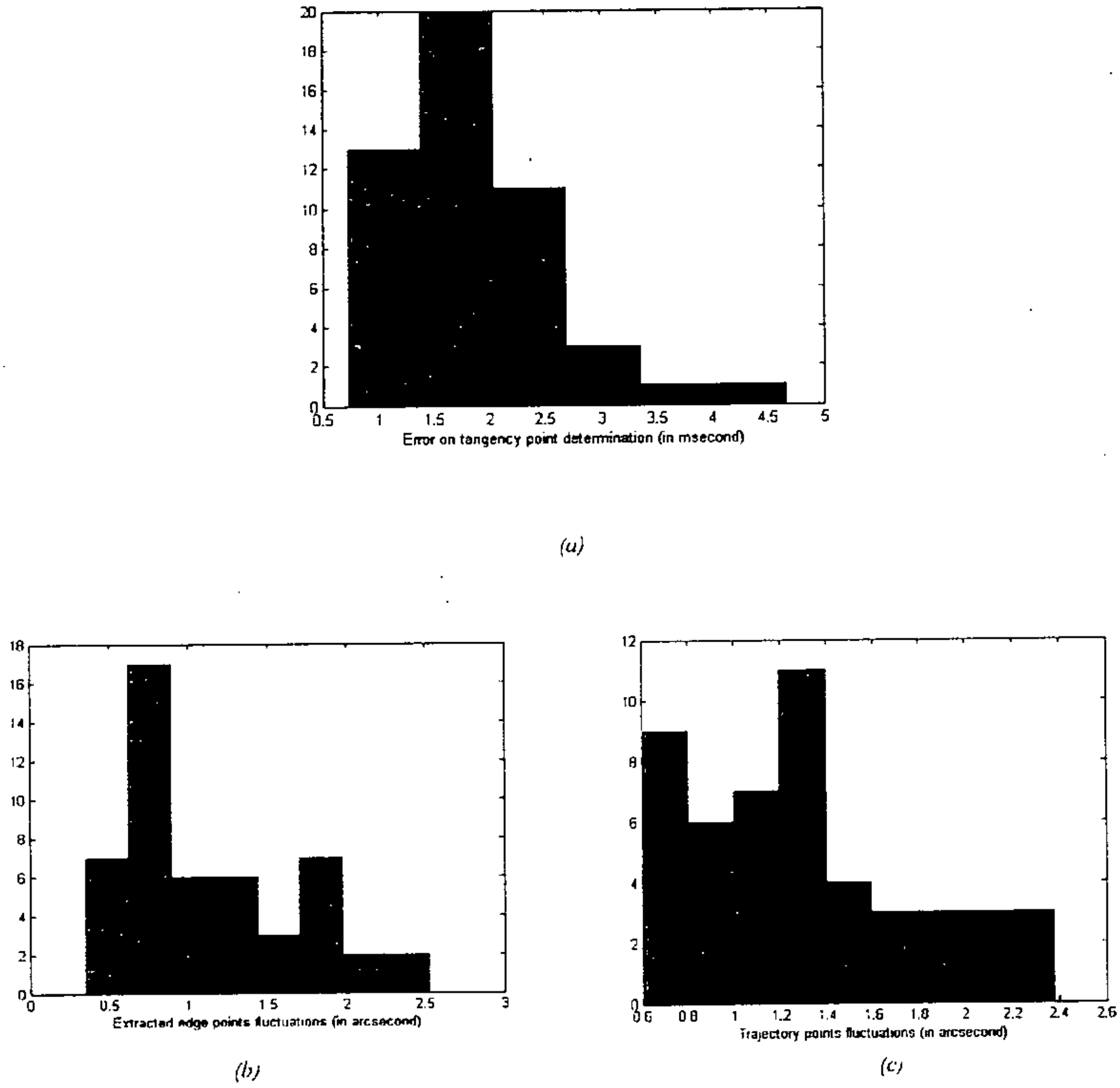

(a)

(b)

(c)

Figure IV-3. (a) *The histogram of the error made on tangency point determination.*(b) histogram of the extracted edge points fluctuations around the parabola of approximation. *(c) histogram of the fluctuation of the summit points defining the two trajectories around the two lines used for their approximation.*

Table1 summarizes the statistical comparison between the results of application of two algorithms on the two sets of Sun image sequences.

Table 1 shows that the two processing methods reveals approximately the same results. Even though that to come with a precise conclusion we have to apply them for a long series of images. At the present case we have to say that there is a big difference between the Mallat algorithm and the *à trous* algorithm in the case of time execution and the simplicity of the process. With Mallat's algorithm we have to process the three details at each stage of the decomposition, where in the *à trous* algorithm we have to process only one detail at each step. Also with Mallat algorithm the decomposition and the reconstruction are effectuated with four filters, in the case of *à trous* algorithm only one filter intervenes. In addition the image resolution using the Mallat algorithm decreases with the increasing number of the resolution levels, in contrary to the *à trous* algorithms where the resolution remains always the same along the decomposition steps.

For simplicity and time execution consideration we will use the *à trous* algorithm with linear interpolation for the scaling function and the Mexican Hat as wavelet type.

	The *à trous* algorithm			Mallat's algorithm		
	Mean value	Max value	Min value	Mean value	Max value	Min value
Error made on tangency point (msec)	1.81	4.83	0.71	1.80	4.66	0.72
Fluctuations around parabolas (arcsecond)	1.36	2.52	0.35	1.07	2.38	0.38
Fluctuations around trajectories (arcsecond)	1.27	2.45	0.58	1.28	2.38	0.61

Table1. The comparison between the *à trous* algorithm and Mallat's algorithm.

IV.4 Solar diameter measurement

Having got the transit instants (UTC1 and UTC2) using the *à trous* algorithm , the steps between the step 5 and the step 11 of the procedure described in section IV.1 are used to calculate the Sun diameter. Table 2 and Table 3 give the results for the two chosen sets with their corresponding one found at Calern observatory. R is the semi-diameter found by the present method and R_c is that found at Calern observatory.

Calculated semi-diameter (R) (arcsecond)	Calern Sun semi-diameter (R_c) (arcsecond)
959.76	959.57
960.10	959.66
960.03	959.41
959.91	959.68
959.75	959.38
959.13	959.76
958.37	959.70
958.55	959.50
959.41	959.44
959.81	959.60
960.10	959.18
959.35	959.66
960.41	959.98
960.57	959.57
Mean: 959.66	Mean: 959.58

Table 2. Sun diameter of the set of 09/09/97.

959.93	959.39
959.86	959.66
959.73	959.69
959.33	959.64
958.95	959.66
958.05	959.51
959.97	959.80
959.62	958.96
959.92	959.14
960.09	959.94
960.27	959.33
Mean: 959.61	Mean: 959.52

Table 3. Sun diameter of the set of 10/09/97.

The difference between the mean values of Sun semi-diameter measurements ($|R-R_c|$), is 0.09 arcsecond for the set of 10/09/97 and 0.08 arcsecond for the set of 09/09/97. Where the relative error is 4.69*10^-5 for the set of 10/09/97 and 5.16*10^-5 for the set of 09/09/97. The small difference between the mean values is due meanly to the planetary theory used to calculate the Sun ephemeredes. At Calern , they use the VSOP87 planetary theory, where the present work uses low accuracy formulae (the accuracy is 0.01° in longitude). In addition to that, the methods used to process the Sun images are not the same. Figure IV-4 and IV-5 present the results of the two sets and their deviation from their corresponding mean values.

The diameter measurement using the astrolabe is subjected to different error sources. One is due in a large part to the fluctuations on the image trajectories that are in one part instrument dependent. Fore example the reflected image is more degraded than the direct image. Thus, the reconstructed trajectory is less well defined. Another cause of the magnitude of the fluctuations is the small size of the astrolabe pupil. Indeed, the image motion is due to the angle formed by the pupil plane with the wavefront slope all over the pupil [36]. The average angle of arrival will cause then a displacement of the image which can be more important when the pupil is small [36]. According to the evolution time of the atmosphere turbulence [36] and the integration of time of the CCD camera, these effects could be more notable for the astrolabe than for other instruments with large pupil. The last effect which can be noted is the displacement of the solar image during the acquisition of the data. In fact, the astrolabe does not compensate for the diurnal motion of the Earth and so, the solar image moves during the integration time of the CCD camera. Consequently, the solar limb function is smoothed and then, the inflection point is not very well defined [36].

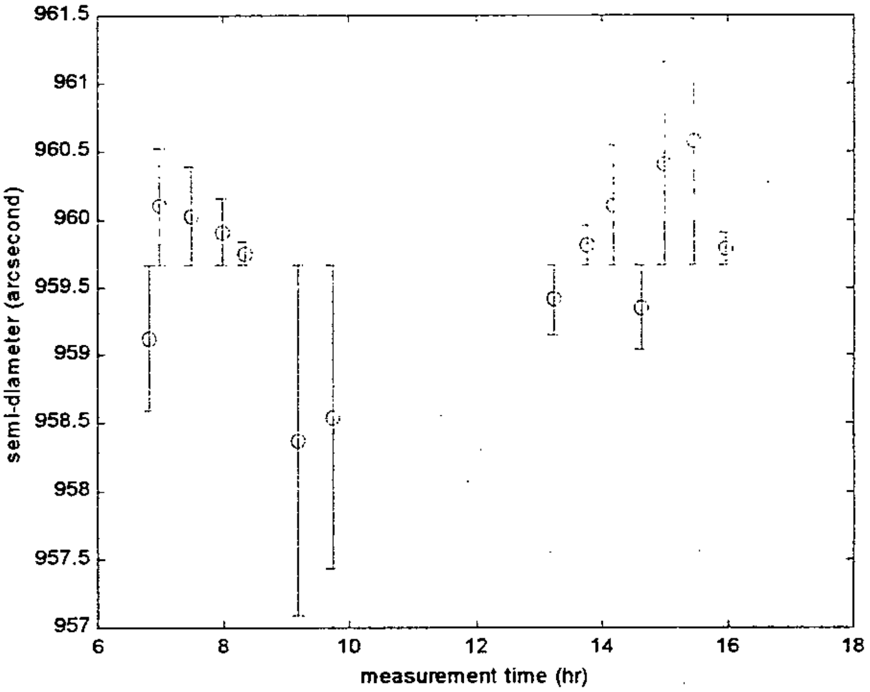

Figure IV.4. Sun semi-diameter results for the set of 09/09/97.

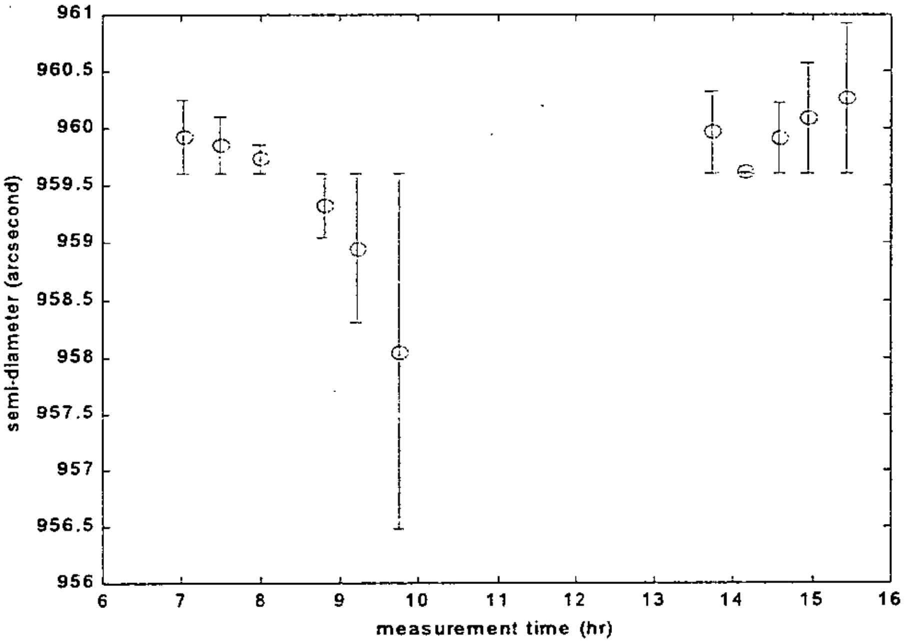

Figure IV.5. Sun semi-diameter results for the set of 10/09/97.

The huge data of visual observations at Calern observatory showed a variation of the Sun semi-diameter with the heliographic latitude. This variation has revealed that the semi-diameter is bigger at the royal zone(around 45°) and smaller toward 75° [14]. This effect is not up to know put in evidence in the case of CCD observations for the small data that exist. Even though, the heliographic latitude for the two sets is calculated and Figure IV-6 and IV-7 show the obtained results.

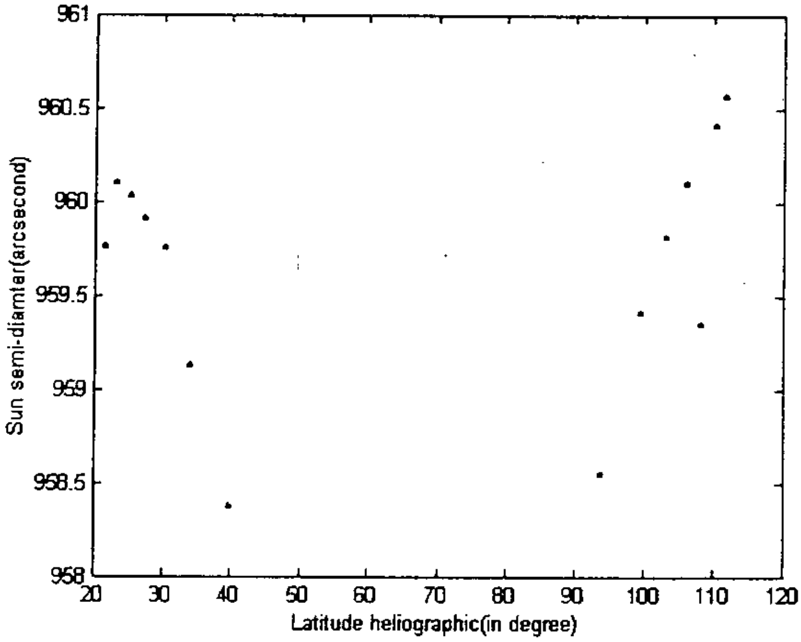

Figure IV-6. Sun semi-diameter vs heliographic latitude for the set of 09/09/1997.

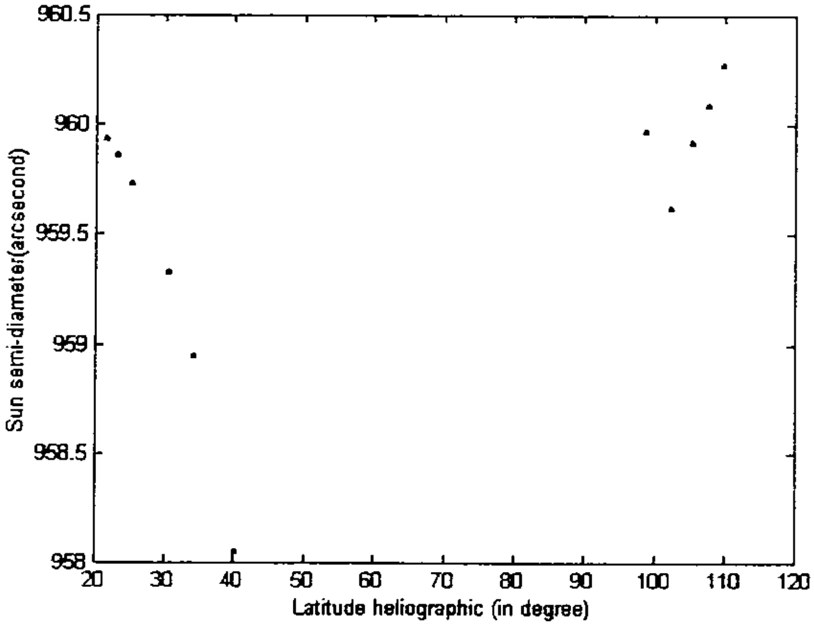

Figure IV-7. Sun semi-diameter vs heliographic latitude for the set of 10/09/1997.

IV.5 Error on diameter measurement

According to the measurement principle, the vertical Sun diameter is a function of the difference between the two zenithal distances at the two points of tangency, see Figure I-8. In this case we cane write,

$$D_v = \int_{t1}^{t2} \left(\frac{dz}{dt} \right) dt \qquad \text{(IV.2)}$$

where D_v is the vertical diameter, $\left(\frac{dz}{dt}\right)$ is the vertical speed of the Sun, and t_1 and t_2 are the two instants when the Sun crosses the defined Almucantar.

The transition instants for the set of 09/09/1997 and the their corresponding vertical Sun speeds are summarised in Table 4. Figure IV-8(a) shows the variation of this later along the period of measurement. We notice that the vertical speed $\left(\frac{dz}{dt}\right)$ varies between the two instants of tangency and the interval time between them is not constant. The variation period between the two instants is represented by Figure IV-8(b). Table 5 and Figure IV-9 illustrate the same thing for the set of 10/09/1997.

The tangency instant(HH:MM:SS,SSS)	The vertical Sun speed (arcsecond/second)
6:59:04.340	9.566
7:02:04,490	9.504
7:27:48,206	8.872
7:30:53,116	8.783
7:57:22,011	7.897
8:00:34,622	7.774
8:19:01,000	6.998
8:22:21,776	6.844
8:45:00,700	5.695
8:48:35,854	5.496
9:09:36,963	4.241
9:13:32,660	3.990
9:41:25,668	2.101
9:46:06,444	1.771
13:12:36,557	1.752
13:17:17,369	2.082
13:45:09,590	3.970
13:49:05,092	4.221
14:10:05,387	5.476
14:13:40,426	5.675
14:36:18,420	6.825
14:39:39,038	6.979
14:58:04,508	7.756
15:01:16,960	7.880
15:27:44,242	8.767
15:30:49,014	8.856
15:56:30,808	9.491
15:59:30,709	9.553

Table 4. The vertical Sun speed variation during the period of measurement.

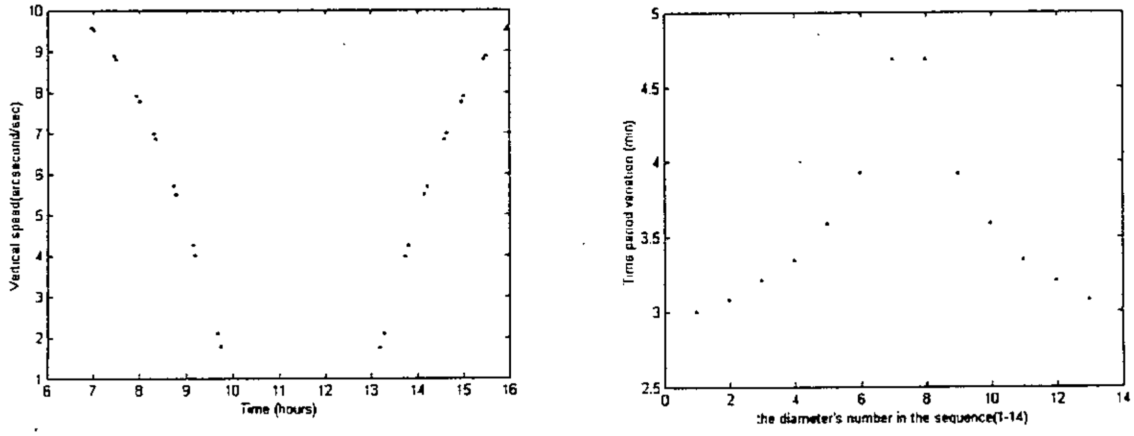

(a)

(b)

Figure IV-8. (a) Vertical speed variation during measurement. (b) Variation of the time period between the two instants of tangency.

The tangency instant(HH:MM:SS;SSS)	The vertical Sun speed (arcsecond/second)
7:00:14,307	9.529
7:03:14,815	9.466
7:29:02,748	8.822
7:32:08:360	8.732
7:58:44,076	7.833
8:01:57,737	7.708
8:46:43,364	5.602
8:50:20,792	5.400
9:11:37,334	4.129
9:15:36,586	3.875
9:44,02,718	1.963
9:48:51,162	1.629
13:42:23,580	3.855
13:46:22,680	4.109
14:07:38,582	5.380
14:11:15,683	5.581
14:34:05,170	6.745
14:37:27,217	6.902
14:55:59,333	7.690
14:59:12,853	7.815
15:25:47,219	8.716
15:28:52,575	8.806

Table 5. The vertical Sun speed variation during the period of measurement.

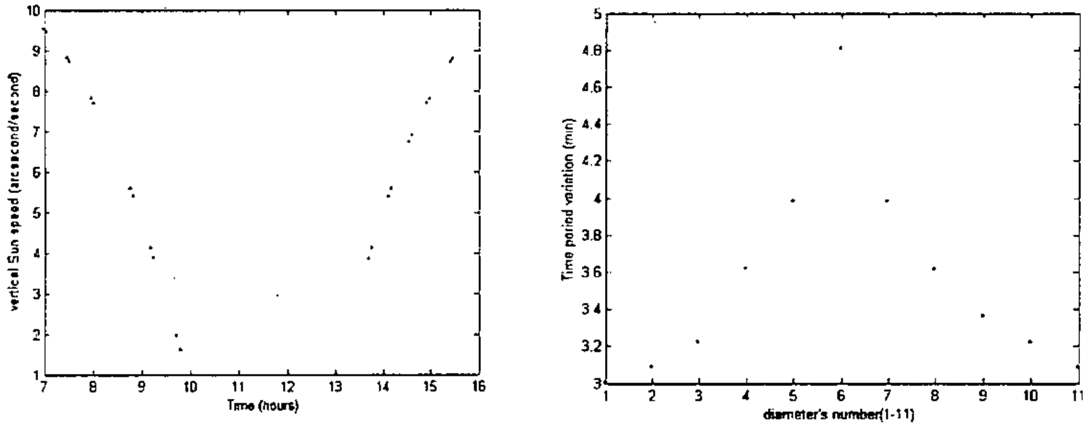

(a) *(b)*

Figure IV-9. Vertical speed variation during measurement. Variation of the time period between the instants of tangency.

From the spherical triangle equations we can get the expression of dz. *It* is given by,

$$\frac{dz}{dt} = \sin(a)\cos\phi \qquad \text{(IV.3)}$$

where a is the azimuth and ϕ is the latitude of the measurement place. So the diameter is given by replacing $\frac{dz}{dt}$ by its expression given by IV-3 in the equation IV-2, we get,

$$Dv = -\cos\phi\left(\cos a(t_2) - \cos(a(t_1))\right) \qquad \text{(IV.4)}$$

The error on the diameter measurement is,

$$\Delta D_v = \cos(\phi)\left[\left|\sin a(t_2)\Delta t_2\right| + \left|\sin(a(t_1)\Delta t_1\right|\right] \qquad \text{(IV.5)}$$

For the sequence of 09/09/1997 the mean error on diameter measurement is found to be equal to 0.0345 arcsecond that is 0.0172 arcsecond for the semi-diameter, and 0.0341 arcsecond on the Sun diameter for the set of 10/09/1997, that is 0.0170 arcsecond for the semi-diameter. From the two result sets the value of the Sun semi-diameter is:

$$959''.64 \pm 0.02''$$

IV.6 Measurement quality with CCD astrolabe

In visual observations it was not easy to observe the atmospheric effects at the moment of observation. With the introduction of CCD astrolabe, it becomes possible to estimate this effect using the numerical data.

IV.6.1 Atmospheric effects: r_o measurement

The parameter that describes the seeing atmospheric quality is the Fried parameter noted generally r0. D.L. Fried introduced it in 1966 [28]. This parameter is based on the size of the coherence areas of the disturbed wavefront arriving at the entrance of the instrument pupil. Its expression integrates the constant of the structure fluctuation of the air refraction index $C^{2}_{n}(h)$ of the atmosphere thickness traversed by the incident rays. It is written as

$$r_0 = \left[16.7\lambda^{-2}(\cos\gamma)^{-1}\int_0^{\infty} C_n^2(h)dh \right]^{-3/5} \qquad \text{(IV.6)}$$

Where λ is the wavelength of observation and γ is the zenithal distance [28].

Another similar formula for r_o directly related to the angle-of-arrival fluctuations σ_s is given by the following expression [33,34],

$$r0 = 8.2510^{5} D^{-1/5} \lambda^{6/5} (\sigma_s^2)^{-3/5} = K(\sigma_s^2)^{-3/5} \qquad \text{(IV.7)}$$

where σ_s is the spatial fluctuations presented on the solar trajectory images averaged over the astrolabe pupil D. It interprets the angle-of-arrival fluctuations. λ is the wavelength of observation.

For each passage the Fried parameter is calculated using equation IV.7. Table 6 gives the Fried's values found from the two sequences for each passage.

Sequence Number	Fried parameter in mm for the set of 10/09/1997	Fried parameter in mm for the set of 09/09/1997
1	79.69	21.73
2	80.79	27.03
3	61.56	53.92
4	62.76	37.10
5	48.05	48.84
6	41.37	42.72
7	18.89	62.58
8	29.64	25.99
9	23.34	40.78
10	17.35	31.22
11	23.86	36.30
12		37.35
13		36.03
14		46.05
	Mean r_o is 44.3 mm	Mean r_o is 33.48 mm

Table 6: The Fried parameter for the two sets of Sun images.

From table 6 we notice that at the morning of the day of 10/09/1997, the condition of observations was good ; the mean value of the Fried parameter exceed 50 mm. At the afternoon the conditions became less favourable, a value of 17.35 mm of Fried parameter is attended. For the set of the day 09/09/97, the atmospheric conditions are stable, and the mean Fried parameter is 38.89 mm. Even though , its a small set of data to make a final conclusion about the condition of observation at Calern observatory, but the study done by A.Irbah et al [36] using the numerical data of the CCD Calern astrolabe between 1989 and 1992 revealed a value of 4 cm for the Fried parameter. The situation that reflects the bad conditions of observation.

The Fried parameter value qualifies the quality of observation of a site. Bigger is the value of the Fried parameter better are the conditions of observation and consequently precise results are obtained. Figure IV-10 and IV-11 represent the variation of the error on tangency point determination with the Fried parameter for the two sets of Sun images.

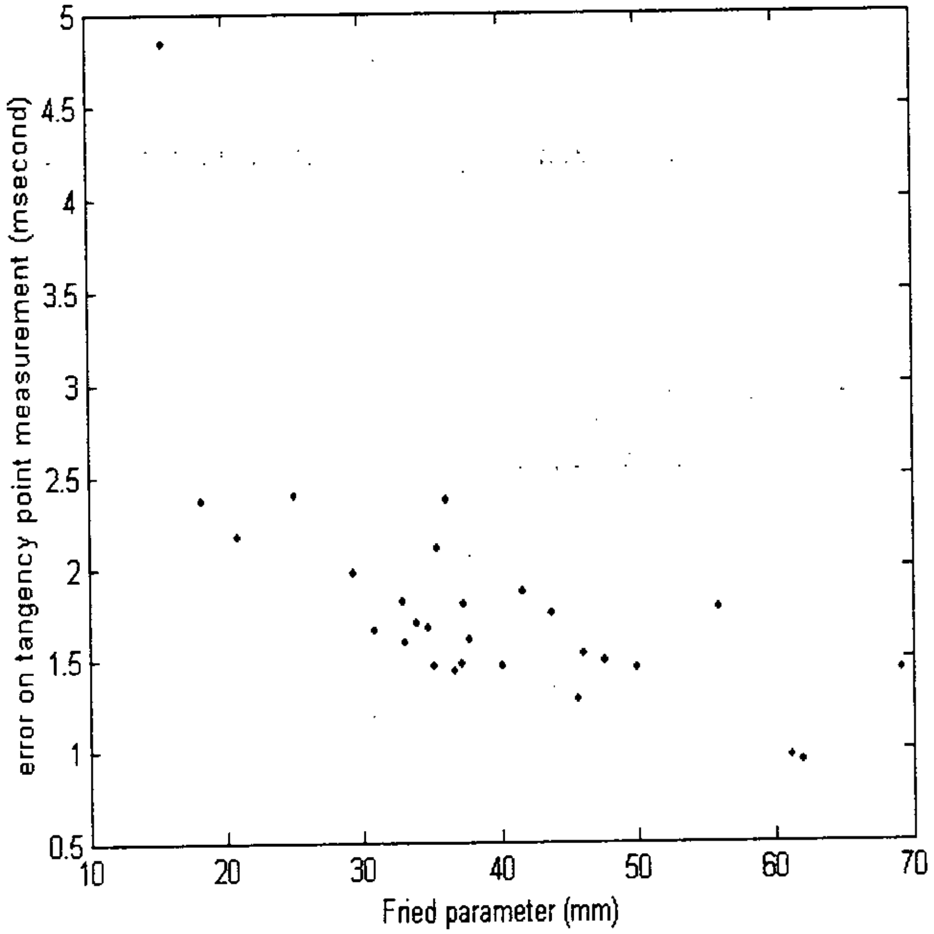

Figure IV-10. Variation of the error made on tangency point determination with the Fried parameter (the set of 09/09/1997)

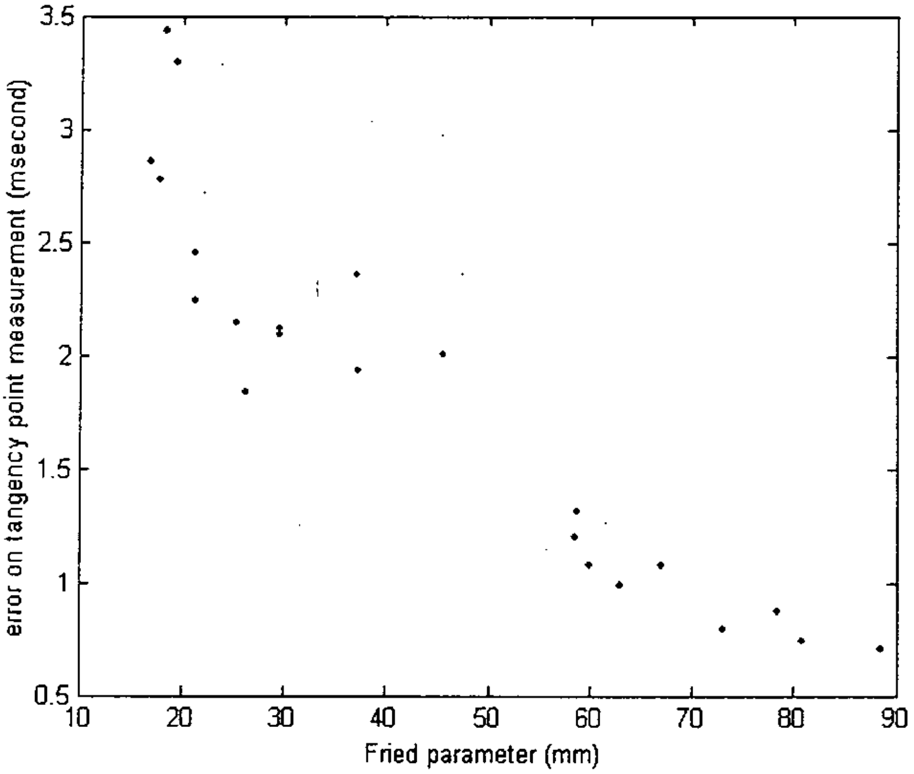

Figure IV-11. Variation of the error made on tangency point determination with the Fried parameter (the set of 10/09/1997)

Its is clear that the error made on tangency point determination decreases with good seeing conditions. The error is equal to 0.7 msecond for r_0 equal to 79.69 mm and increases up to 2.8 msecond for r_0 equal to 18.89 mm for the set of 10/09/1997. For the set of 09/09/1997, the error is equal to 0.95 msecond for r_0 equal to 62.58 mm and increases up to 4.82 msecond for r_0 equal to 15.8 mm. So the error made on tangency point determination is strongly linked to observation conditions. From the two sets the mean Fried parameter is 38.89 mm, which reflects the bad conditions when the observation took place.

The same result is noticed between the error on diameter measurement and Fried parameter. Figure IV-12 and IV-13 illustrates this relation for the two sets. We notice that the error on diameter measurement with the astrolabe increases with decreasing values of the Fried parameter. For example it is equal to 0.02 arcsecond for r_0 equal to 79.7 mm and increases up to 0.06 arcsecond for r_0 equal to 17.3 mm for the set of 10/09/1997. For the set of 09/09/1997 , the error for example is equal to 0.02 arcsecond for r_0 equal to 62.58 mm and increases up to 0.05 arcsecond for r_0 equal to 21.73 mm.

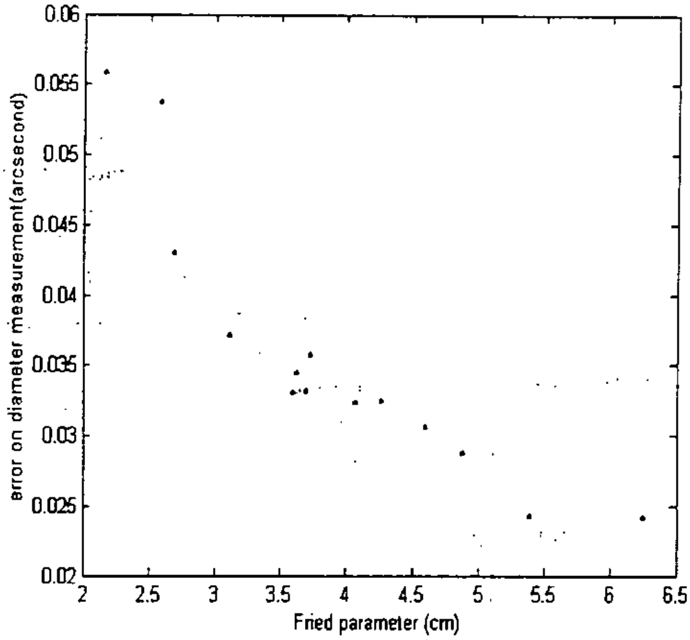

Figure V-12. Variation of error made on diameter measurement with Fried parameter (the set of 09/09/1997) .

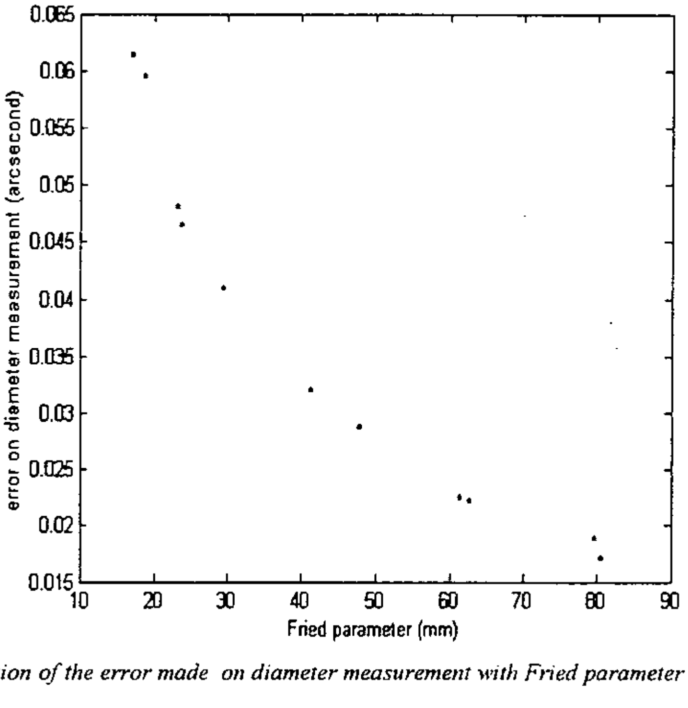

Figure V-13. Variation of the error made on diameter measurement with Fried parameter (the set of 10/09/1997) .

The error that we make on diameter can be less than that obtained from these two sets, if the conditions of observation, characterised by the meteorological state and the atmospheric turbulence are more favourable. The last one is a phenomena that is site dependent and very complex to model. The idea is to dispose of the observation conditions at the moment of measurement in order to moderate the diameter values during their analysis. In addition, to be able to make a correlation between the seeing parameters and the diameter variations. This is the role of Misolfa that will be installed near the DORaySol of Calern observatory. The operation of the two instruments at the same time will qualify the Solar astrolabe measurement by taking into account the transfer function of the atmosphere in the image processing.

At Tamanrasset observatory, there will be no seeing monitor of Misolfa type installed near the astrolabe. But, using a powerful acquisition card and an adapted programming of the whole acquisition system of the astrolabe could supply the necessary seeing parameters.

CHAPTER V ACQUISITION SYSTEM FOR TAMANRASSET OBSERVATORY

In order to prepare the Algiers's astrolabe for future integration in the ground network astrolabes and to be ready for calibration when the microsatellite Picard will be launched in 2006, the old astrolabe, which is an OPL type of Danjon, is currently at Calern observatory (France) where it is being transformed to DORaySol instrument. After describing the operation of the global system, this chapter presents the tested methods for image acquisition. The selected elements to build the acquisition system and the developed algorithms to operate them are presented followed by a description of the global operation of the acquisition system. Finally, the results obtained at the laboratory, using a simulated Sun image, from testing the whole system are given.

V.1 The solar astrolabe for Tamanrasset observatory

The old Algiers's astrolabe is currently in phase of transformation that will touch its optical system and its mechanism. The main optical transformation is the replacement of the refracting telescope with a reflecting one of a Cassegrain focus configuration of 3.5 m in focal distance. In addition it will be equipped with a prism of variable angle. This prism made of Zerodur material and with high temperature stability will enrich the data of diameter measurement during a day. To be completely automated, the necessary adjustments before launching the acquisition will be done via step motors. So, mechanical transformations will be effectuated to fix the necessary motors that control the rotation in azimuth, the solar filter displacement, the variable angle prism positioning and the optical axis tilt. After the necessary transformations, the modified instrument , named DORaySol, that will be installed at Tamanrasset observatory is shown Figure V.1.

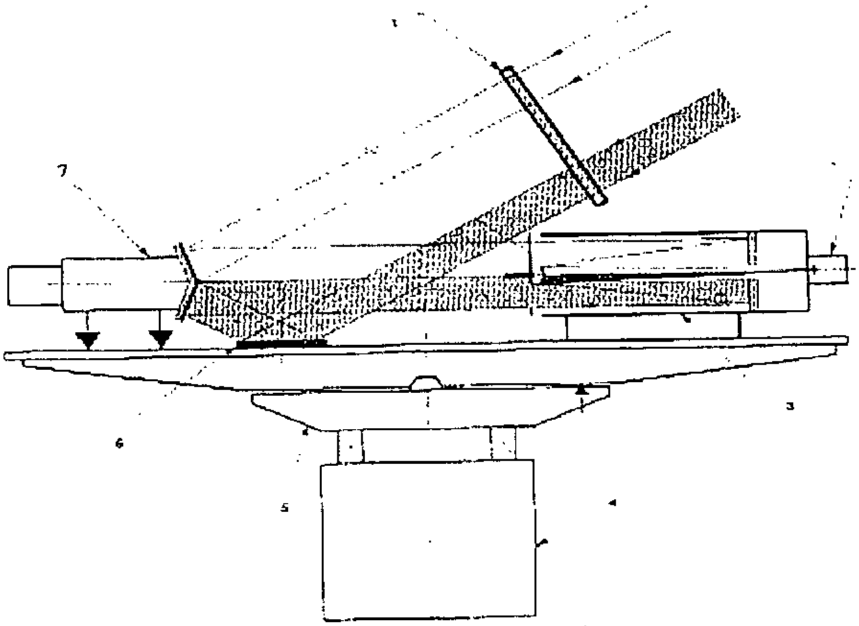

Figure V.1 DORaySol Instrument.
1-Solar filter 2- CCD camera 3- Reflecting telescope 4-fixed plate 5-Rotating plate 6- Mercury bath 7- prism of variable angle .

The proposed instrumental set that will control the acquisition of the Sun images is shown in Figure V-2.

The acquisition of the Sun image is done via the video EureCard Primo piloted by a computer. The shutter in rotation permits to acquire one Sun image, either direct image or reflected one. So, one image of the two appears at a given instant in the field of the objective. It is possible to observe the two images simultaneously on the CCD field. This can be done by eliminating the rotating shutter. Even though, this method has the advantage of eliminating the rotating shutter (the only mechanical piece in movement during the acquisition) and gives access to more information, it causes a problem in tangency point determination. Since at the moment of tangency, the variation of the contrast is higher so that the saturation of the CCD can be reached and consequently the image quality is influenced [14].

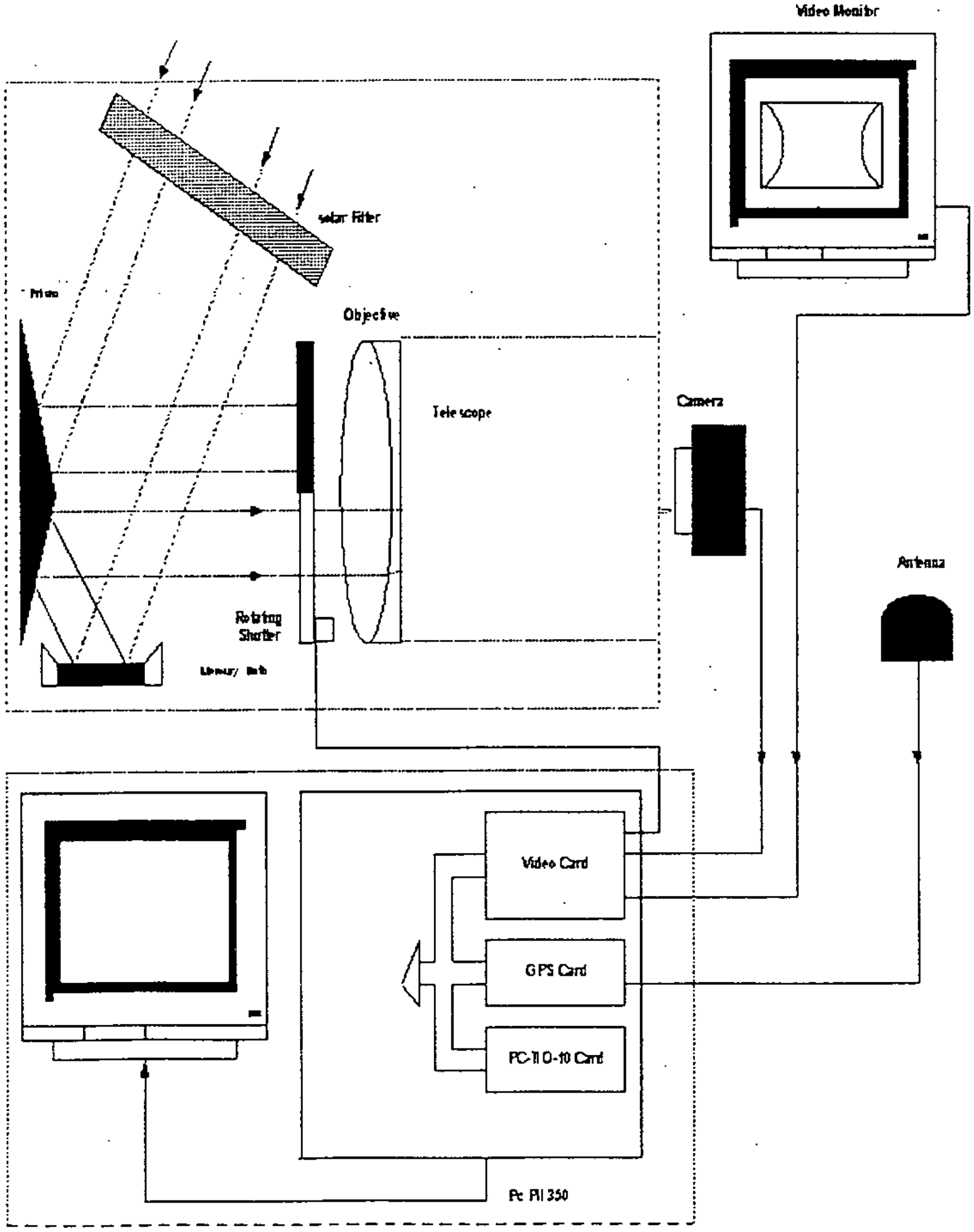

Figure V-2. The instrumental set around TAM astrolabe.

The principle of the measurement is to maintain the trace of the direct and the reflected images on the field of the objective. This must be done in such a way that the tangency line to each one of these two images at their summits is parallel to the horizon (the horizon is represented by the columns of the CCD after some adjustments and corrections). When this condition is verified, the acquisition process is launched for a set number of direct and reflected images. The time period of this acquisition process must covers the tangency instant of the two acquired images.

V.2 The acquisition method

The rotating shutter permits to acquire one solar image at a time, either direct image or reflected image on the mercury bath each 250 ms. Therefore, we have 250 ms to acquire the Sun image, to process it and finally to store it. For this reason, we have to look for the method of acquisition that takes the lowest time and use the smallest space memory. So, to optimize the acquisition we,

1- Acquire only a window inside the whole image by maintaining only the effective part.

2- Since only the displacement of the image along the zenithal distance is important (CCD columns), one line over two can be stored.

3- One field of the video signal is digitized by controlling the camera mode (one field is acquired in 20 ms, and the whole image (two field) in 40 ms). By doing this, the scale along X is divided by two, and so, this will increase the curvature of the solar edge.

The acquired window inside the whole image can be defined by two methods,

The first method:

Before the acquisition, four lines are acquired from the whole image presented in the image memory. The maximum intensity on each line is determined by derivation and sorting. The maximum intensities founded are recorded with their corresponding column numbers. From these maximums, we define a window around the point that has the maximum column number. After that, the acquisition is launched.

This method sometimes does not work because it happens that one of the arbitrary selected lines fall on a sunspot presented in the Sun image; see Figure V-3. In this case, the resulting window is inappropriate and consequently the acquisition will not be the right one. In addition, the derivative calculation and the sorting algorithm take an important time, which slow the acquisition process. F.laclare and G.merlin have used this method with the CCD astrolabe and it was soon abandoned.

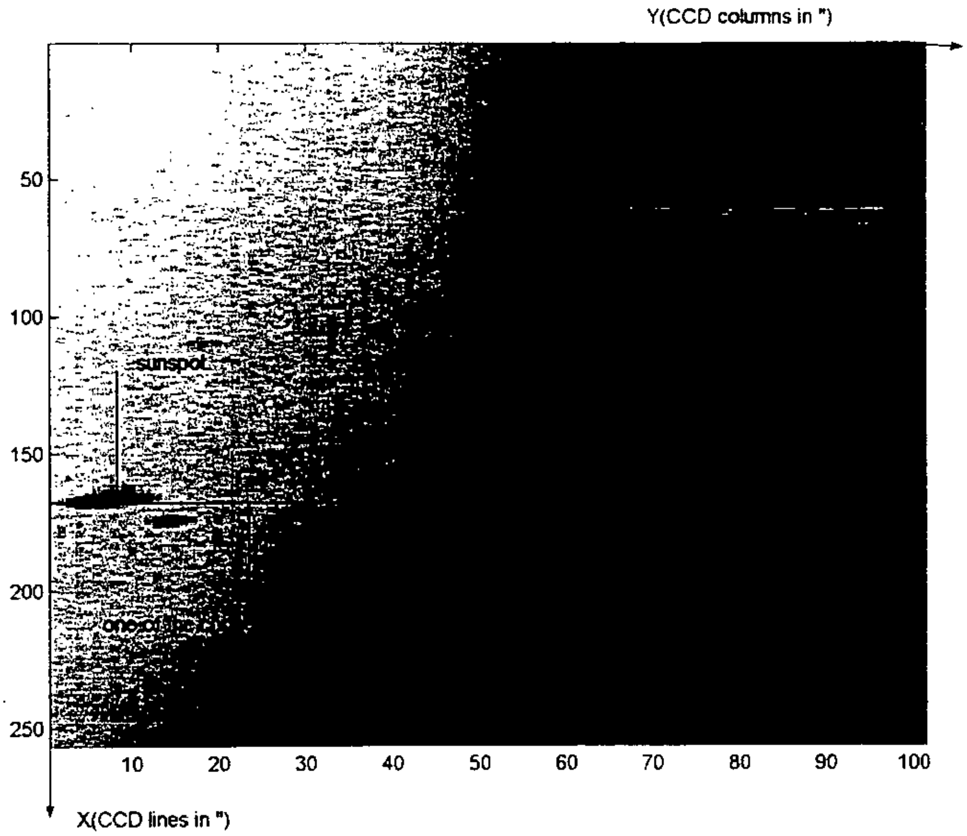

Figure V-3. A solar image containing sunspots.

The second method:

The relation between the horizontal coordinate system and the equatorial one is given by the following equations,

$$\begin{cases} \sin\delta = \sin\varphi\cos z - \cos\varphi\sin z\, coa \\ \cos\delta\sin H = \sin z\sin a \\ \cos\delta\cos H = \cos\varphi\cos z + \sin\varphi\sin z\cos a \end{cases} \tag{V.7}$$

$$\begin{cases} \cos z = \sin\varphi\sin\delta + \cos\varphi\cos\delta\cos H \\ \sin z\sin a = \cos\delta\sin H \\ \sin z\cos a = -\cos\varphi\sin\delta + \sin\varphi\cos\delta\cos H \end{cases} \tag{V.8}$$

$$\begin{cases} \cos S=\cos a\cos H+\sin a\sin H\sin\varphi \\ \sin z\cos S=\sin\varphi\cos\delta-\cos\varphi s\sin\delta\cos H \\ \sin z\sin S=\cos\varphi\sin H \\ \cos\delta\cos S=\sin\varphi\sin z+\cos\varphi\cos z\cos a \\ \cos\delta\sin S=\cos\varphi\sin a \end{cases} \qquad \text{(V.9)}$$

Where δ is the declination, φ the latitude, z the zenithal distance, *a* the azimuth, H the hour angle, and S the parallactic angle.

Given T=H-α (where α is the right ascension ant T is the sidereal time), we have by derivation,

$$\begin{cases} dH=dT \\ d\delta=d\alpha=0 \end{cases} \qquad \text{(V.10)}$$

Where α is the right ascension ant T is the sidereal time.

The equations V.10 assumes that the displacement of the poles and the vernal point are negligible. In this case the diurnal motion is reduced to a uniform rotation. Differentiating V.8 relations, we get

$$\begin{cases} \sin z\,dz=\cos\varphi\cos\delta\sin H\,dH \\ \sin z\cos a\,da+\cos z\sin a\,dz=\cos\delta\cos H\,dH \\ -\sin z\sin a\,da+\cos z\cos a\,dz=-\sin\varphi\cos\delta\sin H\,dH \end{cases} \qquad \text{(V.11)}$$

The first relation in V-10 with the help of V.8 and V.9 relations can be written as:

$$\frac{dz}{dT}=\cos\varphi\sin a=\cos\delta\sin S \qquad \text{(V.12)}$$

The two last relations in V-11 give da/dT by eliminating dz/dT

$$\sin z\frac{da}{dT}=\cos\delta(\cos a\cos H+\sin a\sin\varphi\sin H) \qquad \text{(V.13)}$$

The expression between parentheses is cos S that lets us writing,

$$\frac{da}{dT}=\frac{\cos\delta\cos S}{\sin z}=\sin\varphi+\cos\varphi\cot z\cos a \qquad \text{(V.14)}$$

The zenithal distance z and the azimuth *a* are calculated from the ephemeredes and the coordinates of the astrolabe.

Since the acquisition of each image is done each 0.25 sec, we can calculate then the trajectory of the two images in the field of the matrix CCD during this period of time. The acquisition of the direct and the reflected images is realized alternatively. Two successive positions of the same image are separated by an interval of 0.50 sec. So, the necessary time for a Sun image to cross the CCD matrix can be deduced and the starting position and the ending one of the solar edge on each trajectory can be foreseen. We can then position the first image in such a way that the intersection of the two trajectories is situated as close as possible to the center of the CCD matrix. Figure V-4 shows a trajectory details of one of the two acquired Sun images during each Sun transition. The method consists to acquire alternatively two symmetrical windows each 0.25 sec.

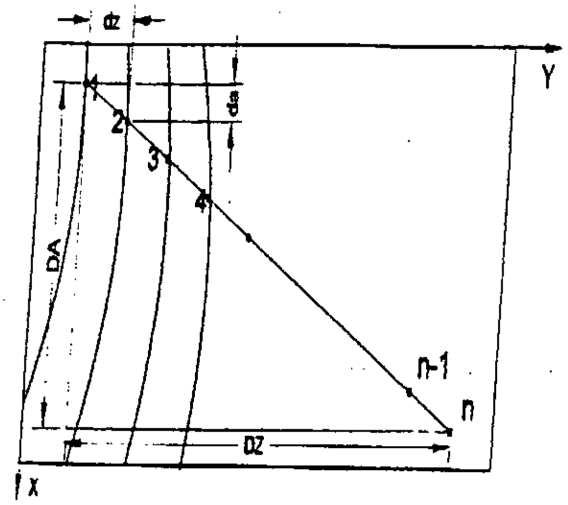

Figure V-4. Apparent movement of the Sun on the CCD frame.
da the displacement in azimuth in 0.5 sec, dz the displacement in zenithal distance in 0.50 sec, DA the total displacement in azimuth, DZ the total displacement in zenithal distance, 1,2,3, positions of successive images.

This method is faster than the first one and it is not affected by the image characteristics. The only thing that we need to have is a program that calculates the Sun ephemeredes in real time. For these reasons, this method is chosen to be used for Sun image acquisition. The Sun displacement on the CCD frame depends on the daily Sun speed variation that governs the number of measurements per day. Faster the Sun displacement greater the number of Sun diameter measurement. The Sun speed variation depends on the day time, on the seasons and on the geographic coordinates of the astrolabe.

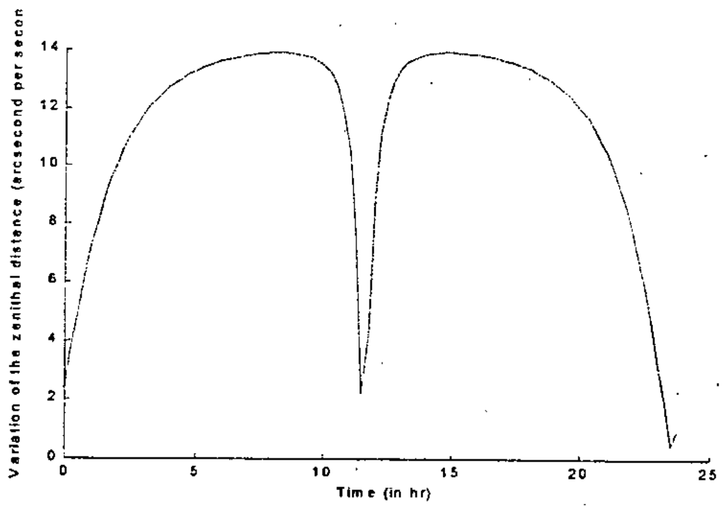

Figure V-5 . Zenithal distance variation of the fist day of Mars 2001.

For all the days, the variation of Sun zenithal distance during a day looks like Figure V-5 that represents the zenithal distance variation of the first day of Mars 2001 using the equation V.6. For example, the mean variation of zenithal distance is 11″.24 per second of time in Mars and 11″.18 per second of time in July.

The Sun moves on the CCD frame in azimuth and height. The variation of the azimuth looks like Figure V-6 that shows the variation of the azimuth of the first day of Mars 2001 using the equation V.7. The mean variation of the azimuth is 9″.29 per second of time in Mars and 9″.97 per second of time in July.

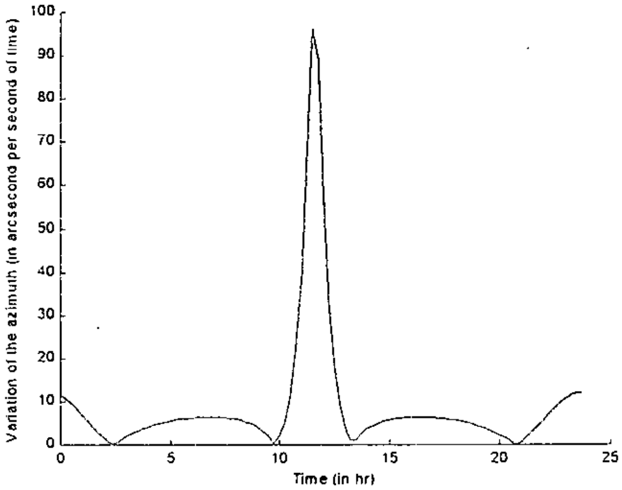

Figure V-6 . Azimuth variation of the fist day of Mars 2001.

V.3 The CCD camera

The solar astrolabes are up to now equipped with black and white CCD cameras. These Cameras are selected for their easy use and their low cost. The selected camera for Tamanrasset astrolabe is the COHU 4710. It is a Frame Transfer mode camera with 699(H) x 576(V) pixels. Each pixel is of 9.2x8.4 µm in dimension. Its output video is digitized on 8 bits by an analog to digital converter that gives a digitized images on 256 gray levels.

The field covered by the CCD camera is function of its dimension and the focal distance of the telescope on which it is mounted. Its expression is given by the following formula,

$$\text{Field} = \arctan\left(\frac{sidesofCCD(mm).10^{-3}}{foacl(m)}\right) \qquad (V.1)$$

Using this equation, the field covered by the COHU 4710 CCD is ~ 6'.3 on the horizontal direction and ~ 4'.8 on the vertical one.

The resolution limit that we can attend with an astrolabe is determined by the telescope diameter, the intrinsic quality of the image and the sampling frequency [41]. The first limitation is due to diffraction phenomena, the second one to the atmospheric turbulence and the third one to the sampling rate of the CCD detector. The sampling step represents the angular portion of the sky seen by the CCD pixel. Its expression is given by.

$$\text{Sampling} = \arctan\left(\frac{pixel(um).10^{-6}}{focal(m)}\right) \qquad (V.2)$$

If the sampling step is in arcsecond per pixel. the pixel dimension in microns and the focal length in millimetres, the formula of the sampling step is written as,

$$\text{Sampling (seconds arc/pixel)} = 206\,\frac{P}{F} \qquad (V.3)$$

Where P is the pixel dimension in μm and F the focal length of the telescope in mm.

The resolution limit imposed by a telescope of diameter D and a wavelength of observation λ is given by,

$$R_{\max} = \lambda / D \qquad (V.4)$$

If f is the focal length of the telescope, the resolution limit in this case is given by,

$$R_{\max} = f.\lambda / D \qquad (V.5)$$

To recover the optical signal , we have to verify the Shannon condition. So, the optical signal must be sampled by a sampling rate Δ_e , such that the following condition is satisfied,

$$\Delta_e \leq R_{\max}/2 \qquad (V.6)$$

The astrolabe of Tamanrasset will be equipped with a telescope of 10 cm in diameter and 3.5 m in focal distance. In addition, since the same optical system as that of Calern astrolabe will be used, the wavelength of observation is 550 nm . Using these characteristics, the resolution limit is 1.14 arcsecond (38.5 μm). In this case, the sampling step must be less or equal to 0.57 arcsecond (19.25 μm).

Using equation V.2, the sampling step is 0.5421 arcsecond along the vertical direction of the CCD and 0.495 arcsecond along the horizontal one. The characteristics that justify the choice of the COHU CCD camera.

V.4 Time reference system

The time accuracy in the experiment is the most important factor, since any error or instability will affect all the experiment. At Calern observatory, the solar astrolabe uses the Universal Time Coordinate provided by the time service to date the acquired Sun images. Since this kind of service does not exist at Tamanrasset observatory, we have to find a solution to overcome this lack. For this, we have selected a time reference system based on Navigation System Satellite, the GPS (Global Positioning System). Its is a GPS ISA TIME that furnishes time with a precision of 130 ns with respect to the universal time. Figure V-7 shows its block diagram.

An active antenna with an RG58 type cable is used to receive the GPS carrier (1575,42 Mhz). The card is equipped with a real time clock and the geographical data (latitude, longitude) are stored in an EEPROM memory. According to these geographical and temporal data, the card chooses the best situated satellites and shorten its time of calculation. In case of losing the GPS signals, the time base of the card varies according to the stability of its oscillator. This stability is 173 ms during 24 hours. The meteorological conditions have only a weak influence on the delays of the propagation of the GPS signals. A software program written in C language is used to detect the GPS card and to access the stored data in real time.

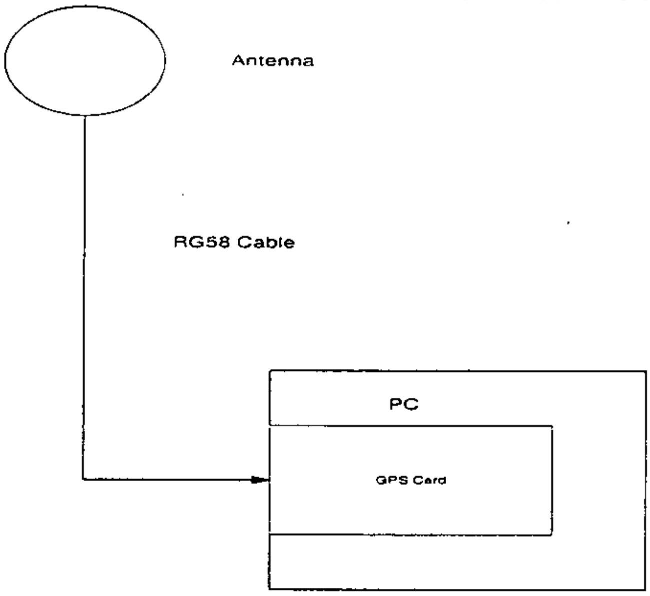

Figure V-7. The time reference for Tamanrasset Observatory Astrolabe.

The following steps illustrate the algorithm of the software program,

Step1: Reading of the base address according to the switch setting on the GPS card.

Step2: -Test the operating mode as follow:
Timetest=Port[base address];if bit1=1, the time is valid (the GPS is working), if 0 the card works on its internal base time.
-Reading the date,
Year=Port[base address].
Month=Port[base address+1].
Day of the month and the day of week=Port[base address+2].

Step3: Reading the time-of day,
Hour=Port[base address+3].
Minute=Port[base address+4].
Second=Port[base address+5].
Thousandths of second=Port[base address+6]+Port[base address+7] .

V.5 The System Timing Controller

The atmospheric refraction measurement is necessary in Sun semi-diameter determination. So, the humidity, the atmospheric pressure and temperature must be measured at the moment of observation . For this a PC-TIO-10 board is chosen to get for the first time the day time with high precision and to provide a future interface for the humidity, pressure and temperature sensors.

The PC-TIO-10 is a timing and a digital I/O board around two System Timing Controllers (STC, Am9513A and the Am9513B integrated circuits) and one MC6821 integrated circuit. The Am9513A is a general-purpose counter/timer with five 16-bit, individually controlled counters and a 4-bit frequency-scaler output. The MC6821 is a 16-bit, bit-configurable, digital I/O device with two interrupt inputs that are edge-programmable. The STCs are the hearth of the PC-TIO-10. These chips have five individually controlled 16-bit counters. The STCs have independently controlled frequency-scaler outputs. They are clocked by an onboard 1 MHz crystal oscillator to give 1 μsec timing resolution. In addition, SOURCE5 and SOURCE10 are clocked at 5 MHz to give a resolution of 200 nsec [37].

Figure V-8 presents the block diagram of PC-TIO-10 that illustrates its key functional components [37].

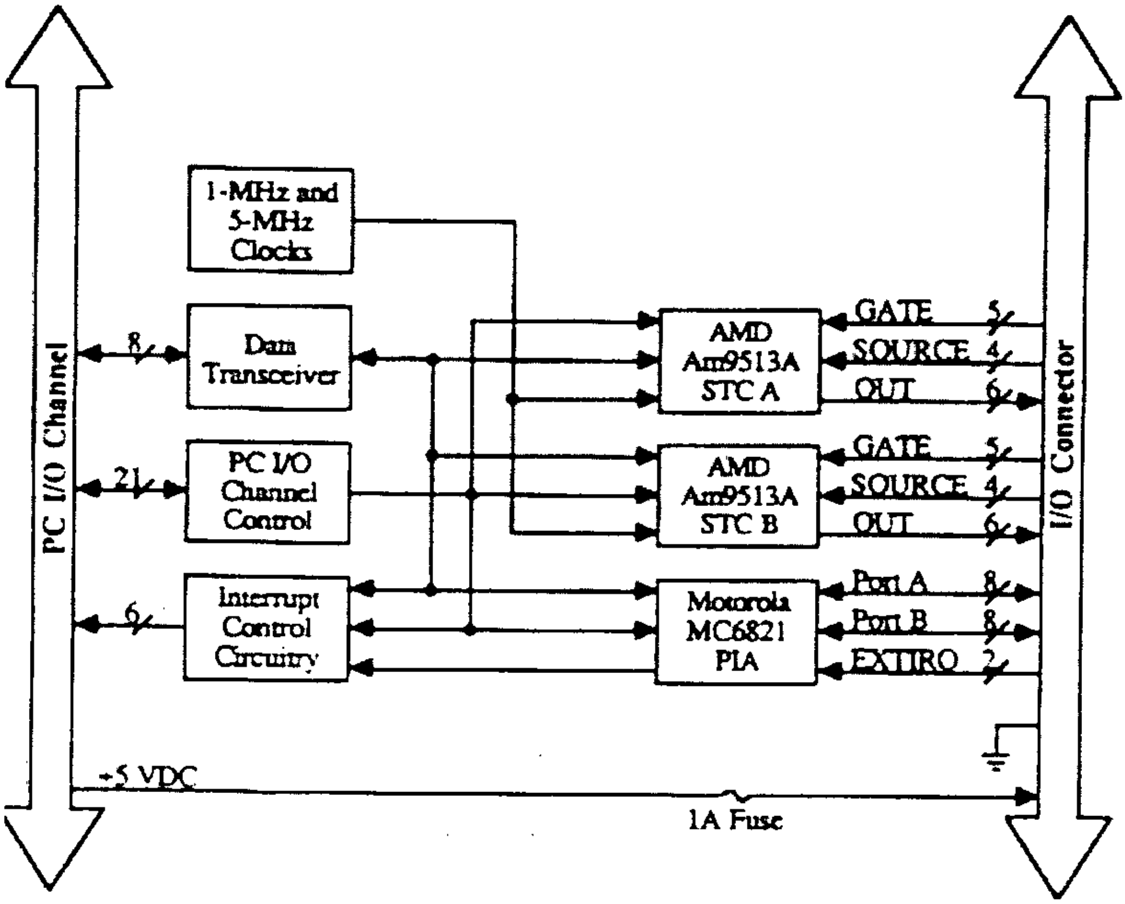

Figure V.8. The PC-TIO-10 block diagram.

V.5.1 Time of day generation with the Am9513A

For Tamanrasset Observatory Astrolabe (TOA), the Am9513A is used to get the time-of day with a precision of 1/1000000 of sec. The bits MM0 and MM1 of the master mode register control the time counting of the day in the Am9513A [37]. When these bits are set to 01, 10, or 11, logic on the counters 1 and 2 are enabled to cause the counters to roll over at the counts required for time-of day accumulation.

Figure V-9 represents the configuration used to get the time-of day for TOA.

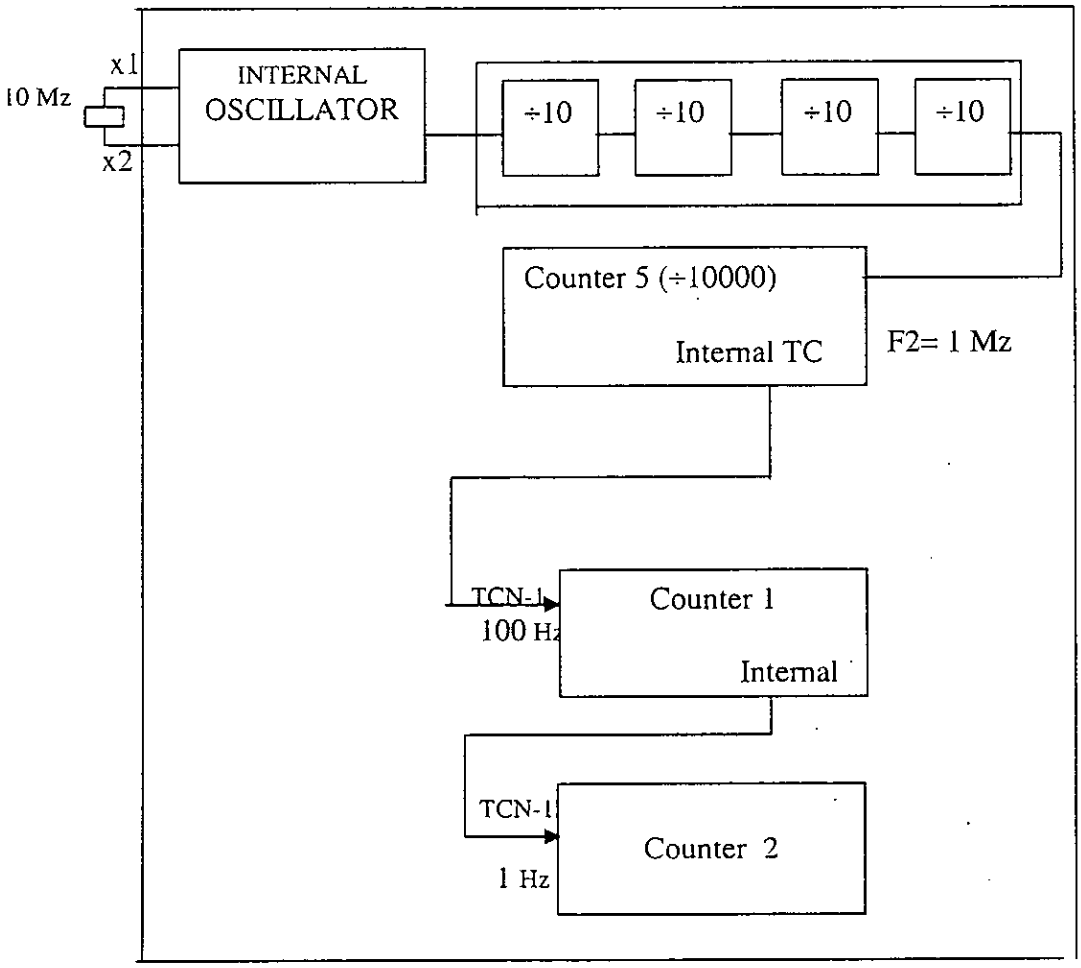

Figure V-9 .The time-of day configuration for Tamanrasset Observatory.

The time-of day circuitry requires a special initialization sequence. The following steps must be performed:

1- Set the Master Mode register and then the Counter Mode registers to the desired values.

2- Initialize the used counters to zero.

3- Set the Load registers of the used counters to the current time.

4- Start the counting process by writing the arm control word to the Am9513's Command register.

In the current application where high precision of time is required, the initialization time is loaded somewhat later than the current time. In addition, the arming process of the Counters is delayed until the current time matches the loaded one from the GPS card. The reading of time from the registers used in the configuration (Figure V-7) can be done each time by issuing a save word command to the three counters. This result in a transfer of their contents to the corresponding holds registers. The time can be then read without disturbing the time-of day process. For a speed reason, a software program written in assembly language is performed to initialize and read the current time.

V.6 The acquisition card

Figure V-10 presents the block diagram of the Eurecard Primo hardware structure used for Tamanrasset Observatory Astrolabe [38].

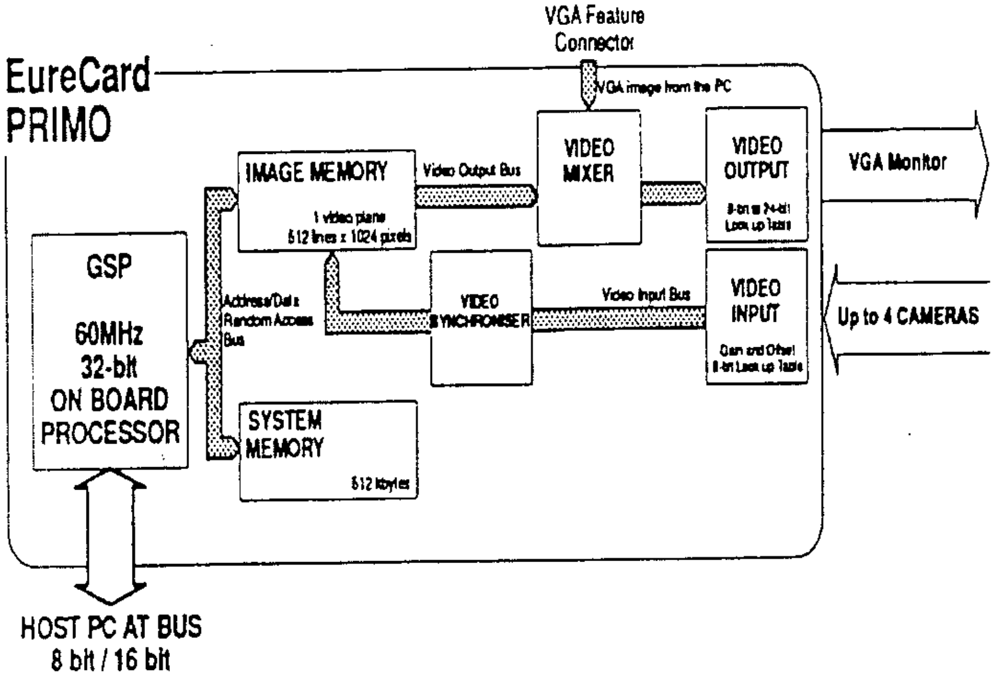

Figure V-10. EureCard Primo Block Diagram.

- The EureCard Primo's main processor is a Graphic System Processor (GSP). Its main features are: 60 MHz clock frequency, 16 bits local data bus, 30 32-bit internal registers, instruction cache memory, pipelining. It provides direct access from the PC to the EureCard Primo.

- A 512-Kbytes system memory is used to store programs and data used by the GSP.

- A 512-Kbytes image memory (one 8-bit, 512 x 10124 plane) used to store images acquired and processed by the EureCard Primo.

- The video input samples and digitizes the signal coming from one of the four cameras.

- The video mixer mixes the image generated by the EureCard Primo with the image coming from the PC.

- The video output is a triple digital to analogue converter and a set of associated circuits. It processes the video signal send to the VGA monitor.

The following algorithm illustrates the EureCard Primo configuration used for the TOA:

1- EureCard Primo detection.

2- Set the monitor configuration to dual mode.

3- Set the trigger event output to a logical positive edge. This input line is connected to the output line of the rotating shutter.

4- Initialize the acquisition to continuous mode.

5- Set the first input channel to which the COHU camera is connected.

6- Set the antialiasing filter, the gain, the offset and the Input Look Up Table of the input module to the appropriate values (see Annex 6).

7- Set the first input channel for input synchronization.

8- Set the pause time waited for after the trigger signal to 0 sec.

9- Set the number of fields to skip before grabbing starts to zero, and the number of field to grab to 1. This step is illustrated by the following timing:

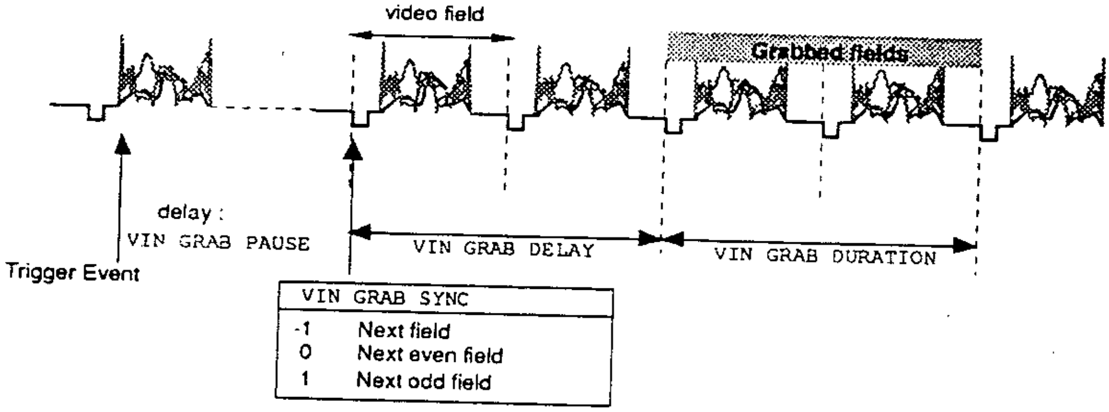

Figure V-11. Steps of Grab Process.

The logical steps of the acquisition program is shown bellow.

1- Initialization of the three cards (EureCard Primo, GPS card, PC-TIO-10 card).

2- Set the PC-TIO-10 to the current time using the GPS card.

3- Position calculation. Wait for a top signal from the rotating shutter.

4- Read the time and acquire the presented image in the image memory(direct or reflected). Wait for a top signal from the rotating shutter. During this waiting state, we process the image by the *à trous* algorithm, calculate the summit of the parabola used for approximation and finally store the whole in the ramdrive . When the top signal of the rotating shutter is presented , this step is repeated from the beginning to acquire the second image.

5- Step 4 is repeated 100 times.

6- Stop the acquisition (the acquired image sequence defines the first passage).

7- Position calculation. Wait for a top signal from the rotating shutter.

8- Read the time and acquire the presented image in the image memory(direct or reflected). Wait for a top signal from the rotating shutter. During this waiting state, we process the image by the *à trous* algorithm, detect its edge, calculate the summit of the parabola used for approximation and finally store the whole in the ramdrive. When the top signal of the rotating shutter is presented , this step is repeated from the beginning to acquire the second image.

9- Step 8 is repeated 100 times (the acquired image sequence defines the second passage).

10- Stop the acquisition and store the acquired image sequences and the corresponding edges in the hard disk. Preparation for the next diameter measurement.

When the proposed instrumental set will be installed around the astrolabe, it will permit us to test the overall system in operation. According to the tests done in laboratory, the acquisition time of a window image of 101x256 pixels is 50 msec. Since the rotating shutter that launches the acquisition makes 250 ms to complete one turn, so we have 250 ms to process the image, to detect the Sun edge and to calculate the summit point of the parabola used for the approximation. The laboratory test, using a computer of 350 *Mhz*, shows that the necessary time to perform these functions is 125 ms. This time can be decreased if we use a faster computer, since the acquisition process depends on the used grabbing card in one way and on the speed of the computer in the other way. After each complete Sun transition and before starting the next semi-diameter measurement, the steps to calculate the Sun semi-diameter can be performed.

CHAPTER VI CONCLUSION AND PERSPECTIVES

VI.1 Conclusion

Sun semi-diameter is one of the important quantities in astrophysics and astronomy domains. It is measured since 1666 by many astronomers and using different instruments. L'astrolabe ,with its principle, is one of the precise instruments in astrometry. In its solar configuration, it has furnished the most lengthy series of Sun diameter measurement at Calern observatory. These measurements were the object of many studies. The interpretation of the obtained results are always difficult. This difficulty is at least due to two main reasons,

- The observed solar edge has not a precise definition and the stability of the observer response was not stable.
- The study of the effects of different phenomenon (atmospheric, instrumentals) on the measurement was not well known due to the lack of information.

In order to improve the Sun diameter measurement, a new generation of Solar astrolabe, named DORaySol, is designed. This automatic instrument provides the observation in different wavelengths. In addition, the introduction of the prism of variable angle permits the acquisition of a huge data set per day, if the methodological conditions were favorable. The use of a CCD camera permits also the estimation of the atmospheric effects on Sun diameter measurement at the moment of observation. After a precise and an automatic instrument exists, the next step is to observe the Sun at lower latitudes and having the best site where the conditions of observation are favorable. To be integrated in the international network of astrolabes, the ancient solar astrolabe of Algiers observatory (Centre de Recherche en Astronomie Asrophysique et Geophysique) is currently in phase of transformation to DoraySol instrument.

In the present work, after the presentation of the principle of Sun diameter measurement, the methodology of observation using the ancient and the new generation of solar astrolabes, several techniques and algorithms are developed and tested in order to be ready for their installation around the solar instrument of Tamanrasset observatory.

VI.1.1 Meteorological study of the site of Tamanrasset observatory

Meteorological conditions are important where the solar astrolabe is installed. For this reason a meteorological study of Tamanrasset site has bee done. This study consisted in evaluating the variations of the atmospheric pressure, temperature, nebulosity, humidity, and wind speed. These quantities are important to qualify the site for the present and future astronomical observations. The study used the data gathered during **1998**, **1999** and **2000**.

The results have shown a mean humidity of **20.5%**, a mean atmospheric pressure of **866.4 hp**, a mean nebulosity of **2 octas**, a mean temperature of **22.8 °C**, and a mean wind speed of **3.7 m/s**. This preliminary study showed that Tamanrasset observatory would be a favorable place for this type of observation. In addition, the study of the **Sun trajectory** over the site showed that the location of Tamanrasset observatory allows the collection of huge data sets of Sun diameter measurements that can exceeds **4000 diameter per year**.

VI.1.2 Sun image processing

The principle of Sun diameter measurement with the CCD observation is based on the best method to extract the solar edge from the acquired digital images. Since the main information is contained in the Sun edges, the techniques used to process the Sun images must be capable to maintain this information during the whole image processing. Generally the Sun images present sunspots, the non-stationary defects, that must be localized and eliminated before edge detection and without affecting the Sun edge resolution. The chosen method is the ***wavelet transform***, the technique that permits the analysis of a signal simultaneously in time and frequency.

VI.1.2.1 Algorithms to implement the wavelet transform

Two algorithms to process the Sun images are used to implement the wavelet transform. These two algorithms are,

1- The ***"à trous" algorithm*** using the wavelet of Mexican Hat. Since this wavelet has not an associated scaling function, two interpolations of this later are tested, the ***linear interpolation*** and the ***B-spline interpolation***.

2- The ***Mallat algorithm*** using the wavelet of ***Daubechies of order 3***.

The comparison between the two algorithms, using a real Sun image acquired by the CCD astrolabe of Calern, showed that the obtained results from the two are comparable. The main difference between the two algorithms is the execution time. With the "à trous" algorithm, one filter is used for image decomposition, there is one approximation image and one detail image at each resolution step and the dimension of the processed image remains the same during the decomposition process. With Mallat algorithm, two filters are used for decomposition and the reconstruction of the processed image, at each step of decomposition there is one approximation image and three detail images and the dimension of the processed image decreases with the number of the resolution steps. Since at the solar astrolabe, we acquire one image each 250 ms, we have to look for the algorithm that takes less time, since our objective is to work in real time. So, the chosen algorithm is the ***"à trous" algorithm*** that uses the ***Mexican Hat wavelet*** ant the ***B_3-spline interpolation for the scaling function***.

VI.1.2.2 Edge extraction of the Sun image

Before the edge extraction , the Sun images are processed in order to locate and eliminate the sunspots and the optical defaults. The elimination method is done by processing the detail images where the signatures of these spots are present. The process consists to apply a ***thresholding*** on the wavelet coefficients of the first detail. ***The threshold value is chosen so that the wavelet coefficients of the detail image are reduced to the noise level.*** This value is chosen equal to ± ***3sigma***, where sigma is the standard deviation of the detail wavelet coefficients.

Even after the spots elimination, there are always a residual noise and a residual signatures of the eliminated spots in the image. In order to increase the signal to noise ratio, the detail images must be filtered before the final reconstruction of the processed Sun image. For that reason, two methods are tested, the method of ***thresholding*** and the method based on ***filtering***. Concerning the fist method, tests have shown that the choice of the threshold value is delicate, since, if the threshold value is not adequately chosen, the thresholding process will modify simultaneously the coefficients that intervene in the edge definition. So, to overcome this difficulty, we have decided to use the second method and several filters are tested. All the filters are of rectangular low pass types. The comparison between the tested filters showed that the low pass filter with coefficients *(¼ ½ ¼)* in one dimension is the most appropriate one.

Due to the :

- Atmospheric turbulence.
- No correction of the diurnal motion using the solar astrolabe.
- Long integration time of the CCD camera (20 ms).

the edge of the acquired images is not sharp and extends over more than ***10 arcseconds*** at Calern observatory. The classical methods of edge detection are applied to extract the edge of the processed and the cleaned Sun images. The results have showed that the edge is not well detected and fluctuations of the extracted edge, with some corrections, around the parabola used for its approximation are considerable. For example, the ***Sobel method*** gives a standard deviation of **3.28 arcseconds**, that of *Laplacian a sigma of 7.69 arcseconds* and those of *Derich and Canny* give a close sigma value of *1.26 arcseconds*. For that reason ***three methods*** are developed to extract the edge with high precision. The comparison between the three methods, using a real and a cleaned Sun image, revealed that ***the method based on the second derivative*** is the appropriate one. With this method, the fluctuations of the extracted edge points after being smoothed by a median filter and approximated by parabola, is ***0.43 arcseconds,*** a value that is less than the pixel resolution (0.74 arcseconds).

VI.1.2.3 Tangency point determination

The tangency point determines the transition instant where the upper edge or the lower edge of the Sun crosses the defined height circle. It is defined by the intersection of the two Sun trajectories (direct trajectory and reflected trajectory) on the CCD frame. The CDD lines (X) define the displacement of the Sun azimuth and the CCD columns (Y) define the displacement of the Sun zenith. In practice, the CCD is never well positioned and there is always an inclination with respect to the horizon. This inclination must be evaluated and the value of the transit instants corrected. The computation showed that this correction is generally small. It is found to be of the order of ***4 to 5 ms*** for a mean inclination of the CCD lines of ***20 arcsecond*** and a mean separation in X of ***20 pixels (22 arcseconds).***

VI.1.3 Sun diameter measurement

The developed programs to process the Sun images and the procedures to calculate the Sun diameter are tested. This test is done using two selected sets of Sun images acquired by the Solar CCD Astrolabe of Calern (France) during the year of 1997. One is dated to 09/09/97 and the other one to 10/09/97. These sets contain an even number of sequences. Each one is a series of one hundred images of 101x256 pixels in dimension(50 reflected images, and 50 direct images).

The results of the measured apparent Sun semi-diameter, showed a mean value of **959".66** for the set of 09/09/97 with an error equal to *0.02"* and *959".61* for the set of 10/09/97 with an error of *0.02"* .The difference between the found mean values and those of Calern is ***0.09 arcseconds*** for the set of 10/09/97 and ***0.1 arcseconds*** for the set of 09/09/97. This difference is mainly due to the planetary theory used to calculate the Sun ephemeredes. At Calern , they use the VSOP87 planetary theory, where the present work uses a low accuracy formulae (the accuracy is 0.01° in longitude). In addition, the methods used to process the Sun images are not the same.

The mean value of Sun semi-diameter (R) from the two sets is:

$$R = 959''.64 \pm 0.02''.$$

VI.1.4 Atmospheric effect measurement

The study of the atmospheric turbulence, characterized by the Fried parameter using the two sets showed a mean value of r_0 equal to *38.89 mm* , the value that reflects the bad seeing conditions at Calern observatory. Also, **a systematic decrease** of the error made on diameter measurement and on the transit instants determination with the best seeing conditions (Fried parameter) is observed. The error on diameter can be less than that obtained from these two sets, if the conditions of observation, characterised by the meteorological state and the atmospheric turbulence were more favorable.

VI.1.5 Instrumentation

The studied and the selected instrumentation that will be installed around Tamanrasset astrolabe is made of an ***EureCard Primo*** for acquiring the Sun images, a ***GPS card*** for time reference and the ***PC-TIO-10 card*** for dating the acquired images. The developed programs that pilot these cards are tested in laboratory using a computer ***of 350 Mhz and a simulated Sun image***. The tests showed that the required time to acquire an image of ***101x256 pixels*** in dimension , to process it (elimination of sunspots and filtering the residual noise), to detect its edge and to calculate the summit point of the parabola used for approximation is *175 msec.* This allow us to work in real time, since each 250 ms we have one Sun image present at the focal plane, either direct or reflected.

VI.2 Perspectives

The Sun is currently one of the most studied celestial body in astrometry . Due to the technical advancement and scientific developments during the last years, many measurements with high resolution will be available to response to various questions that the results of the measurement ask. The simultaneous studies of all the solar parameters, that the observation can access, are necessary.

Many ground CCD astrolabe measurements are operating in different regions in the world, we can name that of **Calern (France), Feira de Santana(Brésil), Malatya (Turquie), Rio de Janeiro (Brésil), and San Fernando (Espagne).** With ground measurement , the knowledge of the seeing parameters is primordial to improve the accuracy of the solar diameter. The optimum solution up to know is to perform this type of measurement out of the atmosphere. It is why the French Agency CNES scheduled the launch of a microsatellite **(PICARD)** in 2006 with its own program of measurements. In addition to its measurement of the solar diameter with an accuracy of a hundred times better than what is done on the ground, the differential rotation, the irradiance and its variations will be measured. So, with **Picard** and its replica on the ground, **Sodism II** and the seeing monitor (**Misolfa**) , all operating simultaneously, will permit the calibration of the ground astrolabes.

At Tamanrasset observatory, there will be no seeing monitor of Misolfa type installed near the astrolabe. But, using a powerful acquisition card and adapted programming could supply the necessary seeing parameters. Finally, the installation of the designed acquisition system around the astrolabe of Tamanrasset, the whole automation of the instrument, will permit to integrate our astrolabe in the ground network and calibrate it when the Picard microsatelite will be launched.

BIBLIOGRAPHY

[1] S. Débarbat, F.Laclare, ACTA ASTRONOMICA, Vol.40, pp.313-319,1990.

[2] E.Ribes and R. Barthalot, Nature, 326,52,1987.

[3] S.Sofia, D.W. Duham, J.B.Duham, and A.D.Fiala, Nature , 304,522,1988 .

[4] C.Smith and D.Messina, Goddard Space Flight Center Workshop, S.Sofia (Ed.), 1981.

[5] M.Toulmonde , A&A, 325, p.1174, 1997.

[6] F.Noel, , A&A, 325, 825-827, 1997.

[7] R. L.Gilliland, AJ, 248:1144-1155, 1981.

[8] F.Chollet and V.Sinceac, A&AS, 139: 219-229 ,1999.

[9] T.M.Brown, J.Christein-Dalsgaard, AJ,500, L195-L198, 1998.

[10] S.Débarbet and B.Guinot, B., « la méthodes des hauteurs égales en Astronomie », Gorden and Breach.

[11] F.Laclare ,G. Merlin , Comptes Rendus Academie des Sciences Paris, Série II, 313, p.211, 1991.

[12] F.Laclare, C.Delmas, J.P.Coin, A.Irbah , Solar Physics, 166:211-229, 1996.

[13] C.Delmas, "Sun Radius ground measurements" , Workshop Oleron, 2000.

[14] V.Sinceac, « Analyse et exploitation des observations de passage du soleil à partir de l'astrolabe de Danjon equipé d'une camera CCD » , These Doctorat, EDAAIF, 1998.

[15] R.H.Dicke and H.M.Goldenberg, Physical Review Letters, 18/9, p.313, 1967.

[16] J.P.Rozelot, J.Rosch , Comptes Rendus Academie des sciences Paris, Série II b, 322, p.637, 1996.

[17] K.Labitzke , 1998, Communication personnelle.

[18] E.Ribes. P.Merlin, J.C.Ribes, R.Barthalot. Annales Geophysicae, 7/4, p.321, 1989.

[19] Borkowski, Bull.Geod.63, 50-56, 1989.

[20] P.C.R.Poppe, N.V.Leister, F.Laclare, C.Delmas, AJ,116, 2574-2582, 1998.

[21] D.J. Gregoris and Yu.S, SJET, 1994.

[22] F.Chollet F., Thèse de Doctorat, l'université Pierre et Marie Curie – Paris, 1981.

[23] A.Danjon , Bulletin Astronomique, 21.p.323, 1958.

[24] B.Guinot, Thèse de Doctorat, Faculté des sciences de l'université de Paris, 1958.

[25] I.Mangombi I, Thèse de Doctorat, Observatoire de Paris, 1986.

[26] D.V.Thomas , Monthly notes of the Astronomical Society of South Africa, 26/1-2. p.2, 1967.

[27] F.Laclare, G.Merlin, C.R.Acad Sci.Paris, t.313, Série II,p.323-330, 1991.

[28] L.Lakhal, Thèse Magister, USTHB,1999.

[29] M.Toulmonde, A&A, 325, 1174-1178, 1997.

[30] S..G.Mallat, IEEE, Vol. 11. No. 7, 1989.

[31] M..J.Shensa, IEEE, Vol.40. NO.10, 1992.

[32] J.L.Stark, Thèse de Doctorat, Univesité de Nice-Sphia Antipolis, 1992.

[33] M.Bouzaria, and R.Moussaoui, Thèse d'ingeniorat , USTHB, 1996.

[34] P.N.Brandit, H.A. Mauter and R.Smarth, A&A, 188,163, 1987.

[35] G.Ricort, J.Borgnino, C.Amie , Solar Physics, 75,377, 1982.

[36] A.Irbah , F.Laclare, J.Borgnino., G.Merlin , Solar Physics, 149, 213, 1994.

[37] National Instruments, PC-TIO-10 user manual, July edition 1993.

[38] EureCard Primo, User manual.

[39] A.Danjon, Astronomie Générale,.

[40] R.T.Dixon, Dynamic Astronomy, 1993.

[41] P.Martinez, A.Klotz , Adagio – Toulouse, 1994.

[42] A.Marion, Acquisition & Visualisation des images, 1997.

[43] S.Leone, Pub.Oss.Astron.Palemo,11,Nuovo Series 20, 1973.

[44] D.W.Duham, S.Sofia, A.D.Fiala, D.Herald and P.M.Muller, Science, 210, 1243, 1980

[45] J.Eddy and A.Boornazian, Bull. Amer.Astron.Soc., 11,437, A. 1979.

[46] J.Parkinson , L.Morrison , R.Stephenson , Nature, 228, 548, 1980,.

[47] R.Gillilland , APJ, 248, 1144. 1981,.

[48] P.Assus, J.Borgnino J, F.Martin, A.Bouzid , M.Chibani, A.Irbah and N. Seghouani, Marrakech Site, Astronomical Site Evaluation in the Visible and Radio Range, Marrakech – Morocco 13-17, 2000.

[49] S. Mallat, Proc. IEEE Trans on Pattern Anal. and Math. intel., Vol. 11, No 7, 1989

[50] M.J.T. Smith and T.P. Barnwell, IEEE ASSP, Vol. 34, pp. 434--441, 1988.

[51] A.Cohen, I. Daubechies, J.C. Feauveau, Comm. Pur. Appl. Math., Vol. 45, p 485--560, 1992.

[52] I. Daubechies, , Comm. Pur. Appl. Math., Vol. 41, p 909--996 , 1988.

ANNEXES

ANNEX 1

Meteorological study of Tamanraset Observatory

Tamanrasset observatory is built in 1932, and it is 2000 km far from the capital of Algeria. Its geographic coordinates are 22.792 ° N in latitude and 5.527 ° E in longitude, and it has an altitude of 1370 m. It is considered as one of the important International Observatories in the world. Its emplacement makes it an important site for many geophysical and astronomical applications. For the case of astronomy, Tamanrasset site is chosen as one point of the solar diameter measurement network.

The present meteorological study of Tamanrasset site consists in studying the variations of the atmospheric pressure, the temperature, the nebulosity, the humidity and the wind speed. These quantities are important to qualify the site for the present and future astronomical observations. The study extends over three years 1998, 1999 and 2000.

1.1 Humidity

It is defined as the quantity of the water in the air. It is measured in percentage (%); a dry air corresponds to 0 %, and a saturated air corresponds to 100%.

1.2 Atmospheric pressure

It is defined as the weight of an air column from the top of the atmosphere to the Earth surface. It is measured in hecto-pascal.

1.3 Nebulosity

The total nebulosity is defined as the fraction of the celestial globe covered by a set of the visible clouds. The nebulosity is estimated visually and measured in Octas; a sky which is three fourth covered by the clouds have a total nebulosity of 6 octas. A clear sky corresponds to a nebulosity of o octas, and a sky totally covered corresponds to a nebulosity of 8 octas.

1.4 Wind speed

It is measured in meter per second (m/sec).

1.5 Temperature

The temperature is measured in Celsius degrees (°C).

1.6 Recording data process and comparison

The parameters, the pressure, the humidity, the temperature, the nebulosity, the direction and the wind speed are recorded eight times each day (at 00 hr, 03 hr, 06 hr, 09 hr, 12 hr, 15 hr, 18 hr, 21hr). The comparison between these parameters for the three years is given bellow.

1.6.1 Humidity

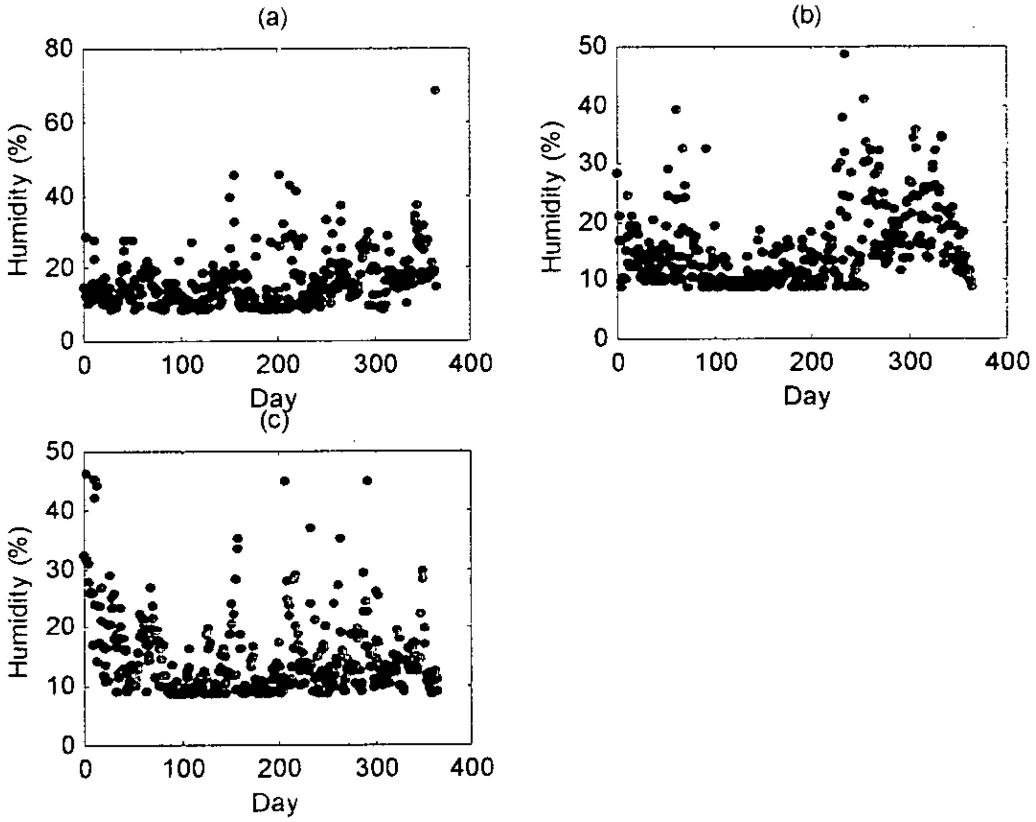

Figure 1.1. Daily mean humidity of each year.(a) 1998,(b) 1999, (c) 2000.

The year 1998: The maximum humidity is 81% and the minimum one is 9%. The mean value is 21.18 %.
31.23 % of the days have humidity less than 15 %.

The year 1999: The maximum humidity is 85 % and the minimum is 9 %. The mean value is 20.56 %.
35.68 % of the days have humidity less than 15 %.

The year 2000: The maximum humidity is 87% and the minimum is 9%. The mean value is 19.76%.
48.56 % of the days have humidity less than 17 %.

I.6.2 Nebulosity

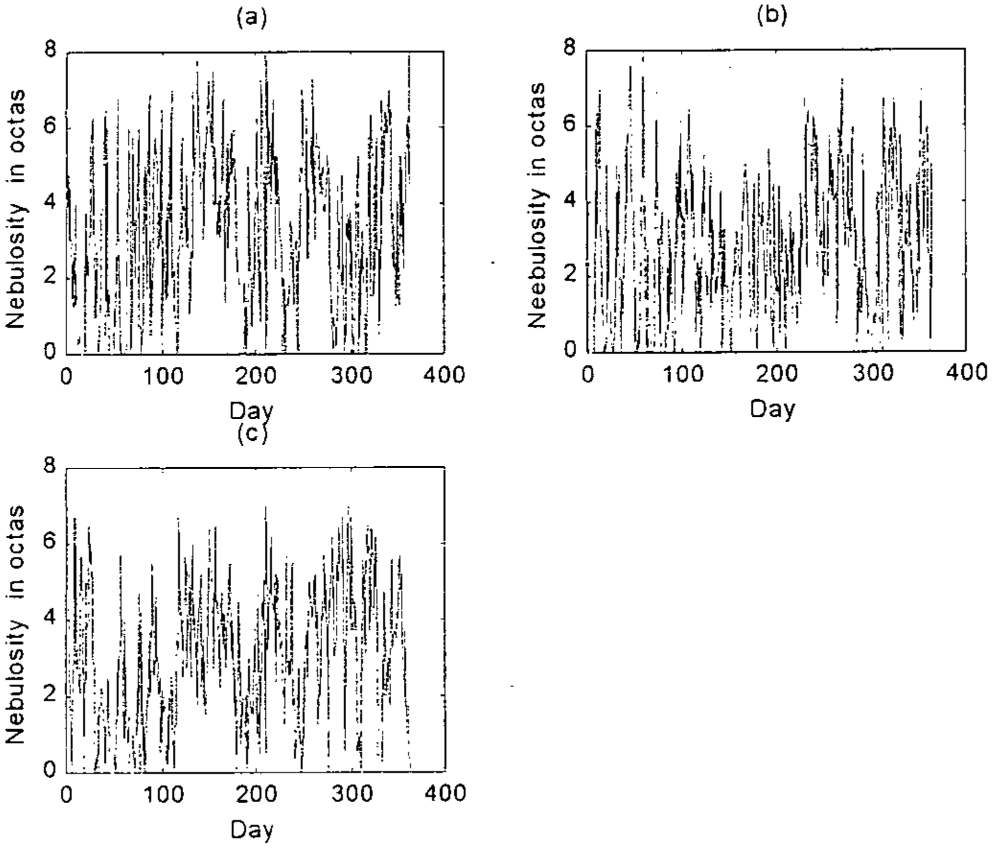

Figure I.2. Daily mean nebulosity of each year.(a) 1998,(b) 1999, (c) 2000.

The year 1998: The maximum nebulosity during all the year is 8 octas and the minimum is 0 octas. The mean value is 2.84 octas.

60.96 % of the days have nebulosity less or equal to 3 octas and 29.90 % with zero octas.

The year 1999: The maximum nebulosity during all the year is 8 octas and the minimum is 0 octas. The mean value is 2.45 octas.

66.92 % of the days have nebulosity under or equal to 3 octas and 34.38 % with zero octas.

The year 2000: The maximum nebulosity during all the year is 8 octas and the minimum is 0 octas. The mean value is 2.71 octas.

4.25 % of the days have a nebulosity more than 6 octas and 28.46 % with zero nebulosity.

1.6.3 Atmospheric pressure

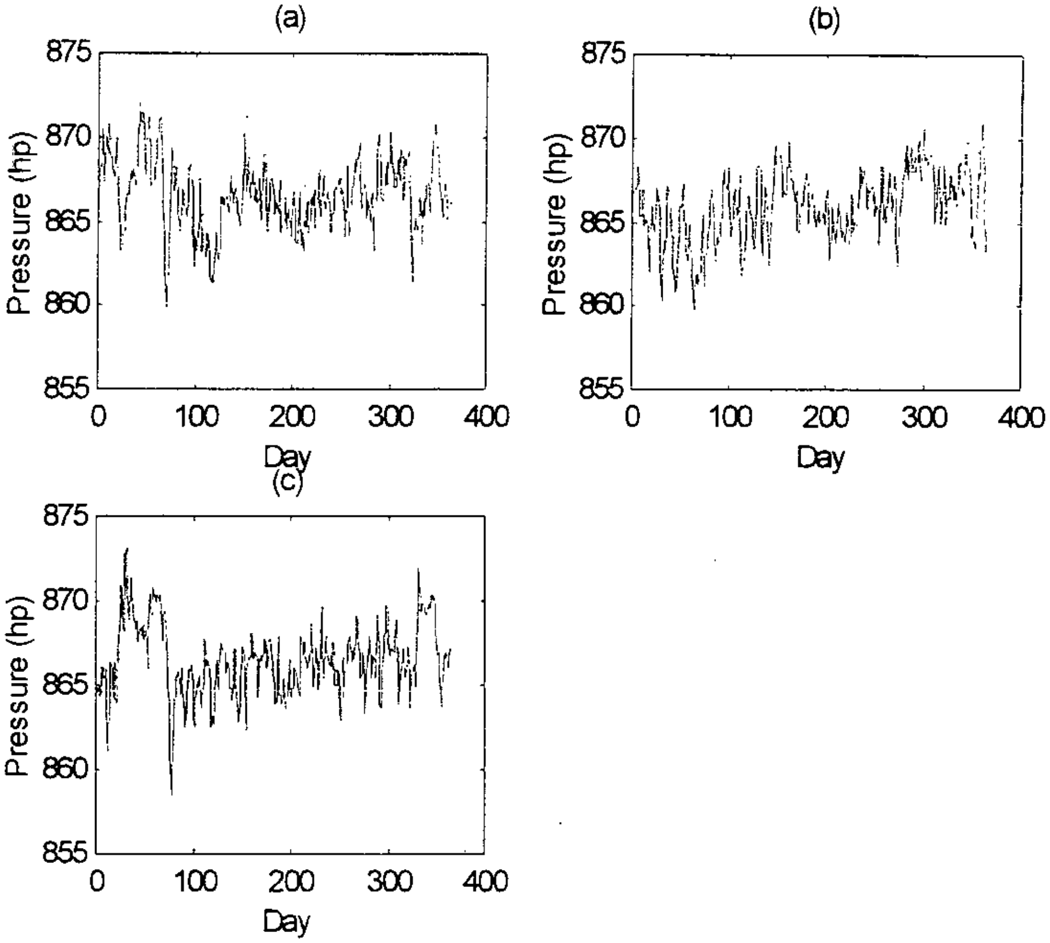

Figure 1.3. Daily mean atmospheric pressure of each year. (a) 1998, (b) 1999, (c) 2000.

The year 1998: The maximum atmospheric pressure is 874.4 hp and minimum is 858.8 hp. The mean value is 966.67 hp.

The year 1999: The maximum atmospheric pressure is 872.3 hp and the minimum is 858.1 hp. The mean value is 966.00 hp.

The year 2000: The maximum atmospheric pressure is value is 874.3 hp and the minimum is 857.7 hp. The mean value is 966.54 hp.

1.6.4 Temperature

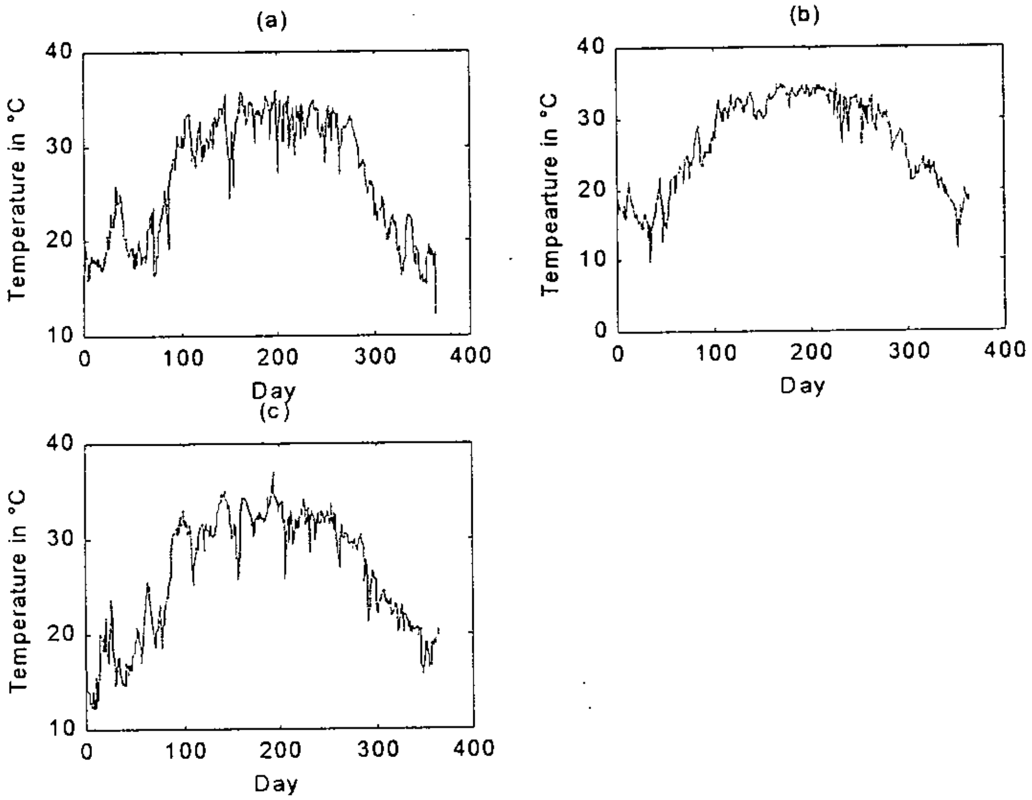

Figure 1.4. Daily mean temperature of each year.(a) 1998,(b) 1999, (c) 2000.

The year 1998: The maximum temperature value is 38 °C and the minimum is 1.5 °C. The mean value is 23.00 °C.

The year 1999: The maximum temperature is 36.6 °C and the minimum is -1 °C. The mean value is 22.69 °C.

The year 2000: The maximum temperature is 38.5 °C and the minimum value is 0.5 °C. The mean value is 22.60 °C.

1.6.5 Wind speed

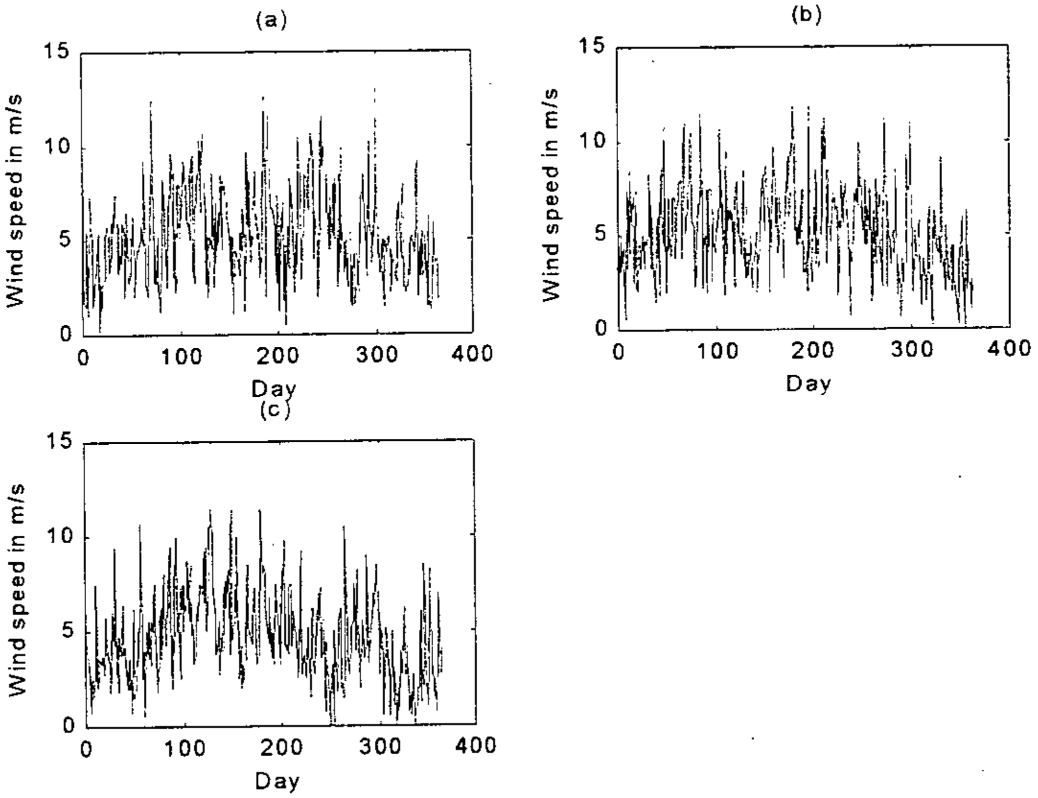

Figure 1.5. Daily mean wind speed of each year .(a) 1998,(b) 1999, (c) 2000.

The year 1998: The maximum wind speed is 17 m/s. The mean value is 3.78 m/s. 35.03 % of the days have a wind speed less than 3 m/s and 33.22 % of days with no wind.

The year 1999: The maximum wind speed is 18 m/s. The mean value is 3.74 m/s. 49.42 % of the days have a wind speed less or equal to 3 m/s and 31.99 % of the days with no wind.

The year 2000: The maximum value is 21 m/s. The mean value is 3.44 m/s. 52.84 % of the days have a wind speed less than 3 m/s and 36.17 % with no wind.

ANNEX 2

2.1 Spherical trigonometry

A great-circle arc is the analogue of a straight line. Where two such arcs intersect, we can define the spherical angle. A spherical triangle is made up of three arcs of great circles all less than 180°. The sum of the angles is not fixed, but will always be greater than 180°. Consider a triangle ABC on the surface of a sphere with radius = 1 [39].

Let OXYZ be a system of rectangular axes,

O is at the centre of the sphere;
OZ passes through A;
OX passes through arc AB (or the extension of it);
OY is perpendicular to both.

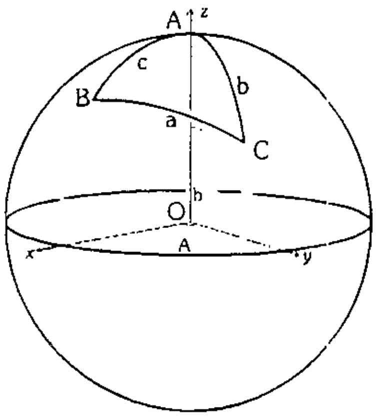

Figure 2-1 Celestial sphere.

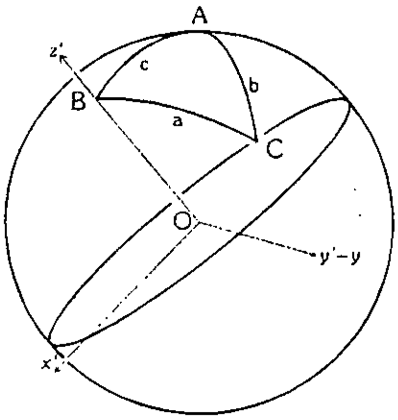

Figure 2-2. Celestial sphere after pole movement.

The coordinates of C in this system are,

$$\begin{aligned} x &= \sin(b)\cos(A) \\ y &= \sin(b)\sin(A) \\ z &= \cos(b) \end{aligned} \qquad (2.1)$$

Now we create a new set of axes by keeping the y-axis fixed and moving the "pole" from A to B; see Figure 2.2.

The new coordinates of C are

$$\begin{aligned} x' &= \sin(a)\cos(180-B) = -\sin(a)\cos(B) \\ y' &= \sin(a)\sin(180-B) = \sin(a)\sin(B) \\ z' &= \cos(a) \end{aligned} \qquad (2.2)$$

The relation between the old and new system is simply a rotation of the x,z-axes through the angle c,

$$\begin{aligned} x' &= x\cos(c) - z\sin(c) \\ y' &= y \end{aligned} \qquad (2.3)$$

$$z' = x \sin(c) + z \cos(c)$$

That is:

$$\begin{aligned} \sin(a)\cos(B) &= \sin(b)\cos(A)\cos(c) - \cos(b)\sin(c) \\ \sin(a)\sin(B) &= \sin(b)\sin(A) \\ \cos(a) &= \sin(b)\cos(A)\sin(c) + \cos(b)\cos(c) \end{aligned} \tag{2.4}$$

The first relation in (2.4) is the transposed cosine rule.

The second relation gives the sine rule. Rearrange this later, we have:

$$\sin(a)/\sin(A) = \sin(b)/\sin(B) \tag{2.5}$$

Similarly,

$$\sin(b)/\sin(B) = \sin(c)/\sin(C), \text{ etc.} \tag{2.6}$$

So the sine rule is usually expressed as:

$$\sin(a)/\sin(A) = \sin(b)/\sin(B) = \sin(c)/\sin(C) \tag{2.7}$$

The third relation gives the cosine rule:

$$\cos(a) = \cos(b)\cos(c) + \sin(b)\sin(c)\cos(A) \tag{2.8}$$

and similarly:

$$\cos(b) = \cos(c)\cos(a) + \sin(c)\sin(a)\cos(B) \tag{2.9}$$

$$\cos(c) = \cos(a)\cos(b) + \sin(a)\sin(b)\cos(C) \tag{2.10}$$

2.2 Earth rotation and the equatorial coordinates

By the standards of modern astrometry, the Earth is quite a wobbly platform from which the sky is observed. The Earth's rotation rate is not uniform. Its axis of rotation is not fixed in space, and even its shape and relative positions of its surface locations are not fixed. For the purposes of pointing a telescope to one-arcsecond accuracy, we need not worry about shape and surface feature changes, but changes in the orientation of the Earth's rotation axis are very important. In a sense, equatorial sky coordinates are a compromise between an earth-based system and one fixed with respect to distant stars. Right ascension and declination are quite analogous to longitude and latitude on the Earth's surface. They share the same polar axis and equator, but the sky coordinate grid does not rotate with the Earth's daily spin. However, apparent right ascension and declination are not fixed with respect to the stars because their coordinate frame follows the motion the Earth's pole and equator.

In practice, celestial coordinates are tied to observed objects because the location of the vernal equinox is hard to measure directly. The B1950 coordinate grid location is defined by the publish positions of stars in the Fourth Fundamental-Katalog (FK4). The J2000 system is based on FK5. These catalogs list mostly nearby stars, so any definition of coordinates tied to these catalogs is subject to errors due to motions of the stars on the sky. The FK4 equinox is now known to drift with respect to the FK5 equinox by about 0.085 arcseconds per century.

Currently, the most stable definition of J2000 coordinates is one based on about 400 extragalactic objects in the Radio Optical Reference Frame. This is heavily biased toward VLBI radio sources, but it will soon be tied to many more optical objects by the HIPPARCOS satellite. The RORF is stable to at least 0.020 arcseconds per century, and this is improving with better observations and a longer time base. The positional accuracy of the set of 400 objects is about 0.0005 arcseconds.

For partly historical and partly practical reasons, the time variability of the direction of the Earth's rotation axis and an observatory's relation to it are divided into four components: precession, nutation, celestial pole offset, and polar motion. By definition, precession and nutation are mathematically defined through the adoption of the best available equations. Celestial pole offset and polar motion is observed offsets from the mathematical formulae and are not predictable over long periods of time.

2.3 Precession

Neither the plane of the Earth's orbit (the ecliptic), nor the plane of the Earth's equator is fixed with respect to distant objects. The dominant motion is the precession of the Earth's polar axis around the ecliptic pole. The Earth's axis sweeps out a cone of 23.5 degrees half angle in 26,000 years.

The ecliptic pole moves more slowly. If we imagine the motion of the two poles with respect to very distant objects, the Earth's pole is moving about 20 arcseconds per year and the ecliptic pole is moving about 0.5 arcseconds per year. The combined motion and its effect on the position of the vernal equinox are called general precession. The predictable short-term deviations of the Earth's axis from its long-term precession are called nutation. Equations, accurate to one arcsecond, for computing precession corrections to right ascension and declination for a given date within about 20 years of the year 2000 are:

$$RA = RA(2000) + (3.075 + 1.336 * \sin(RA) * \tan(Dec)) * y \qquad (2.11)$$

$$Dec = Dec(2000) + 20.04 * \cos(RA) * y \qquad (2.12)$$

Where y is the time from January 1, 2000 in fractional years, and the offsets in RA and Dec are in seconds of time and arcseconds, respectively.

2.4 Nutation

Predictable motions of the Earth's rotation axis on time scales less than 300 years are combined under nutation. This can be thought of as a first order correction to precession. The currently standard nutation theory is composed of 106 non-harmonically-related sine and cosine components, mainly due to second-order torque effects from the sun and moon, plus 85 planetary correction terms. The four dominant periods of nutation are 18.6 years (precession period of the lunar orbit), 182.6 days (half a year), 13.7 days (half a month) and 9.3 years (rotation period of the moon's perigee). The following approximation for nutation is good to about an arcsecond .

$$\text{delta } RA = (0.9175 + 0.3978 * \sin(RA) * \tan(Dec)) * dL - \cos(RA)*\tan(Dec)*dE \qquad (2.13)$$

$$\text{delta } Dec = 0.3978 * \cos(RA) * dL + \sin(RA) * dE \qquad (2.14)$$

Where delta RA and delta Dec are added to mean coordinates to get apparent coordinates. The nutations in longitude (dL) and obliquity of the ecliptic (dE) may be computed from the two largest terms in the general theory with

$$dL = -17.3 * \sin(125.0 - 0.05295 * d) - 1.4 * \sin(200.0 + 1.97129 * d \tag{2.15}$$

$$dE = 9.4 * \cos(125.0 - 0.05295 * d) + 0.7 * \cos(200.0 + 1.97129 * d) \tag{2.16}$$

Where d = Julian Date - 2451545.0.The sine and cosine arguments are in degrees. dL and dE are in arcseconds.

2.5 Celestial pole offset

The celestial pole offset is the unpredictable part of nutation. These offsets are published in IERS Bulletin as offsets in dL and dE. For telescope, pointing they are not important since they are of the order of 0.03 arcseconds.

2.6 Polar motion

Because of internal motions and shape deformations of the Earth, an axis defined by the locations of a set of observatories on the surface of the earth is not fixed with respect to the rotation axis that defines the celestial pole. The movement of one axis with respect to the other is called polar motion. For a particular observatory, it has the effect of changing the observatory's effective latitude as used in the transformation from terrestrial to celestial coordinates. The International Earth Rotation Service definition of the terrestrial reference frame axis is called the IERS Reference Pole (IRP).

The dominant component of polar motion called Chandler wobble is a roughly circular motion of the IRP around the celestial pole with amplitude of about 0.7 arcseconds and a period of 14 months. Shorter and longer time scale irregularities, due to internal motions of the earth, are not predictable and must be monitored by observation. The sum of Chandler wobble and irregular components of polar motion are published weekly in IERS Bulletin along with predictions for a number of months into the future.

ANNEX 3

Systems of time

There are two widely used time standards. One is the rotation of the earth, and the other is the frequency of atomic oscillations (mainly the cesium-133 atom). The Earth's rotation is not uniform. Its rate exhibits both periodic changes and long term drifts on the order of a second per year. Atomic standards are the closest approximations we currently have to a uniform time with accuracies on the order of microseconds per year.

Since the advent of atomic time in 1955 there was a steady transition from reliance on the Earth's rotation to the use of atomic time as the primary standard. Before atomic time, the closest approximation to a uniform time was Ephemeris Time (ET), which used the best available theory of the Earth's rotation to remove its known changes in rotation rate. The use of Ephemeris Time continued until 1984.

Several important time scales still follow the rotation of the Earth. The most notably are, civil and sidereal time. Actually, they are derived from atomic time through a combination of earth rotation theory and actual measurements of the Earth's rotation and orientation.

In basing the measurement of time upon the rotational motion of the Earth the ideal unit of time would be the period of one complete rotation around the instantaneous axis. The sidereal time, defined by the apparent diurnal motion of the equinox, is therefore adopted as the empirical intermediary. Mean solar time, determined in principle by diurnal motion of the conventional mean Sun and obtained in practice from its relation to sidereal time, is the practical measure of the time defined by the rotation of the Earth.

3.1 Atomic times

3.1.1 TAI - International Atomic Time

International Atomic Time (TAI) is the primary time standard in the world today. It is the combined input of many clocks around the world, each corrected for known environmental and relativistic effects. In relativistic terms, TAI is an Earth-based time since it is defined for a gravitational potential and inertial reference on the surface of the Earth. TAI is the standard for the SI (System International) second. The zero point of TAI was somewhat arbitrarily defined by early atomic clocks. Its offset from Ephemeris Time was precisely defined as 32.184 seconds for January1, 1977.

The difference between Ephemeris Time and atomic time $\Delta T(A)$ provides a first approximation to $\Delta T = E.T. - U.T$,

$$\Delta T(A) = TAI + 32^{s}.184 - UT1 \qquad \text{post} - 1972. \qquad (3.1)$$

3.1.2 UTC - Coordinated Universal Time

By definition, UTC and TAI have the same rate, but UTC stays close to Mean Solar Time by adding integer numbers of seconds, called leap seconds, from time to time. This keeps solar noon at the same UTC (averaged over the year), even though the rotation of the Earth is slowing down. The offset is changed as needed to keep UTC within about 0.7 seconds of Earth rotation time, UT1. Leap seconds are typically added once per year at the end of December or June, but they can be added (or subtracted) at other designated times throughout the year.

$$\text{UTC} = \text{TAI} - (\text{number of leap seconds}) \qquad (3.2)$$

3.1.3 TDT or TT - Terrestrial Dynamic Time

Before atomic clocks, Ephemeris Time (ET) was the closest available approximation to a uniform time for planetary motion calculations. Terrestrial Dynamic Time, which is tied to atomic time by a constant offset of 32.184 seconds, replaced ET at the beginning of 1984. The purpose of the offset is to maintain continuity between ET and TDT at the transition. Planetary motions are now computed using Barycentric Dynamic Time (TDB), which is more uniform than TT because it accounts for relativistic corrections due to the Earth's motion in the gravitational potential of the solar system.

$$\text{TT} = \text{TAI} + 32.184 = \text{UTC} + (\text{number of leap seconds}) + 32.184 \qquad (3.3)$$

There is a subtle relativistic distinction between coordinate time and dynamic time, which is not significant for most practical purposes. The counterpart to TT is Geocentric Coordinate Time (TCG), which differs in rate from TT by about 0.7 parts per billion. TT and TCG were coincident on January 1, 1977 and now differ by 0.42 seconds. The rate difference from TT can be important to long term measurements.

3.1.4 TDB - Barycentric Dynamic Time

Barycentric Dynamic Time (TDB) is the same as Terrestrial Dynamic Time (TT) except for relativistic corrections to move the origin to the solar system barycentre. These corrections amount to as much as about 1.6 milliseconds and are periodic with an average of zero. The dominant terms in this correction are have annual and semi-annual periods.

$$\text{TDB} = \text{TT} + 0.001658 \sin(g) + 0.000014 \sin(2g) \text{ seconds} \qquad (3.4)$$

Where

$$g = 357.53 + 0.9856003\,(\text{JD} - 2451545.0) \quad \text{degrees} \qquad (3.5)$$

and JD is the Julian Date.

There is a subtle relativistic distinction between coordinate time and dynamic time, which is not significant for most practical purposes. The counterpart to TDB is Barycentric Coordinate Time (TCB), which differs in rate from TDB by about 15.5 parts per billion. TDB and TCB were coincident on January 1, 1977 and now differ by 9.3 seconds. The rate difference from TDB can be important to long term measurements.

3.2 Earth rotation times

3.2.1 UT1 - Universal Time

Universal Time (UT1) is a measure of the actual rotation of the Earth. It is independent of observing location. UT1 is essentially the same as the now discontinued Greenwich Mean Time (GMT). It is the observed rotation of the Earth with respect to the mean sun corrected for the observer's longitude with respect to the Greenwich Meridian and for the observer's small shift in longitude due to polar motion.

Since the Earth's rotation is not uniform, the rate of UT1 is not constant, and its offset from atomic time is continually changing in a not completely predictable way. As of December 1995, UT1 was drifting about 0.8 seconds per year with respect to atomic time (TAI or UTC). Since UTC is intentionally incremented by integer seconds (leap seconds) to stay within 0.7 seconds of UT1. The difference between UT1 and UTC is never greater than this. The difference, DUT1 = UT1 - UTC is monitored by the International Earth Rotation Service and published weekly in IERS Bulletin A along with predictions for a number of months in the future.

$$UT1 = UTC + DUT1 \text{ (from the IERS bulletin A)} \tag{3.6}$$

Note that when a leap second is added to or subtracted from UTC, the value of DUT1 is discontinuous by one second. UT1 is continuous, and UTC is incremented or decremented by integer seconds to stay within 0.7 seconds of UT1.

3.2.2 The UT0

UT0 (UT-zero) is an observatory-specific version of UT1 in the sense that UT0 contains the effect of polar motion on the observed rotation of the Earth. Polar motion is equivalent to a change in latitude and longitude of points on the Earth's surface with respect to the Earth's instantaneous rotation axis. The conversion from UT1 to a local observatory time with respect to the mean sun or stars is now done as a set of coordinate rotations that do not explicitly use UT0 as an intermediate step.

$$UT1 = UT0 - \left[\frac{x}{15}\sin\lambda_0 + \frac{y}{15}\cos\lambda_0\right]\tan\varphi_0 \tag{3.7}$$

Where λ_0 and $\varphi 0$ are the mean geographic coordinates for a given instrument, referring to a mean position Po of the geographic North Pole. x and y are the coordinates of an instantaneous pole of rotation in a horizontal frame centered at Po and oriented at the Greenwich meridian. These coordinates are computed a posteriori when the polar motion is exactly known and published at the end of the year by the IERS (International Earth Rotation Service, Bulletin A). The observation, which is made at the point of coordinates, (λ,φ) can be exactly known this way:

$$\varphi = \varphi_0 + x\cos\lambda_0 - y\sin\lambda_0 \tag{3.8}$$

$$\lambda = \lambda_0 + (x\sin\lambda_0 + y\cos\lambda_0)\tan\varphi_0 \tag{3.9}$$

3.2.3 The UT2

UT2 appears to be of mostly historical interest. Before 1972 the time broadcast services kept their time signals within 0.1 seconds of UT2, which is UT1 with annual and semi-annual variations in the Earth's rotation removed. The formal relation between UT1 and UT2 is

$$\begin{aligned} UT2 = UT1 &+ 0.022 * \sin(2 * Pi * t) - 0.012 * \cos(2 * Pi * t) - \\ &0.006 * \sin(4 * Pi * t) + 0.007 * \cos(4 * Pi * t) \end{aligned} \qquad (3.10)$$

Where

$$t = 2000.0 + (MJD - 51544.03) / 365.2422 \qquad (3.11)$$

is the Besselian day fraction, and MJD is the Modified Julian Date (Julian Date - 2400000.5).

3.2.4 Sidereal Time

Sidereal time is the time derived from the Earth's rotation with respect to the stars. Apart from small effects of rapid fluctuations in the Earth's rotation rate and polar motion, local sidereal time is the hour angle of the true sidereal equinox. Because of precession and nutation, the equinox is not fixed on the celestial sphere. In addition, the motion of the geographic poles and the lunisolar variations of the vertical, the local meridian plane is not fixed relative to the Earth. The motion of the equinox in hour angle is the resultant of the separate motions of the meridian and the equinox on the celestial sphere. The measure of the time by diurnal motion of the true equinox is known as the apparent sidereal time. The expression for the hour angle of the true equinox, referred to the instantaneous local celestial meridian, in terms of the uniform dynamical measure of time t is given as,

$$\begin{aligned} \tau = \tau_0 + \int \omega dt & \qquad \text{Rotation of the Earth} \\ + \psi_1 \cos\varepsilon^0 - a & \qquad \text{General precession in right ascension} \\ + \Delta\psi\cos\varepsilon_0 - \frac{1}{2}\Delta\psi\sin\varepsilon_0 & \qquad \text{Equation of equinoxes} \\ + \Delta h & \qquad \text{Polar motion} \\ + \delta h & \qquad \text{Variation of vertical} \end{aligned} \qquad (3.12)$$

Where ε^0 is the mean obliquity of the epoch, ε_0 the mean obliquity of the date, w the angular rate of rotation and $\Delta\psi_1$ the lunisolar nutation in longitude referred to the ecliptic epoch. The apparent inequality in apparent sidereal time is the equation of the equinox. The measure of the time defined by the diurnal motion of the mean equinox is the mean sidereal time. It is the apparent sidereal time minus the equation of the equinoxes.

The mean sidereal day is the duration of the time interval between two successive upper transits of the mean equinox of date relative to a fixed meridian. An apparent sidereal day is simply defined with respect to transit of the true equinox of date. It follows from definition that the mean sidereal day is shorter than the Earth's sidereal period of rotation ($P_\oplus$) by the daily precession in right ascension, $0^s.008412 + 5^s.1 \times 10^{-6}\, T_E$,

$$(1 \text{ mean sidereal day}) / P_\oplus = 0.999999902907 - 5.9 \times 10^{-11}\, T_E \qquad (3.13)$$

Here T_E is the time interval measured in Julian centuries since 12h Jan.0, 1900 E.T= Jan .$0^d.5$, 1900.

$$(1 \text{ mean solar day} / 1 \text{ mean sidereal day}) = [24^h + (\frac{1}{36525}\frac{d\alpha_{FMS}}{dT_U})] / 24^h$$
$$= 1.002737909265 + 5.89 \times 10^{-11}\, T_U \qquad (3.14)$$

Alternatively, apart from the negligible secular term, the ratio of sidereal day of 86400 mean sidereal seconds to this interval is,

$$(\text{Mean sidereal day} / \text{mean solar day}) = 0.997269566414 \qquad (3.15)$$

The universal time at any instant is obtained by multiplying the sidereal interval since 0^h U.T. by this fixed conversion factor. Inversely, the ratio of the mean solar day to the mean: sidereal day is 1.002737909265 [40].

3.2.5 GMST - Greenwich Mean Sidereal Time

By convention, the reference points for Greenwich Sidereal Time are the Greenwich Meridian and the vernal equinox (the intersection of the planes of the Earth's equator and the Earth's orbit, the ecliptic). The Greenwich sidereal day begins when the vernal equinox is on the Greenwich Meridian. Greenwich Mean Sidereal Time (GMST) is the hour angle of the average position of the vernal equinox, neglecting short-term motions of the equinox due to nutation.

In conformance with IAU conventions for the motion of the Earth's equator and equinox, GMST is linked directly to UT1 through the equation

$$\text{GMST (in seconds at UT1=0)} = 24110.54841 + 8640184.812866 * T + 0.093104 * T\text{^}2 - 0.0000062 * T\text{^}3 \qquad (3.16)$$

Where T is in Julian centuries from 2000 Jan. 1 12h UT1

$$T = d / 36525 \qquad (3.17)$$

$$d = JD - 2451545.0 \qquad (3.18)$$

3.2.6 GAST - Greenwich Apparent Sidereal Time

Greenwich Apparent Sidereal Time (GAST) is Greenwich Mean Sidereal Time (GMST) corrected for the shift in the position of the vernal equinox due to nutation. The smoothly varying part of the change in the Earth's orientation (precession) is already accounted for in GMST. The right ascension component of nutation is called the "equation of the equinoxes"

$$\text{GAST} = \text{GMST} + (\text{equation of the equinoxes})$$

3.2.7 LMST - Local Mean Sidereal Time

Local Mean Sidereal time is GMST plus the observer's longitude measured positive to the east of Greenwich. This is the time commonly displayed on an observatory's sidereal clock.

$$\text{LMST} = \text{GMST} + (\text{observer's east longitude}) \tag{3.19}$$

3.2.8 LST - Local Sidereal Time

The definition of Local Sidereal Time given in the glossary of the Explanatory Supplement to the Astronomical Almanac is "the local hour angle of a catalog equinox." This fits the common textbook definition

$$\text{Hour Angle} = \text{LST} - \text{Right Ascension} \tag{3.20}$$

Where the right ascension can be specified in one of the catalog coordinate systems B1950 (FK4) or J2000 (FK5).

ANNEX 4

The CCD camera

In the years 80, to shoot one sunset was an impracticable operation with a video camera. The tubes of the camera did not resist. With the apparition of the CCD sensors, the operators could finally use the video camera as the film cameras, to record some stages to high contrasts. A Charge Coupled Device (CCD) is a semiconductor device in which finite isolated charge-packets are transported from one position in the semiconductor to the adjacent one by sequential clocking of an array of gates [41].

4.1 CCD geometric features

The present CCDs are matrixes of two dimensions. The sizes are given in numbers of pixels that define the resolution of images for an optical data. The most current matrixes have sizes typical of 340 x280 pixels. The biggest can present matrixes up to 4000 x 4000 pixels. The pixels themselves have variable sizes according to the models. They can go from 6 to 40 µm (distances between centres of the pixels). The photosensitive area of a CCD depends on whether the chip is interline-transfer or frame transfer. Full frame transfer chips frequently offer the best sensitivity since the photosensitive area is virtually 100% of the entire CCD .

4.2 Reading of the CCD matrixes

The exposition of the CCD matrix to light causes the accumulation of the electric charges in its photosites. The Reading process consists in bringing these charges in sequence toward the output of the CCD, where an electric current can be measured.

The accumulated charges are displaced toward the output with the help of clock signals produced by a control circuit. There are two types of clock signals:

1- Vertical clocks: these clocks shift all lines by one row.

2- Horizontal clocks: these clocks shift the content of the horizontal register toward the output of the CCD.

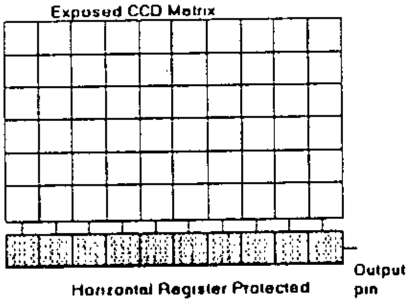

Figure 4-1. Reading of a CCD Matrix.

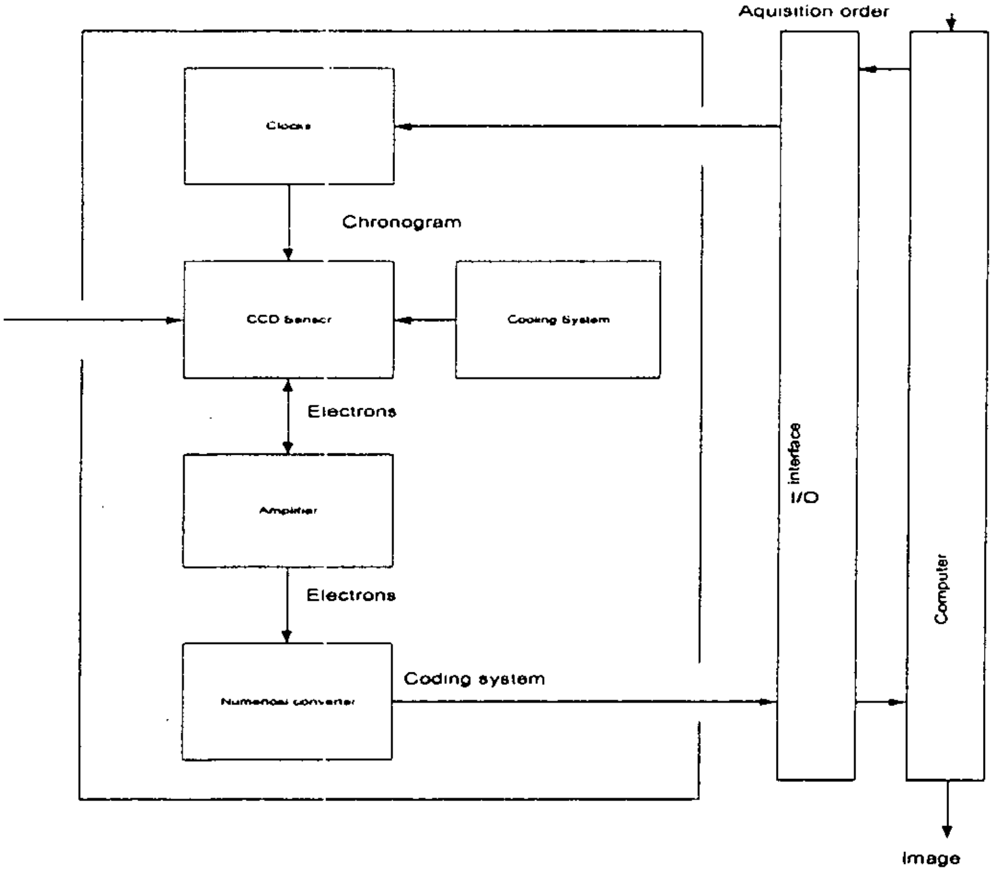

Figure 4-2 CCD output control circuit.

The output signal is read and amplified by an analog stage, then converted to a digital signal. Figure 4-2 shows the elements that control the output of the image from a CCD camera.

4.3 Image integration

When no clock signal is active, no pixel is transferred. In this state all the received light on the pixels generate the electronic image. When the integration of an image is finished, the totality of pixels are transferred to the output. Depending on how the storage CCD arrays are configured, different methods have been developed to read the light intensity values from the storage array. These modes are:

a- Frame Mode: it is the standard interlace mode of horizontal line transfer. For each frame, the odd lines are transferred first followed by the even lines. In this mode, every line of sensors is read separately each 0.04 sec.

b- Field Mode: in this mode, two adjacent lines are combined together and shifted out during each transfer.

c- Enhanced Vertical Definition Mode: it is used to establish a compromise between the advantages and the disadvantages of the two above operation modes. In this mode, each line is read separately during 50 sec.

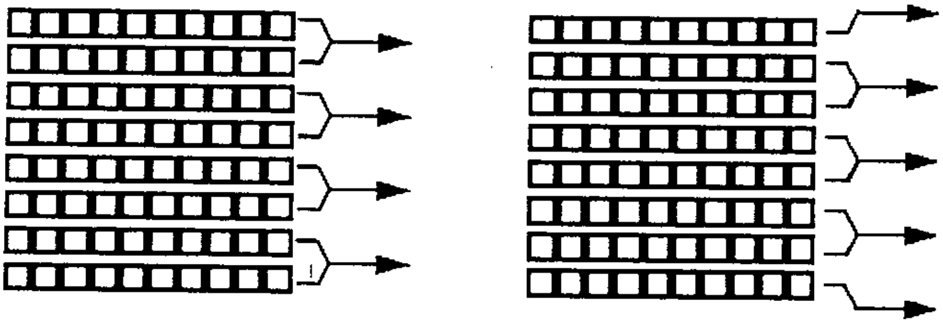

Field Mode

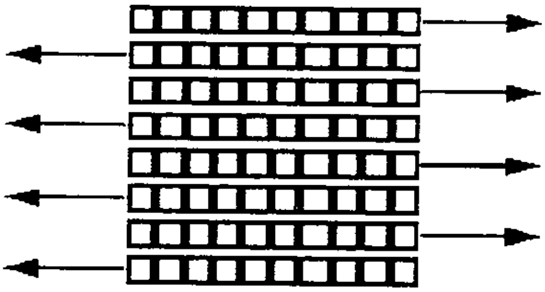

Frame Mode

Figure 4-3. Reading modes of the CCD sensors.

During the exposure operation, the clock cycles are stopped and the charges are accumulating in the CCD. At the end of exposition, the clock cycles are launched to transfer and to measure the accumulated charges. This process can be long enough that parasitic charges continue to accumulate on the image. This parasitic signal is more important for the lines situated at the bottom of the image than those situated on top. If the exposure time is shorter compared to the time of reading, a trail upwards on the image is produced (smearing). This problem can be resolved by two ways:

1- The placement of an electronic shutter in front of camera. The shutter is opened at the beginning of the exposition and closed before the reading process is started.

2- The transfer of the useful part of the matrix in a protected area on the CCD [42].

The transfer itself can be done by several ways:

(a) Full frame transfer

The Full Frame Transfer is a mode where all the CCD lines are exposed to the light and participate in the image formation. The problem with this kind of matrices is that, during the reading process the photosites remain exposed to light. Since the reading time is not negligible, an important trail is produced on all the image pixels. To prevent this problem, a Full Frame CCD must be provided with an electromagnetic control shutter. Figure 4.4(a) shows the CCD of the Full Frame Transfer mode [42].

(b) Half frame transfer

Cameras working in this mode are full frame CCDs without electromagnetic control shutter. The matrix of this type is divided in two equal parts. The upper half is used for image integration and the lower one is protected. At the end of integration time, the charges in photosites of the upper half of the CCD matrix are transferred quickly to the protected lower half.

(c) Frame Transfer

In this mode of operation, the entire CCD sensors contents are shifted to a protected area in the chip before being read out. One half of the CCD area is used for detecting the image while the other is used for readout. Images acquired in the sensing region are transferred in a few milliseconds to the readout region. This process occurs concurrently with the subsequent exposures. This approach allows the detection to continue almost completely without interruption. Figure 4-4 (b) shows the CCD of the Frame Transfer mode [42].

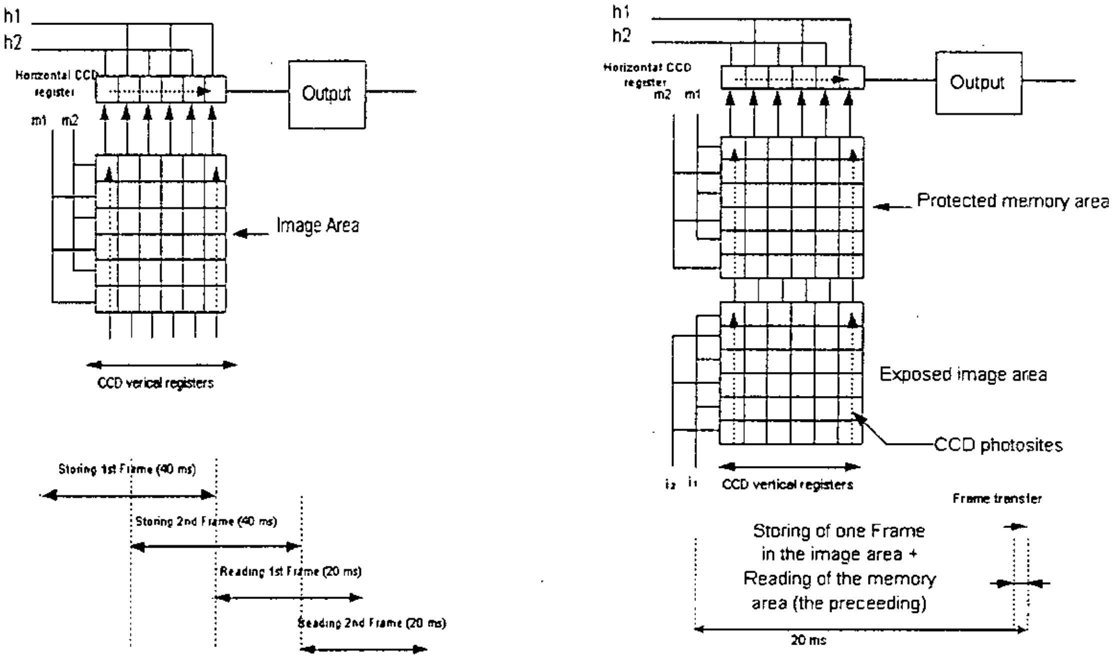

(a) *(b)*

Figure 4-4. (a) The Full Frame Transfer, (b) The Frame transfer.

(d) Interline transfer

In this mode, each active pixel of the CCD sensor is transferred to an adjacent shielded one. Then it is shifted to an output register for final readout. So, the electronic shuttering is not needed in this mode of operation. Figure 4.5 shows the CCD of Interline Frame Transfer mode.

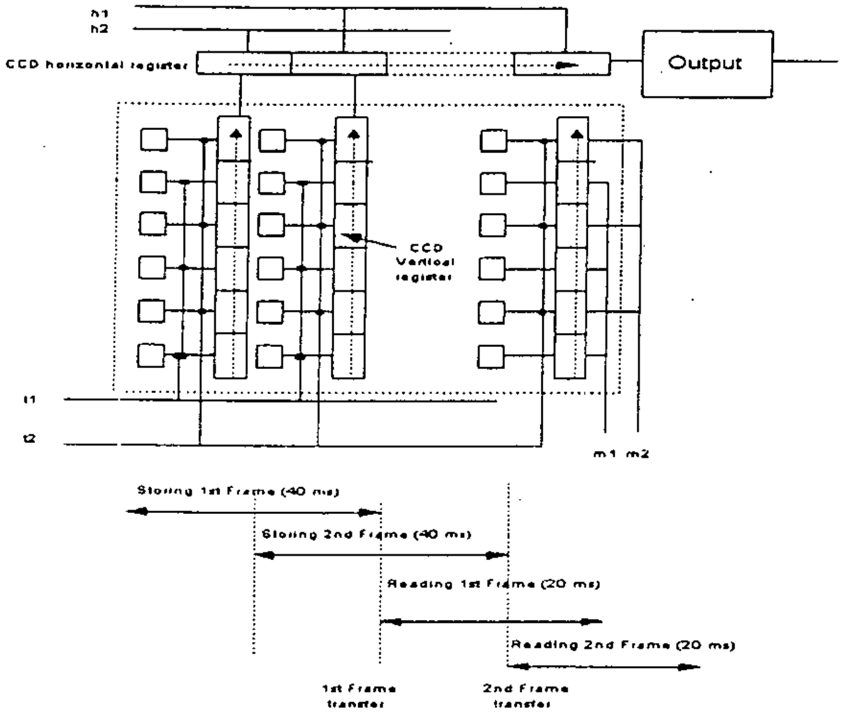

Figure 4-5. The Interline Frame Transfer.

ANNEX 5

5.1 Register map of the PC-TIO-10

Register	Offset Adresse (Hex)	Size	Type
Am9513A Register Group			
STCA			
Data Register	00	8 bits	Read and write
Command Register	01	8 bits	Write only
Status Register	01	8 bits	Read only
STCB			
Data Register	02	8 bits	Read and write
Command Register	03	8 bits	Write only
Status Register	03	8 bits	Read only
MC6821 Register Group			
PIA			
Port A Data Register	04	8 bits	Read and write
Port A Control Register	05	8 bits	Read and write
Port B Data Register	06	8 bits	Read and write
Port B Control Register	07	8 bits	Read and write

Table 1.1 The register map of the PC-TIO-10.

5.2 Register description

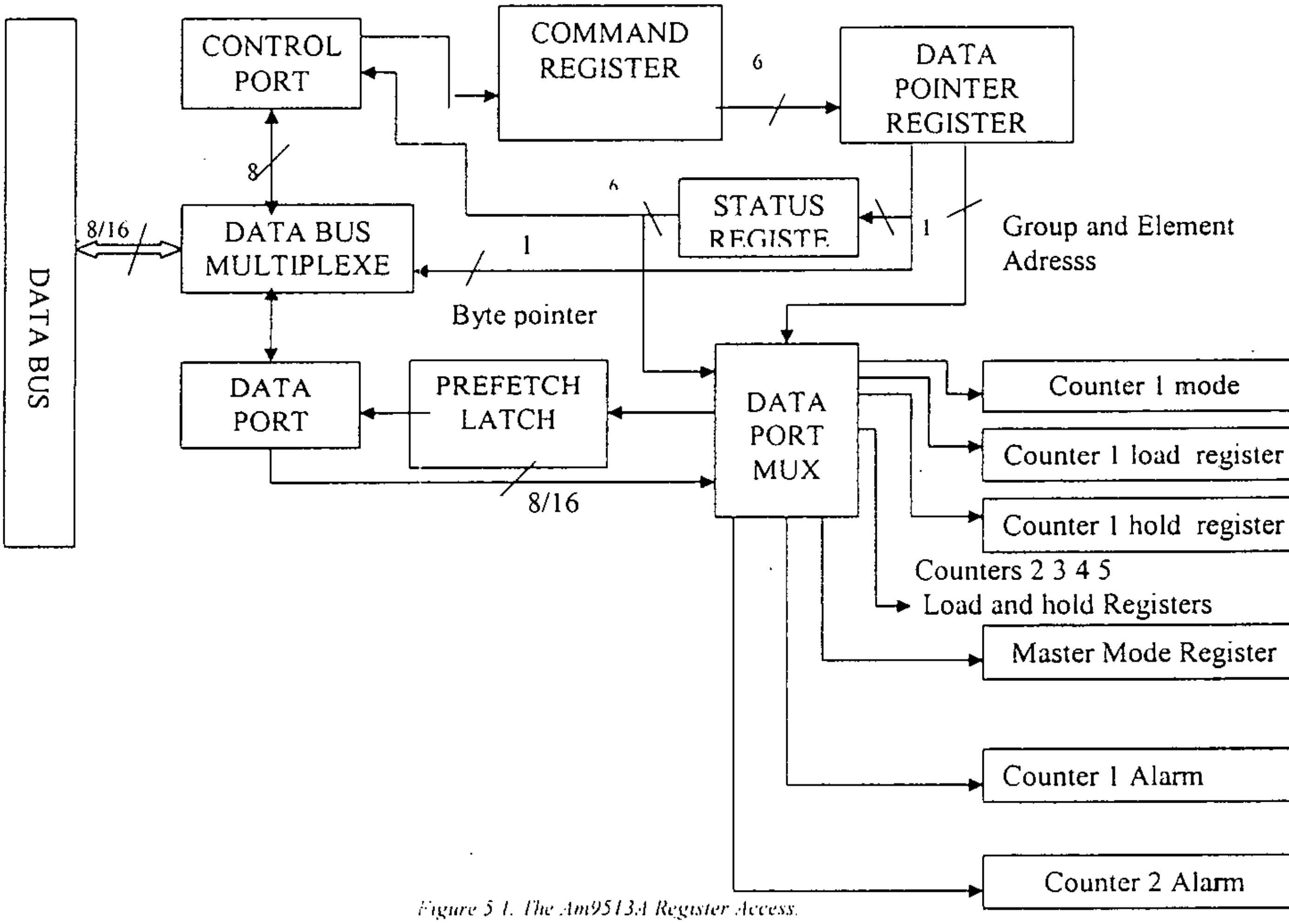

Figure 5.1. The Am9513A Register Access.

5.3 The Data Pointer Register

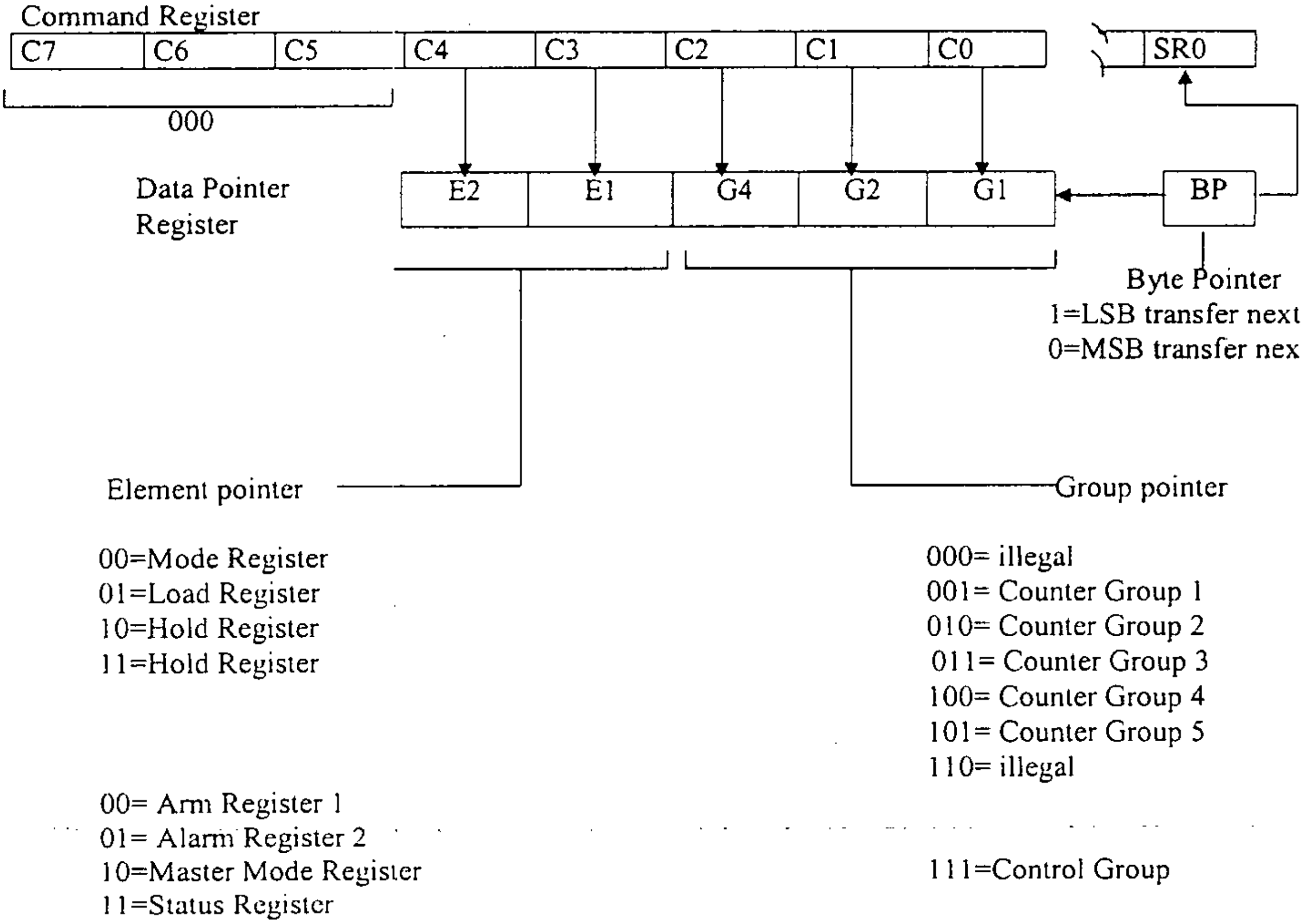

Figure 5.2. The Data Pointer Register.

5.4 The Master Mode Register

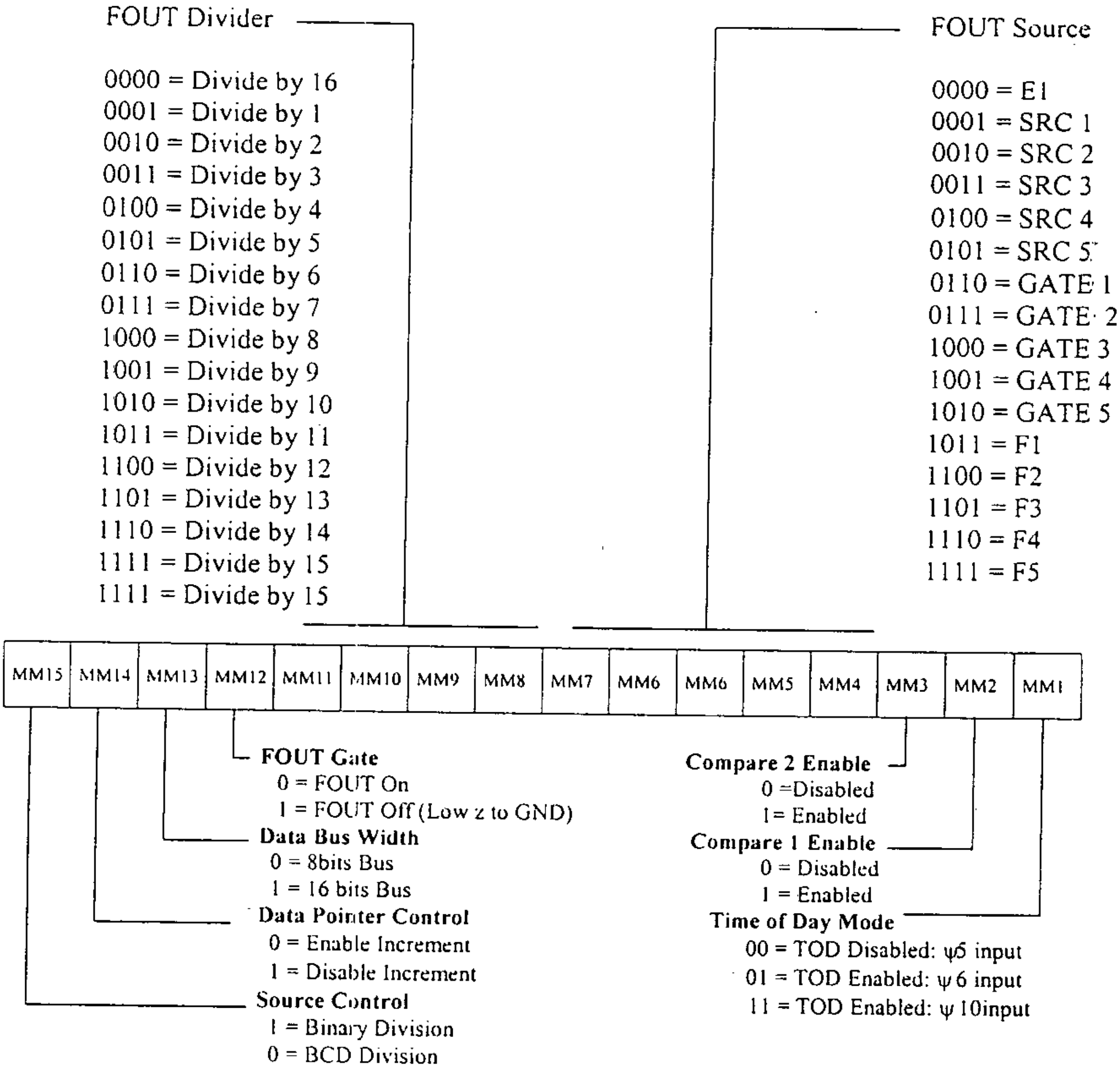

FOUT Divider

0000 = Divide by 16
0001 = Divide by 1
0010 = Divide by 2
0011 = Divide by 3
0100 = Divide by 4
0101 = Divide by 5
0110 = Divide by 6
0111 = Divide by 7
1000 = Divide by 8
1001 = Divide by 9
1010 = Divide by 10
1011 = Divide by 11
1100 = Divide by 12
1101 = Divide by 13
1110 = Divide by 14
1111 = Divide by 15
1111 = Divide by 15

FOUT Source

0000 = E1
0001 = SRC 1
0010 = SRC 2
0011 = SRC 3
0100 = SRC 4
0101 = SRC 5
0110 = GATE 1
0111 = GATE 2
1000 = GATE 3
1001 = GATE 4
1010 = GATE 5
1011 = F1
1100 = F2
1101 = F3
1110 = F4
1111 = F5

FOUT Gate
0 = FOUT On
1 = FOUT Off (Low z to GND)

Data Bus Width
0 = 8bits Bus
1 = 16 bits Bus

Data Pointer Control
0 = Enable Increment
1 = Disable Increment

Source Control
1 = Binary Division
0 = BCD Division

Compare 2 Enable
0 =Disabled
1= Enabled

Compare 1 Enable
0 = Disabled
1 = Enabled

Time of Day Mode
00 = TOD Disabled: ψ5 input
01 = TOD Enabled: ψ6 input
11 = TOD Enabled: ψ 10input

Figure 5.3 The Master Mode Register.

5.5 The Frequency Scaler Ratios

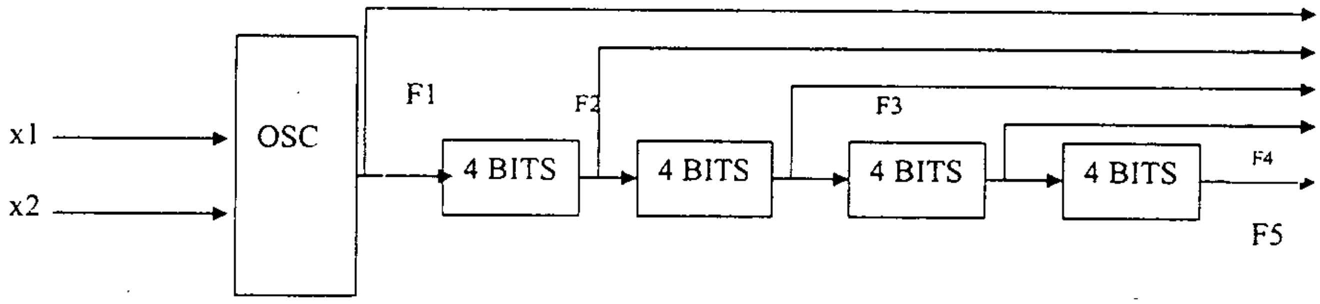

FREQUENCY SCALER

Frequency	BCD Scaling MM15=1	Binary Scaling MM15=0
F1	OSC	OSC
F2	F1 ψ10	F1ψ16
F3	F1ψ100	F1 ψ256
F4	F1ψ1000	F1 ψ4,096
F5	F1ψ10,000	F1ψ65,536

Figure 5.4. The Frequency Scaler Ratios.

5.6 The Counter Mode Register

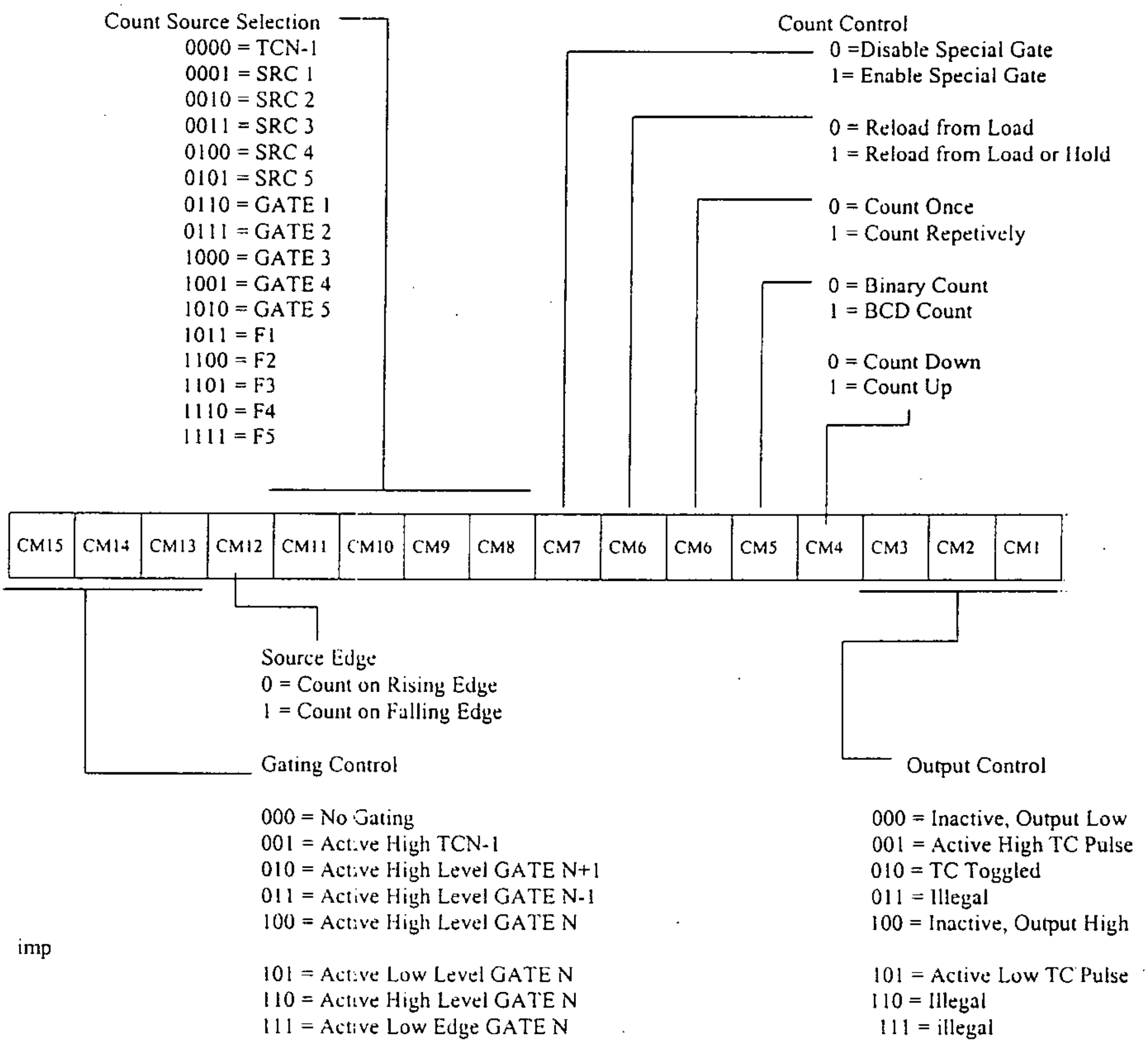

Figure 5.5.The Counter Mode Register.

It exists 25 modes of operation according to bits state of the counter mode register.

5.7 The Am9513A Data Register

The data Registers are used to read from or write to any of the 18 internal registers of teham9513A. The Am9513A Command Registers must be written to in order to select the register to be accessed by the Am9513A Data Registers. The internal registers accessed by the Am9513A Data Registers are as follow:

- Counter Mode Registers for Counters 1, 2, 3, 4, and 5.
- Counter Load Registers for counters 1, 2, 3, 4, and 5.
- Counter Hold Registers for counters 1, 2, 3, 4, and 5.
- Compare Registers for counters 1 and 2.

- Master Mode Register.

All these registers are 16-bit registers that must be accessed through an 8-bit port, least significant byte first.

Address: Base address + 00(hex) for the Am9513A STCA.
Base address + 00(hex) for the Am9513B STCB

Figure 5.7 shows the internal am9513 registers and their logic counter logic groups.

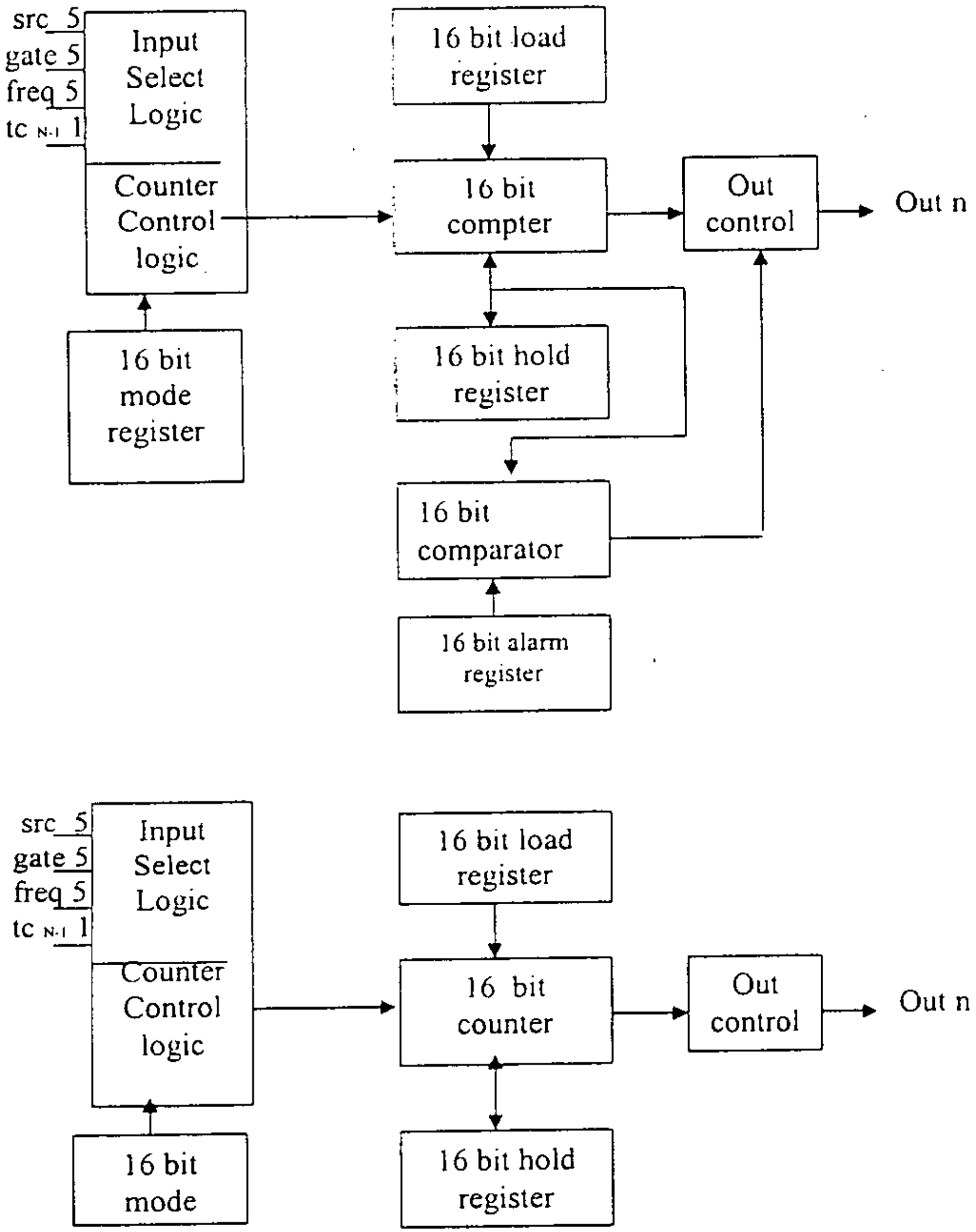

Figure 5.6 The Counter Logic Groups.

5.8 The Am9513A Command Register

The Am9513A command registers are 8-bit registers. They control the overall operation of the Am9513A Counter/Timer and the selection of the internal registers that are accessed through the Am9513A Data Registers.

Address:

Base address + 01(hex) for the Am9513 STCB.

Base address + 03(hex) for the Am9513 STCB.

The possible commands are summarized on the following table:

Command Code								Command Description
C7	C6	C5	C4	C3	C2	C1	C0	
0	0	0	E2	E1	G4	G2	G1	Load Data Pointer with contents of E et G fields
0	0	1	S5	S4	S3	S2	S1	Arm counting for all selected counters
0	1	0	S5	S4	S3	S2	S1	Load counting of specified source into all selected counters
0	1	1	S5	S4	S3	S2	S1	Load and Arm all selected counters
1	0	0	S5	S4	S3	S2	S1	Disarm and save all selected counters
1	0	1	S5	S4	S3	S2	S1	Save all selected counters
1	1	0	S5	S4	S3	S2	S1	Set Toggle out (HIGH) for counter N(001<=N<=101)
1	1	1	S5	S4	S3	S2	S1	Clear Toggle out (LOW) for counter N N(001<=N<=101)
1	1	1	0	1	N4	N2	N1	Step Counter NN(001<=N<=101)
1	1	1	0	0	N4	N2	N1	Set MM14 (Disable Data Pointer Sequencing)
1	1	1	1	0	N4	N2	N1	Set MM12 (Gate off FOUT)
1	1	1	0	1	0	0	0	Set MM13 (Enter 16 bits bus mode)
1	1	1	0	1	1	1	0	Clear MM14 (Enable Data Pointer Sequencing)
1	1	1	0	1	1	1	1	Clear MM12 (Gate on FOUT)
1	1	1	0	0	0	0	0	Clear MM13 (Enter 8 bits bus mode)
1	1	1	0	0	1	1	0	Enable Prefetch for operations

Table 2.2.The word commands of Command Register.

5.9 The Status Registers

The Am9513A Status registers give information about the output pin of each counter in the Am9513A. In addition, these registers indicate the current setting of the Byte pointer, which indicates whether the next byte to be accessed is in the most significant byte or the least significant byte.

Address:

Base address + 01(hex) for the Am9513 STCB.

Base address + 03(hex) for the Am9513 STCB.

ANNEX 6

6.1 Images in the EureCard Primo

The flow of images in the EureCard Primo is shown in Figure 6-1 [38].

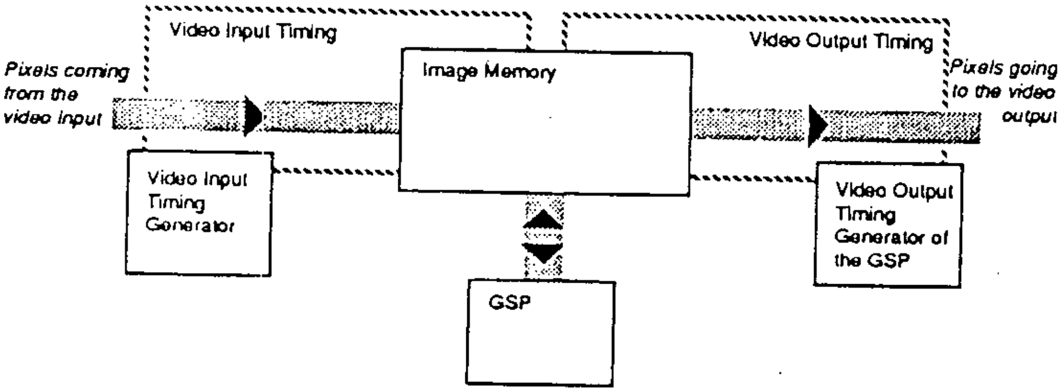

Figure 6-1. Images flow in the EureCard Primo.

The image memory is dedicated to contain images. Three devices have got access to this memory:

- The video input, which writes images into the memory.
- The video output, which reads stored images to display them.
- The GPS, which is able to read and write the image memory at any time in order to process and analyze stored images.

6.2 Data transfer

The digitized pixels are stored in the video memory by the DMA machine through the memory random access bus. During an acquisition, this bus is shared by the GPS and the acquisition machine; see Figure 6-2.

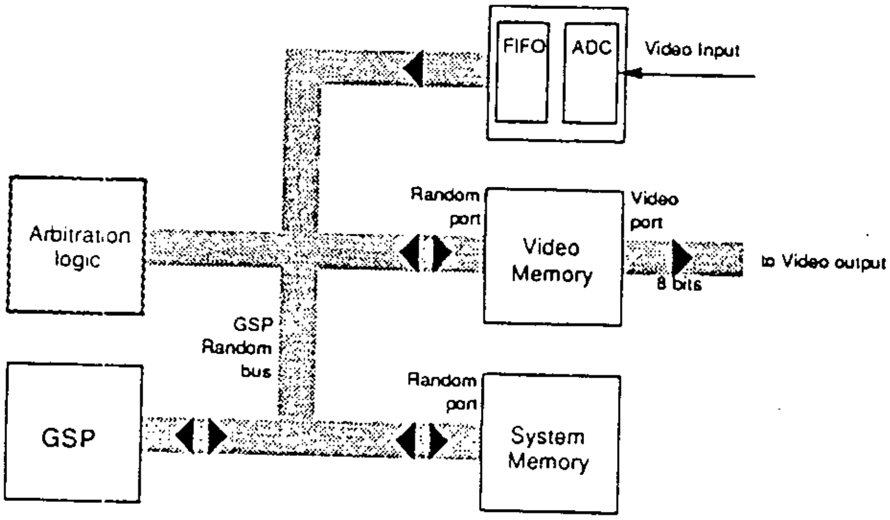

Figure 6-2. Data transfer block diagram.

6.3 Input video to the EureCard Primo

Figure 6-3 shows the block diagram of the video input module structure [38].

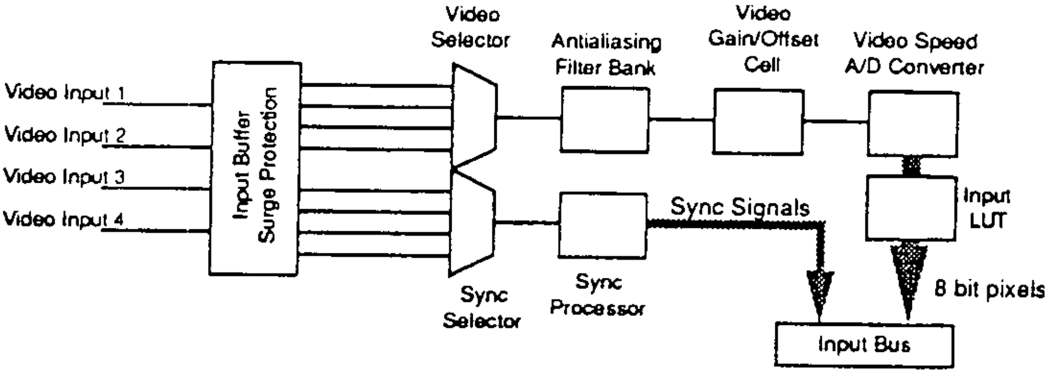

Figure 6-3. The input Video Module.

The video signal enters by one of the four inputs. The first path processes the video signal:

a- Selection of one of the four input channels; [0.3].

b- Antialiasing filter bank ranges from [0.5]:
    0: no filter.
    1: 5 MHz cut off frequency.
    2: 2.5 MHz cutoff frequency.
    3: Pal filter.
    5: NTSC filter.

c- Gain and offset control, [0.255].

d- Analogue to digital conversion and Input look Up table.

The second path deals with the synchronization information:

a- Selection of one of the four input channels for synchronization; [0.5]:
    0: synchronize on channel 0.
    1: synchronize on channel 1.
    2: synchronize on channel 2.
    3: synchronize on channel 3.
    5: internal synchronization.

b-Extraction of the synchronization signals (horizontal and vertical) and the level of the sync detector selection [0.3]:
    0: 50 mV
    1: 75 mV
    2: 100 mV
    3: 125 mV

6.4 Image acquisition and visualisation

The EureCard Primo has a special devices dedicated to acquire images. Video memories are associated with busses that carry images between processing devices. The video output deceives digital images and generates a video signal suitable for driving a VGA monitor. In all case, a hardware device is very important: the mapper.

The mapper manages in a programmable way the memory, the input and output video buses.

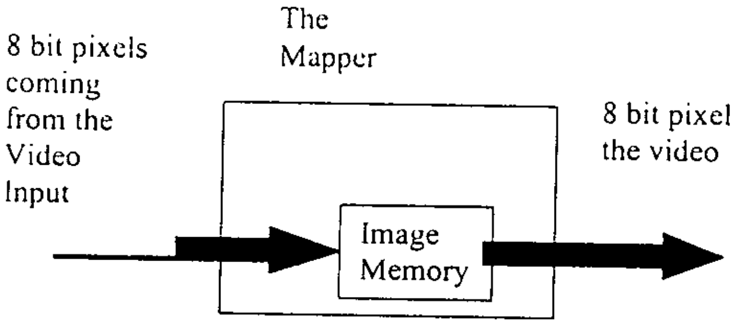

Figure 6-4. The Mapper.

Several modes of acquisition can be selected:

1- **Normal acquisition:**

It is represented by the waveforms shown in Figure 6-5 [38].

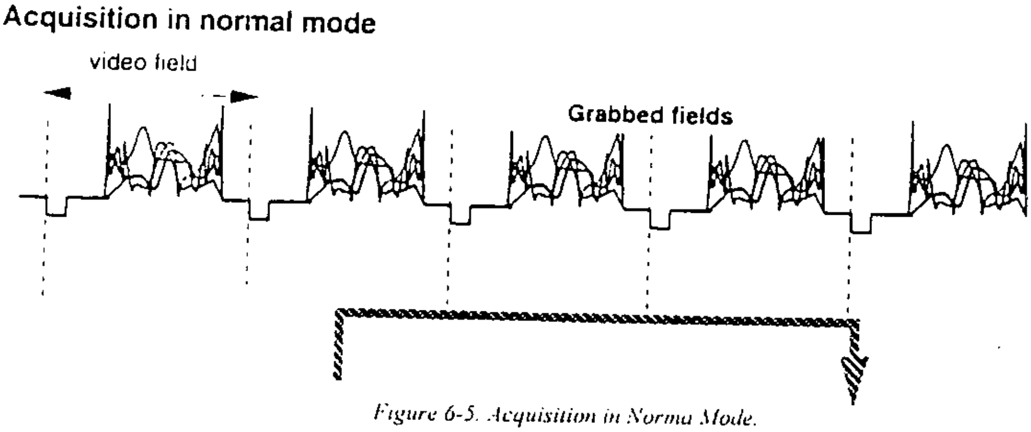

Figure 6-5. Acquisition in Norma Mode.

2- **Continuous Mode**

It is described by the waveforms shown in Figure 6-6.

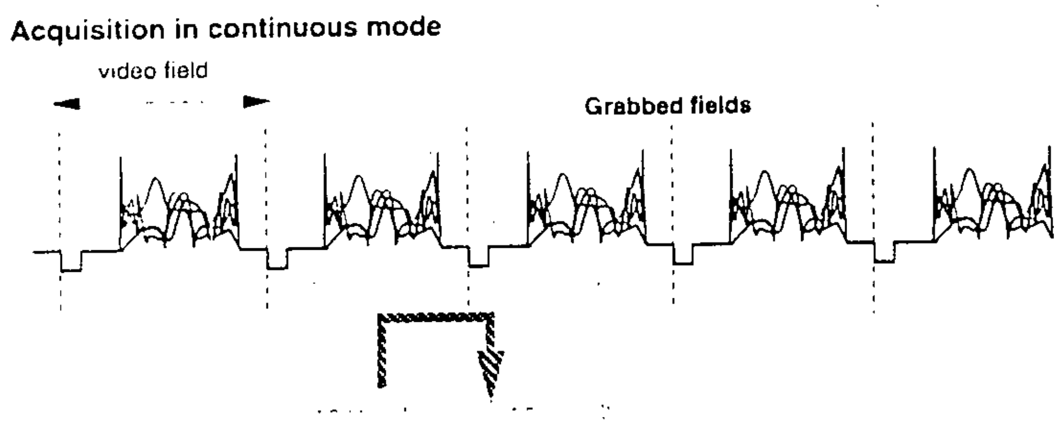

Figure 6-6. Acquisition in Continuous Mode.

3- Background Mode

This mode allows easy parallel processing between the acquisition process and the GSP. This acquisition is automatically stopped after the specified number of fields. It is represented by the waveforms shown in Figure 6-7.

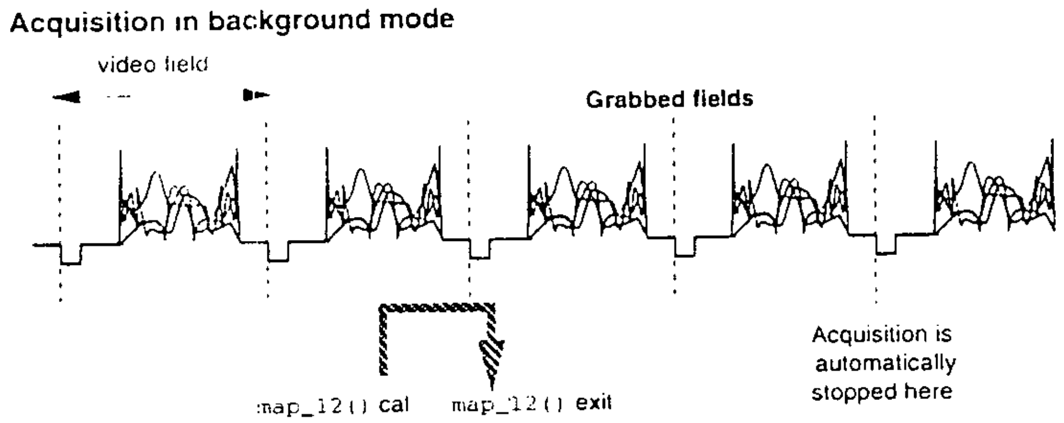

Figure 6-7. The Acquisition in Background Mode.

6.5 Video output

The EureCard Primo supports two display configurations:

1- Single monitor configuration: in this mode the monitor is connected to the PC's VGA card. The image stored in the EureCard Primo memory is mixed with the PC's image to go to a single VGA monitor.

2- Dual monitor configuration: in this mode the EureCard Primo uses its own VGA monitor to display its images. The principle of output operation is shown in Figure 6-8 [38].

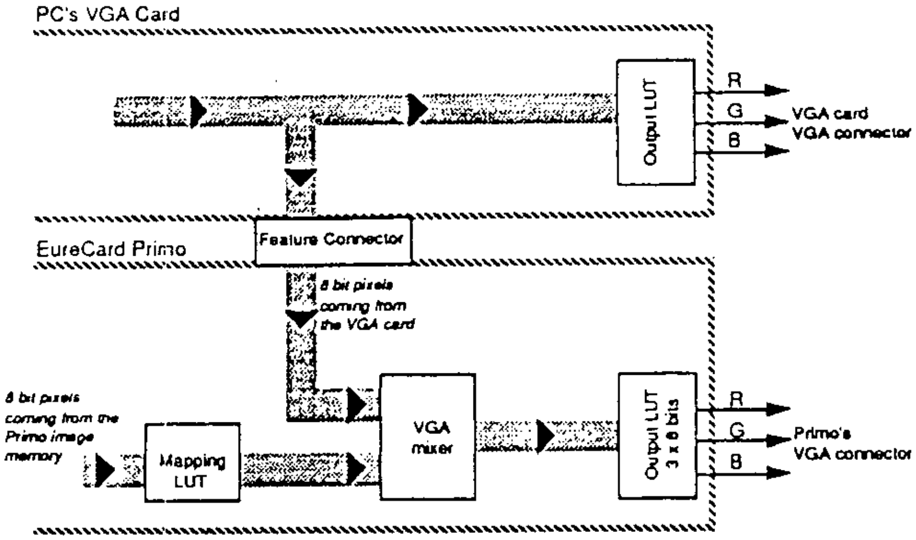

Figure 6-8. The Video Output Principle.

The pixels coming from the VGA card are read through the VGA feature connector. They are sent with pixels coming from the EureCard Primo image memory to the VGA mixer. The VGA mixer is responsible for the selection of pixels that will come either from the VGA card or from the EureCard Primo image. Its output is fed to the video Digital to Analog Converter, which includes a triple 8-bit look up table. Inside the VGA mixer, the pixels coming from the VGA card are continuously compared with a Key color. An 8-bit value restricts the comparison to some bits; see Figure 6.9.

The result is mixed with the blanking signal coming from the GSP to generate the final selection signal.

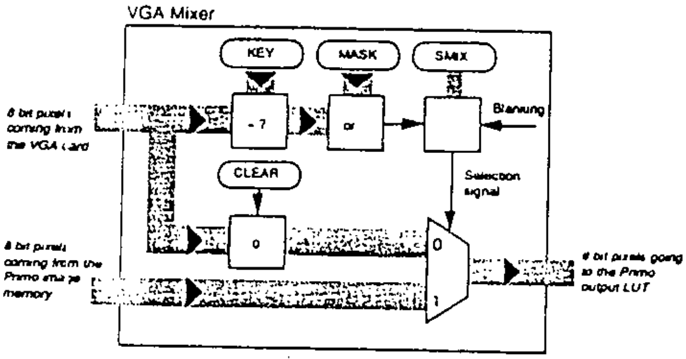

Figure 6-9. The VGA Mixer.

6.6 Output Look Up Table

The Eurecard Primo output LUT is used to display both the pixels coming from the Eurecard Primo image and the PC's image. Its 256 entries must be shared between these two sources. The «mapping LUT», which maps every gray level of the EureCard Primo image into a valid entry of the output LUT, performs this operation; see Figure 6-10.

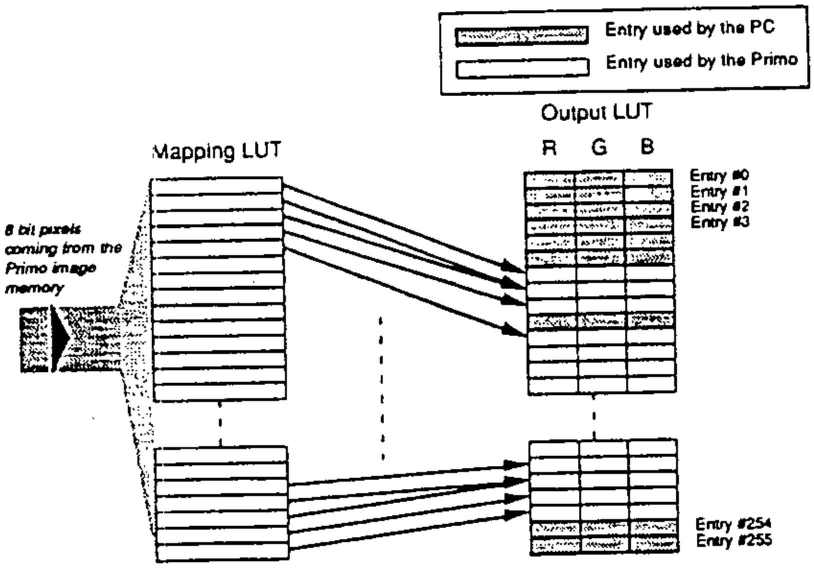

Figure 6-10. The Output Look Up Table.

6.7 Inputs and outputs control

The EureCard Primo provides a set of digital input and output lines. These states control the generation of trigger and strobe events used by grabbing operations. The trigger event specifies a combination of the input signals used to trigger an acquisition operation. It informs the EureCard Primo that the object to be grabbed is in position. The strobe event specifies a state to be imposed to the output signals during an acquisition operation.

6.7.1 Trigger event

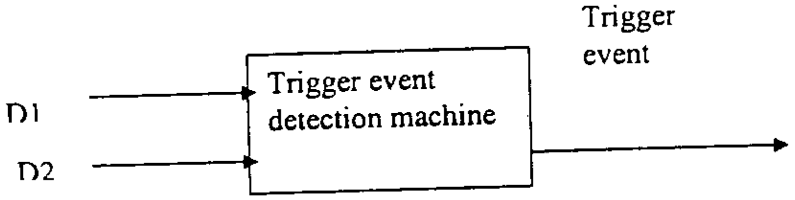

Figure 6-11. The trigger event.

The trigger event is computed from the status of D1 and D2 signals. The effect of each signal on the trigger event can be controlled, and therefore controlling the acquisition process. The input lines D1 and D2 can be programmed for a certain type of input signals. Those that exist on the EureCard Primo are:

- Check for a logical 'zero' state.
- Check for a logical 'one' state.
- Wait for a logical positive edge.
- Wait for a logical negative edge.
- Wait for a logical positive or negative edge.
- Don't care condition.

ANNEX 7

7.1 The filter associated with the linear interpolation

In the case of linear interpolation, the coefficients of the one dimensional filter h calculated from $\phi(x)$ are (1/4 1/2 1/4). In two dimension they are:

$$h(n) = \begin{pmatrix} 1/16 & 1/8 & 1/16 \\ 1/8 & 1/4 & 1/8 \\ 1/16 & 1/8 & 1/16 \end{pmatrix}$$

The filter h is a triangular low pass filter as shown in Figure 7.1. Its transfer modulus is represented in Figure 7.2.

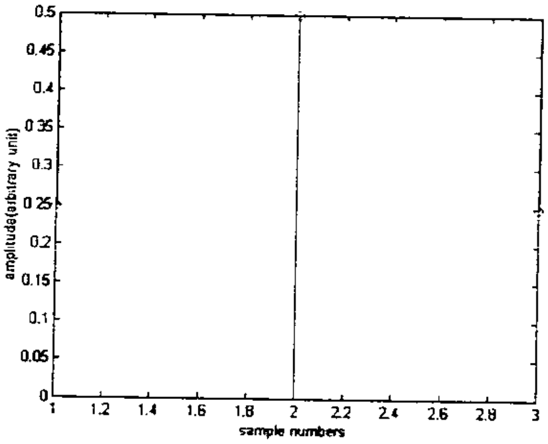

Figure 7.1. The filter h(n).

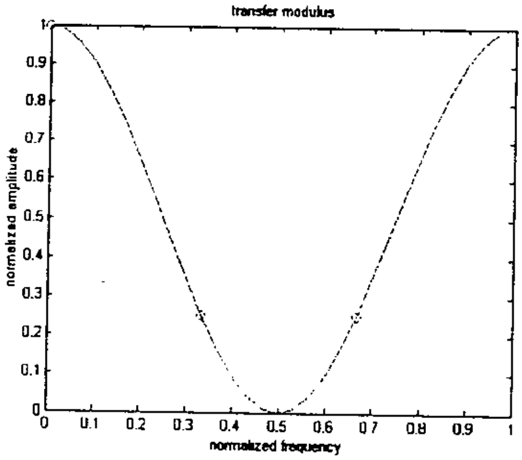

Figure 7.2. The transfer modulus.

7.2 Filters to reduce the noise in Sun images

Three types of low pass filters are tested on the detail images to reduce the residual noise in the processed Sun images. These filters are,

a . The first filter

Its coefficients in one dimension are (1/4 1/2 1/4). In two dimension, they are,

$$h(n) = \begin{pmatrix} 1/16 & 1/8 & 1/16 \\ 1/8 & 1/4 & 1/4 \\ 1/16 & 1/8 & 1/16 \end{pmatrix}$$

its characteristics are shown in Figure 7.1 and 7.2.

b. The second filter

Its coefficients in one dimension are (1/16 1/4 3/8 1/4 1/16). In two dimension, they are,

$$h(n) = \begin{pmatrix} 1/256 & 1/64 & 3/128 & 1/64 & 1/256 \\ 1/64 & 1/16 & 3/32 & 1/16 & 1/64 \\ 3/128 & 3/32 & 9/64 & 3/32 & 3/128 \\ 1/64 & 1/16 & 3/32 & 1/16 & 1/64 \\ 1/256 & 1/64 & 3/128 & 1/64 & 1/256 \end{pmatrix}$$

The filter *h* is a low pass filter as shown in Figure 7.3. Its transfer modulus is represented in Figure 7.4.

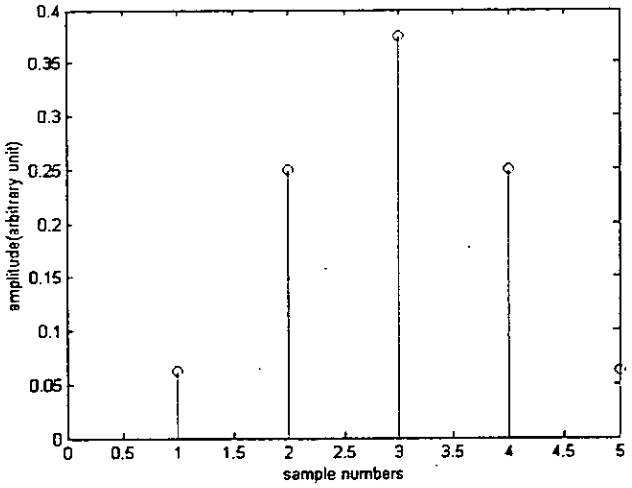

Figure 7.3. The filter h(n).

6.7.2 Strobe event

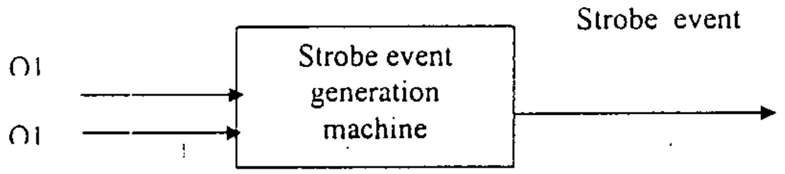

Figure 6-12. The Strobe event.

The output Strobe signal generation can also be controlled by programming the output lines Q1 and Q2. The possible programming states supplied by the EureCard Primo are:

- Immediately imposes a logical zero at this output.
- Immediately imposes a logical one at this output.
- The strobe machine controls the output; output a positive pulse during the strobe event.
- The strobe machine controls the output; output a negative pulse during the strobe event.

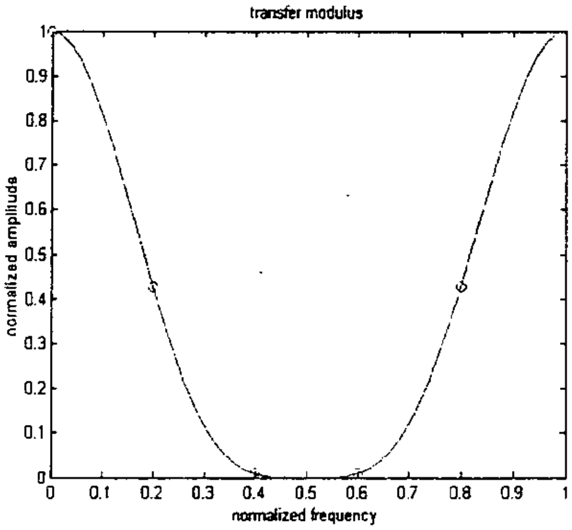

Figure 7.4. The transfer modulus.

c. The third filter

This filter is characterized in one dimension by the coefficients (1/64 3/32 15/64 5/16 15/64 3/32 1/64). In two dimension its coefficients are,

$$h(n) = \begin{pmatrix} 0.0002 & 0.0015 & 0.0037 & 0.0049 & 0.0037 & 0.0015 & 0.0002 \\ 0.0015 & 0.0088 & 0.0220 & 0.0293 & 0.0220 & 0.0088 & 0.0015 \\ 0.0037 & 0.0220 & 0.0549 & 0.0732 & 0.0549 & 0.0220 & 0.0037 \\ 0.0049 & 0.0293 & 0.0732 & 0.0977 & 0.0732 & 0.0293 & 0.0049 \\ 0.0037 & 0.0220 & 0.0549 & 0.0732 & 0.0549 & 0.0220 & 0.0037 \\ 0.0015 & 0.0088 & 0.0220 & 0.0293 & 0.0220 & 0.0088 & 0.0015 \\ 0.0002 & 0.0015 & 0.0037 & 0.0049 & 0.0037 & 0.0015 & 0.0002 \end{pmatrix}$$

The filter *h* is always a triangular low pass filter as shown in Figure 7.5. Its transfer modulus is represented by Figure 7.6.

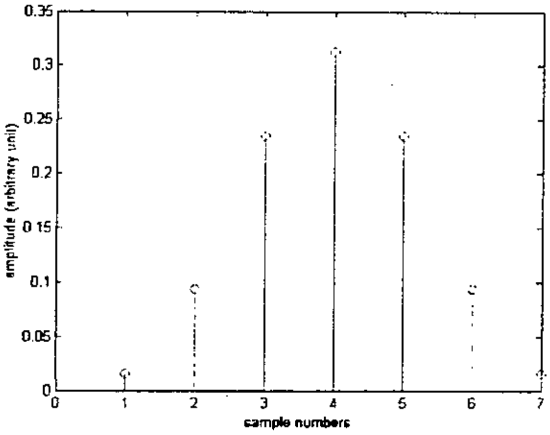

Figure 7.5. The filter h(n).

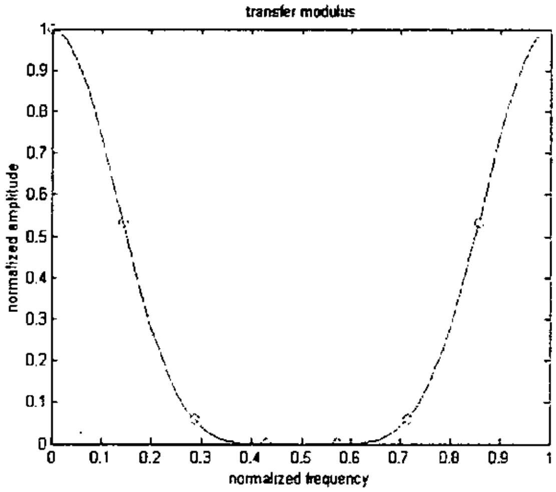

Figure 7.6 . The transfer modulus.

Résumé

Ce sujet s'inscrit dans le cadre de l'astronomie de position et comprend trois objectifs. Le premier consiste en l'étude de l'instrument utilisé pour observer le soleil ainsi que le développement des programmes nécessaires pour le calcul du diamètre solaire. Le deuxième comprend le développement des méthodes de traitement des images du Soleil acquise à l'astrolabe solaire. Le troisième étant l'étude de l'instrumentation choisie qui sera installé autour de l'astrolabe de Tamanrasset ainsi que le développement des programmes nécessaire pour son opération.

Mots clés: *Soleil, astrolabe solaire, diamètre solaire, distance zénithale, les ondelettes, paramètre de Fried.*

Abstract

This work deals with positional astronomy and with three objectives in sight. The first objective is to study the instrument used for Sun observation and provide the necessary programs to calculate the Sun diameter. The second objective is to develop the appropriate methods to process the acquired Sun images with the solar astrolabe. The third one is oriented to study the selected instrumentation that will be installed around the solar astrolabe of Tamanrasset and to develop the necessary software programs that control its operation.

Keywords: *Sun, solar astrolabe, solar diameter, zenithal distance, wavelets, Fried parameter.*

ملخص

هذه الوظيفة تدخل في إطار علم الفلك الموقعي، و تشتمل على ثلاثة محاور رئيسية.

المحور الأول: يتضمن دراسة معمقة للأسترلاب الشمسي و كيفية سيره و طريقة استعماله بالإضافة إلى تطوير البرامج الأساسية لحساب قطر الشمس.

المحور الثاني: يشتمل على تحضير البرامج المناسبة لمعالجة الصور الشمسية الملتقطة بواسطة الأسترلاب.

المحور الثالث: فيخص اختيار القطع الإلكترونية الملائمة و المكونة لجهاز التقاط الصور التي سيتم تنصيبها حول استرلاب تمنراست زيادة على إعداد البرامج الضرورية لسير هذه القطع.